Colloid mobility controlling processes in single fractures – a bottom-up approach

Dissertation
(kumulativ)
zur Erlangung des Grades doctor rerum naturalium
(Dr. rer. nat.)

vorgelegt dem Rat der Chemisch-Geowissenschaftlichen Fakultät
der
Friedrich-Schiller-Universität Jena

von Diplom Geologin Madeleine Stoll
geboren am 21.06.1987
in Mainz, Deutschland

Gutachter:

1. Prof. Dr. Thorsten Schäfer (Friedrich-Schiller-Universität Jena)
2. Prof. Dr. Eva Schill (Technische Universität Darmstadt)
3. Prof. Dr. Ruben Kretzschmar (Eidgenössische Technische Hochschule Zürich)

Tag der öffentlichen Verteidigung: 04.07.2018

To my family

“Your assumptions are your windows on the world.
Scrub them off every once in a while, or the light won't come in.”

— Isaac Asimov

Declaration of authorship

I herewith declare that I autonomously carried out my Ph.D. thesis entitled "Colloid mobility controlling processes in single fractures – a bottom-up approach".

The chapters 2, 3, 4, and 5 of my cumulative Ph.D. thesis are peer reviewed publication manuscripts, which are either already published in or submitted to international scientific journals. In the following, the journals, the status of the manuscripts, the involved co-authors and their contribution to the respective manuscript are listed:

Chapter 2: **Stoll, M., Huber, F.M., Darbha, G.K., Schill, E. and Schäfer, T., 2016.** Impact of gravity, collector surface roughness and fracture orientation on colloid retention kinetics in an artificial fracture. **Journal of Colloid and Interface Science, 475: 171–183.** DOI: 10.1016/j.jcis.2016.04.045.

> The conceptual design of the experiments evolved in discussions with Thorsten Schäfer, Florian M. Huber and Gopala K. Darbha. I was responsible for the preparation, the conduction of the experiments and the data evaluation. The AFM measurements of both granodiorite and acrylic glass disc were done by Gopala K. Darbha with my assistance. The 2-D model generation was done by Florian M. Huber and the modelling of the experiments in 2-D were done under his guidance by myself. The preparation of the manuscript was in my responsibility in close collaboration with all co-authors.

Chapter 3: Extract of **Meller, C. (editor), Bremer, J., Baur, S., Bergfeldt, T., Blum, P., Canic, T., Eiche, E., Gaucher, E., Hagenmeyer, V., Heberling, F., Held, S., Herfurth, S., Isele, J., Kling, T., Kuhn, D., Kumar, A., Mayer, D., Müller, B., Neumann, T., Nestler, B., Nitschke, F., Nothstein, A., Nusiaputra, Y., Orywall, P., Peters, M., Sahara, D., Schäfer, T., Schill, E., Schilling, F., Schröder, E., Selzer, M., Stoll, M., Wiemer, H.-J., Wolf, S., Zimmermann, M., Kohl, T., 2017.** Review: Integrated Research as Key to the Development of a Sustainable Geothermal Energy Technology. **Energy Technology, 2017, 5, 965.** DOI: 10.1002/ente.201600579.

> The work presented in this chapter is a part of a review paper. The title of this part is "Particle deposition in granitic fractures". The conceptual design of the experiments evolved in discussions with Thorsten Schäfer and Gopala Darbha. I was responsible

for the preparation and the conduction of the experiments, the data evaluation and the preparation of the manuscript.

Chapter 4 **Stoll, M., Huber, F.M., Schill, E. and Schäfer, T., 2017.** Parallel-plate fracture transport experiments of nanoparticulate illite in the ultra-trace concentration range investigated by Laser-Induced Breakdown Detection (LIBD). **Colloids and Surfaces A: Physicochemical and Engineering Aspects, 222–230.** DOI: 10.1016/j.colsurfa.2017.05.067.

The conceptual design of the experiments based on the previous work (see Chapter 2) and evolved in discussions with Thorsten Schäfer. I was responsible for the preparation, the conduction of the experiments and the data evaluation. The preparation of the manuscript was in my responsibility in close collaboration with Florian M. Huber and Eva Schill and Thorsten Schäfer.

Chapter 5 **Stoll, M., Huber, F.M., Trumm, M., Enzmann, F., Meinel, D., Wenka, A., Schill, E. and Schäfer, T., 2017.** Experimental and numerical investigations on the effect of fracture geometry and fracture aperture distribution on flow and solute transport in natural fractures **(submitted to Water Resources Research on 20.12.2017).**

The concept and the design of the fracture flow cell experiments evolved in discussions with Florian M. Huber and Thorsten Schäfer. I was responsible for the preparation, the conduction of the experiments and the data evaluation. The generation of the transport model from the µ-CT data was done by me in close collaboration and under the guidance of Florian M. Huber and the calculations of the experiments were done by me. Frieder Enzmann organized the µ-CT measurements at BAM and carried out the segmentation of the fractures. Dietmar Meinel was responsible for the CT measurements. Michael Trumm determined the local roughness values of the fracture surfaces of the digital microscopic data. Achim Wenka gave helpful suggestions for the numerical model. The core selection was done with the support of Eva Schill. The manuscript was written by me in close collaboration with all co-authors.

I did not receive any assistance in return for payment by consulting agencies or any other person. No one received any kind of payment for direct or indirect assistance in correlation to the content of the submitted thesis.

The experimental work for the thesis was carried out at the Karlsruhe Institute of Technology (KIT) – Institute for Nuclear Waste Disposal (INE).

The thesis has not been submitted elsewhere for an exam, as thesis or for evaluation in a similar context.

I hereby affirm the above statements to be complete and true to the best of my knowledge.

....	....
(Ort, Datum)	(Unterschrift)

Acknowledgement

The prevailing Ph.D. thesis would not have been possible without the support of many people, whom I would like to thank. My special gratitude goes to:

- Prof. Dr. Thorsten Schäfer, my supervisor, for the excellent guidance and support throughout the Ph.D. work. His enthusiasm and wide knowledge deeply influenced me. His motivation and ideas helped me to go further and get through every difficulty in the research.
- Prof. Dr. Eva Schill, my second supervisor, for giving me feedback and helpful suggestions, and who kindly agreed to be second reviewer of this thesis.
- Dr. Florian M. Huber, for spending hours discussing experimental data with me and introducing me into the world of CFD modelling. I benefited greatly from his help and his ideas. He constantly motivated me throughout the Ph.D. research.
- Prof. Dr. Horst Geckeis, for giving me the opportunity to do the Ph.D. research at his institute.
- Dr. Gopala K. Darbha, for introducing me into working with colloids, his experimental ideas and the AFM measurements.
- Dr. Frieder Enzmann, for the CT measurements of the Soultz granite cores and the fracture segmentation
- Dr. Johannes Lützenkirchen, for the streaming potential measurements
- Dr. Michael Trumm, for the surface roughness calculations and mathematical support.
- The INE Analytic team – especially Stephanie Kraft for the ICP-OES and Eva Soballa for SEM/EDX measurements of my samples.
- The INE workshop team, especially Volker Krepper for the technical advices and the construction of my fracture flow cells.
- All my colleagues and the Ph.D. students at INE for creating such a pleasant atmosphere in the institute. Special thanks go to the Ph.D. students of room 108: Dr. Franz Rinderknecht and M.Sc. Felix Rieder for all the discussions, help and fun in our office.
- Julia Bielefeld, for the loving support and encouragement over the years and for the final proof reading of the papers.
- Last but not least, my friends and family for their patience and support, especially during the stressful time of writing the Ph.D. thesis.

Abstract

Rock fractures can serve as water conducting structures for fluid flow and mass transport within the Earth's crust. Large apertures, which enable high flow velocities, and a rock matrix with several orders of magnitude lower permeability, are accountable that those structures serve as preferential conduits for solutes and colloids. The mechanistic understanding of fundamental transport and retention processes is essential to make reliable predictions of the fate of solutes and colloids in the subsurface. This comprehensive topic is of paramount importance in many areas of geo-engineering, for example disposal of nuclear waste in deep geological formations, enhanced geothermal systems, CO_2 sequestration, gas and oil industry, and contaminant transport in groundwater systems.

This cumulative Ph.D. thesis deals with the investigation of the impact of flow channel geometry on solute and colloid transport through natural rough fractures. The bottom-up approach used in this thesis helped to investigate separately the mechanisms and the processes on mass transport (solute and colloids) in four steps. All experiments in this thesis were conducted under hydraulic and chemical settings establishing laminar flow and overall unfavorable colloid attachment conditions.

In the first step of this approach the interaction of monodisperse fluorescent carboxylated polystyrene colloids (25 nm and 1000 nm diameter) with a plain cut granodiorite surface (Grimsel granodiorite, Aar Massif, Switzerland) or with acrylic glass was investigated experimentally and numerically. Colloid transport experiments in a synthetic parallel-plate fracture flow cell (simulating a simplified fracture) revealed a dependence of colloid retention on surface roughness, fracture orientation, residence time in the fracture and colloid size. It was shown that the colloid mobility of 25 nm colloids, which is purely diffusion driven, is affected by surface roughness and surface inhomogeneities, while fracture orientation does not affect the colloid retention behavior under the experimental conditions chosen. However, despite the low density, 1000 nm colloids show a gravity dependent residence time behavior, which results in significant sedimentation effects in horizontal orientated fractures, due to the shorter sedimentation length to the bottom fracture wall. Fracture surface roughness, however, does not affect the colloid mobility. Those observations were verified by additional atomic force microscopy measurements using the so-called colloid probe technique, and by 2-D numerical simulations.

Moreover, using fluorescent microscopy and surface roughness values for different regions of interest on the granodiorite surface, it was shown that the 1000 nm colloids deposited homogeneously on the fracture surface and are therefore independent of mineralogy and roughness.

In the second step, the colloid material was changed from synthetic monodisperse microspheres to polydisperse Na-illite colloids. Similar transport experiments were conducted using nanoparticulate Na-illite in the ultra-trace concentration range and laser-induced breakdown detection (LIBD) as monitoring technique. Despite the higher density, the experiments indicate that the illite colloids experienced less retention than the monodisperse polystyrene colloids used in step one, which was attributed to the difference in shape, surface charge distribution and colloid size distribution. Therefore, it was shown that polystyrene colloids, which are frequently used in comparable experiments, are non-ideal analogues for polydisperse clay colloids, in order to predict the residence time behavior.

In the third step, the impact of flow channel geometry on fluid flow and non-reactive solute transport was investigated experimentally and numerically on two differently altered naturally fractured granite cores. Tomographic imaging and surface roughness measurements illustrated that both fractures are significantly different in terms of spatial heterogeneities and aperture distribution. Based on the 3-D digital data obtained by computed tomography 2.5-D numerical models were generated for both fractures by interpolating the measured aperture distributions onto the 2-D fracture geometries. Via three in- and three outlets at top and bottom of the fractures, different dipole flow fields were examined. The differences between both fractures were clearly reflected by the fluid flow and the solute transport behavior. It was shown in both experiments and simulations that fluid flow and solute transport in the altered fracture are dominated by the fracture geometry, while, in case of the unaltered fracture, the aperture distribution is the dominating parameter. In the presented case, the pronounced tailings can be attributed to complex internal heterogeneities and simple parallel-plate models fail to describe the experimental findings. Those observations demonstrate that the geometry and internal heterogeneities of fractures need to be implemented in numerical simulations in order to model precisely fluid flow and solute transport.

In the last and most complex step, colloid transport through the same natural granite fractures was investigated for the Na-illite colloids in the ultra-trace concentration range using LIBD as monitoring technique, as introduced in the second step. The flow rates applied and the geochemical unfavorable attachment conditions caused an almost total recovery of the colloids for both fractures. Retardation factors < 1 were obtained in all experimental cases, indicating faster colloid transport in contrast to the solute tracer. It was shown that the retardation factors of the experiments through the altered fracture are considerably smaller, compared to the ones in the unaltered fracture, which breakthrough curves show significant tailing. Moreover, a positive correlation between applied flow rate and acceleration of the colloid was found, which was more pronounced in case of the unaltered fracture. It was assumed that the retardation factors depend on an interaction between internal composition and geometry of the fractures and the sum of exclusion mechanisms and Taylor dispersion. However, based on the experimental and numerical data, a clear discrimination of the dominating process leading to the observed colloid acceleration is not unambiguously possible and needs further investigations.

Kurzfassung

Gesteinsklüfte dienen als wasserführende Strukturen innerhalb der Erdkruste. Verantwortlich dafür sind große Aperturen, welche hohe Strömungsgeschwindigkeiten ermöglichen, sowie eine Gesteinsmatrix, die eine um mehrere Größenordnungen geringere Permeabilität aufweist. Ein mechanistisches Verständnis grundlegender Transport- und Retentionsprozesse ist essentiell, um verlässliche Prognosen über das Verhalten von gelösten Stoffen und Kolloiden im Untergrund zu treffen. Dieses umfassende Thema ist in vielen Bereichen des Geo-Engineerings von größter Bedeutung, wie z.B. die Entsorgung radioaktiver Abfälle in tiefen geologischen Formationen, Geothermie, CO_2-Sequestrierung, Öl- und Gasindustrie und Schadstofftransport in Grundwassersystemen.

In dieser kumulativen Doktorarbeit wird der Einfluss der Fließkanalgeometrie natürlicher Klüften auf den Transport von gelösten und kolloidalen Stoffen untersucht. Der in dieser Arbeit verwendete *bottom-up* Ansatz ermöglicht es die Mechanismen und Prozesse von Massentransport (d.h. gelöste und kolloidale Stoffe) in getrennten Schritten zu untersuchen. Alle Experimente in dieser Arbeit wurden unter laminarer Strömung und unter chemisch ungünstigen Kolloidanlagerungsbedingungen durchgeführt.

Im ersten Schritt des *bottom-up* Ansatzes wurde die Wechselwirkung von monodispersen Polystyrolkolloiden (25 nm und 1000 nm Durchmesser) mit einer gesägten Granodiorit- (Grimsel Granodiorit, Aare Massiv, Schweiz) oder Acrylglasoberfläche experimentell und numerisch untersucht. Kolloidtransportexperimente in einer künstlichen Durchflusszelle mit parallel orientierten Wänden (zur Simulation einer vereinfachten Kluft) zeigten, dass die Kolloidretention in Abhängigkeit zur Oberflächenrauheit, Kluftorientierung, Verweilzeit in der Kluft und Kolloidgröße steht. Die Kolloidmobilität von 25 nm Kolloiden, die rein diffusionsgetrieben ist, wird durch Oberflächenrauheit und Oberflächeninhomogenitäten beeinflusst. Die Kluftorientierung übte unter den gewählten experimentellen Bedingungen keinen Einfluss aus. Trotz der geringen Dichte zeigten die 1000 nm Kolloide ein gravitationsgetriebenes Verweilzeitverhalten und sedimentierten in horizontalen Klüften zur Kluftoberfläche. Die Kluftoberflächenrauheit spielte indes keine Rolle. Diese Beobachtungen wurden durch zusätzliche Rasterkraftmikroskopie-Messungen unter Verwendung der sogenannten *colloid probe*-Technik, sowie durch numerische 2-D Simulationen verifiziert.

Weiterhin konnte mithilfe von Fluoreszenzmikroskopie und Oberflächenrauheitswerten gezeigt werden, dass sich die 1000 nm Kolloide homogen auf der Granodioritoberfläche ablagern und sich somit unabhängig von Mineralogie und Oberflächenrauheit verhalten.

Im zweiten Schritt wurden anstelle der synthetischen monodispersen Polystyrolkolloide polydisperse Na-Illitkolloide verwendet. Hierzu wurden vergleichbare Transportexperimente im Ultraspurenbereich mittels Laser-induzierter Breakdown Detektion (LIBD) durchgeführt. Trotz der höheren Dichte zeigten die Experimente, dass die Illitkolloide unter den experimentellen Bedingungen weniger retardiert wurden als die monodispersen Polystyrolkolloide. Dies wurde auf Unterschiede in Kolloidgeometrie, Oberflächenladungs- und Kolloidgrößenverteilung zurückgeführt. Daran konnte gezeigt werden, dass sich Polystyrolkolloide, die in Transportexperimenten oftmals als Analoga für polydisperse Tonkolloide verwendet werden, hierfür nur sehr bedingt eignen.

An zwei unterschiedlich alterierten, geklüfteten Granitbohrkernen wurde im dritten Schritt der Einfluss der Fließkanalgeometrie auf Strömung und nicht-reaktiven Stofftransport experimentell und numerisch untersucht. Computertomographische Aufnahmen und Oberflächenrauheitsmessungen zeigten, dass sich beide Klüfte in Bezug auf räumliche Heterogenitäten und Aperturverteilung signifikant unterscheiden. Basierend auf den durch Computertomographie erhaltenen 3-D-Datensätzen wurden von beiden Klüften 2,5-D numerische Modelle generiert, indem die gemessenen Aperturverteilungen auf die 2-D Kluftgeometrien interpoliert wurden. Unter Verwendung von drei Ein- und Auslässen an der Ober- und Unterseite der Kerne wurden verschiedene Dipol-Fließfelder untersucht. Das Strömungs- und Transportverhalten in beiden Klüften spiegeln deren geometrischen Unterschiede deutlich wieder. In den Experimenten und Simulationen wurde gezeigt, dass die Strömung und der Stofftransport in der alterierten Kluft von der Kluftgeometrie dominiert werden, wohingegen, im Falle der unalterierten Kluft, die Aperturverteilung den bestimmenden Parameter darstellt. Im vorliegenden Fall können die ausgeprägten *Tailings* in den Durchbruchskurven auf komplexe interne Heterogenitäten zurückgeführt werden. Vereinfachte Modelle mit konstanter Apertur können die experimentellen Durchbruchskurven nicht reproduzieren. Diese Beobachtungen unterstreichen, dass Geometrie und Aperturverteilung von Klüften in numerischen Simulationen implementiert werden sollten, um die Strömung und den Stofftransport möglichst präzise zu modellieren.

Im letzten und komplexesten Schritt wurde der Kolloidtransport durch die beiden natürlichen Klüfte für nanopartikulären, polydispersen Na-Illit im Ultraspurenbereich mittels LIBD untersucht. Die verwendeten Fließgeschwindigkeiten und die gewählten geochemisch ungünstigen Kolloidanlagerungsbedingungen waren für einen fast vollständigen Wiedererhalt des Kolloids in beiden Klüften verantwortlich. In allen experimentellen Fällen wurden

Retardationsfaktoren < 1 ermittelt, wodurch ein schnellerer Kolloidtransport im Vergleich zum gelösten Tracer belegt werden konnte. Es wurde gezeigt, dass die Retardationsfaktoren der Experimente in der alterierten Kluft wesentlich kleiner sind als die in der unalterierten Kluft, bei der die Durchbruchskurven signifikante Tailings aufwiesen. Darüber hinaus wurde eine positive Korrelation zwischen der Fließrate und der Kolloidbeschleunigung ermittelt, die im Fall der unalterierten Kluft deutlicher ausgeprägt war. Es wird angenommen, dass die Retardationsfaktoren von einem Zusammenspiel zwischen interner Struktur bzw. der Geometrie der Klüfte, der Summe der Kolloidgrößen- und Ladungsausschlussmechanismen sowie der Taylor-Dispersion abhängen. Eine exakte Unterscheidung der dominierenden Prozesse ist auf Basis der vorliegenden experimentellen und numerischen Daten nicht eindeutig möglich und bedarf weiterer Untersuchungen.

Table of content

List of figures

List of tables

List of symbols and abbreviations

Acronym	Description	Unit
A	area	[m²]
a	aperture	[m]
a, c	half-axis of the ellipsoid	[m]
a_h	hydraulic aperture	[m]
C	concentration	[kg/m³]
C_0	initial concentration	[kg/m³]
C_N	colloid number concentration	[1/m³]
$D; D_\infty$	molecular diffusion coefficient	[m²/s]
D_{Taylor}	Taylor dispersion coefficient	[m²/s]
d	colloid diameter	[m]
e	electronic charge	[As]
F	body force	[N]
F_B	Brownian motion force	[N]
F_D	drag force	[N]
F_{ext}	additional forces	[N]
F_g	gravity force	[N]
g	gravity	[m/s²]
h	height	[m]
I	Ionic strength	[-]
i	point	[-]
J	deposition flux	[1/(m²s)]
k_B	Boltzmann constant	[m²kg/(s²K)]
L	characteristic length	[m]
L_D	diffusion length	[m]
L_S	sedimentation length	[m]
m	mass of the colloid	[kg]
N	Number of deposited colloids	[-]
n	number of points	[-]
n_0	number of ions per cubic meter	[1/m³]
p	pressure	[Pa]
Pe	Péclet Number	[-]
PV	pore volume	[L]
Q	flow rate	[m³/s]
R	colloid radius	[m]
Re	Reynolds Number	[-]

R_f	retardation factor or acceleration factor	[-]
$R_{P,a}$ $R_{P,c}$	correction factors of the ellipsoid half axes a and c	[-]
Rq	root mean square roughness	[m]
Sh	Sherwood number	[m]
T	absolute temperature	[K]
t	time	[s]
t_R	residence time	[s]
u	flow velocity	[m/s]
u_C	velocity colloid	[m/s]
u_{max}	maximum flow velocity	[m/s]
u_{sed}	sedimentation velocity	[m/s]
$\mathbf{u}$	flow velocity vector $[u,v,w]$	[m/s]
V	volume	[m³]
V_B	Born interaction potential energy	[kT]
V_{EDL}	electric double layer interaction potential energy	[kT]
V_{vdW}	van der Waals interaction potential energy	[kT]
V_T	total interaction potential energy	[kT]
W	width of the fracture	[m]
x	distance from surface	[m]
Z_i	valence of the ion	[-]
z_i	height at point i	[m]
ε_0	permittivity of free space	[F/m]
ε_r	relative permittivity	[F/m]
η	dynamic viscosity	[kg/ms]
κ	reciprocal of double layer thickness	[1/m]
λ	wave length	[m]
ρ	density	[kg/m³]
ρ_f	fluid density	[kg/m³]
ρ_p	colloid or particle density	[kg/m³]
ζ	Zeta potential	[V]
σ_0	surface charge	[C/m²]
τ	stress tensor	[Pa]
τ_p	colloid velocity response	[s]
ν	kinematic viscosity	[m²/s]
ψ	diffuse layer potential	[V]
Ψ_0	surface potential	[V]

Abbreviations

AFM	atomic force microscopy
BTC	breakthrough curve
CPS	carboxylated polystyrene spheres
EDL	electric double layer
EDX	energy-dispersive X-ray spectroscopy
LIBD	Laser-induced breakdown detection
PCS	photon correlation spectroscopy
PZC	point of zero charge
ROI	region of interest
SEM	scanning electron microscopy
vdW	van der Waals
µ-CT	micro computer tomography

1 General introduction

1.1 Outline of the thesis

The prevailing thesis comprises three first author papers and one contribution in a review paper. All studies are published or submitted to peer-reviewed internationally recognized scientific journals. The papers have been re-edited in order to follow the layout of the thesis. Appendices I–III summarize the supporting information of each paper.

The thesis is outlined as follows:

Chapter 1 gives a general introduction in colloid transport through fractured media on the basis of related literature. Subsequently the motivation and the scope of this work are presented.

Chapter 2, 3, 4 and 5 present the published or submitted papers, which are as follow:

Chapter 2: **Stoll, M., Huber, F.M., Darbha, G.K., Schill, E. and Schäfer, T., 2016.** Impact of gravity, collector surface roughness and fracture orientation on colloid retention kinetics in an artificial fracture. **Journal of Colloid and Interface Science, 475: 171–183.** DOI: 10.1016/j.jcis.2016.04.045.

Chapter 3: Extract of **Meller, C. (editor), Bremer, J., Baur, S., Bergfeldt, T., Blum, P., Canic, T., Eiche, E., Gaucher, E., Hagenmeyer, V., Heberling, F., Held, S., Herfurth, S., Isele, J., Kling, T., Kuhn, D., Kumar, A., Mayer, D., Müller, B., Neumann, T., Nestler, B., Nitschke, F., Nothstein, A., Nusiaputra, Y., Orywall, P., Peters, M., Sahara, D., Schäfer, T., Schill, E., Schilling, F., Schröder, E., Selzer, M., Stoll, M., Wiemer, H.-J., Wolf, S. , Zimmermann, M., Kohl, T., 2017.** Review: Integrated Research as Key to the Development of a Sustainable Geothermal Energy Technology. **Energy Technology, 2017, 5, 965.** DOI: 10.1002/ente.201600579.

Chapter 4: **Stoll, M., Huber, F.M., Schill, E. and Schäfer, T., 2017.** Parallel-plate fracture transport experiments of nanoparticulate illite in the ultra-trace concentration range investigated by Laser-Induced Breakdown Detection (LIBD). **Colloids and Surfaces A: Physicochemical and Engineering Aspects, 222–230.** DOI: 10.1016/j.colsurfa.2017.05.067.

Chapter 5: **Stoll, M., Huber, F.M., Trumm, M., Enzmann, F., Meinel, D., Wenka A., Schill, E., Schäfer, T., 2017.** Experimental and numerical investigations on the effect of fracture geometry and fracture aperture distribution on flow and solute transport in natural fractures (submitted in Water Resources Research).

Chapter 6 presents the colloid transport experiments in the two natural rock fractures using nanoparticulate Na-illite investigated by laser-induced breakdown detection.

Chapter 7 presents the major conclusion and draws the future perspectives.

The Appendix I–V presents the supporting information to the publications and additional information.

1.2 Theoretical background

This chapter provides an overview over the general terms and relationships needed. It is structured by an introduction in rock fractures and fluid flow dynamics, followed by a definition of colloids, colloid stability, and mass transport in fractured media. A state of the art on colloid transport in fractured rocks finalizes this chapter.

1.2.1 Fractures

Rock fractures are generally seen as structures for fluid flow and mass transport within the Earth's crust. The flow rates in fractures can be orders of magnitude greater than in the surrounding media. Reported flow velocities in fractured rocks range from 0.3 m/d to 8000 m/d (Pekdeger and Matthess, 1983). A rock fracture is the resulting structure generated by stress in the rock body. The origin of that stress can be highly diverse, e.g. (i) tectonic stress induced by rock deformation; (ii) contraction stress provoked by shrinking of a cooling magma; (iii) near-surface displacements e.g. movement of landslides or glaciers; and (iv) weathering effects resulting in irregular extension (Singhal and Gupta, 2010). Fractures are widespread features in bedrock formations and can be subdivided in single fractures and fracture networks. The focus of this thesis is on single fractures, which are besides size and orientation characterized by aperture and surface roughness (Berkowitz, 2002; Sahimi, 2011).

1.2.1.1 Fracture aperture

The term fracture aperture describes the direct separating distance between two adjacent rock walls. In addition to fully open fractures, where the developed void space in between is either air- or water-filled (Singhal and Gupta, 2010), there are partially or fully filled fractures with loose or solid substances (e.g. fault gauge material) (Reiche et al., 2016). Due to lithostatic pressure apertures are generally narrow. Dissolution and erosion processes, in particular at near-surface, lead to increasing apertures. A general aperture classification is given in Table 1 (Singhal and Gupta, 2010).

Table 1: Aperture classification by size from Singhal and Gupta (2010).

Aperture [mm]	Term
< 0.1	Very tight
0.1–0.25	Tight
0.25–0.50	Partly open
0.50–2.50	Open
2.50–10.0	Moderately wide
> 10	Wide

In the present thesis, two types of apertures are relevant (Adler and Thovert, 1999; Jing and Stephansson, 2007; Shojaei and Shao, 2017; Singhal and Gupta, 2010): the mechanical aperture a_m and the hydraulic aperture a_h. The mechanical aperture represents the arithmetic or quadratic mean of the local apertures. The term ‘mean aperture’ is frequently used to describe this aperture type. In contrast, under equal pressure gradient, the hydraulic aperture represents the aperture of a smooth-walled fracture producing the same flow rates as the real rough-walled fracture. It is defined by the cubic law (Equation 1), which is only valid for parallel-plate type fractures (Singhal and Gupta, 2010; Snow, 1965; Witherspoon et al., 1980; Zvikelsky and Weisbrod, 2006). The values needed are obtained from back analysis from hydraulic or tracer test.

$$Q = -\frac{W a_h^3 \rho g}{12\eta}\frac{\Delta h}{L}$$ **Equation 1**

where Q [m³/s] is the fluid flow rate, W [m] is the width of the fracture perpendicular to the direction of flow, a_h [m] is the hydraulic aperture, ρ [kg/m³] is the fluid density, g [m/s²] is the acceleration due to gravity, η [kg/ms] is the dynamic viscosity, h [m] is the hydraulic head differential along L and L [m] is the length of the fracture along the direction of flow.

In case of smooth parallel fracture walls the hydraulic aperture is equal to the mechanical aperture (Figure 1 top). However, fractures possess rough and irregular fracture surfaces and highly variable aperture distributions (Shojaei and Shao, 2017). The fracture aperture distributions are usually limited by a minimum of zero and tend to follow lognormal aperture distribution (Keller, 1998). The obtained hydraulic aperture is usually smaller, compared to the mechanical aperture. This is due to the flow tortuosity in rough fractures (Shojaei and Shao, 2017), which in consequence means that the hydraulic aperture represents the fluid flow conducting void space (Figure 1 bottom) (Jing and Stephansson, 2007).

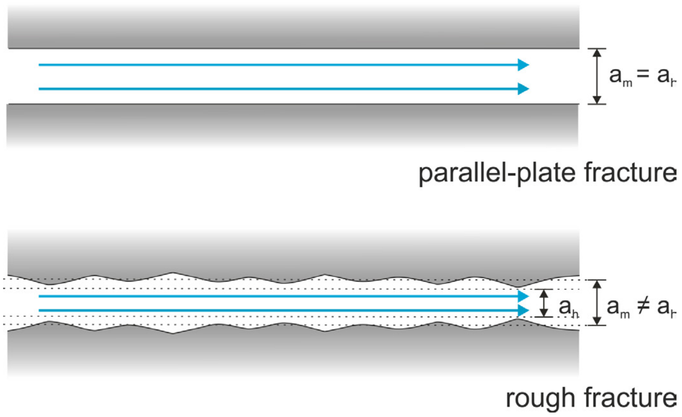

Figure 1: Smooth parallel-plate fracture compared with a rough fracture. In a parallel-plate fracture (top) the hydraulic aperture a_h is equal to the mechanical aperture a_m, due to a lack of surface inhomogeneities and irregularities (asperities). In case of the rough fracture (bottom) the local apertures vary, resulting in a smaller effective hydraulic aperture compared to the mechanical aperture ($a_h < a_m$).

1.2.1.2 Fracture roughness

Irregularities along the fracture surface are called asperities and touching asperities asperity contacts, respectively. The presence of those asperities reduces the effective void and thus the conductivity of a fracture. Those spatial heterogeneities affect the fluid flow through the fracture, resulting in a heterogeneous velocity distribution and preferential flow field (Brown et al., 1998; Neretnieks, 1990; Singhal and Gupta, 2010). Surface roughness can be measured by a sharp stylus, which is dragged over the fracture surface, recording the varying heights along a line. This technique is called profilometry (Adler and Thovert, 1999; Council, 1996). Moreover, there are different optical measurement techniques to determine the roughness of a fracture surface e.g. laser scanning microscopy (Chae et al., 2004; Evans and Donahue, 2008) and vertical scanning interferometry (Darbha et al., 2012a; Fischer et al., 2012).

In order to entirely characterize the surface roughness of an object, there are different determinable surface roughness parameters. The most common parameter is the roughness parameter *Rq* [m], which is defined as the root mean square deviation of the profile (Jorgensen et al., 1993):

$$Rq = \sqrt{\frac{1}{n}\sum_{i=1}^{n} z_i^2} \qquad \textbf{Equation 2}$$

where n is the number of points in the profile, and z_i [m] is the height value at point i.

1.2.1.3 Hydrothermal alteration

Beside the rock physical properties, both the fracture surface and the fracture aperture are most likely be affected by hydrothermal alteration, which in turn influences the fluid flow pattern and the hydraulic properties (see Section 1.2.3). Under the requirement of negligible applied pressure (e.g. near-surface regions), as a consequence of mineral dissolution processes, the fracture aperture increases, whereas the aperture decreases in terms of mineral precipitation (Singhal and Gupta, 2010). Newly formed or unaltered rock fractures are characterized by high surface roughness and heterogeneous topography. However, along with hydrothermal alteration, dissolution and precipitation, either the asperities are reduced or the area between the asperities is filled, which leads to a smoothing of the fracture surfaces. Due to this reduction of asperities, which naturally avoid fracture closing, the aperture consequently may decrease or vanish (Morrow et al., 2001; Sausse, 2002).

Hydrothermal liquids are defined as hot, chemically enriched aqueous solutions of temperatures ranging between 50–500°C. The origin of those waters can be highly divers. Possible sources are: seawater, meteoric, connate, metamorphic, juvenile or magmatic water. As those waters get heated up while penetrating deep into the Earth’s crust (e.g. in consequence of burial diagenesis or as seawater interacting with mid-ocean ridges), they get mineralized in various elements (Pirajno and Cawood, 2008).

The circulation of such hydrothermal fluids through fractured media leads to physico-chemical changes in the rock formations, which are referred to hydrothermal alteration (Pirajno and Cawood, 2008). After Utada (1980), hydrothermal alteration takes place under conditions of local thermal gradients higher than the surrounding general thermal gradients of an area. New mineral assemblages develop due to dissolution and precipitation processes along with this alteration. Which kind of alteration the rock formations undergoes, is dependent on the nature of the rock mass, the temperature, the chemical composition and the pressure of the percolating fluid present (Pirajno and Cawood, 2008). In general, there are two types of alteration to differentiate, which describe the end-member: the vein alteration and the pervasive alteration. While the vein alteration is mostly limited to the fluid flow path ways and the adjacent rock walls (e.g. fissures, fractures, and open voids with some contact alteration of the matrix), the pervasive alteration affects large volumes of rock up to kilometers at inter-grain level (Meunier and Velde, 2013). The interaction of percolating enriched fluids with the surrounding rock material results in a formation of secondary minerals, especially phyllosilicates, which are the dominant species. In extreme cases, this formation leads to a sealing of fissures and fractures. Those resulting structures are called hydrothermal veins. In case of vein alteration, the surrounding rock remains unaltered (Velde, 1995). The pervasive alteration can be subdivided into “pervasive” and “selectively pervasive”. The pervasive alteration is characterized by the replacement of all original rock forming minerals with minerals more stable under the conditions present along with an alteration of the rock texture. The selectively pervasive alteration is associated with the replacement of distinct minerals of the mineral assemblage, e.g. plagioclase replaced by sericite. For this type the original texture is preserved (Pirajno and Cawood, 2008).

There are three different mechanisms producing clay minerals along with hydrothermal alteration: (i) the transformation of pre-existing high-temperature silicates, (ii) the transformation of preexisting clay minerals and (iii) the direct precipitation from enriched hydrothermal fluids (Velde, 1995).

1.2.2 Colloids

Colloids are dispersed solid materials ubiquitous in surface and subsurface waters. Originally, the term colloid dates back to 1861, introduced by Thomas Graham. The name derives from the Greek word “kolla”, meaning “glue” (Graham, 1861; Russel et al., 1989). Colloids are influenced by Brownian motion, attractive and repulsive forces, gravity and fluid drag (Reimus, 1995). The International Union of Pure and Applied Chemistry (IUPAC) provides a well-established size-definition, which defines solids with at least one dimension in the size range from 1 nm to 1 µm as colloids, while solids > 1 µm are defined as particles (Lead and Wilkinson, 2007). In addition, the term nanoparticles is recently used for small colloids of ≤ 100 nm in size (e.g. Frimmel and Delay, 2010; Huber et al., 2012; Schäfer et al., 2012). Note, that the size definition for colloids is not always consistent and that the introduction of an “equivalent diameter” is suggested in order to account the variation of colloids in structure and shape (Degueldre et al., 1989; Zhang et al., 2012).

The size definition is extended by a macroscopic property, the homogenous distribution in the dispersion medium, which stays unchanged over a defined observation period (> hours–days). Colloids are components with dominating surface properties, including surface area and surface charge over the solid-state properties, e.g. chemical composition. Thus, e.g. sorption processes at the colloid surface play an important role. With increasing size the surface properties get less relevant, due to the decreasing reactive surface to volume ratio (Lead and Wilkinson, 2007).

Embraced by the term colloids are inorganic and organic materials, including mineral precipitates (e.g. oxides, hydroxides, carbonates, silicates and phosphates), rock and mineral fragments (e.g. phyllosilicates and weathering products of mineral phases), biocolloids (e.g. viruses and bacteria) and macromolecules (e.g. humic and fulvic acids, polysaccharides) (Figure 2) (McCarthy and McKay, 2004; Zhang et al., 2012). For example, manganese or iron-ions show a strong tendency for hydrolysis and form hydroxides. In the course of polymerization, those hydroxides agglomerate or accumulate to colloids, more precisely "eigencolloids" (intrinsic colloids). This kind of formation was also observed for lead and actinide iones (Matschullat et al., 2013). Especially, for the radioactive waste community the term eigencolloids is very common and of high relevance. The actinides Th(IV) and Pu(IV) show by far the strongest tendency of eigencolloid formation (Poinssot and Geckeis, 2012).

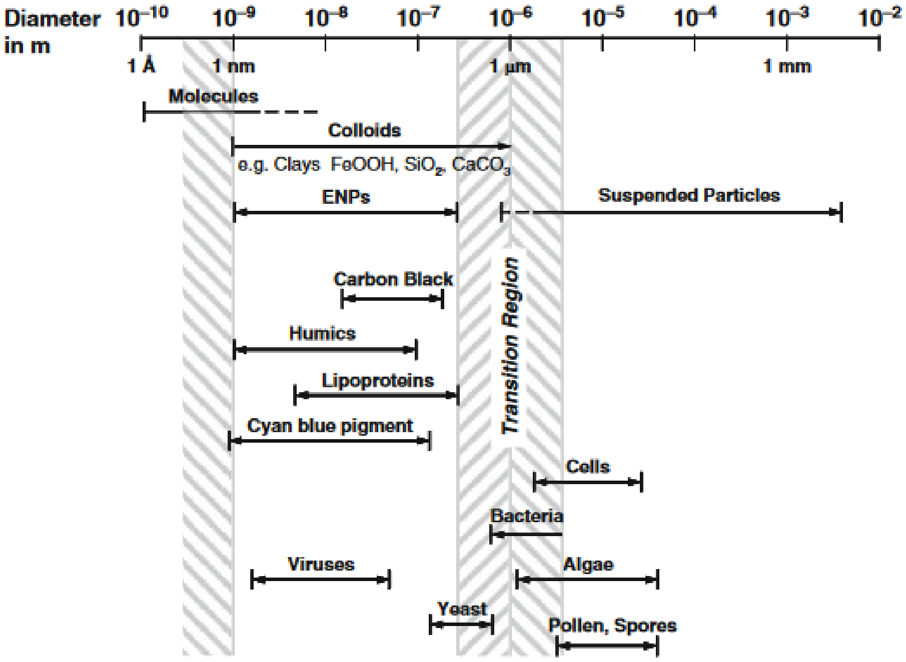

Figure 2: Different natural and artificial particles and colloids (Frimmel and Delay, 2010).

The sources of natural colloids in fractures are diverse. In literature mentioned colloids are generated due to: (1) micro-erosion of rock matrix; (2) mechanical dynamics in the fragile material of the rock; (3) the scouring of fracture filling; (4) precipitation processes as consequence of changes in geochemical conditions, e.g. hydrothermal alteration; and (5) transported colloids from overlying soil (Degueldre et al., 1989; Ryan and Elimelech, 1996; Weisbrod et al., 1999; Zhang et al., 2012).

1.2.2.1 Fluorescent monodisperse carboxylated spheres

Fluorescent monodisperse carboxylated polystyrene spheres (CPS) are spherical particles in the colloidal size range. In literature CPS are frequently used in transport experiments (e.g. Mondal and Sleep, 2013; Reimus, 1995; Zvikelsky et al., 2008) due to their clearly defined material properties: (i) neutrally buoyant (colloid density 1.055 g/cm^3); (ii) monodisperse (diameters have a stated standard deviation); (iii) detectable at low concentration; (iv) chemical stable in a suspending solution; (v) available in the size range of natural colloids; and (vi) well defined surface properties (Reimus, 1995; Reno et al., 2006).

CPS have carboxyl (COOH) surface functionalized groups, resulting in hydrophilic surfaces of negative surface charge. The surface charge of those colloids is pH dependent, resulting in negative charged surfaces at pH higher 5. This negative surface charge prevents flocculation and aggregation effects, which promotes a stable dispersion (Becker et al., 1999; Wan and Wilson, 1994). Moreover, the negative surface charge hinders a direct attachment to negative charged collector surfaces, e.g. fracture walls. Exposing fluorescent colloids to a defined wave length (e.g. by using a fluorescence spectrometer), results in a re-emission of light of a higher wave length, which enables the detection of colloids already at low concentrations down to ppb-level (Reno et al., 2006).

1.2.2.2 Illite

The non-swelling clay mineral illite, formed by weathering or hydrothermal alteration of feldspar and smectite, is a dioctahedral and triple layer phyllosilicate (2:1-layer silicates) of mica-like structure (Figure 3) (Blume et al., 2009; Meunier and Velde, 2013; Okrusch and Matthes, 2006). The dioctahedral structure is characterized by two ions occupying two of three possible octahedral sites in the unit cell, which results in a vacant lattice position in the octahedral layer (e.g. Markl, 2014). Table 2 summarizes the crystal and structural properties of illite. The term illite describes a mineral group of different type and degree of isomorphous substitution (Van Olphen, 1977). Illite is formed along with the recrystallization of smectite and the incorporation of non-hydrated potassium into the interlayer (Blume et al., 2009; Jasmund and Lagaly, 1993; Velde and Meunier, 2008). The crystalline structure of illite is monoclinic and composed of two silica tetrahedral sheets (T) around an octahedral sheet (O) in between. This arrangement is classified as TOT-layer. The elemental cell is completed by the interlayer (I) containing higher coordinated, bigger potassium cations (e.g. Markl, 2014). This resulting layer spacing is around 1 nm (10 Å) (Blume et al., 2009). This defines the minimum size for colloids. Illite crystallites consist of multiple TOT units, resulting in a thickness determined by the number of stacked fundamental units (Van Olphen, 1977). The net negative charge in the 2:1-layers is caused by octahedral substitution (Al^{3+} and Fe^{3+} with Mg^{2+} and Fe^{2+}) and tetrahedral substitution (Si^{4+} with Al^{3+}), which causes, in contrast to mica, in a lower potassium content in the interlayer. The negative layer charge of illite is between 0.6 and 0.9 per formula unit (Blume et al., 2009; Jasmund and Lagaly, 1993). The potassium cations in the interlayer, compensating the negative charge, are fixed and therefore not available for exchange. Potassium has the right size to establish favorable 12-fold coordination with the oxygen ions, resulting in the non-swelling character. Since only potassium ions at the edge sites can be substituted with other cations, the cation exchange capacity is lower compared to e.g. montmorillonite (Van Olphen, 1977).

Illite has a surface charge anisotropy, namely a permanent and a variable surface charge in aqueous suspensions. The permanent charge associated with the clay faces (basal planes) is attributed to the isomorphic substitution in the clay lattice (Van Olphen, 1977). In the dry state the resulting surface negative layer charge of illite is compensated by exchangeable cations at the surface. However, in the presence of aqueous solutions, the cations on the surface dissociate, causing a negative charged surface and the formation of the electric double layer (see Section 1.2.2.3) (Tchistiakov, 2000). The crystal edges are formed of silanol (Si–OH) and aluminol (Al–OH) groups, as the dominating species, and M^{2+}–OH or M^{3+}–OH bonds (M = metal) (Velde and Meunier, 2008). Those edges possess, because of the functional groups, a variable, pH-dependent charge in the presence of aqueous solutions. The hydroxyl groups can either receive or release protons from/to the surrounding solution. At low pH, the edges are positively charged, due to the adsorption of protons, whereas at high pH, the edges are negatively charged, due to the release of protons. If the edge sites are positively or negatively charged at a certain pH, is defined by the point of zero charge (pH_{PZC}). The pH_{PZC} is mineral specific and describes a pH of a net zero charge, due to an equilibrium of positively and negatively charged mineral surfaces. The pH_{PZC} of illite is between pH 2–3 (Blume et al., 2009).

Illite is often accompanied with smectite by means of alternating layers, which has an impact on the swelling properties of the clay. Reported alternating layer or mixed-layer combinations are illite/smectite, illite/chlorite/smectite and illite/smectite/vermiculite (Blume et al., 2009;

Jasmund and Lagaly, 1993). The maximum size of illite particles is commonly less than 0.6 µm (Jasmund and Lagaly, 1993). Their morphology is more variable compared to micas. Thus, illite can be formed of elongated lath like structures or of hexagonal platelets during diagenesis (Velde and Meunier, 2008).

Table 2: Crystal and structural properties of illite (Markl, 2014; Okrusch and Matthes, 2006; Velde and Meunier, 2008; Wypych, 2016). Nomenclature: x: Al^{3+} for Si^{4+} substitution in the tetrahedral layer; y: Mg^{2+}, Fe^{2+} for Al^{3+}, Fe^{3+} in the octahedral layer.

Classification	Phyllosilicate of the mica group
Structural formula of the half unit cell	$[Si_{4-x}Al_x]O_{10}[Al_{2-y}(Fe^{2+},Mg)_y](OH)_2K_{x+y}$ $-0.3 < x < -0.7$; $-0.2 < -0.6$; IC $\cong 0.9$
Crystal structure	monoclinic
Crystal class	prismatic (2/m)
Crystal habit	micaceous aggregates
Cleavage	(001) perfect
Density	2.6–2.9 g/cm³
Mohs hardness	1–2
Negative layer charge	0.6–0.9 per formula unit
pH_{PZC}	2–3
Layer spacing	1 nm (10 Å)
Specific surface	50–200 m²/g
Cation exchange capacity	25–40 [cmol/kg]

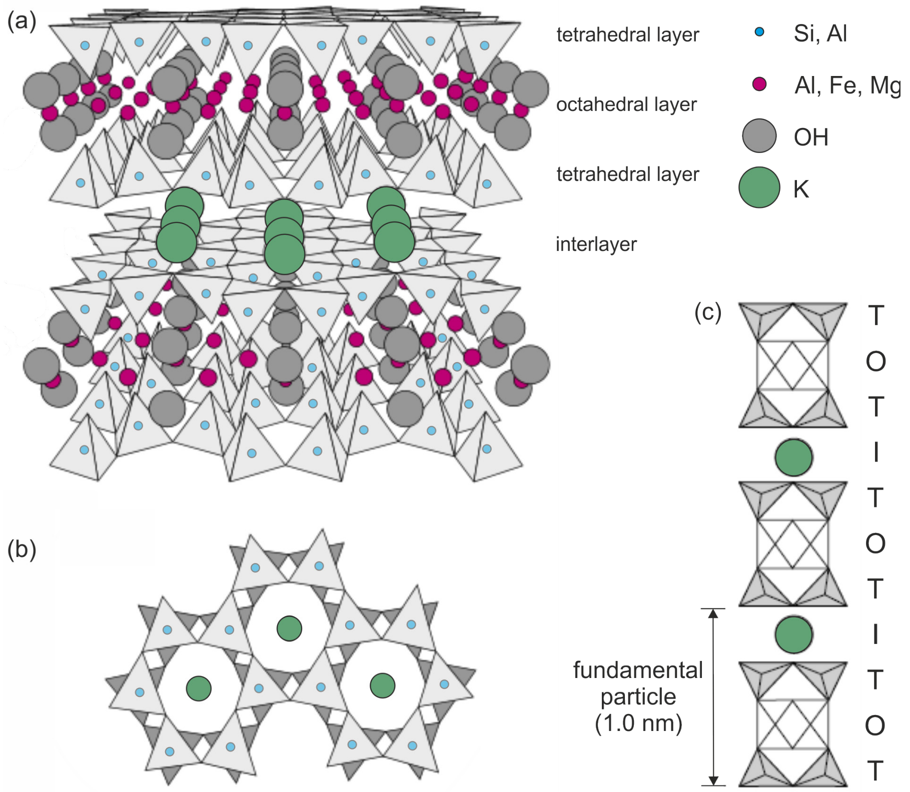

Figure 3: Crystal structure of illite: (a) perpendicular to the c-axis (b) parallel to the c-axis (imaged are silica tetrahedra and interlayer cations (circles) and, (c) T-O-T I T-O-T structure type (tetrahedral layer **T**, octahedral layer **O** and interlayer **I**). Image modified after Markl (2014).

The clay colloids utilized in this thesis is sodium exchanged Illite du Puy. This material was extensively characterized within the EU FP7 collaborative Project CP CatClay (Processes of cation migration in clayrocks) (Altmann et al., 2015). In order to obtain a homoionic Na-illite for the project CatClay, natural Illite du Puy was acid treated, multiple times washed, dialyzed and freeze dried (Montoya et al., 2017).

1.2.2.3 Basics on colloid stability and surface interaction

The stability of colloids is an important factor in terms of mobility processes in fractured media. This part serves as a brief introduction in the basic terminology of colloid stability and interface interactions.

Colloid charge. Colloids immersed in a liquid, e.g. water, carry positive or negative surface charge. Origins for this surface charge are (Butt et al., 2006; Tadros Tharwat, 2015) (Figure 4):

a) Ionization of surface groups: When surface functional groups of respective colloids are ionized, those colloids can become charged. This ionization is controlled by the prevailing pH of the solution, leading either to protonation or deprotonation of the functional groups (e.g. silanol and aluminol groups).

b) Ion adsorption: When a colloid cannot be ionized, e.g. due to a lack of functional groups, ionic surfactants added provoke an adsorption of ions from the dispersion medium, which in turn results in a charged surface.

c) Dissolution of ionic solids: Some ionic solids show differential loss of ions from the crystal lattice when placed in e.g. water. For example, a crystal of silver iodide dissolves preferentially, leaving a negative charged crystal surface.

d) Isomorphic substitution: This process is already described above on the example of illite (see 1.2.2.2).

(a) Ionization of surface groups

(c) Dissolution of ionic solids

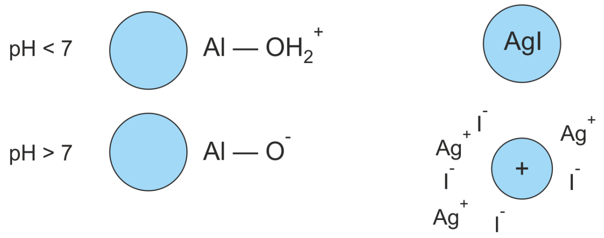

(b) Ion adsorption

(d) Isomorphous substitution

Figure 4: Origins of surface charge of colloids immersed in a liquid (Image modified after Cosgrove (2010)).

Those mechanisms give the colloid surface an electric surface potential ψ_0 [mV], also known as Nernst potential, and the surface charge σ_0 [C/m²].

Electric double-layer. In course of electrostatic interactions between the surface and the dispersion medium, the surface potential ψ_0 is compensated by the formation of an ionic cloud around the colloid. This formation is called the electric double-layer (EDL), a structure appearing on surfaces of objects exposed to fluids (Ohshima, 2012) (Figure 5). The model of Gouy-Chapman (diffuse double-layer) (Chapman, 1913; Gouy, 1909) assumes the surface potential to be uniform and describes the ionic cloud as an unequal distribution of point charged counter ions (ions of the opposite charge) and co-ions (ions of the same charge) of the dispersion medium (counter-ions > co-ions) located from the surface to some distance. The concentration of the counter-ions increases towards the colloid surface, whereas the co-ion concentration decreases, respectively. With increasing distance from the surface the amount of both types of ions converge (Tadros Tharwat, 2015). Stern (1924) introduces to the diffuse double-layer concept a non-diffuse part called the Stern-layer, which is a tightly bound counter-ion layer around the colloid surface. Grahame (1947) distinguished between two types of bounding ions: (i) physically adsorbed counter-ions (outer Helmholtz plane, outer sphere complexes), which stay hydrated and (ii) chemically adsorbed ions that loose a part of their hydration shell (inner Helmholtz plane, inner sphere complexes) (Molina, 2016; Tadros Tharwat, 2015). Therefore, while the ions in the diffuse layer are fully hydrated, the ions in the Stern layer are assumed to be partly dehydrated, because of the intensive attraction to the surface (Blume et al., 2009). The potential in the Stern-layer decreases linearly and the potential in the diffuse layer exponentially. The exponential decay of the diffuse layer potential ψ [mV] with the distance x [m] from the surface can be expressed with the Debye-Hückel approximation (Tadros Tharwat, 2015):

$$\psi = \psi_0 \exp(-kx)$$ **Equation 3**

where ψ_0 [mV] is the surface potential and κ [1/m] is the reciprocal of the "double layer thickness". This thickness is called the Debye-length $1/\kappa$ [m] of the double layer, which is defined as:

$$\left(\frac{1}{\kappa}\right) = \left(\frac{\varepsilon_r \cdot \varepsilon_0 \cdot k_B \cdot T}{2n_o \cdot Z_i^2 \cdot e^2}\right)^{1/2}$$ **Equation 4**

where $\mathcal{E}_r$ [F/m] is the relative permittivity, $\mathcal{E}_0$ [F/m] is the permittivity of free space, k_B [$m^2 \cdot kg/(s^2 \cdot K)$] is the Boltzmann constant, T [K] the absolute temperature, n_0 [m^{-3}] is the number of ions per cubic meter, Z_i [-] is the valence of the ion and e [A·s] is the electronic charge. The thickness of the electric double-layer depends on the ionic strength and the valence of each ion. An increasing ionic strength, therefore, results in a compression of the electric double layer and vice versa (Tadros Tharwat, 2015). The Stern-potential (thermodynamic potential) is often considered to be the relevant potential in order to estimate colloid interaction (Gregory and O'Melia, 1989). However, there is no direct way to measure the potential at the Stern plane, therefore the kinetic potential, called the zeta potential (ζ-potential) is generally used for calculations (Tchistiakov, 2000). The zeta potential is the potential decrease across the mobile part of the double layer and it is taken at the slipping plane (shear plane). The slipping plane separates the liquid adhering to the solid surface from the mobile liquid, which in itself is depending on the ionic strength (Stumm and Morgan, 1996).

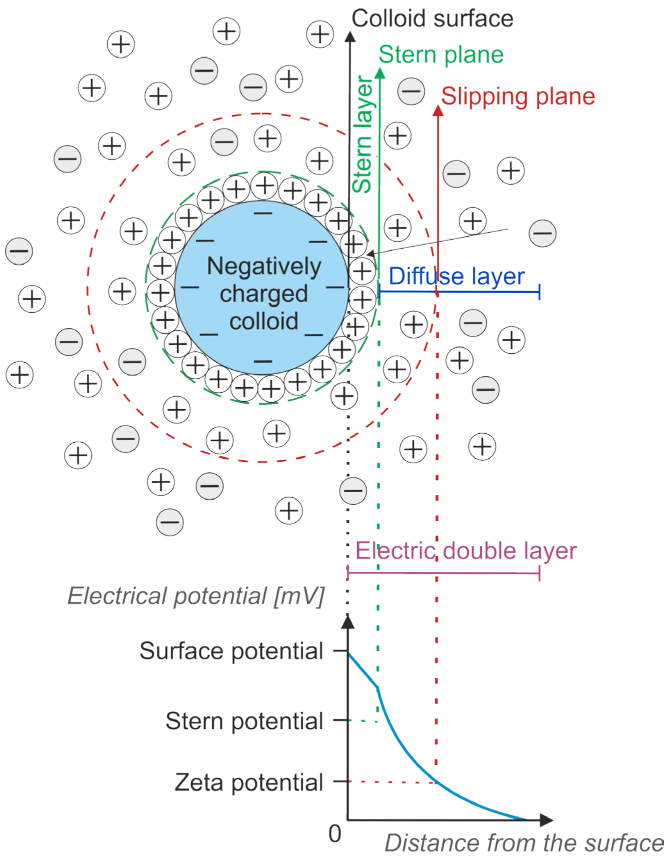

Figure 5: Schematic representation of the electric double-layer around a spherical negatively charged colloid (Image is modified after Vandamme et al. (2013) and Kaszuba et al. (2010)).

Colloid stability and DLVO theory. In context of colloids and colloid systems, the term stability refers to the physical state of colloids to be well dispersed in the dispersion medium without the formation of aggregates over a period of time. Transport of colloids through both porous and fractured media is affected by various factors: interaction between colloids, interstitial fluid, and fracture surfaces (Goldman et al., 1967). While the colloid transport depends on hydrodynamic and chemical interaction with the collector surface material (Lindstrom et al., 1971), the stability of colloids and moreover the total interaction energy between surfaces is controlled by interbody interactions described by the DLVO theory (Elimelech et al., 2013; Logan, 2012).

The DLVO theory, named after Derjaguin and Landau (1941) and Verwey and Overbeek (1955), postulates that colloid stability is controlled by the sum of van der Waals attractive V_{vdW} and electrostatic repulsive forces, including electric double-layer interactions V_{EDL} and Born interactions V_B, between two charged surfaces (Elimelech et al., 2013) (Equation 5).

$$V_T = V_{vdW} + V_{EDL} + V_B$$ **Equation 5**

Van der Waals forces are attractive volume forces existing between all bodies, molecules and electrons, which show to be in most cases attractive. In contrast to those attractive forces, the overlapping of two electric double layers (EDL interaction) or of atomic electron shells (Born interaction) results in repulsion (Elimelech et al., 2013; Henry et al., 2012). The DLVO theory describes the evolution of the total interaction energy as a function of the separation distance (Elimelech et al., 2013). Therefore, as far as there is an energy barrier, using the DLVO theory it is possible to predict the potential energy a colloid needs to overcome to allow attachment with a fracture surface or another colloids surface.

A typical energy distance profile is shown in Figure 6. The shape of this profile depends on various physicochemical parameters, such as particle size, zeta potential, electrolyte composition and Hamaker constant (a material constant that measures the relative strength of the attractive van der Waals forces) (Elimelech et al., 2013). With decreasing separation distance, a secondary energy minimum may occur, which is attributed to the different distance dependencies of the van-der Waals and the electric forces. While, the van der Waals forces follow the power law, the electric forces decline exponentially with increasing distance. This secondary minimum enables the formation of weakly bounded aggregates (flocculation). With further decrease in separation, there can be an energy barrier, which prevents the contact between colloids or colloids with surfaces (aggregation). However, with increasing ionic strength or decreasing zeta potential, this energy barrier lowers and the possibility of contact increases. After overcoming this energy barrier, the colloids are held by van der Waals forces in the primary minimum. Short-range repulsion forces, such as the Born repulsion, prevent further approach, keeping the attraction forces finite. In general, when the repulsive forces are dominating, which means that the resulting total energy is positive, the colloid is considered stable. In contrast, in case of a negative total energy, attractive forces are dominating, leading to agglomeration of the colloids (Elimelech et al., 2013).

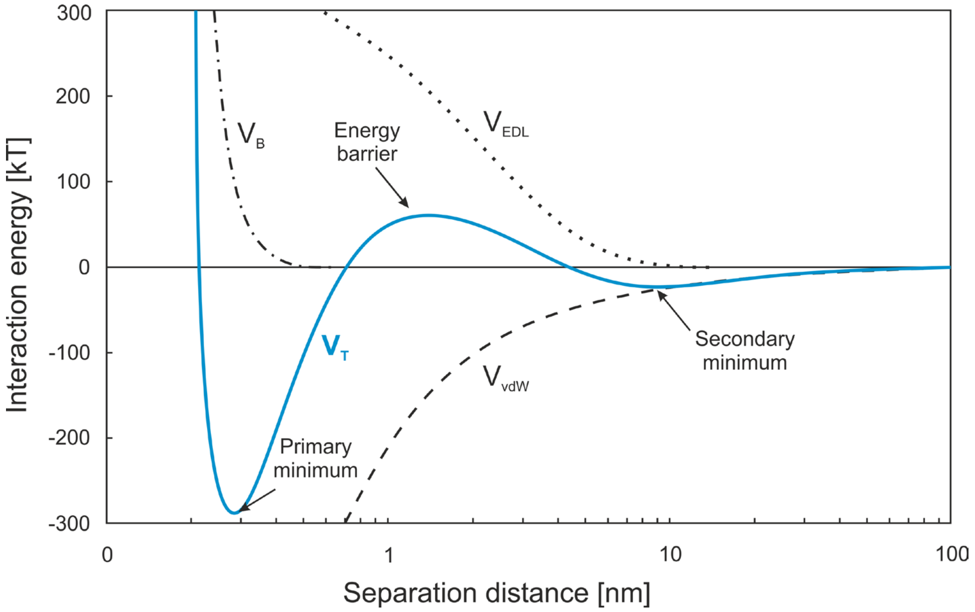

Figure 6: Typical energy distance profile (solid blue line). The energy profile of the van der Waals force is represented by the dashed line, the electric double layer energy profile by the dotted line and the Born energy profile by the alternating dotted and dashed line, respectively (Image modified after Hofmann (2004)).

There are conditions where the DLVO theory cannot sufficiently describe the interaction forces. In those cases, additional forces, called non-DLVO forces need to be included, e.g. steric interaction or hydration effects (Elimelech et al., 2013).

In the context of colloid transport in fractures, it is important to mention that destabilized colloids can still be transported as aggregates through a fracture. However, this happens only based on the premise that the aggregates are small enough relative to the fracture aperture and that hydrodynamic conditions transporting those aggregates are given (Chrysikopoulos, 1999).

1.2.3 Fluid flow and mass transport through fractured media

1.2.3.1 Fluid flow through single fractures

The permeability of fractured rock mass is in general greater than the permeability of porous media. In low-permeable geological formations, fluid flow takes predominantly place in rock fractures (Boutt et al., 2006; Zimmerman and Bodvarsson, 1996). This section describes the fluid flow through a single fracture in interaction with geometry and topography of the fracture walls.

Under the assumption of an incompressible, single phase Newtonian viscous fluid, laminar fluid flow can be described by the Navier-Stokes equations. The Navier-Stokes equations based on the conservation of mass and momentum and provide the most rigorous and mechanistic description of fluid flow through fractures (Batchelor, 1967; Bird, 2002; Zimmerman and Bodvarsson, 1996):

(i) Momentum equation

$$\rho \cdot (\mathbf{u} \cdot \nabla)\mathbf{u} = -\nabla p + \eta \nabla^2 \mathbf{u} \qquad \textbf{Equation 6}$$

(ii) Continuity equation:

$$\nabla \cdot \mathbf{u} = 0 \qquad \textbf{Equation 7}$$

where ρ [kg/m^3] is the fluid density, $\mathbf{u} = [u,v,w]$ [m/s] is the velocity vector, p [Pa] is the pressure and η [kg/ms] is the dynamic viscosity. Standard properties for water are $\rho = 1000$ kg/m^3 and $\eta = 0.001$ kg/ms). The inertial forces are represented by the expression on the left side of the momentum equation (Equation 6). They describe fluid mass and velocity changes over time. The terms on the right side represent the applied pressure gradient and the viscous forces. The continuity equation (Equation 7) expresses the conservation of mass, which is in case of an incompressible fluid directly equivalent to conservation of volume (Bird, 2002; Zimmerman and Bodvarsson, 1996).

In general, high computational and numerical efforts are necessary to solve Navier-Stokes. Therefore, numerous simplifying assumptions are often used to describe the fluid flow in fractured media. The Navier-Stokes equation can be simplified by reducing the left hand side term, assuming that the inertial forces are negligible small. This simplification, which is easier to solve, is called Stokes equation and is defined as (e.g. Bird, 2002):

$$0 = -\nabla p + \eta \nabla^2 \mathbf{u} \qquad \textbf{Equation 8}$$

Further simplified approaches to describe the fluid flow in fractures are for example the cubic law (Equation 1) (Witherspoon et al., 1980) or the local cubic law equation, which are based on the approach that the flow rate Q is proportional to the hydraulic aperture a_h (Chen et al., 2017). The cubic law is a parallel-plate approach and is applicable for fractures with smooth and wide apertures. This approach does not include rough fracture surfaces and tortuous flow paths created by asperities (Brown, 1987; Sisavath et al., 2003). Due to the geometrical simplification, the predicted fracture flow rates are shown to be overestimated (Konzuk and Kueper, 2004; Nicholl et al., 1999). Consequently, in complex geometries like natural fractures the full version of the Navier-Stokes equation (Batchelor, 1967) needs to be solved to simulate precisely the fluid flow (Cardenas et al., 2007; 2009).

In order to characterize the fluid dynamics in a fracture and/or to validate the use of simplified approaches, the dimensionless Reynolds number Re [-] is determined, which is defined as:

$$Re = \frac{u \cdot L}{\nu} \qquad \textbf{Equation 9}$$

where u [m/s] is the fluid velocity, L [m] is the characteristic length (here the arithmetic mean of the aperture) and ν [m²/s] the kinematic viscosity. Fluid flow through a narrow rough fracture can be classified as laminar when Re < 100. A turbulent hydraulic flow regime prevails when Re > 100 (Kohl et al., 1997). Note that especially groundwater flow through fractures is generally considered laminar, however, complex aperture distributions in natural fractures induce locally regions of turbulence. Therefore, simplifications of the Navier-Stokes equations that do not incorporate those areas, might not be valid in all regions (Brush and Thomson, 2003; Cardenas et al., 2007).

In general, laminar fluid flow through fractures is described as a parabolic velocity profile with no-slip boundary condition, which is called Poiseuille flow (Figure 7). The Poiseuille flow is a solution of the Stokes equation and describes the ideal parabolic velocity profile developing between smooth fractures walls with a constant aperture a. In consequence, in the vicinity to the fracture wall the fluid velocity is approaching zero and the center is characterized by the highest flow velocities (Adler et al., 2012). However, numerical studies investigating fluid flow in synthetic rough-walled fractures reveal that inertial forces, which are neglected in the Stokes equation, and surface roughness may cause a significant deviation from the parabolic type, which should be considered (Brush and Thomson, 2003).

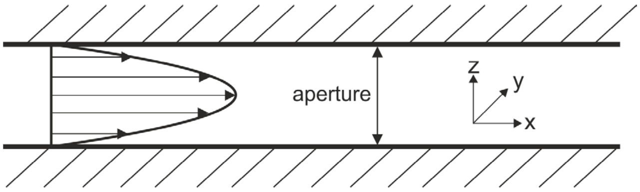

Figure 7: Schematic of the flow velocity profile through a parallel-plate fracture.

1.2.3.2 Mass transport in fractured media

This section gives an introduction in single phase flow solute transport in the saturated zone, under steady-state laminar flow conditions. Focus is lead on low-permeability rocks, where advection through the matrix is negligible compared to the contribution of the fracture. The physical mechanisms affecting the transport of a non-reactive tracer through a fracture are (i) advection, (ii) hydrodynamic dispersion, (iii) molecular diffusion, (iv) channeling effects and (v) matrix diffusion (Bodin et al., 2003).

Advection. Advection describes the bulk movement with the mean flow velocity in the primary direction of travel. The mass distribution stays constant in shape and concentration. The mass experiences only a translational displacement in flow direction (Kinzelbach and Rausch, 1995).

Hydrodynamic dispersion. Mass (solute and particulate) transport through fractured media is accompanied by hydrodynamic dispersion, which is the combination of mechanical dispersion and molecular diffusion, representing the spatial spreading of injected mass within the flow field (Langguth and Voigt, 2013). In case of transport of solutes, dispersion leads to dilution and to earlier first arrival times of the breakthrough due to the spreading of the plume during the transport process (Bodin et al., 2003).

Hydrodynamic dispersion develops in fractures independently of the aperture. In smooth-walled fractures with an almost constant aperture, the Taylor-Aris dispersion (Aris, 1956; Taylor, 1953) is the only effective dispersion mechanism. It is represented by the parabolic velocity profile between two non-slip fracture walls. In rough-walled fractures, hydrodynamic dispersion is found to be intensified by surface roughness (Ippolito et al., 1994; 1993). Resulting heterogeneous velocity distributions, due to variable apertures in fractures, cause an additional dispersion mechanism (Keller et al., 1999; Moreno et al., 1988; Roux et al., 1998). In summary, in natural fractures the sum of three independent dispersion mechanisms act on solutes: (i) Taylor dispersion, due to the parabolic velocity profile, induced by friction between two no-slip fracture walls (Bodin et al., 2003); (ii) macrodispersion, due to spatial heterogeneities resulting in preferential flow paths; and (iii) molecular diffusion due to a developing concentration gradient (Roux et al., 1998). Roux et al. (1998) distinguished the impact of flow velocity on the contribution of the different dispersion mechanisms and found aperture variability to be dominant at intermediate flow velocities, while at higher velocities Taylor-Aris dispersion prevails. Dispersion can also occur due to diverse advective velocities of different channels (Detwiler et al., 2000; Lee et al., 2003), resulting in increased dispersion compared to a homogeneous fracture. Moreover, the exchange of mobile fluid fraction in the fracture and immobile fluid fraction, e.g. fluid in low flow zones or in the matrix, may cause additional dispersion (Becker and Shapiro, 2000).

Molecular diffusion (Brownian motion). In contrast to mechanical dispersion and advection, molecular diffusion (Brownian motion) is independent from fluid flow velocity and flow direction, meaning it is truly isotropic. Molecular diffusion is a spreading mechanism, since it is a consequence of concentration gradients. The isotropic character of diffusion reduces the impact of mechanical dispersion in natural fractures, due to a diffusive transport between flow channels (Grisak and Pickens, 1980). Since molecular diffusion is a comparably slow process compared to advection and dispersion, its contribution has been considered to be detectable in the tailing region of a breakthrough curve (BTC) (Gouze et al., 2008).

In natural fractures, there are often areas to which the main flow has little access. Consequently, very low flow velocities are dominant. Besides mechanical dispersion, solutes reach those areas by molecular diffusion. The low flow velocities contribute to the enhance trapping, which results in longer retardation and thus the formation of more pronounced tailings of the BTC (Boutt et al., 2006).

Channeling. Highly increased contrast in the fluid velocity field due to aperture variability, results in preferential flow path, so called channeling (Brown et al., 1998; Neretnieks, 1990; Tsang and Tsang, 1989). The fluid flow is channeled along tortuous paths following the lowest hydraulic resistance. With respect to the entire fracture, elevated flow velocities prevail in those regions. Generally, those channels cover only 5–20% of the fracture plane (Bodin et al., 2003; Brown et al., 1998). Channeling is a common feature, which was observed both in laboratory (Brown et al., 1998) and in field experiments (Abelin et al., 1994). There are typical shapes in BTCs, which can be explained by fluid flow channeling, e.g. multimodal curves in case of independent channels (Moreno et al., 1988; Park et al., 1997) and tailing effects (Moreno et al., 1988; Tsang, 1984).

Matrix diffusion. The diffusive exchange between the mobile fluid in the fracture with the immobile fluid in the fracture matrix is called “matrix diffusion”. This effect is a widely used explanation for observed tailings of BTC (Becker and Shapiro, 2000). It was found that especially for fractured media with high matrix porosity (e.g. chalk) the impact of hydrodynamic dispersion and fracture geometry are subordinated to matrix diffusion. Depending on the porosity of the fractured media, the transport of masses can be slowed down and the concentration in the peak reduced under the influence of matrix diffusion (Bodin et al., 2003). Several researches (e.g. Neretnieks, 1980; Neretnieks, 2014; Neuman, 2005; Zhou et al., 2007) showed that the impact of matrix diffusion on solute transport in fractured media should not be neglected.

Governing equations. In general, in order to simulate mass transport through fractures the advection-diffusion equation (often also called convection-diffusion equation) is solved, which is defined as (Cardenas et al., 2009):

$$\frac{\partial C}{\partial t} = D\nabla^2 C - \nabla \cdot \mathbf{u}C \qquad \textbf{Equation 10}$$

where C [kg/L] is the solute concentration, t [s] is the time and D [m²/s] is the molecular diffusion coefficient of the transported mass. Note that this version of the advection-diffusion equation does not include the contribution of sinks and sources. The first term on the right side describes the diffusive transport, while the second term represents the advective transport. The Péclet Number Pe [-] indicates the balance between advection and diffusion in a system and shows which transport process is dominant. Pe is defined as:

$$Pe = \frac{u \cdot L}{D} \qquad \textbf{Equation 11}$$

where L [m] indicated the characteristic length, which is in transport in fractures generally equal to the mean aperture. In case of $Pe > 1$ advection dominates, while for $Pe < 1$ the solute transport is mainly controlled by molecular diffusion.

1.2.4 Colloid transport in saturated single fractures – State of the art

Based on the special behavior and properties of colloids summarized above, colloids became center of attention within the last decades, especially, in environmental science and geo-engineering. Colloid transport in the subsurface environment is an interdisciplinary topic and current areas of research are:

- (colloid-facilitated) contaminant transport in groundwater (Chrysikopoulos, 1999; Kretzschmar and Schäfer, 2005; McCarthy and Zachara, 1989; Weisbrod et al., 2002)
- colloid-facilitated radionuclide transport due to sorption of radionuclides on groundwater colloids (Geckeis et al., 2004; Grindrod, 1993; Kersting et al., 1999; Möri et al., 2003; Smith and Degueldre, 1993; Utsunomiya et al., 2009)
- pore clogging during extraction of fluids from the subsurface (Civan, 2011; Rosenbrand et al., 2014)

- local alteration of physical properties (e.g. permeability) due to the deposition of clay material on the fracture surfaces (Evans et al., 2005; Geiermann and Schill, 2010)

The transport of colloids through fractured media is less well investigated and not yet fully understood (Zhang et al., 2012). From the hydrogeological point of view, rock fractures are geological structures of high relevance, because they are widespread and serve as preferential conduits for both solutes and colloids. This is a consequence of (i) large flow diameters that enable high flow velocities compared to the surrounding matrix, (ii) mostly unfavorable conditions for attachment due to negatively charged surfaces of colloids and fractured walls and (iii) negligible matrix diffusion of colloids in contrast to solutes (Alonso et al., 2007a; Chrysikopoulos, 1999; McKay et al., 2002; Schäfer et al., 2012). The major colloid transport and retardation mechanisms in saturated fractured media are illustrated in Figure 8.

Typically, the following colloid types are used: (1) low density (buoyant) monodisperse latex spheres including surface functionalized colloids such as carboxylated polystyrene microspheres, (2) monodisperse silica spheres, (3) polydisperse clay colloids (such as kaolinites, illites and smectites) and (4) polydisperse biocolloids (bacteria). They are differentially transported or retained in fractured media. Moreover, there are different types of fracture media present, which come with a variety of distinct material features, such as surface charge, roughness and matrix porosity. Table 3 displays this variety in an incomplete selection of published experiments on colloid transport in fractured media.

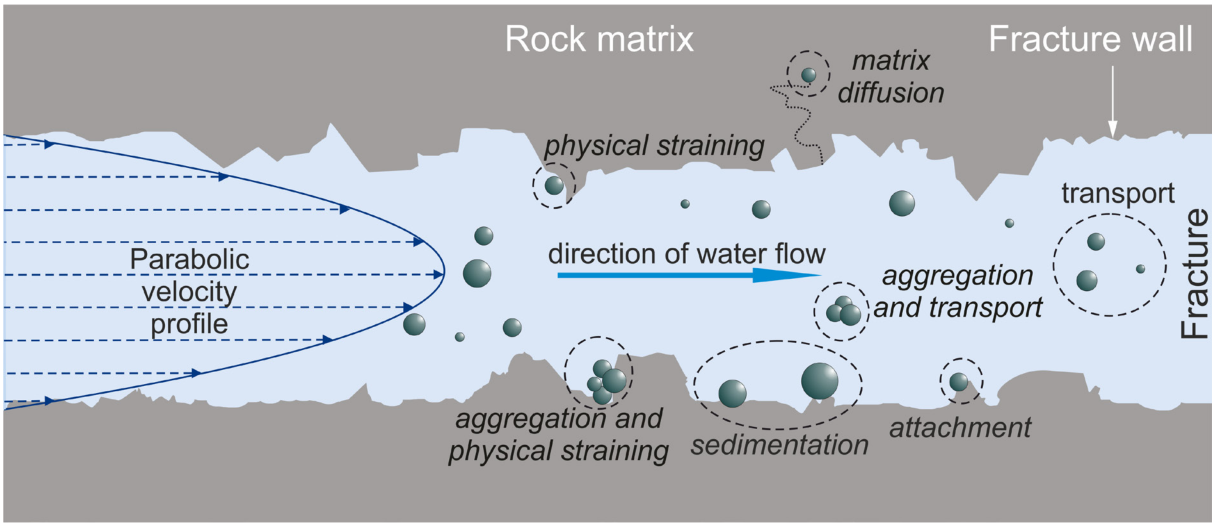

Figure 8: Major colloid transport and colloid retention mechanisms in a saturated fracture (modified after Zhang et al. (2012)).

Table 3: Selection of published studies on colloid transport in fractured media (partly adopted from Zhang et al. (2012)). Not specified values are notated with “n.s.”.

Colloid type	Size [nm]	Surface charge	Particle density [g/cm^3]	Recovery [%]	Surface	Fractured media	Reference
Fluorescent latex microspheres	100	n.s.	n.s.	< 6	n.s.	Fractured shale saprolite (laboratory)	McCarthy et al. (2002)
	500			< 36			
	1000			< 16			
	2100			< 15			
Fluorescent latex microspheres	20	Negative	1.055	75–77	n.s.	Fractured chalk (laboratory)	Zvikelsky and Weisbrod (2006)
	100			86			
	200			93–99			
	1000			89–91			
Fluorescent latex microspheres	360	Negative	1.06	6	Hydrophilic	Fractured granite (field)	(Becker et al., 1999)
	830			2			
Carboxylated-modified Polystyrene Microspheres	300	Negative	1.055	> 95	Hydrophilic	Fractured tuff (laboratory)	Reimus (1995)
	1000						
Silica	300	Negative	2.65	79–80	Hydrophilic	Fractured tuff (laboratory)	Reimus (1995)
Bacteria	1400–1900	n.s.	n.s.	0.13	n.s.	Fractured crystalline bedrock (field)	(Becker et al., 2003)
	1500–2200			0.63			
	1200–2000			3.5			
	500–800			2.3			
Bacteriophage	62	n.s.	n.s.	n.s.	n.s.	Fractured shale saprolite (field)	(McKay et al., 2000)
	20–26						
Clay	700	Negative	2.35	70	n.s.	Fractured chalk (laboratory)	(Tang and Weisbrod, 2009); Zvikelsky et al. (2008)
Clay	250–400	Negative	1.05–1.20	32–100	n.s.	Fractured granite (laboratory)	(Albarran et al., 2013)
Gold	40	Negative	19.30	9–59	n.s.	Fractured granite (laboratory)	(Albarran et al., 2013)

1.2.4.1 Colloid transport accelerating mechanisms

In both laboratory and field studies, a faster transport of colloids compared to solute conservative tracers was observed. This implies an enhanced mean transport velocity of colloids compared to solute conservative tracers (Becker et al., 1999; Champ and Schroeter, 1988; Geckeis et al., 2004; Hinsby et al., 1996; Knapp et al., 2000; McCarthy et al., 2002; McKay et al., 2002; Möri et al., 2003; Reimus, 1995; Tang and Weisbrod, 2009; Zvikelsky and Weisbrod, 2006; Zvikelsky et al., 2008). The magnitude of this enhancement depends on multiple factors, e.g. the size of the colloids, the fracture dimensions and the applied flow velocity. The observed faster transport is attributed to a combination of three effects: (1) size exclusion, (2) charge exclusion and (3) Taylor dispersion (Becker et al., 1999; Zvikelsky and Weisbrod, 2006). Note that in literature those terms are often used inconsistently. (1) Compared to the size of pore throats, colloids are in many cases much larger and thus not able to enter the rock matrix, meaning they are excluded due to their size. Therefore, colloids tend to remain in the fastest fluid streamlines (Becker et al., 1999; Grindrod, 1993; Smith and Degueldre, 1993; Zvikelsky and Weisbrod, 2006). Consequently compared to solutes, there is a smaller effective volume of higher flow velocities available for these colloids (Reimus, 1995). In contrast, truly dissolved solutes can enter this matrix, which results in an increased retardation of the solutes and thus a faster transport of colloids compared to solutes is observed. (2) When both colloid and fracture surfaces are negatively charged, e.g. under natural groundwater conditions, repulsion forces prevail between colloid and the fracture walls. This repulsion concentrates colloids in the middle of the fracture, where they are accelerated due to the parabolic flow velocity profile (shown in Figure 8 and described in Section 1.2.3) (Becker et al., 1999; Chrysikopoulos and James, 2003). (3) The large difference between colloids and solutes is the respective diffusion coefficient. The diffusivity of a solute in water is between 1E–9 and 1E–10 m^2/s (Reimus, 1995). Whereas the diffusion coefficient of colloids, which depends on size, density and shape, ranges between 1E–9 and 1E–14 m^2/s (Adamczyk, 2006). For fracture flow, this difference shows a significant influence on the dispersion of the transported species. Taylor dispersion is the result of diffusion across all streamlines in a long narrow channel, such as a fracture. While solutes are affected by all streamlines many times, resulting in the mean transport velocity like the fluid, colloids tend to stay at the same streamline during the entire residence time, due to their slow diffusivity (Reimus, 1995). According to the Stokes-Einstein equation (Einstein, 1905) this effect increases with increasing colloid size because of a colloid radius dependent lower diffusion coefficient. This results in an earlier arrival and faster travel times of large colloids before smaller colloids, which was numerically shown by Chrysikopoulos and Abdel-Salam (1997). Those three mechanisms mentioned are the responsible factors for colloids travel midstream, following the fastest streamlines and disperse less while migrating through the fracture. Consequently, colloids can facilitate e.g. contaminant movement. Especially in radioactive waste repository, this special behavior is the main concern, since colloids can carry strongly sorbing radionuclides and transport them over large distances without radionuclide specific retention behavior (Albarran et al., 2013).

1.2.4.2 Colloid retention mechanisms

Compared to porous media, in fractured systems the interaction between colloid and fracture wall is supposed to be smaller, due to comparably large apertures and flow directions parallel to the fracture planes. However, colloid retention occurs to a certain extend. There are several mechanisms provoking colloid retention within saturated fractures. The main mechanisms include sedimentation, (matrix) diffusion, physical straining, and adsorption (Figure 8) (Zhang et al., 2012). Note that in case of fractures, which are not fully open, e.g. due to a filling of fault gauge material, the system could be treated as a porous medium.

Sedimentation. Colloids are influenced by gravity and Brownian motions. As far as the portion of sedimentation exceeds the portion of diffusion, for example for big or dense colloids or aggregates, colloids settle out of the flow stream and sediment to the fracture bottom. The sedimentation velocity u_{sed} [m/s] is described by the Stokes settling formula, which assumes laminar flow (Ohshima, 1998):

$$u_{sed} = \frac{2\Delta\rho \cdot R^2 \cdot g}{9\eta}$$ **Equation 12**

where $\Delta\rho$ [kg/m³] is the fluid-colloid density difference, R [m] is the colloid radius, g [m/s²] is the gravity acceleration and η [kg/ms] is the dynamic viscosity. Once colloids have settled to the fracture surface, they can be remobilized in the course of changes in hydrodynamic or chemical conditions (Zhang et al., 2012).

(Matrix) diffusion. Brownian motion is a process independent from fluid flow velocity and direction. The diffusion coefficient D [m²/s] for colloids is described by the Stokes-Einstein equation (Einstein, 1905):

$$D = \frac{k_B \cdot T}{6 \cdot \pi \cdot \eta \cdot R}$$ **Equation 13**

where k_B [$m^2 \cdot kg/(s^2 \cdot K)$] is the Boltzmann constant and T [K] is the temperature. The diffusion coefficient is inversely correlated with the colloid size, i.e., small colloids, of high diffusivity, are more likely to diffuse to the vicinity of the fracture walls than bigger colloids (Taylor, 1953).

Generally, the matrix of fractured rock is characterized by lower porosity compared to porous media. However, the colloid size and shape control the penetration of the colloids into the rock matrix and whether they are physically trapped at the pore throats causing clogging of the pores (Cumbie and McKay, 1999; Knapp et al., 2000). As far as the colloid size is small enough, colloids can enter the rock matrix and are thereby eliminated from the colloid transport process in the fracture. This process is called matrix diffusion (Alonso et al., 2007b; Champ and Schroeter, 1988; Cumbie and McKay, 1999; Grindrod and Lee, 1997; Zvikelsky and Weisbrod, 2006). The probability and impact of matrix diffusion on colloid retention increases with smaller colloid size, higher matrix porosity and decreasing flow rates (Knapp et al., 2000; McCarthy et al., 2002; Zvikelsky and Weisbrod, 2006).

In earlier experimental studies, either limited matrix diffusion or adsorption was attributed to be responsible for the observed colloid retardation (Bales et al., 1989; Cumbie and McKay, 1999; Mckay et al., 1993b). But all studies suggested that the loss of colloids to matrix diffusion is very small. The impact of matrix diffusion on colloid transport at different scales was usually not considered in numerical simulations (Abdel-Salam and Chrysikopoulos, 1995a; Chrysikopoulos and Abdel-Salam, 1997; Kosakowski, 2004). Numerical studies by James and Chrysikopoulos (1999) showed when the porosity of the matrix becomes high enough, colloid diffusion can be a dominant controlling mechanism in colloid transport for small colloids. However, there is still limited research, which is the reason of inconsistent results. Thus, the impact of matrix diffusion on colloid transport remains at least partly a matter of debate.

Physical straining or mechanical filtration. In contrast to matrix diffusion, larger colloids or aggregates are rather affected by physical straining. Straining can occur in regions of extremely small apertures (Knapp et al., 2000; McKay et al., 2002) or in down-gradient pore throats (Cumbie and McKay, 1999; McKay et al., 2002) that are too small for the particles to passage. Kosakowski (2004), who studied colloid transport through a shear zone, attributed straining or gravitational settling to the observed systematical decrease in colloid recovery with increasing colloid size. However, colloid retention due to straining is more significant in porous media, and is often considered as insignificant in fractured media (Knapp et al., 2000; Zvikelsky and Weisbrod, 2006).

Adsorption. Physical and chemical processes, such as colloid settling, viscous drag, Brownian motion or dispersion, bring colloids, in the vicinity of the fracture surfaces (Zhang et al., 2012). The subsequent attachment process depends on the interaction forces between the colloids and the collector surface discriminating between electrostatically favorable and unfavorable conditions of attachment (Chinju et al., 2001). This electrostatic dependent interaction is described above by the DLVO-Theory (see Section 1.2.2.3). Moreover, already attached colloids may have an influence on the attachment behavior of colloids in suspension, due to arising repulsive forces, reducing the attachment sites on the surface (surface exclusion) (Chrysikopoulos and Abdel-Salam, 1997; James and Chrysikopoulos, 1999). The transport and the attachment process of colloids is summarized in the term colloid deposition (Elimelech and O'Melia, 1990) and the rate of each process determines the overall kinetic. The colloid deposition is often described by a deposition coefficient (Elimelech et al., 2013; Van de Ven, 1989). This coefficient includes a variety of deposition mechanisms induced by Brownian motion, van der Waals and electric double layer forces (Abdel-Salam and Chrysikopoulos, 1994; Chrysikopoulos and Abdel-Salam, 1997). Atomic force microscopy (AFM) based on force-distance measurements (Alonso et al., 2009; Darbha et al., 2012b) is a way to determine this coefficient. The deposition or remobilization of colloids is rarely studied and often excluded in the modelling. Generally, desorption of colloids is induced by chemical or physical perturbations (Zhang et al., 2012). Forces, which favor desorption are dragging and lifting forces, whereas electrostatic and gravitational forces hinder the desorption of attached colloids (Bedrikovetsky et al., 2011; 2012; Li et al., 2005).

1.2.4.3 Impact of colloid size, density and shape

Because of the high diversity in colloid types, the impact of colloids size, density and shape on colloid transport are a matter of research. In studies on low density carboxylated polystyrene spheres, Cumbie and McKay (1999) found a significant influence of colloid diameter on transport and retention in fractured shale saprolite. They determine an optimum transported colloid size of 500 nm, which was validated by McCarthy et al. (2002). Both smaller (50–100 nm diameter) and bigger (1000 nm diameter) colloids were retained to a higher extend within the fracture. They conclude that smaller colloids are retained due to diffusion to or in the fracture walls and bigger colloids due to sedimentation on the fracture bottom. Those conclusions verify the experimental results and conceptual model by Reimus (1995) on synthetic microspheres in saturated fractured tuff. Despite variations in size due to different colloid diameters utilized, comparable observations were made by Becker et al. (1999) (0.36 µm over 0.83 µm latex spheres in fractured granite) and Zvikelsky and Weisbrod (2006) (0.2 µm over 0.02 and 1.0 µm latex spheres in fractured chalk). In addition to various studies made on monodisperse colloids, numerical studies on polydisperse colloid suspensions reveal that the colloid plume experienced higher hydrodynamic dispersion, in terms of spreading, compared to a monodisperse one. This effect increases with increasing variance of the colloid diameter (James and Chrysikopoulos, 1999; 2000). Moreover, in colloid transport experiments using polydisperse clay suspension (mean colloids size 1.34 µm) in chalk rock fracture, Zvikelsky et al. (2008) observed a decrease in the mean colloid size of the mobile colloid fraction. The authors attributed the higher density of the clay colloids to the observed colloid deposition and colloid size fractionation. Furthermore, they found an increase of colloid recovery while repeating the experiments, which was explained with full surface coverage, because of the preceding experiments resulting in fewer sites available for attachment.

In static batch experiments, the influence of collector surface orientation on colloid deposition was investigated in detail by Dokou et al. (2001). For this purpose, colloids of different sizes and densities and vertical or horizontal coated glass surfaces are used. Under stagnant conditions, they reveal that gravity is negligible for low density colloids (1.05 g/cm^3) with sizes < 1 µm. Bigger or denser colloids (2.07 g/cm^3 or 19.20 g/cm^3) showed higher colloid deposition on horizontal glass samples than on vertical glass samples. Studies of Chrysikopoulos and James (2003); James and Chrysikopoulos (2004); (2011) showed that even under advective conditions dense colloids are more affected by gravitational forces, which slow them down or transport them in regions of slow or no flow within the fractures.

Studies investigating transport differences of colloids of different materials, sizes and shapes have been conducted by Albarran et al. (2013) and Schäfer et al. (2004). Albarran et al. (2013) investigate the transport behavior of gold, latex and smectite colloids in artificial granite fractures under unfavorable attachment conditions. Higher colloid recovery of clay colloids compared to the latex and gold colloids of comparable sizes was observed. These results were attributed to the nature of the clay colloids: the charge distribution and the platelet shape.

1.2.4.4 Impact of spatial heterogeneities and fracture roughness at unfavorable attachment conditions

It is well understood that colloid retention is provoked by electrostatic conditions favorable for attachment. Those conditions are dependent on pH and ionic strength affecting mineral and colloid surface properties (Landkamer et al., 2013; Yao et al., 1971). However, in both field- and laboratory experiments, a significant retention of colloids was found even under electrostatically unfavorable conditions, where repulsive forces dominate (Alonso et al., 2009;

Missana et al., 2008; Schäfer et al., 2004). For example, Albarran et al. (2013), who investigated the transport behavior of different colloid types (gold, smectite and latex) through a rough granite fracture, observed a retention for all colloid types and sizes. They conclude that this retention was independent from the chemical composition of the minerals but most likely provoked by mineral porosity, surface roughness, crystal defects, grain boundaries or small scale chemical and/or charge heterogeneities. Comparable observations and conclusion were made in several different studies as well (e.g. Bradford and Torkzaban, 2013; Chinju et al., 2001; Darbha et al., 2012a; Fischer et al., 2012). A possible explanation, are the findings of Suresh and Walz (1996); (1997), who showed in theoretical and experimental measurements that surface roughness, even of only tens of nanometers, lowers the repulsive barrier of the collector material. The simulations of Shen et al. (2012) showed that the surface roughness of fracture walls promote particle retention, because of adhesion forces and that retention is more likely in the secondary energy minimum, than in the primary minimum, which implies an reversible retention. Moreover, James and Chrysikopoulos (1999) found in numerical simulations that colloid deposition is inversely proportional to the aperture of the fracture. In natural rough and irregular fractures with spatial variable apertures, the mechanisms provoking or hindering colloid deposition are highly complex. Because even minor roughness can affect colloid deposition and therefore the prediction of colloid deposition coefficients in advance is very difficult. Thus, often lumped parameters are used (Chrysikopoulos, 1999).

On a bigger scale, in colloid transport experiments through a natural fractured granite block (83×90×60 cm) Vilks and Bachinski (1996) investigated the influence of colloid size, velocity, flow direction and flow path on colloid retention. They showed that the transport of colloids is highly sensitive to variations in flow path and flow direction. Moreover, in contrast to solutes, they found that colloid recovery at lower flow velocities (32 m/a and 240 m/a) was significantly decreased compared to higher velocities (> 400 m/a). Solute recovery, however, showed to be much less affected by flow velocity.

Flow channeling is a typical fracture flow feature (Bodin et al., 2003; Huber et al., 2012; Keller et al., 1999; Moreno et al., 1988; Neretnieks et al., 1982; Tsang and Neretnieks, 1998). Therefore, in rough and spatial heterogeneous fractures exclusion and Taylor dispersion mechanisms on colloids are superimposed. The effect of colloid exclusion is increased, because colloids will rather be transported on preferential flow paths, than diffuse to low flow velocity zones in consequence because of their comparably low diffusion coefficient. This effect is therefore more pronounced for larger colloids (Becker et al., 1999; Taylor, 1953). Researches attempting to investigate exclusion mechanisms in variable aperture fractured media are rare. However, numerical studies of Abdel-Salam and Chrysikopoulos (1995b) and Chrysikopoulos and Abdel-Salam (1997) showed that the size exclusion effect increases the dispersion of the colloid plume, leading to earlier breakthrough.

Kosakowski (2004) observed in colloid transport experiments through a shear zone early first arrival and pronounced tailing (non-Fickian transport behavior), and attributed those observation to the geometry and structure of the shear zone. Comparable findings and conclusions were made for solute tracers by Becker and Shapiro (2000). They called this effect non-diffusive breakthrough tailing.

1.3 Motivation and scope of the work

Colloids are ubiquitous in surface and subsurface waters and their migration behavior deviates considerably from ionic species (see above). Because of their size, surface properties and transport behavior, colloids are subject of high relevance since several decades, especially in environmental research. As pointed out above, the transport through fractures is not yet completely understood and the impact of fracture aperture and flow channel geometry needs to be investigated further on, in order to predict and quantify the fate of colloids. This applies above all especially in terms of contaminant or colloid facilitated transport, where fractures serve as preferential conduits.

The prevailing Ph.D. thesis is motivated by the transport of colloids through preexisting fractures and the physical mechanisms acting on the colloids during transport. This work presents a contribution to the following issues:

The impact of

- colloid size and type: 25 and 1000 nm carboxylated polystyrene spheres and 85–350 nm Na-illite colloids;
- residence time: 1–24 h with the help of stop-flow experiments;
- gravity: variation of fracture orientation;
- collector surface roughness: cut granodiorite, natural rough granite, polished acrylic glass;
- flow path heterogeneity and aperture: two differently altered fractured granite cores;

on colloid transport.

As many properties affect colloid transport, the thesis is based on a systematical bottom-up approach, increasing the complexity for both the used colloids and the fracture flow cells in four steps (Figure 9). All experiments in this Ph.D. thesis are conducted under laminar flow, low ionic strength and unfavorable colloid attachment conditions:

(i) The first step contains continuous and stop-flow experiments in a simple circular parallel-plate fracture flow cell. The interaction of monodisperse fluorescent carboxylated polystyrene spheres (25 nm and 1000 nm diameter) with a cut granodiorite surface (Grimsel granodiorite; Switzerland) and with acrylic glass is examined both experimentally and numerically. The investigations focus on the impacts of surface roughness, fracture orientation, residence time and colloid size. Using atomic force microscopy (AFM) and, more specifically, the colloid probe technique, surface roughness and force distance information of the collector material as a function of probe size (cantilever) are obtained. The experiments are quantitatively modeled using 2-D numerical simulations.

In the framework of this work additional investigations are made observing the colloid deposition behavior on the granodiorite disc as a function of colloid concentration and flow velocity.

(ii) In the second step, the experiments are repeated by using polydisperse clay suspensions in order to investigate the transport behavior of natural colloids and the appropriateness of monodisperse carboxylated polystyrene spheres as clay colloid analogues. For this purpose nanoparticulate Na-illite in ultra-trace concentration range is used. Laser-induced breakdown detection (LIBD) is applied with the regard to detect and quantify the colloids.

(iii) In order to get an understanding of fluid flow and solute transport through a natural rough fracture, in the third step, two differently altered fractured granite drill cores are utilized. The impact of flow channel geometry on conservative solute transport is investigated experimentally and numerically on different dipole flow fields induced by three in- and extraction locations at top and bottom. The residence time distribution of the injected solute solvent is recorded by means of fluorescence spectroscopy. Based on tomographic data of the fractures 2.5-D numerical models are generated to simulate different experimental cases. In order to study purely the physical transport process an advection-diffusion approach was chosen without incorporating chemical and physical interactions with the fracture surface (e.g. sorption, matrix diffusion), expect for molecular diffusion.

(iv) The final step is based on the combined findings from step two and three. Step four draws colloid transport experiments through the two differently altered granite fractures using nanoparticulate Na-illite. Colloid concentrations in ultra-trace range are used in order to avoid full surface coverage or flocculation effects. LIBD is applied with the purpose to detect and quantify the injected colloids.

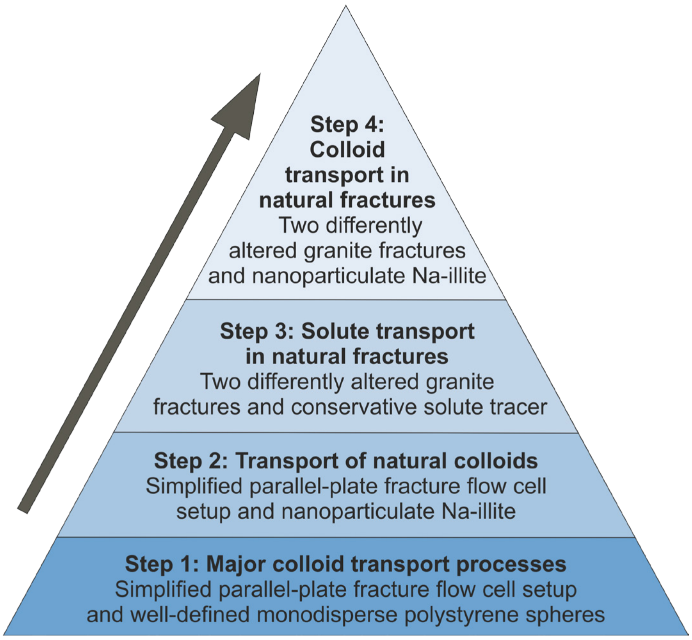

Figure 9: Bottom-up approach of the thesis.

2 Impact of gravity, collector surface roughness and fracture orientation on colloid retention kinetics in an artificial fracture

M. STOLL[1*], F. M. HUBER[1], G. K. DARBHA[1,2], E. SCHILL[1], T. SCHÄFER[1,3]

[1]Karlsruhe Institute of Technology (KIT), Institute for Nuclear Waste Disposal (INE), P.O. Box 3640, 76021, Karlsruhe, Germany

[2]National Institute of Technology, Tadepalligudem, Andhra Pradesh, 534101, India

[3]Karlsruhe Institute of Technology (KIT), Institute of Applied Geosciences (AGW), Environmental Geology, Karlsruhe, Germany

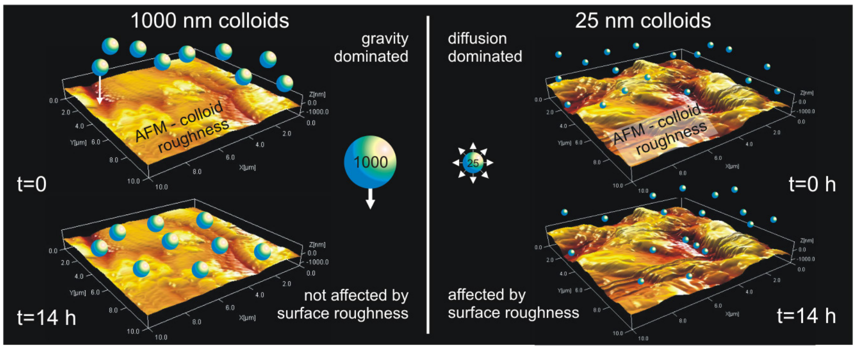

Graphical abstract

2.1 Abstract

The interaction of monodisperse fluorescent carboxylated polystyrene colloids (25 nm and 1000 nm diameter) with a cut granodiorite surface (Grimsel granodiorite; Switzerland) and with acrylic glass is investigated both experimentally and numerically. Colloid transport experiments are conducted in a parallel-plate type fracture flow cell with an aperture of 0.75 mm at pH 5 under low ionic strength (1 mM NaCl) and under laminar flow (7 mL/h) conditions. The study focuses on the effect of residence time, colloid size, collector material and fracture orientation on colloid retention. Long colloid residence times are achieved by stop-flow experiments. Using atomic force microscopy and, more specifically, the colloid probe technique, surface roughness and force distance information of the collector material (granodiorite or acrylic glass) as a function of probe size (cantilever) are obtained. The experiments are modeled using COMSOL Multiphysics® (2-D numerical simulations). The experimental and the modeled results lead to the conclusion that large colloids (1000 nm diameter) undergo sedimentation and deposition on the surface during stop-flow. Collector interaction is not affected by the surface roughness variation. Contrariwise, for the investigated 25 nm colloids sedimentation does not play a role under the experimental conditions and collector interaction is triggered by surface inhomogeneities such as surface roughness.

2.2 Introduction

Colloids such as clay minerals and humic substances are ubiquitous in surface and subsurface waters. Because of the low settling velocity, small colloids (≤ 1 µm) can travel long distances, e.g. through fractures or porous media (Kim et al., 1983; Schäfer et al., 2012). Colloid transport in geological formations has been studied for decades. For example, there are environmental issues such as contaminant transport in groundwater (Chrysikopoulos, 1999; Kretzschmar and Schäfer, 2005; McCarthy and McKay, 2004; McCarthy and Zachara, 1989; Weisbrod et al., 2002) and more specifically colloid facilitated radionuclide transport *inter alia* at the Nevada Test Site and in the Underground Research Laboratory (URL) experiments at the Grimsel Test Site (Geckeis et al., 2004; Kersting et al., 1999; Möri et al., 2003; Utsunomiya et al., 2009). Besides negative economic issues such as pore clogging (formation damage) during extraction of fluids from the subsurface (e.g. Civan, 2011; Rosenbrand et al., 2014), in fractured reservoirs, deposition of clay colloids enhances reactivation potential and thus, permeability (Evans et al., 2005; Geiermann and Schill, 2010). In this study we focus on fractured media. Fractures serve as preferential conduits for colloids. This is due to (i) large flow diameters that enable high flow velocities compared to the surrounding matrix, (ii) mostly unfavorable conditions for attachment due to negatively charged surfaces of colloids and fractured walls and (iii) negligible matrix diffusion of colloids in contrast to solutes (Alonso et al., 2007a; Chrysikopoulos, 1999; McKay et al., 2002; Schäfer et al., 2012). The mechanistic understanding of colloid transport determining processes in fractured rocks is a key to make reliable long-term predictions on the fate of hazardous elements attached to colloids. Major processes acting on colloids during the transport in saturated fractures are advection, dispersion, adsorption, desorption and physical straining (Zhang et al., 2012). Colloids are transported through conductive fractures by advection. Under high groundwater flow conditions it has been shown that the mean colloid transport velocity is enhanced in contrast to solute conservative tracers (Becker et al., 1999; Champ and Schroeter, 1988; Geckeis et al., 2004; Hinsby et al., 1996; Knapp et al., 2000; McCarthy et al., 2002; McKay et al., 2002; Möri et al., 2003; Reimus, 1995; Tang and Weisbrod, 2009; Zvikelsky and Weisbrod, 2006; Zvikelsky et al., 2008). This can be explained by a combination of three effects: size exclusion, charge exclusion and Taylor dispersion (Becker et al., 1999; Zvikelsky and Weisbrod, 2006). Thus, colloids migrate through a comparably smaller effective volume and due to their small diffusivity the colloids diffuse too slowly to enter low or stagnant flow zones (Reimus, 1995). According to the Stokes-Einstein equation (Einstein, 1905) this effect increases with increasing colloid size because of a colloid radius dependent lower diffusion coefficient. James and Chrysikopoulos (2003) showed that colloids follow the highest flow velocities in the center of the fracture. Thus, colloids follow a parabolic velocity profile and travel midstream while migrating through a fracture.

Beside the fraction that is transported unretarded, colloid retention occurs to a certain extent. The main mechanisms for retention are physical straining, sedimentation, (matrix) diffusion, and adsorption/desorption (Zhang et al., 2012). Colloid deposition on solid surfaces is subdivided into two processes: transport and attachment (Elimelech and O'Melia, 1990). The transport process can be described by advection-diffusion equations and it depicts the movement of the colloids from the bulk fluid to the vicinity of the fracture surface. The attachment process depends on the interaction forces between the colloids and the collector surface (e.g. fracture wall) discriminating between electrostatically favorable and unfavorable conditions of attachment (Chinju et al., 2001). This electrostatic dependent interaction is often described by the DLVO-Theory (for further information see e. g van Oss et al. (1990)). However, both field- and laboratory experiments found significant colloid retention even under electrostatically unfavorable conditions, where repulsive forces dominate (Missana et al., 2008; Schäfer et al., 2004; Shen et al., 2010). For example, Albarran et al. (2013) analyzed the transport behavior of artificial (gold and latex) and natural (smectite) colloids in colloid transport experiments through a rough granite fracture under unfavorable attachment conditions. They observed colloid retention for all colloid types and sizes. They concluded that this retention is not driven by the chemical composition of the minerals but rather by mineral porosity, surface roughness, crystal defects, grain boundaries or small scale chemical and/or charge heterogeneities. This conclusion was made in several comparable studies as well (e.g. Bradford and Torkzaban, 2013; Chinju et al., 2001; Darbha et al., 2012a; Fischer et al., 2012). On a bigger scale, in colloid transport experiments through a natural fractured granite block (83 × 90 × 60 cm) Vilks and Bachinski (1996) investigated the influence of colloid size, velocity, flow direction and flow path on colloid retention. They showed that the transport of colloids is highly sensitive to variations in flow path and flow direction.

In studies on low density carboxylated polystyrene spheres Cumbie and McKay (1999) discovered a significant influence of colloid diameter on transport and retention in fractured shale saprolite. The optimum transported colloid size was found to be 500 nm. In accordance with filtration theory (Tufenkji and Elimelech, 2004; Yao et al., 1971), both smaller (50–100 nm diameter) and bigger colloids (1000 nm diameter) showed higher filtration factors and therefore lower recovery – the smaller colloids due to diffusion and the bigger colloids due to sedimentation. This conclusion verifies the experimental results and conceptual model of Reimus (1995). The influence of collector surface orientation on colloid deposition was investigated in detail by Dokou et al. (2001) by means of static batch experiments using colloids of different sizes and densities and vertical or horizontal coated glass surfaces. They found that under stagnant conditions gravity is negligible for low density colloids (1.05 g/cm³) with sizes < 1 µm. In experiments using bigger or denser colloids (2.07 g/cm³ or 19.20 g/cm³) they observed a higher amount of colloids on horizontal glass samples than on vertical glass samples. The impact of gravity on transported colloids was shown in numerical studies of James and Chrysikopoulos (2011) who investigated the influence of fracture orientation on colloid transport through a single fracture.

In all these studies mentioned above, the influence of collector roughness on colloid retention as a function of colloid size was not investigated in detail. Therefore, the aim of this study is to gain process understanding of colloid size dependent transport and deposition on cut granodiorite surfaces by a combination of the following methodical approaches:

(i) Macro-scale colloid transport experiments under laminar flow conditions (7 mL/h) using a parallel-plate type fracture flow cell and a background electrolyte of 1 mM NaCl at pH 5 establishing bulk unfavorable colloid attachment conditions.

(ii) Micro- to nano-scale investigations on the colloid–collector interaction by means of atomic force microscopy (AFM) characterizing (a) the collector surface roughness and (b) the interaction forces using the colloid probe technique.

(iii) The experiments are accompanied by 2-D numerical simulations using COMSOL Multiphysics®. The laminar flow and the colloid transport are solved using the Navier-Stokes equation and a Lagrangian particle tracing approach. Implemented forces, which are acting on the colloids are gravity, drag force and Brownian motion.

Parameter variations in the macro-scale experiments included (a) the flow velocity with flow interruptions (“stop-flow”) to simulate long residence times, (b) the collector surface roughness in comparison to acrylic glass as reference material, (c) the fracture orientation to sound the potential influence of gravity and (d) the colloid size by using 25 nm and 1000 nm polystyrene carboxylated spheres.

2.3 Material and methods

2.3.1 Artificial fracture flow cell

A parallel-plate type fracture flow cell made of acrylic glass (Polymethyl methacrylate, PMMA, trademark Plexiglas®) has been designed and constructed. The scheme in Figure 10a shows the fracture cell dimensions and design. The main parts consist of two cylindrical bodies: one larger body with an inlet and an outlet and one disc like body. A cavity with the dimensions of 38.3 mm diameter and 0.75 mm depth has been drilled into the bottom side of the larger upper body. After assembling the flow cell, the cavity represents the artificial fracture aperture with the top side surface always consisting of acrylic glass, whereas the lower body can be exchanged to, e.g. granodiorite as shown in Figure 10b or acrylic glass. The volume of the fracture is 0.86 mL (inclusive inlet and outlet channels 0.99 mL in total). With the help of an O-ring the fluid cell is sealed and leak-proof. The construction is fixed along its sides by six screws (shown in Figure 10b). The advantage of this set-up is the possibility to open it after each experiment for post mortem analyses.

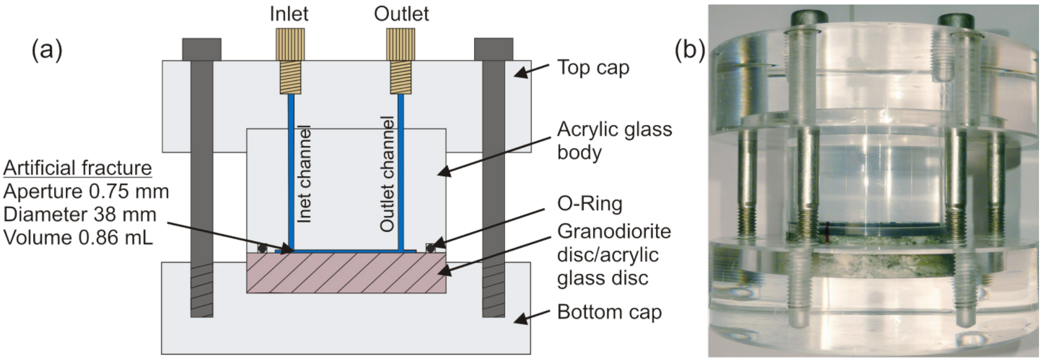

Figure 10: (a) Scheme of the synthetic fracture flow cell. The exchangeable disc is marked in purple. (b) Fracture flow cell with installed granodiorite disc. Marks on the rim of the disc assure the correct position of the disc in the casing each time after assembling.

The granodiorite disc used with a diameter of 54 mm originates from the Aar Massif in Switzerland, taken at the Grimsel Test Site (GTS, Switzerland). This disc is cut without further treatment (e.g. polishing). After installing the disc in the fracture cell, the flow-wet surface is 2236 mm². The Grimsel granodiorite consists mineralogically of quartz (32.8 vol.-%), K-feldspar (17.2 vol.-%), plagioclase (36.5 vol.-%), biotite (6.4 vol.-%), mica and sericite (2.1 vol.-%) and accessory minerals (5.0 vol.-%) (mean values taken from Jokelainen et al. (2013)). The acrylic glass disc (Polymethyl methacrylate, PMMA, trademark Plexiglas®) with a cut and polished surface (preparation of the acrylic glass disc see SI) has the identical dimensions as mentioned above.

2.3.2 Collector material properties

Streaming potential measurements have been carried out to determine the zeta potential under the geochemical conditions prevailing in the experiments for both collector surface materials: granodiorite and acrylic glass. To determine the zeta potential, streaming current measurements are carried out using the SurPass Apparatus (Anton Paar, dimensions streaming channel: 10 × 20 × 0.5 mm) (Lützenkirchen and Richter, 2013). For an ionic strength of 1 mM NaCl and pH 5.1 the obtained overall zeta potential for the Grimsel granodiorite is –38 mV and for acrylic glass –49 mV, respectively.

In order to determine the interaction between colloids and the different mineral phases of the granodiorite sample in AFM measurements (Dimension 3100 atomic force microscope equipped with a nanoscope IV controller, Bruker, Germany), the mineralogy of a narrow area on the sample is characterized using scanning electron microscopy (SEM) and energy-dispersive X-ray spectroscopy (EDX). SEM analyses are performed using a QUANTA 650 FEG environmental scanning electron microscope (FEI, USA). Furthermore, the detection of characteristic X-rays allows quantitative determination of atomic concentrations at a micrometer scale (EDX).

2.3.3 Colloid suspension and conservative solute tracer

The colloids used for the investigations presented here are monodisperse fluorescent carboxylated polystyrene spheres with diameters of 25 nm (Postnova Analytics GmbH, Germany) and 1000 nm (Sigma Aldrich GmbH, Germany). Important properties are summarized in Table 4. Under the chemical conditions present in the transport experiments, the stability of the colloid suspension (stock diluted in background electrolyte to 0.001 M NaCl and pH 5) is controlled by Photon Correlation Spectroscopy; PCS (ZetaPlus system, Brookhaven Inc., USA). For both colloid types the measured size stays constant for > 24 h, thus, no coagulation occurs and the colloid suspensions are considered stable throughout the transport experiments (Table 4).

Table 4: Colloid properties implemented in the studies. Improvement of Henry's mobility formula by Ohshima (2001) used to calculate zeta potential values.

Colloid size stated [nm]	Colloid size measured [nm]	Ex./Em. wavelength [nm]	Density [g/cm³]	Experimental concentration [ppm]	Colloids per mL stock	Colloids per 5 mL pulse	Zeta potential [mV]
25	35 ± 1	552/580	1.030	1.00	1.20E+15	6.00E+11	–46.3 ± 1.0
1000	1181 ± 29	470/505	1.045	1.00	4.55E+10	9.09E+06	–42.0 ± 1.8

To characterize the hydrodynamics and residence time distribution in the fracture flow cell conservative tracer experiments have been conducted using a conservative solute tracer. The conservative tracer used is a 10 ppb UV-fluorescent 7-amino-1.3-naphthalene disulfonate (Amino-G, Postnova Analytics GmbH, Germany) dye.

2.3.4 Experimental set-up

A scheme of the experimental set-up is shown in Figure 11. The fracture flow cell is connected to a peristaltic pump (REGLO Digital MS-4/8, Ismatec, Germany) during the transport experiments. In order to prevent colloid sorption to the experimental set-up, PEEK tubing has been used whenever possible. The outlet of the fracture cell is connected to a flow-through cuvette (100 µL, Hellma, Germany) inside a luminescence spectrometer (Luminescence Spectrometer 55, Perkin Elmer, USA). The fluorescence signal of the tracer and the colloids is measured continuously yielding residence time distributions (breakthrough curves; BTC). The "Time Drive" application software (BL studio, Germany) enables time-dependent fluorescence measurements at a fixed wavelength. A short data interval (interval between two measuring points: $\Delta t = 3$ s) and the low dead volume of the flow-through cuvette result in a high time resolution dataset. In order to measure the pH and determine the exact flow rate, the eluate is collected and weighed after passing the fluorescence device at the outlet using a balance. The length of the tubing has been kept to a minimum to minimize artificial dispersion by the experimental set-up. The pump is installed directly after the fluorescence spectrometer to limit tubing length before the fluorescence measurement device. The total dead volume of the set-up has been quantified to be 330 µL by performing experiments bypassing the fracture cell. In comparison to the dead volume the fracture volume is 860 µL (inclusive inlet and outlet channels 990 µL in total). Three-way valves (3-Way Flow Switching Valve, Upchurch Scientific, Germany) are utilized for switching between colloid and background electrolyte and for switching between fracture flow cell and bypass in the stop-flow experiments.

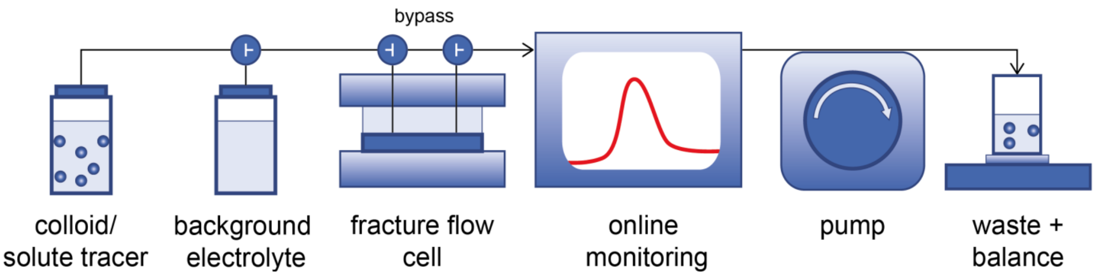

Figure 11: Scheme of the experimental set-up (horizontal fracture orientation).

For all experimental conditions and both colloid types calibration curves are taken to convert the fluorescence intensity into a concentration value. Before each experiment, fresh background electrolyte is prepared, in which the granodiorite disc is saturated and equilibrated overnight. After installing the disc and flushing it for at least one hour, the pH of the eluate is checked. Before and after every experiment the initial concentration C_0 of the tracer/colloid suspension is measured by injecting the tracer or colloid suspension directly into the flow-through-cuvette using a syringe. Thus, slight fluctuations of the output signal can be compensated by taking the mean fluorescence intensity of both measurements.

To start a continuous flow experiment, the colloid suspension or the solute tracer is pumped into the fracture flow cell. A pulse of 5 mL is used to ensure a constant colloid concentration in the whole fracture. The flow rate in all experiments is set to 7.0 ± 0.1 mL/h. After saturating the fracture flow cell, the injection fluid is switched to the background electrolyte and the system is flushed. The flushing step is stopped when the fluorescence intensity value reaches the background level. Due to the small spatial dimensions and void volume of the fracture flow cell and the limitation of the pump in performing small flow rates (min. 2 mL/h), the longest residence time in a continuous flow experiment is ≈ 30 min. Therefore, to achieve longer residence times (> 1 h), flow interruptions ("stop-flow") are conducted. After injecting 5 mL of the colloid suspension, the cell is disconnected by switching to the bypass and the injection solution is switched to the background electrolyte. Thereby the colloids within the cell are captured and the whole tubing is flushed to be colloid free. After the desired residence time is reached, the cell is reconnected to the flow and the mobile colloids can be detected as a breakthrough curve.

With the help of the stop-flow method, residence times of 1 h, 3 h, 14 h and 24 h are achieved. Furthermore, the fracture is either orientated vertically or horizontally to investigate the influence of gravity on colloidal transport. In case of the vertical fracture orientation, the inlet and the outlet channels are oriented in the horizontal direction (injection always from the bottom), whereas for the horizontal fracture orientation the inlet and the outlet channels are positioned vertically. In order to assure that the material surfaces are colloid free before starting an experiment, the set-up is opened and the single parts are ultra-sonicated in a slight alkaline solution (pH 7–9) after each experiment. Additionally, in case of 1000 nm colloids the colloid free surface is verified using fluorescence microscopy.

To normalize the data, the ratio of measured concentration $C(t)$ to initial concentration C_0 is plotted as a function of replaced pore volume PV [-], which is defined as:

$$PV = \frac{Q \cdot t_R}{V} \qquad \textbf{Equation 14}$$

where Q [m³/s] is the estimated flow rate, t is the time [s] and V is the volume of the artificial fracture [m³]. For continuous flow experiments the average residence time t_R [s] is defined as:

$$t_R = \frac{V}{Q} \qquad \textbf{Equation 15}$$

where V [m³] is the fracture volume and Q [m³/s] is the applied flow rate. For stop-flow experiments the residence time is taken as the duration time of the stop plus the calculated residence time of the continuous flow.

2.3.5 AFM and colloid probe technique

AFM in combination with the colloid probe technique is used to study (i) the roughness that a colloid experienced while moving along the granodiorite surface and (ii) the interaction forces between a colloid and the different mineral phases composing the granodiorite (quartz, plagioclase, K-feldspar and biotite) and the acrylic glass surface. With the colloidal probe technique the interacting forces between colloids and/or planar surfaces can be measured. The cantilever probes modified with carboxylated polystyrene colloids (Ø = 1000 nm) are purchased from Novascan Technologies (USA). The properties of the colloid attached to the cantilever are similar to that used in the transport experiments. Due to the limitation of the colloid size that can be attached to the cantilever, to mimic the 25 nm colloid, a sharp silicon nitride tip (Ø = 25 nm) (Bruker, Germany) is used.

(i) The surface topography and the surface profile of the collector surfaces are obtained using both the colloid probe and the sharp tip in contact mode. The obtained data sets are processed for tilt correction and image analysis using scanning probe image processing software (Image metrology, Denmark). The surface topography is quantified using the roughness parameter Rq, which is defined as the root mean square deviation of the profile (Jorgensen et al., 1993):

$$Rq = \sqrt{\frac{1}{n}\sum_{i=1}^{n} z_i^2} \qquad \textbf{Equation 16}$$

where n is the number of points in the profile, and z_i [nm] is the height value at point i.

(ii) In order to determine the diffuse layer potential of the collector surface materials, force-volume measurements are conducted. The force-volume measurements are obtained over 256 data points using the colloid probe technique between the 1000 nm probe and the granodiorite surface in the electrolytic media. For a specific mineral, an average of these 256 data points is considered to be a representative force curve. From the spring constant of the cantilever (0.12 N/m), the force-voltage curves are converted to force-distance curves. Initially, the force curves between polystyrene colloid against a surface with known surface potential, e.g. acrylic glass are, obtained. The DLVO equation is applied to fit the approach force curve to predict the unknown potential of the sphere attached to cantilever. Next, using the same colloid, the force curves are obtained on the granodiorite surface at varying surface sites and the potential distribution is determined using DLVO equation as described before.

2.3.6 Modeling

To facilitate the analysis and interpretation of the experimental findings, numerical flow and colloid transport calculations have been conducted using the Finite Element code COMSOL Multiphysics® (Version 5.0) (COMSOL, 2015).

A 3-D computational model of the artificial fracture flow cell has been constructed with COMSOL. Based on the 3-D model, a 2-D model has been extracted using one of the two symmetry planes of the fracture (Figure 12). To accurately resolve the flow within the fracture cell, a hybrid mesh (prismatic boundary layers and triangular elements) consisting of in total 87,187 elements has been generated.

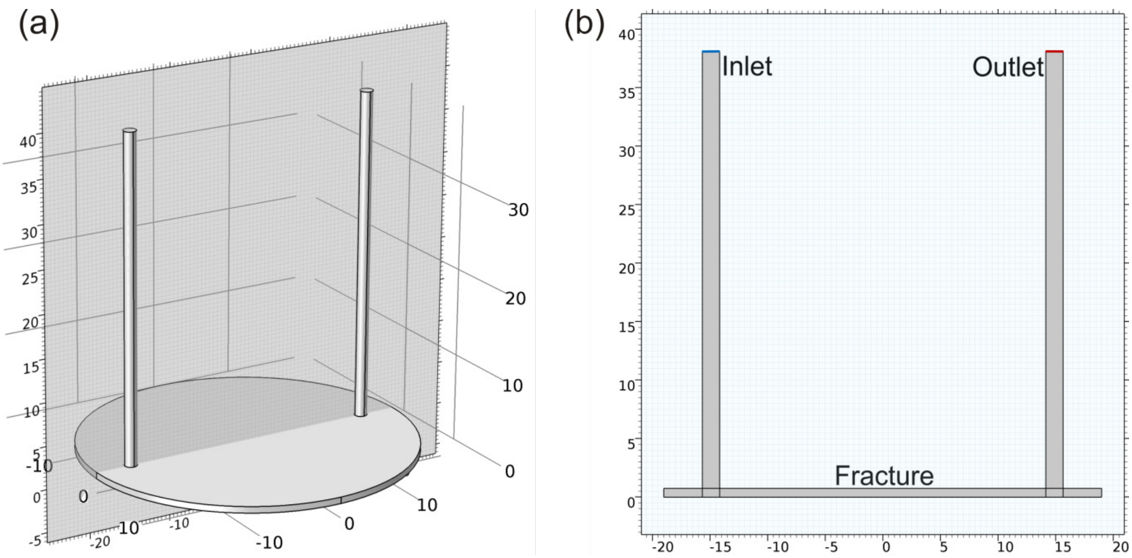

Figure 12: (a) 3-D model of the fracture flow cell. The grey plane indicates the symmetry plane used in the construction of the 2-D model; (b) 2-D model of the fracture flow cell used in the simulations. Blue indicates the inlet, red the outlet of the model (numbers given in the figures are length units in mm).

2.3.6.1 Colloid–wall interaction boundary conditions

Since both the colloids and the collector (fracture; acrylic glass and/or Grimsel granodiorite) surface are negatively charged, only a very weak electrostatic interaction is expected. Though, it has been shown by e.g. Darbha et al. (2012a) that even under unfavorable attachment conditions colloids may be deposited or even attached on the surface due to surface roughness effects or surface charge heterogeneities.

This is why two different cases have been considered in the model to approach the experimental results:

1) No sorption (unfavorable attachment conditions): When a colloid hits the collector surface, it is reflected with the same angle and velocity with which it has hit the surface. This case accounts for sedimentation only without any attachment (attractive forces acting) of the colloid to the surface.
2) Full sorption (favorable attachment conditions): When a colloid hits the surface, it immediately sticks irreversibly to the surface and cannot be removed again from the surface afterwards. This condition may represent an extreme unlikely case given the experimental conditions presented in the manuscript. Nevertheless, it offers an impression of the maximum attachment possible under the hydrodynamic conditions within the fracture flow cell (including also all the additional forces acting on the colloid as mentioned below (Section 2.3.6.2)).

Since there can be also a retention of colloids on acrylic glass, both cases (no sorption and full sorption) are applied for the whole model and not exclusively for the collector surfaces within the fracture. Therefore, a possible retention within the channels, which connect inlet/outlet with the fracture, is implemented.

2.3.6.2 Simulation set-up

The Navier-Stokes equations are solved using the Laminar Flow option of COMSOL Multiphysics®. A mass flow rate boundary condition is applied at the inlet and a pressure condition at the outlet, respectively. The mass flow rate from the experiment (1.972E–6 kg/s) is divided by 2π to account for the 2-D model dimension. No-slip flow boundaries ($v = 0$) are applied to the fracture walls. The COMSOL Particle Tracing Module® is used to solve the colloid transport. Colloid–fluid interaction is modeled by one-way coupling. That is, since the colloid volume fraction in the injection suspensions used in the experiments are below 10%, it is justified to assume no influence of the colloids on the flow field. Moreover, under this diluted condition, colloid–colloid interactions can be neglected as well. This allows solving for the steady state fluid flow and using the simulated stationary flow field in the colloid transport simulation. The colloids are distributed to the flow field at the inlet as a function of the flow velocity distribution. Thus, in the center of the inlet the colloids are more densely distributed compared to the outer area of the inlet. This boundary condition is chosen for both the 1000 nm and the 25 nm colloids. Especially for the 1000 nm colloids, it has been shown that bigger colloids tend to be transported in the center where the highest flow velocities occur (James and Chrysikopoulos, 2003). In all the experiments, a 5 mL pulse of colloid suspension is used. In the model, this pulse is modeled by injecting every second 25 colloids at the inlet for the duration of the pulse. After 2,535 s injection time no further colloids are injected. In case of the stop-flow experiments, the flow field is re-initialized after 2,535 s to set all flow velocities to zero. Thus, the only forces acting on the colloids during the stop-flow conditions are Brownian motion and gravity. After the desired flow interruptions, the original flow field is re-initialized again and the transport of the colloids resumed. In all simulations, the total number of colloids introduced accumulates to 63,400. This number of colloids accounts to 0.7% of the total number of colloids used in the 1000 nm experiments (9.09E+06 colloids) and 0.00001% in the 25 nm experiments (6.00E+11 colloids), respectively. Nevertheless, this number is a compromise concerning the computational duration increasing with the modeled particle number. A sensitivity study with varying particle number was performed to assure that the chosen colloid number is high enough.

2.4 Results and discussion of the colloid transport experiments

This section is subdivided in the results of the continuous flow experiments (section 2.4.1) and the "stop-flow" experiments (section 2.4.2). The reproducibility of the experiments was confirmed by repeating experiments randomly (see supporting information A.I 1).

2.4.1 Continuous Flow experiments and conservative solute tracer

Continuous flow experiments with a flow rate of 7 mL/h for both colloid sizes and both fracture orientations have been conducted. According to Equation 15 the residence time of the colloids in the fracture is 7.4 min. Figure 13 shows the BTCs of the experiments conducted with a horizontal fracture orientation (left) and with a vertical fracture orientation (right). Compared to the conservative tracer Amino-G, the colloid results show earlier first arrivals for both colloid types and slightly more pronounced tailings in the measured breakthrough curves for the 1000 nm colloids. As mentioned before, the earlier arrival of the colloid is likely due to size exclusion, charge exclusion and Taylor dispersion (e.g. Becker et al., 1999; Zvikelsky and Weisbrod, 2006).

The recoveries of the colloid experiments (Table 5) deviate in < 4% and all recoveries are > 95%. No dependence of colloid retention on fracture orientation can be detected for both colloid types. Slightly less recovery is observed for 25 nm colloids compared to 1000 nm colloids for equal transport conditions, but this deviation is in the range of the error (≈ 2–3%).

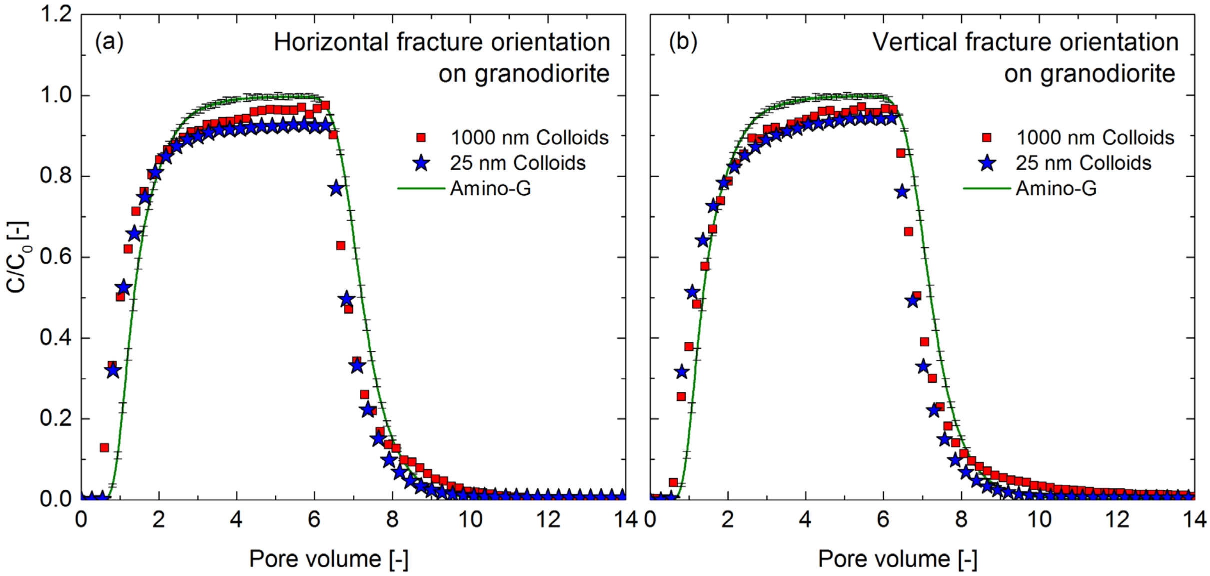

Figure 13: BTCs of continuous transport experiments using 25 nm and 1000 nm colloids and Amino-G on granodiorite (colloid/tracer pulse: 5 mL).

Table 5: Recoveries of the continuous flow experiments (uncertainties of the recovery calculation 2–3%).

Experiment	Flow rate [mL/h]	Residence time [min]	Recovery [%] Horizontal fracture orientation	Recovery [%] Vertical fracture orientation
1000 nm	7	7.4	98	97
25 nm	7	7.4	95	96
Amino-G	7	7.4	99	99

2.4.2 Stop-flow experiments

To investigate whether an increase in residence time has an effect on colloid retention, “stop-flow” experiments are performed (Table 6). Contrary to the section 2.4.1, in this section only the BTCs obtained flushing the fracture flow cell after the stop phase are shown. That means the injection of the colloids into the fracture flow cell and the flushing of the tubing during the stop phase are not shown.

Table 6: Experimental cases and residence times of the “stop-flow” experiments.

Fracture orientation	*1000 nm Colloid*		*25 nm Colloid*	
	Granodiorite	**Acrylic glass**	**Granodiorite**	**Acrylic glass**
Horizontal	1 h, 3 h, 14h , 24h	1 h, 3 h, 14h , 24h	1 h, 3 h, 14h , 24h	1 h, 3 h, 14h , 24h
Vertical	1 h, 3 h, 14h , 24h	1 h, 3 h, 14h , 24h	1 h, 3 h, 14h , 24h	1 h, 3 h, 14h , 24h

Figure 14(a–d) shows the breakthrough curves of the 1000 nm polystyrene colloids and Figure 15(a–d) of the 25 nm polystyrene colloids, respectively. In all cases the heights of the BTCs decrease with increasing residence time. In case of the 1000 nm colloids (Figure 14(a–d)) for the same fracture orientation (a & b or c & d), no striking difference between experiments using granodiorite or acrylic glass can be observed. By comparing the vertical and the horizontal experiments using the same collector surface, both the heights and the shapes of the breakthrough curves differ for residence times ≥ 3 h. For example, with increasing residence time the BTCs of the vertical experiments decrease in height but the shape of the BTCs stays constant. In contrast, in the horizontal experiments after 3 h residence time the peak of the BTC is broadened and a flat plateau shape evolves. After 14 h and 24 h the BTCs have a double peak shape with a larger first peak and a smaller second peak. This feature is not visible in the vertical experiments. Regarding these results, for 1000 nm polystyrene colloids there is an influence of fracture orientation on colloid retetion, but no influence of collector surface, respcetively.

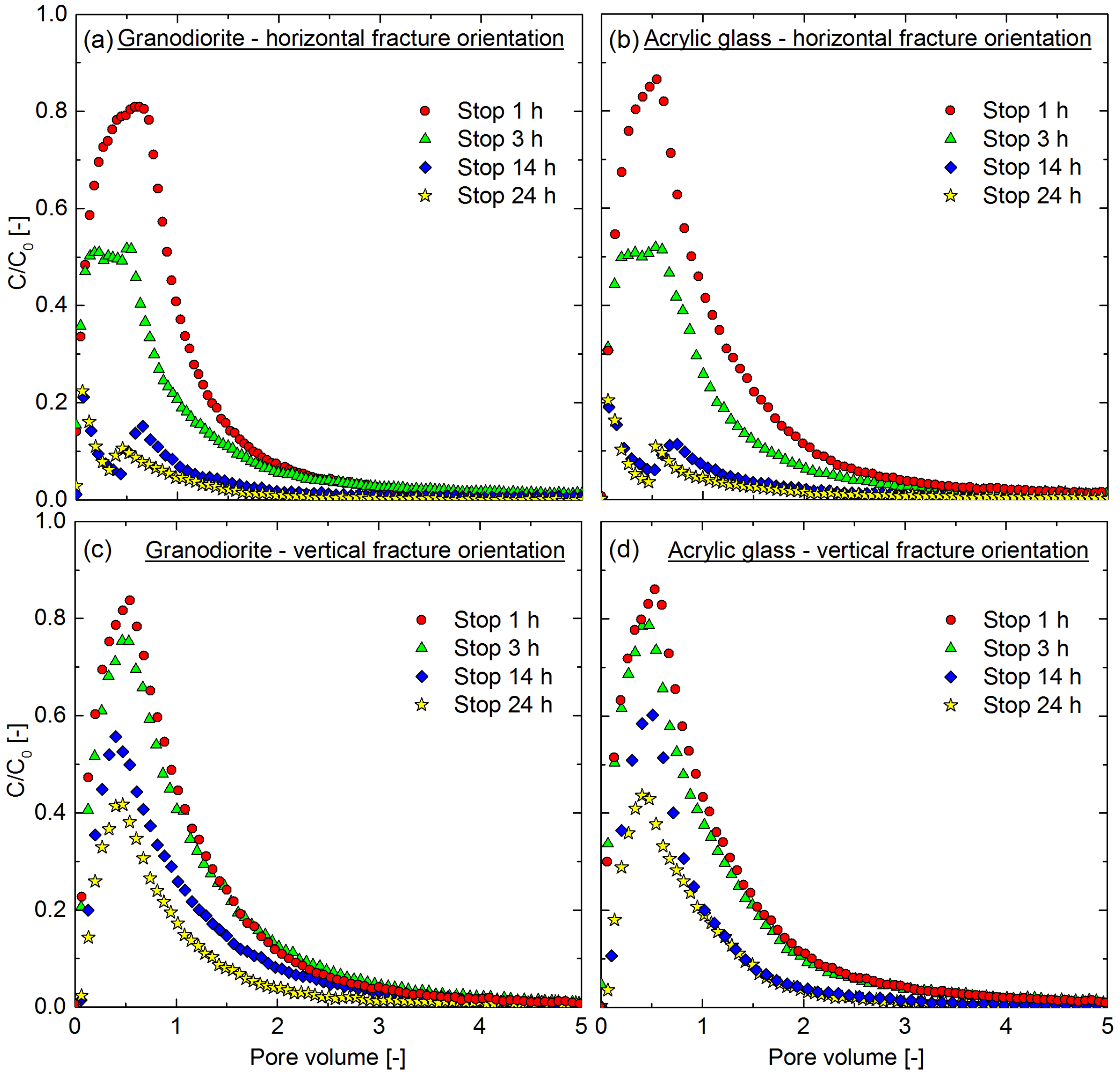

Figure 14: BTCs of "stop-flow" experiments on granodiorite (a & c) and acrylic glass (b & d) using 1000 nm colloids for horizontal (top) and vertical (bottom) fracture orientation.

Contrary to that, the BTCs of the 25 nm colloid experiments (Figure 15(a–d)) show an influence of the collector surface on colloid retention but an influence of fracture orientation is not visible. For equal fracture orientation the heights of the BTCs differ between granodiorite and acrylic glass with higher BTCs in experiments on acrylic glass. Comparable with the horizontal 1000 nm colloid experiments after residence times of 14 h and 24 h, a double peak shape evolves in all cases.

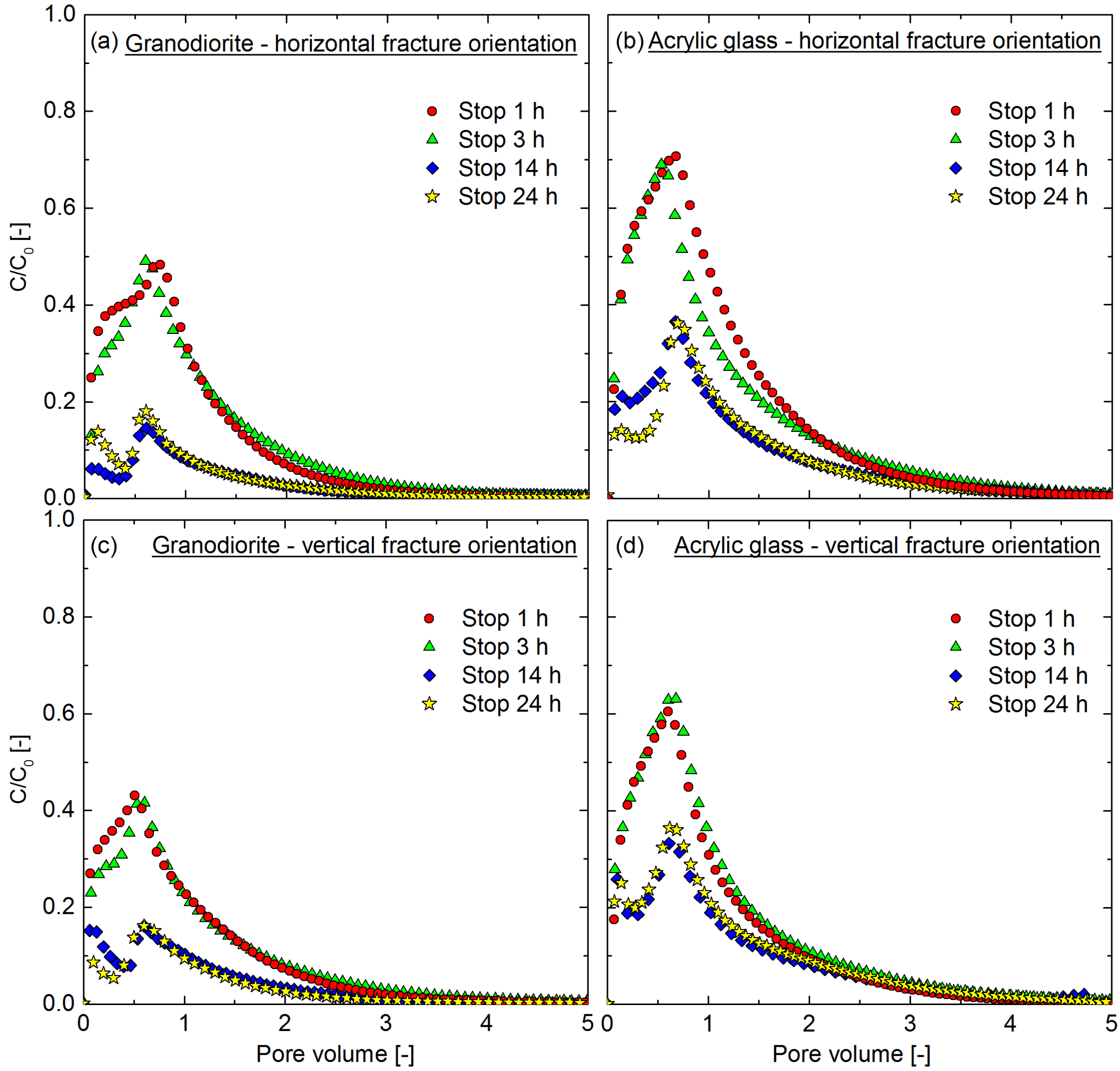

Figure 15: BTCs of "stop-flow" experiments on granodiorite (a & c) and acrylic glass (b & d) using 25 nm colloids for horizontal (top) and vertical (bottom) fracture orientation.

Figure 16 shows the corresponding recoveries as a function of residence time for 1000 nm colloids and 25 nm colloids. An exponential fit (first order exponential decay function) is used to describe the 1000 nm colloid data. However, a second order exponential decay function is needed to describe the 25 nm colloid data due to the comparably high colloid retention within the first hour of stop-flow in all experimental cases. By comparing the recoveries with the obtained BTCs, the observed features are visible as well. In all cases the recovery decreases with increasing residence time. In case of the 1000 nm colloids for short residence times (1 h and 3 h) the recoveries are similar between the vertical and the horizontal case. But for the long residence times in the vertical case the recoveries are more than three times higher compared to the horizontal case. The deviation between horizontal and vertical cases increases with increasing residence time. In case of the 25 nm colloids, the colloid recovery decreases with increasing residence time more pronounced in the experiments using granodiorite compared to acrylic glass. In experiments using granodiorite, after 1 h residence time the recovery is < 50%. The adaption of a second order exponential decay function shows that two mechanisms influence the colloid retention both on granodiorite and on acrylic glass for the 25 nm colloids. Within the first hour a fast kinetic prevails with the rate of $> 4\ \text{h}^{-1}$. With increasing residence time the kinetic slows down, which leads to smaller rates ($< 0.1\ \text{h}^{-1}$).

The progress of the recoveries shows a correlation between fracture orientation and colloid retention for the 1000 nm colloids and a correlation between collector surface material and colloid retention for the 25 nm colloids. This indicates that the 1000 nm colloids undergo sedimentation during their residence within the fracture and that the 25 nm colloids interact with the collector material.

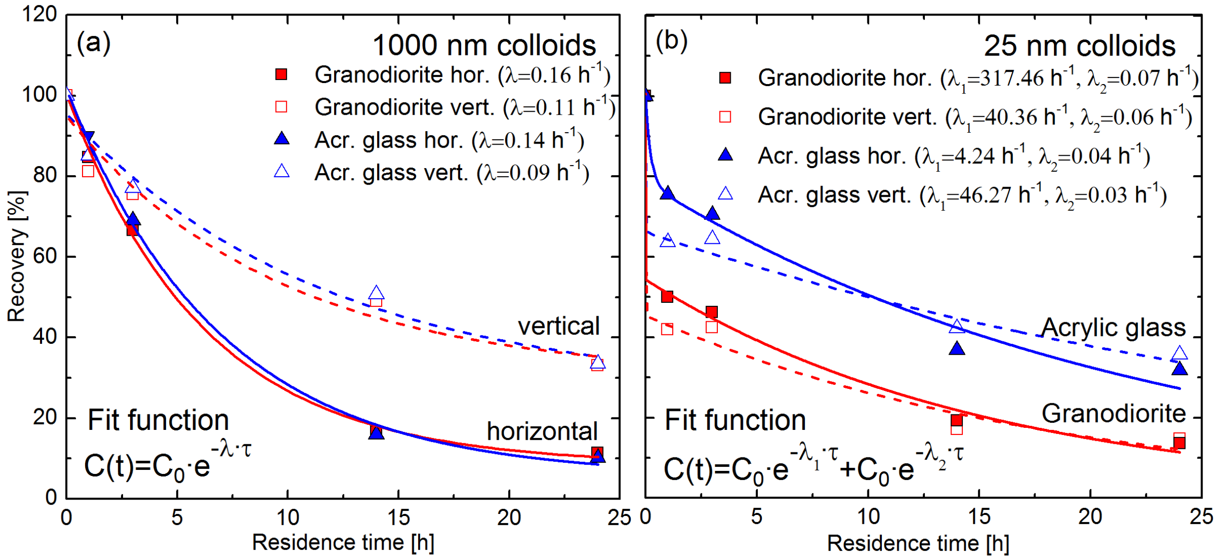

Figure 16: Colloid recovery over residence time of “stop-flow” experiments using (a) 1000 nm colloids and (b) 25 nm colloids. The solid lines represent the fit function of the horizontal experiments and the dotted lines of the vertical experiments.

Based on the results of the breakthrough curves, it is not possible to differentiate, whether the retained colloids are attached irreversibly to the fracture set-up or if all colloids are flushed out as soon as the flushing time is long enough. Because colloids, which are deposited to the fracture surface, need longer to leave the fracture, due to low flow velocity in the vicinity of the surface than colloids, which are in the middle stream assuming a parabolic flow field. This might lead to a dilution effect and generates a concentration beneath the detection limit.

The BTCs generated with the 2-D model (see A.I 2 and A.I 3) show comparable results. In case of the 1000 nm models with and without sorption, an evolution of double peaks is visible for horizontal fracture orientation. In case of the vertical simulations with increasing residence time, the evolution of one single peak is visible with and without sorption. This supports the observation that the retention of the 1000 nm colloids is not dependent on the collector surface material. The model also confirms the experimental results for the 25 nm colloids. There are no differences between vertical and horizontal cases with and without sorption which supports the experimental observations. In case of sorption, double peak shapes evolve in both vertical and horizontal cases, which also supports the experimental results that the retention of 25 nm colloids are influenced by the collector material and not by the fracture orientation. A comparison is not made between the experimental recoveries and the modeled recoveries because of the geometrical deviation between the real fracture flow cell and the 2-D model.

2.4.2.1 Impact of colloid size

To clarify the impact of colloid size on colloid retention, it is important to understand the dominating forces acting on the colloids during the stop-flow phase. The prevailing deposition mechanism that brings a colloid to the fracture surface during the stop-flow phase is either sedimentation or Brownian motion and it is dependent on the density and size of the colloids. The relative influence of both mechanisms can be analyzed by comparing the ratio of the characteristic sedimentation length and diffusion length for both types of colloid sizes. The sedimentation length L_S [m] for spherical colloids is defined as the product of the Stokes settling rate and the residence time of the colloids in the fracture (Becker et al., 1999):

$$L_S = \left(\frac{1}{18\eta}\right)(\rho_p - \rho_f) g d_p^2 t_R$$ **Equation 17**

where η [kg/ms] is the dynamic viscosity in water, ρ_f and ρ_p [kg/m³] are the fluid density and the colloid density, g [m/s^2] is the acceleration of gravity, d_p [m] is the colloid diameter, and t_R [s] is the particular residence time in the fracture.

The diffusion length L_D [m] is defined as (Becker et al., 1999):

$$L_D = \sqrt{2Dt_R}$$ **Equation 18**

where D [m²/s] is the Stokes Einstein diffusion coefficient, which is defined by the Stokes-Einstein equation (Einstein, 1905):

$$D = \frac{k_B \cdot T}{6 \cdot \pi \cdot \eta \cdot R}$$ **Equation 19**

where k_B [$m^2 \cdot kg/(s^2 \cdot K)$] is the Boltzmann constant, T [K] is the temperature and R [m] is the mean colloid radius.

The ratio of L_S/L_D represents the relative influence of the two deposition mechanisms: sedimentation or Brownian motion. If the ratio is ≈ 1, both mechanisms are expected to be in equilibrium. Otherwise, sedimentation (ratio > 1) or Brownian motion (ratio < 1) dominates (Becker et al., 1999).

$$L_S/L_D > 1 \qquad\qquad L_S/L_D < 1$$ **Equation 20**

Gravity prevailing Diffusion prevailing

In Figure 17 the ratio of L_S/L_D is shown for 1000 nm and 25 nm colloids as a function of residence time. Already after 1 h the dominating force acting on the 1000 nm colloids is gravity. For the 25 nm colloids the overall force bringing the colloids to the surface is Brownian motion because the ratio of L_S/L_D stays for all residence times < 1. The L_S/L_D ratio stays in close relation to the dimensionless Péclet number, which describes colloid motion as well and which is defined as the ratio of sedimentation and diffusion ($Pe > 1$: sedimentation dominated system; $Pe < 1$: diffusion dominated system):

$$Pe = \frac{u_{sed} \cdot L}{D}$$ **Equation 21**

The sedimentation velocity u_{sed} [m/s] is obtained by Equation 17 setting t_R to 1 s. The aperture of the artificial fracture represents in our case the characteristic length L [m]. This results in $Pe = 47.59$ for the 1000 nm colloids and $Pe = 4.46E–4$ for the 25 nm colloids. By comparing the obtained recoveries of the 1000 nm colloid and 25 nm colloid experiments (Figure 16) with the L_S/L_D ratios and the Péclet numbers, it is reasonable to assume that two mechanisms are responsible for 25 nm colloid retention and only one mechanism, namely sedimentation, for 1000 nm colloid retention. The working hypothesis for the 25 nm colloid retention is that beside Brownian motion an influence of surface roughness might be responsible for the measured surface retention difference between acrylic glass and the granodiorite surface.

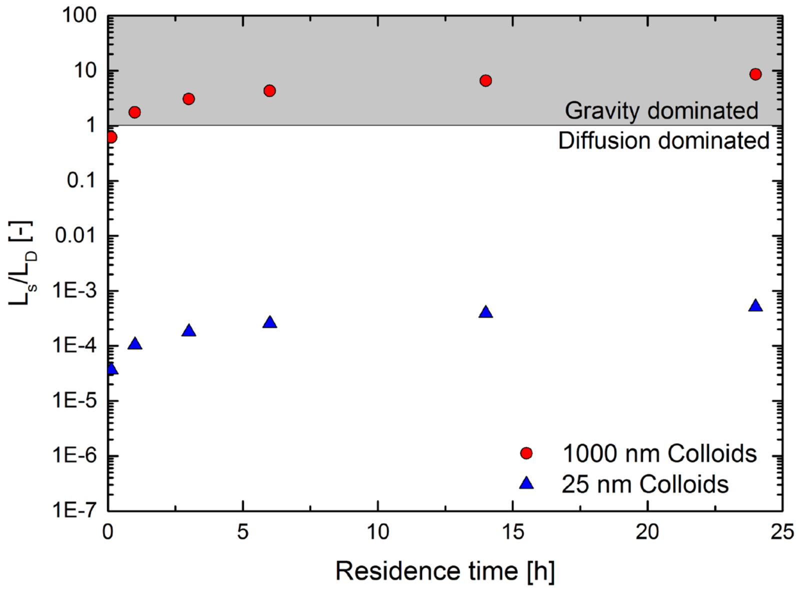

Figure 17: Calculated ratio of L_S/L_D as a function of residence time (7.4 min, 1 h, 3 h, 6 h, 14 h, 24 h) for 1000 nm and 25 nm colloids.

2.4.2.2 Impact of collector surface material on colloid retention

Both electrostatic interaction and surface inhomogeneities, e.g. surface roughness, may trigger the observed colloid retention. In respect to the negative zeta potentials of the bulk materials (Grimsel granodiorite: –38 mV and acrylic glass: –49 mV) and the negative diffuse layer potentials of the mineral phases (K-feldspar: –55 mV; biotite: –51 mV; plagioclase: –62 mV; quartz: –68 mV; more information on the force curves see A.I 4) we assume that the observed colloid retention is not due to electrostatic interactions with the collector surfaces.

For the measurement on the granodiorite disc, a feldspar crystal and on acrylic glass a random area has been chosen to be representative. Each area is first scanned using the 1000 nm colloid attached to the cantilever and in the next step with the 25 nm sharp silicon nitride tip as a representative of the 25 nm polystyrene colloid.

Figure 18 shows the topographic images of the investigated area of the granodiorite (a & b) and the acrylic glass (c & d) surface, scanned by either a 1000 nm colloid or the sharp silicon nitride tip. The 3-D topographic data are projected to denote lateral and height variations on the granodiorite/acrylic glass surfaces as indicated by the color bar with the scale (notice the changing scale range in the color bars). Comparing the topographic images of granodiorite obtained by a 1000 nm colloid versus a 25 nm tip, there are significant differences. The images obtained with a 1000 nm colloid are blurred with rounded edges. No sharp features are visible and the surface is smoother in contrast to the images received by the 25 nm sharp tip. The images of the tip show more details and depth. A four times higher root mean square roughness value (*Rq*) is calculated for the same surface region for the 25 nm sharp tip in comparison to the 1000 nm colloid. In contrast, in case of the acrylic glass topographic data, this difference is less pronounced. *Rq* increases only by a factor of about 1.2 times.

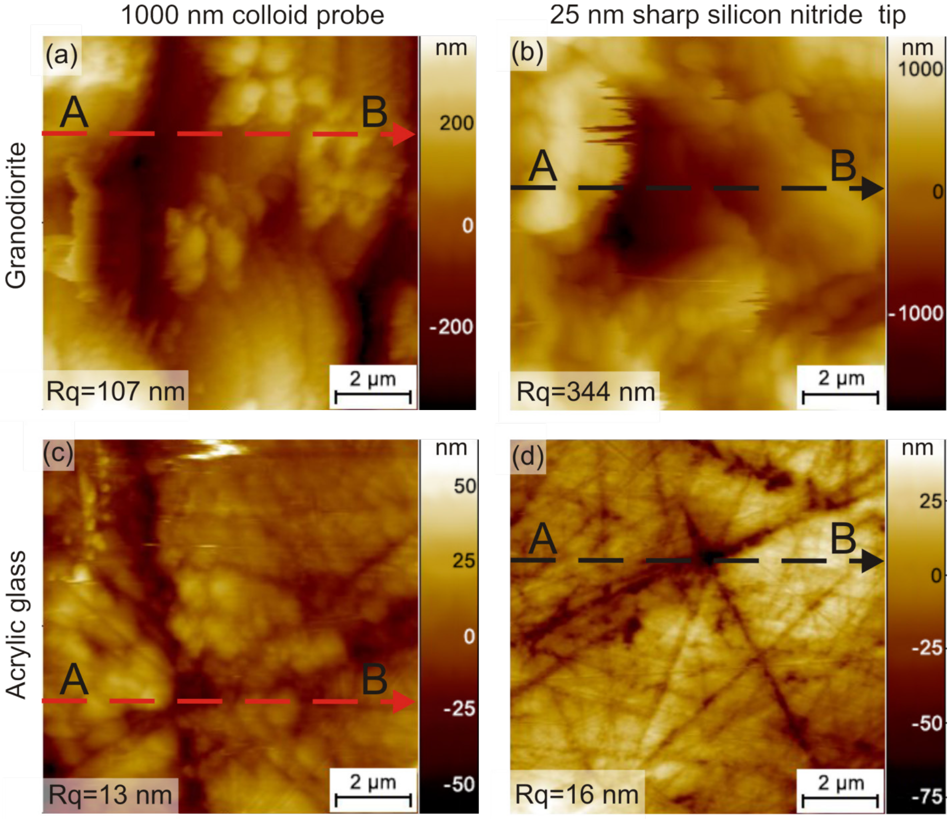

Figure 18: Topographic data obtained from AFM by scanning the granodiorite (top) and the acrylic glass (bottom) surfaces using (a & c) a tip modified with a 1000 nm polystyrene colloid or (b & d) a 25 nm sharp silicon nitride tip. The investigated areas are 8 × 8 µm each. The red and black dotted arrows mark the scanning path and direction of the surface profile scan (Figure 19).

In the form of surface roughness profiles of the same area, Figure 19 illustrates this increase in surface roughness by changing from the 1000 nm colloid (red line) to the 25 nm sharp tip (black line). This means for granodiorite (Figure 19a) that smaller colloids see higher surface roughness in the vicinity of the granodiorite fracture surface. For this particular area *Rt* (maximum height of the profile from the lowest point to highest point) is around 2000 nm. This corresponds to 80 times the colloid size of the 25 nm colloids. Using the sharp tip, grain boundaries and also deep structures within minerals can be visualized. This is not possible with a 40 times bigger 1000 nm colloid. This explains the increase in roughness of the same surface area using a sharper tip. The difference by scanning acrylic glass is less significant

(Figure 19b). The roughness stays more or less constant. This is because acrylic glass is much smoother and homogeneous compared to the granodiorite disc.

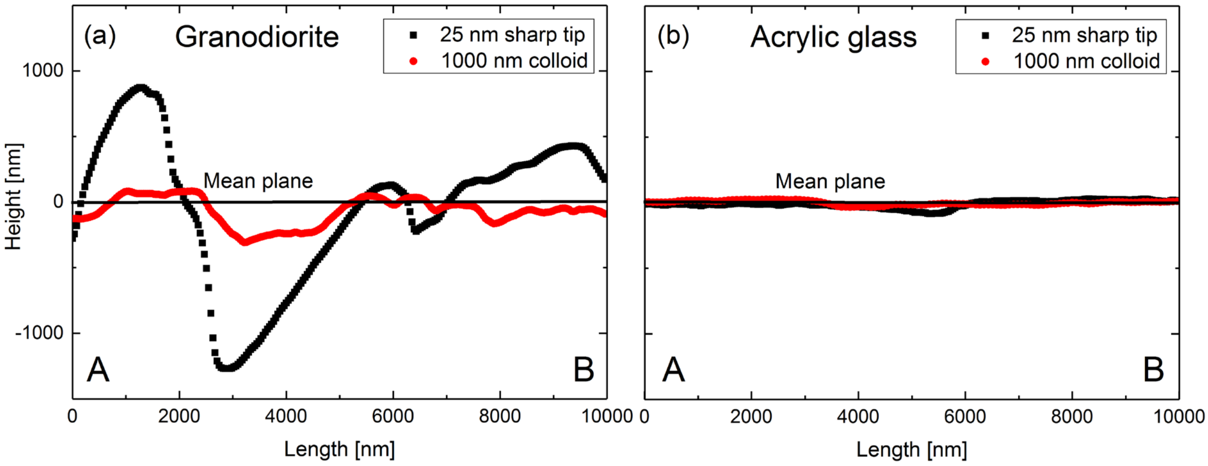

Figure 19: Surface roughness profiles obtained on the granodiorite (a) and the acrylic glass (b) surfaces using a tip modified with a 1000 nm polystyrene colloid (red line) or a 25 nm sharp silicon nitride tip (black line).

These results support the working hypothesis that the colloid retention can be directly correlated with the increased roughness seen by the smaller colloids (25 nm) compared to bigger colloid sizes (1000 nm). Therefore, the higher colloid retention on granodiorite is due to the higher surface roughness compared to acrylic glass. As observed by Darbha et al. (2012b), the effect of surface roughness is dependent on the ratio between the asperity to the interacting colloid. For a constant asperity, smaller colloid sizes experience more surface roughness as clearly documented here. This result explains the double peak shape in the BTC of the 25 nm experiments for long residence times. As already mentioned, the double peak shape is not an effect of the fracture orientation. The colloids, which are inside the fracture show a higher retention than the colloids, which are inside the inlet channel and the outlet channel made of acrylic glass. The roughness and the surface area of both granodiorite and acrylic glass are so high that the colloids are retained on these collector surfaces rather than in the inlet and the outlet channels. In consequence, a double peak shape in the BTC evolves under both fracture orientations and collector surface materials.

2.4.2.3 Impact of fracture orientation on colloid retention and the shape of the BTC

To understand the impact of the fracture orientation on the colloid retention, the colloid distribution within the fracture flow cell during the stop phases has been investigated with the help of the 2-D model. The black boxes in Figure 20 and Figure 21 show the regions of interest (ROIs) that are investigated more closely of (a) the inlet channel and the fracture in horizontal fracture orientation and (b) the outlet channel and the fracture in the vertical fracture orientation. In both cases the results are shown for the colloid distributions in the flow cell after injection (2,535 s), 6 h stop-flow and 14 h stop-flow under conditions without sorption (unfavorable attachment conditions). It can be seen that after injection the colloids are homogeneously distributed in the whole flow cell. Only the stagnant flow areas in the fracture part of the cell are free of colloids.

In case of the 1000 nm colloids (Figure 20), with increasing stop-flow time the colloids settle due to gravity. In the horizontal case (a) after 14 h all colloids, which are initially homogeneously distributed in the fracture have settled to the fracture bottom. Below the inlet (and outlet) there are still colloids since these colloids settle from the inlet area into the fracture area. In contrast, in the vertical case (b) after 14 h almost all colloids initially homogeneously distributed in the outlet channel (and inlet channel) have settled to the outlet channel bottom (and inlet channel bottom). Contrariwise, the fracture stays colloids filled. Based on these results, the development of the double peak in the horizontal case is due to the colloid filled inlet and outlet channels, which form the two peaks in the BTC. The colloid free fracture forms the gap between those peaks. In the “no sorption” case, these colloids are mobilized little by little, which results in the pronounced and long tailings (see A.I 2). In the vertical case, the single peak represents the signal of the homogeneously distributed colloids in the fracture because in these cases the settled colloids in inlet and outlet channels need to be mobilized in the first place as well. Differences in the BTCs between no sorption and full sorption arise in the subsequent flushing stages of the flow cell after the different stop-flow times since in case of the favorable conditions, the attached colloids cannot be mobilized again.

In contrast to that, for 25 nm colloids (Figure 21), it can be seen that after injection the colloids stay evenly distributed within inlet/outlet channels and fracture with increasing residence time. The stagnant flow areas become more colloid filled because of undirected colloid diffusion. This corroborates that the colloids will not undergo sedimentation and that the development of the double peaks in the experimental BTCs is due to higher retention of the colloids within the fracture than in inlet and outlet channels for both collector surface materials. In addition, the retention on granodiorite is higher compared to acrylic glass. But there is no effect of gravity and fracture geometry on colloid retention for 25 nm colloids.

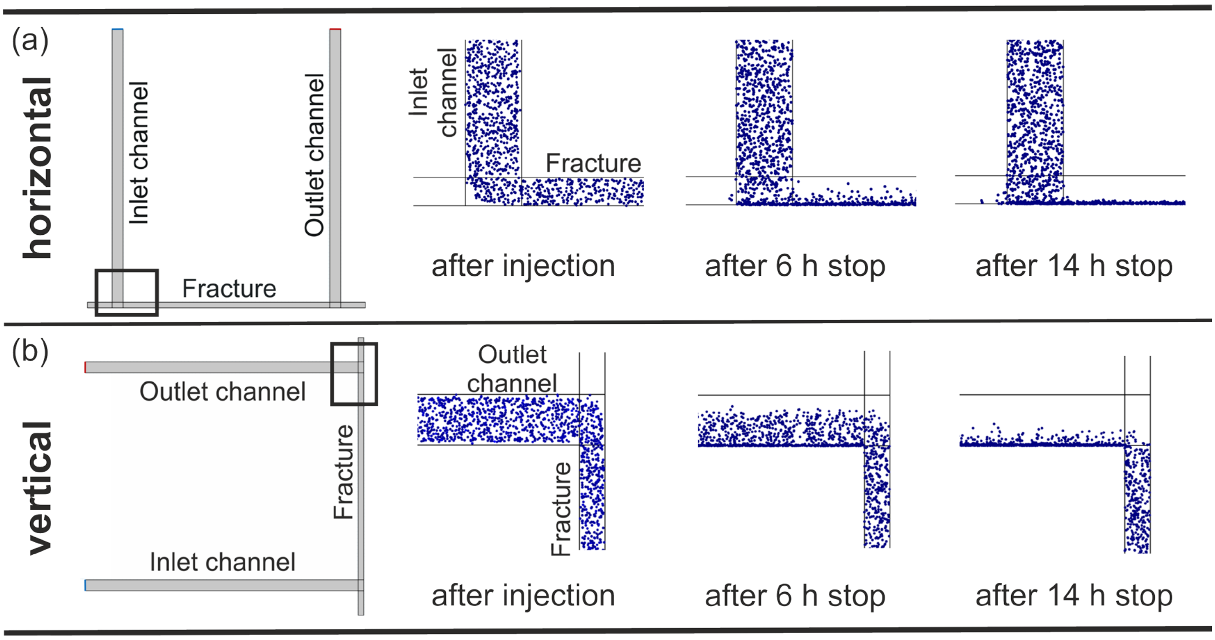

Figure 20: Colloid distribution after injection, after 6 h stop and after 14 h stop of 1000 nm colloids in case of (a) horizontal fracture orientation and (b) vertical fracture orientation. The pictured sizes of the colloids are out of scale.

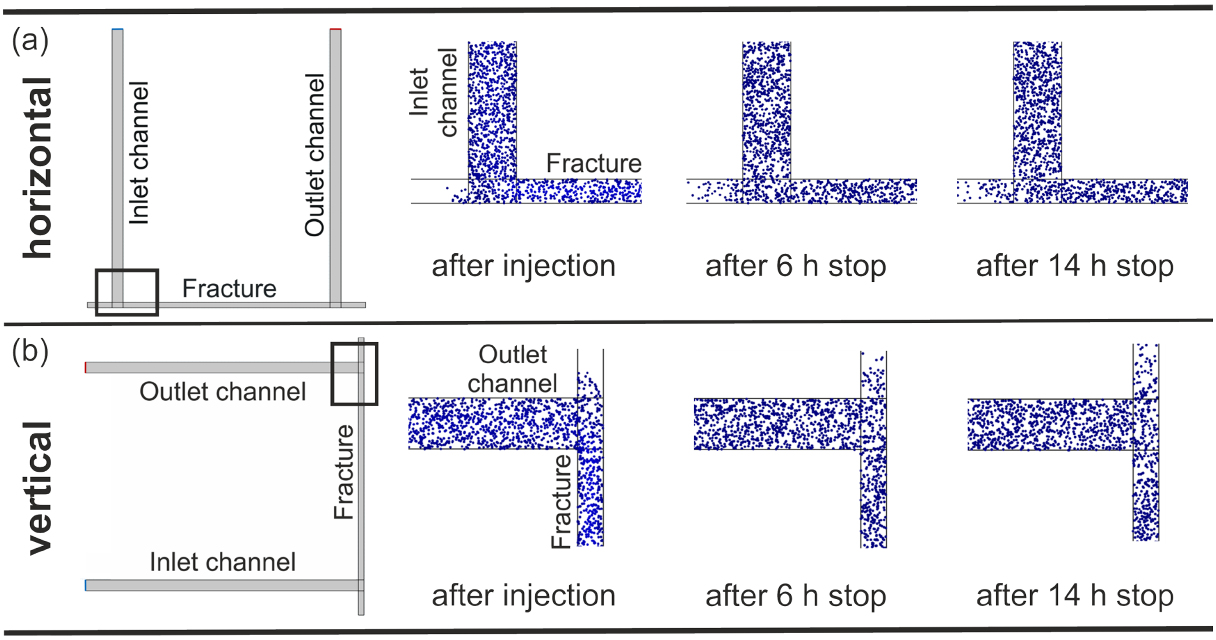

Figure 21: Colloid distribution after injection, after 6 h stop and after 14 h stop of 25 nm colloids in case of (a) horizontal fracture orientation and (b) vertical fracture orientation. The pictured sizes of the colloids are out of scale.

2.5 Summary and conclusion

In this study the interaction of monodisperse fluorescent carboxylated polystyrene colloids with a cut granodiorite surface (Grimsel granodiorite; Switzerland) and with an acrylic glass surface was investigated both experimentally and numerically. For this, 1000 nm and 25 nm carboxylated polystyrene colloids were used. By means of colloid transport experiments in an artificial fracture flow cell, residence time and fracture orientation were varied for both collector surface materials and for both colloid types. The experiments were conducted at pH 5 under low ionic strength (1 mM NaCl) and under laminar flow (7 mL/h) conditions. For 1000 nm and for 25 nm colloids a positive correlation between residence time and colloid retention was found on both collector surfaces. Due to the geometry of the fracture set-up it was possible to see a dependence on fracture orientation, more precisely the effect of gravity over Brownian motion on 1000 nm colloid retention. This was not found for 25 nm colloids. In our case, the deposition of 25 nm colloids is controlled by Brownian motion. However, it was found that the colloid retention of 25 nm colloids is influenced by the collector surface material with a higher retention on granodiorite. This was confirmed by atomic force microscopy measurements using the colloid probe technique. Compared to 1000 nm colloids, 25 nm colloids are exposed to a higher surface roughness on granodiorite, whereas the “felt” roughness for acrylic glass is comparable. Additionally, according to the small colloids, the roughness of granodiorite is many times higher than on acrylic glass. This difference is less for 1000 nm colloids. Thus, 1000 nm colloids overcome this surface roughness without significant retention. These findings led to the conclusion that 1000 nm colloids undergo sedimentation due to a higher influence of gravity over Brownian motion. 25 nm colloids are retained by surface roughness due to their small colloid size and higher diffusivity into cracks and scratches of the material. The breakthrough curves generated with the help of the 2-D model represent qualitatively the experimental findings for both colloid sizes. The observed double peak (in the horizontal experiments using 1000 nm colloids and all experimental cases using 25 nm colloids) and the single peak (in the vertical experiments using 1000 nm colloids) after long residence times (14 h and 24 h) can be reproduced/simulated by the 2-D model. The colloid deposition and diffusion behavior was well shown by means of visualizing the colloid distribution in the inlet/outlet channels and the fracture after distinct residence times. These findings have applications in very different fields:

- Polystyrene microspheres can be seen as an analogue to micro plastics, which are frequently found in surface waters (Teuten et al., 2009). The transport of these polystyrene nano-particles in fractures and the identification of the dominant retention processes are of paramount importance to evaluate the risk for these vulnerable groundwater systems.

- The erosion of compacted bentonite under low ionic strength groundwater conditions and the long-term prognoses of the integrity of the so called geo-engineered barrier in contact with a water conducting feature/fracture is a key topic for the safety assessment of deep geological repositories in crystalline rocks. Numerous experiments on the bentonite erosion issue have been performed within the CP BELBaR project using acrylic glass as a synthetic fracture material, partly implementing the natural surface roughness (Reid et al., 2015). However, the fracture surface interaction of released clay colloids in the size range of 20 nm–1000 nm is not investigated in detail. The use of monodisperse colloidal material covering the smallest and largest size class observed in the released clay material covers the spectrum of surface interaction processes potentially occurring. This study gives mechanistic details on the retention processes expected in fractures under unfavorable conditions as a function of the fracture orientation and shows the size dependent retention.
- Although obtained in simplified geometries and under low ionic strength groundwater conditions, the data presented here shows the significant effect of fracture orientation on colloid deposition. Having high suspension load, as expected in geothermal reservoirs, permeability variation with orientation of the fracture network due to reactivation potential might be triggered additionally by colloid/particle deposition. The experiments presented here, using low colloid load and very simplified fracture orientation, are a first step towards this problem.

2.6 Acknowledgement

This study was carried out in the framework of the HGF portfolio project “Geoenergy” under the Helmholtz topic “Geothermal Energy Systems”. The work has received partial funding by the Federal Ministry of Economics and Technology (BMWi) under the joint KIT-INE, GRS research project “KOLLORADO-e” (02E11203B) and the European 7th Framework Programme (FP7/2007-2011) under grant agreement no. 295487 (BELBaR Project). We want to thank Dr. Ingo Blechschmidt (NAGRA) for providing the granodiorite drill core, Dr. Johannes Lützenkirchen for the streaming potential measurements, Dr. Frank Heberling for providing the python code to fit the DLVO equations and Eva Soballa for the SEM measurements.

3 Integrated research as key to the development of a sustainable geothermal energy technology

C. MELLER[1*], J. BREMER[1], S. BAUR[2], T. BERGFELDT [3], P. BLUM[1], T. CANIC[2], E. EICHE[1], E. GAUCHER[1], V. HAGENMEYER[4], F. HEBERLING[5], S. HELD[1], S. HERFURTH[2], J. ISELE[4], T. KLING[1], D. KUHN[2], A. KUMAR[6], D. MAYER[2], B. MÜLLER[1], T. NEUMANN[1], B. NESTLER[3], F. NITSCHKE[1], A. NOTHSTEIN[1], Y. NUSIAPUTRA[1], P. ORYWALL[2], M. PETERS[1], D. SAHARA[1], T. SCHÄFER[5], E. SCHILL[5], F. SCHILLING[1], E. SCHRÖDER[2], M. SELZER[3], **M. STOLL**[5], H.-J. WIEMER[2], S. WOLF[2], M. ZIMMERMANN[7], T. KOHL[1]

[1]Institute of Applied Geosciences, Karlsruhe Institute of Technology, Adenauerring 20b, 76131 Karlsruhe (Germany)

[2]Institute for Nuclear and Energy Technologies, Karlsruhe Institute of Technology, Hermann-von-Helmholtz-Platz 1, 76344 Eggenstein-Leopoldshafen (Germany)

[3]Institute of Applied Materials, Karlsruhe Institute of Technology, Hermann-von-Helmholtz-Platz 1, 76344 Eggenstein-Leopoldshafen (Germany)

[4]Institute of Applied Informatics, Karlsruhe Institute of Technology, Hermann-von-Helmholtz-Platz 1, 76344 Eggenstein-Leopoldshafen (Germany)

[5]Institute of Nuclear Waste Disposal, Karlsruhe Institute of Technology, Hermann-von-Helmholtz-Platz 1, 76344 Eggenstein-Leopoldshafen (Germany)

[6]College of Engineering, Texas A&M University, 3126 TAMU, College Station, TX 77843-3126 (USA)

[7]Institute of Catalysis Research and Technology Karlsruhe Institute of Technology, Hermann-von-Helmholtz-Platz 1, 76344 Eggenstein-Leopoldshafen (Germany)

3.1 Particle deposition in granitic fractures

Little attention has been paid to the presence of colloids within the permeable fractures and their impact on porosity and permeability in geothermal reservoirs (Tchistiakov, 2000). In addition to negative economic issues, such as pore clogging (formation damage), during extraction of fluids from the subsurface or reinjection into the reservoir (e.g. Civan, 2011; Rosenbrand et al., 2014), in fractured reservoirs, the deposition of clay colloids enhances reactivation potential, and thus, permeability (Evans et al., 2005; Geiermann and Schill, 2010).

Investigations into the effects of mineralogy and surface roughness on controlling particle deposition/attachment can be found in the literature, including work from KIT (e.g. Darbha et al. (2010), (2012a) and Mondal and Sleep (2012)). We use the combination of fluorescence microscopy, laser scanning microscopy (LSM), and SEM as a methodological approach to obtain information on the colloid deposition/attachment behavior and spatial distribution as a function of, for example, mineralogy, surface roughness, and fracture orientation (horizontal/vertical). To prove the feasibility of this technique, postmortem analyses of the fracture surface are performed on continuous-flow experiments with horizontal fracture orientation on a cut Grimsel granodiorite core with a parallel-plate aperture of 0.75 mm by using synthetic monodisperse 1000 nm carboxylated fluorescence colloids. In these experiments, the flow velocity (1.66E–5 and 5.47E–5 m/s) and colloid concentration (1 and 10 ppm) was varied. Further information on the experimental conditions, setup, and sample location can be found in Stoll et al. (2016).

After transport experiments, the flow cell is opened, and the granodiorite disc is removed for postmortem analysis. After installation and adjustment of a pinhole aperture, the colloids are observed directly by using a fluorescence microscope (Axioplan 2 Imaging, Fluorescence Microscope, Zeiss, 10x magnification, image size 1401×1048 μm^2). Focus stacking, also known as z-stacking, is used in this case to obtain images with a greater depth of field (DOF) to compensate for surface roughness. To compare the results with LSM and SEM measurements, the same areas on the surface are investigated. By using ImageJ software (Schneider et al., 2012), the z-stacking files are displayed on one plane. With the “Particle and Pore” tool implemented in the SPIP™ software package (Image Metrology), the colloids are quantified.

The colloid deposition (kinetics) is determined by calculating the dimensionless Sherwood number Sh. The Sherwood number (Sh) is defined as (Darbha et al., 2012a):

$$Sh = \frac{J \cdot R}{C_0 \cdot D}$$ **Equation 22**

where J [$1/(m^2 \cdot s)$] is the deposition flux, R [m] is the mean colloid radius, C_0 [colloids/m^3] is the bulk colloidal concentration and D [m/s^2] is the molecular diffusion coefficient. D is defined by the Stokes-Einstein equation (Einstein, 1905):

$$D = \frac{k_B \cdot T}{6 \cdot \pi \cdot \eta \cdot R}$$ **Equation 23**

where k_B is the Boltzmann constant [1.3806481E–23 $m^2 \cdot kg/(s^{-2} \cdot K)$], T is the temperature [K] and η [$N \cdot s/m^{-2}$] is the dynamic viscosity. J is defined as (Darbha et al., 2012a):

$$J = \frac{N}{t_R \cdot A}$$ **Equation 24**

where N represents the number of the deposited particles, t_R [s] is the residence time in the fracture and A [m^2] the field of view. The average residence time t_R [s] is calculated by (Albarran et al., 2013):

$$t_R = \frac{V}{Q}$$ **Equation 25**

where V [m^3] is the fracture volume and Q [m^3/s] the applied flow rate.

The surface roughness parameter Rq [m] is defined as the root mean square deviation of the profile (Jorgensen et al., 1993):

$$Rq = \sqrt{\frac{1}{n}\sum_{i=1}^{n} z_i^2}$$ **Equation 26**

where n is the number of points in the profile, and z_i [m] is the height value at point i.

Post mortem analysis was performed on 12 regions of interest (ROIs), covering 1.5% surface area (17.63 mm^2) of the total Grimsel granodiorite disc surface (1134.12 mm^2). Under the prevailing geochemical conditions (pH 5, 1 mM NaCl), colloid retention values calculated on the basis of measured experimental breakthrough curves (BTCs) show an overall low colloid retention (maximum 5%) and tend to increase with decreasing flow velocity (=increasing residence time). Retention on the granodiorite surface obtained by fluorescence microscopy is an extrapolated value based on the sum of the counted colloids in the abovementioned 12 ROIs. In the range of the error, the extrapolated percentage is, in all cases, comparable to or higher than the percentage obtained by BTC analysis. Colloid concentration variation revealed a limited site capacity for colloid retention under the experimental conditions. However, the use of fluorescence microscopy single-colloid analysis revealed no influence of flow velocity under the uncertainties of 2–3% given.

By comparing the calculated *Sh* numbers under these unfavorable attachment conditions as a function of surface roughness (Figure 22), the highest values of colloid attachment could be observed for low colloid concentration and high flow velocity (1 ppm, 5.47E–5 m/s) with a tendency of *Sh* to increase with roughness most probably overcoming electrostatic repulsion. In contrast, lower *Sh* numbers are visible for experiments, including 10 ppm colloid concentration under the same flow velocity (7 mL/h or 5.47E–5 m/s), and lowest *Sh* values for low (1 ppm) colloid concentration at low flow velocity (2 mL/h, 1.66E–5 m/s).

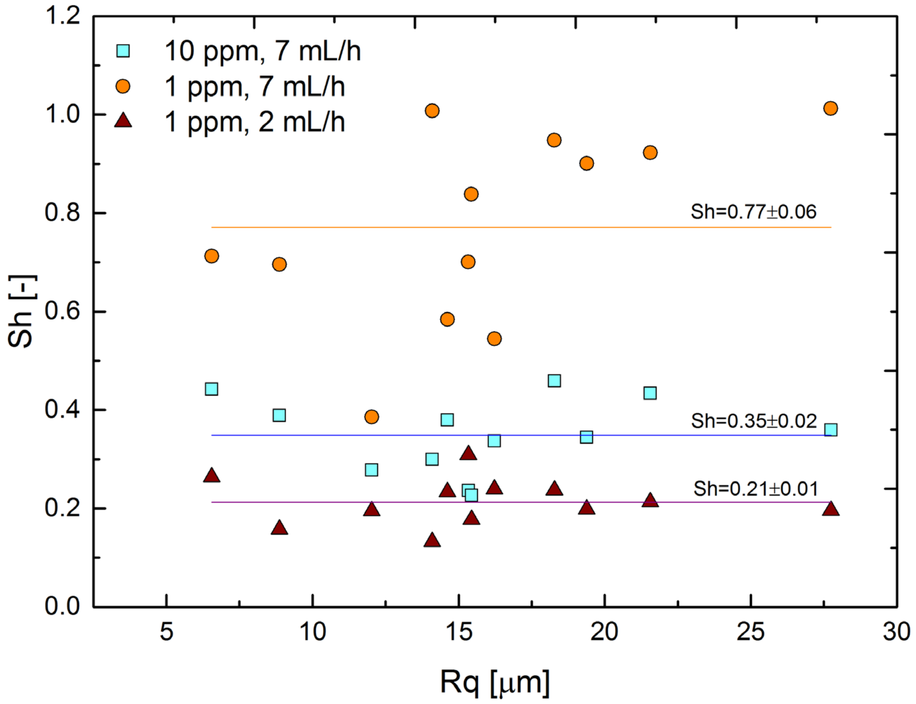

Figure 22: Sherwood number *Sh* as a function of surface roughness of continuous flow experiments with varying colloid concentration and flow velocity for 1000 nm colloids (lines with average *Sh* to guide the eye).

When comparing these findings to AFM measurements (see Stoll et al. (2016)), it is reasonable to assume that there is no influence of surface roughness on colloid retention on 1000 nm colloids. The L_S/L_D ratio, which describes the dominating influence of either gravity ($L_S/L_D > 1$) or Brownian diffusion ($L_S/L_D < 1$) by comparing the ratio of the characteristic sedimentation length and diffusion length, is 1.19 for 1000 nm colloids at 1.66E–5 m/s. Based on this value, colloid deposition at 1.66E–5 m/s is neither fully dominated by gravity nor by diffusion. Both forces act equally on the colloids. Under these conditions, a significant effect of colloid deposition by gravity, relative to the higher flow velocity (5.47E–5 m/s), is not expected.

In a further study, the specific role of fracture orientation and gravity on colloid retention is studied by simulating stagnant phases by stop–flow conditions (similar to geothermal power plant downtime periods), as partly documented in Stoll et al. (2016). Both experiments and numerical simulations by using COMSOL Multiphysics® (Version 5.0) could univocally show that gravity plays a major role for colloids ≥ 1 µm.

To investigate colloid retention on granodiorite minerals, the self-fluorescent signal of the minerals obtained by changing the filter cubes of the microscope was compared with mineral deposition information. This additional procedure was performed exclusively for an experiment that involved a 1 ppm colloid suspension at 1.66E–5 m /s. Information from SEM/EDX measurements of each ROI helps to identify the mineral phases. The combined image is shown in Figure 23 with marked mineral phases. The colloids are distributed evenly over the whole investigated ROI. No mineral-dependent increase or decrease of colloid deposition is detectable. This finding supports surface potential measurements and force volume measurements obtained by means of AFM, which show overall negative surface potentials and unfavorable repulsive conditions. Comparable observations are made for the remaining ROIs.

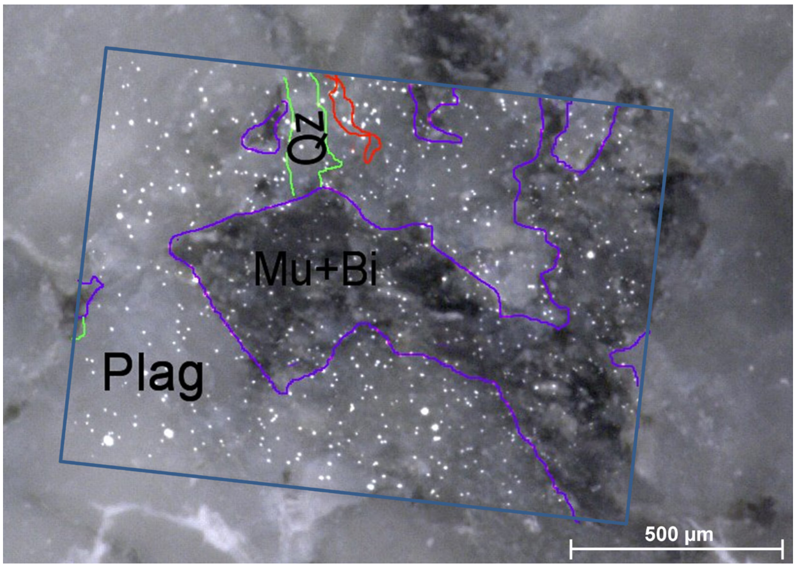

Figure 23: Colloid distribution (white spots) on granodiorite mineral phases of plagioclase (Plag), quartz (Qz), and micas muscovite (Mu) and biotite (Bi) in a continuous-flow experiment with a 1 ppm colloid concentration and 1.66E–5 m/s flow velocity (ROI 90_2).

In summary, the results presented herein demonstrate that the multimethod approach of using macroscopic flow experiments and microscopic postmortem analysis provides an in-depth process understanding on the colloid–granodiorite surface interactions under well-constrained laboratory conditions. By using this method, spatially resolved colloid deposition was quantified as a function of mineralogy and surface roughness. Current research is heading towards more realistic boundary conditions concerning hydro-geochemical parameters (higher ionic strength, higher flow velocity) and especially the use of natural clay colloids separated from the Soultz system (Figure 24).

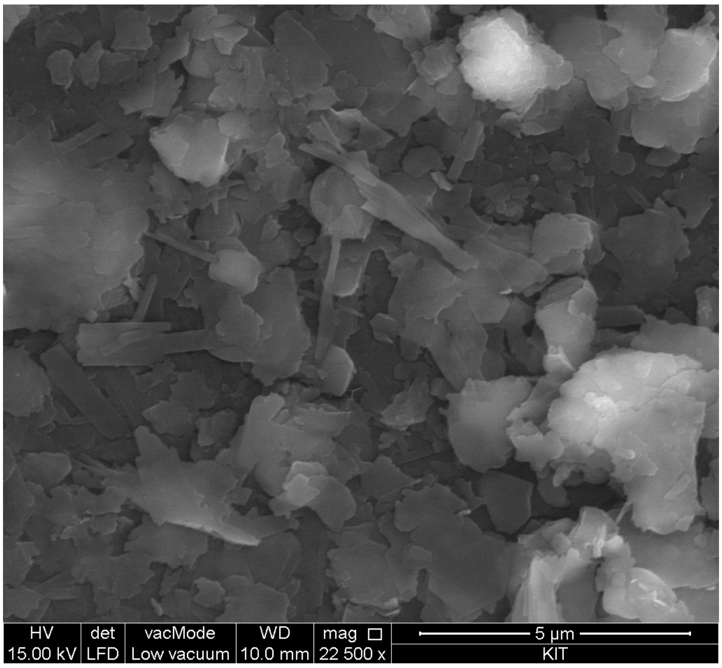

Figure 24: SEM image of natural illite-dominated colloids obtained from the fracture surface of drill core K117 at exploration well EPS-1 from the geothermal test site Soultz-sous-Forêts.

4 Parallel-plate fracture transport experiments of nanoparticulate illite in the ultra-trace concentration range investigated by Laser-Induced Breakdown Detection (LIBD)

M. STOLL[1*], F. M. HUBER[1], E. SCHILL[1], T. SCHÄFER[1,2]

[1]Karlsruhe Institute of Technology (KIT), Institute for Nuclear Waste Disposal (INE), P.O. Box 3640, 76021 Karlsruhe, Germany

[2]Friedrich-Schiller-University Jena (FSU), Institute of Geosciences, Applied Geology, Burgweg 11, 07749 Jena, Germany

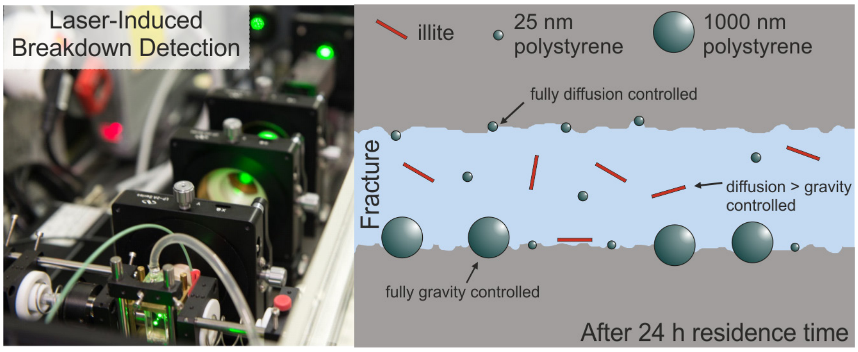

Graphical abstract

4.1 Abstract

This study investigates the appropriateness of monodisperse carboxylated polystyrene spheres as clay colloid analogues. Colloid transport experiments using Na-illite are conducted within a parallel-plate fracture flow cell with an aperture of 0.75 mm at pH 5 under low ionic strength (1 mM NaCl) and laminar flow (7 mL/h) conditions. The effects of collector surface material (Grimsel granodiorite or acrylic glass), fracture orientation and residence time on colloid retention are examined. In order to avoid full surface coverage effects, ultra-trace (30 ppb) Na-illite colloid concentrations are used. Laser-induced breakdown detection is applied in order to detect and quantify the Na-illite colloids. The results are directly compared to the experiments of Stoll et al. (2016) who investigated the transport and surface interaction of carboxylated polystyrene spheres (25 and 1000 nm diameter) using the same experimental setup and conditions. It is concluded that polystyrene spheres are no ideal analogue to predict the mobility and transport behavior of a polydisperse clay colloid suspension. Despite the higher solid density, the Na-illite colloids show higher mobility compared to the polystyrene spheres without significant impact of surface roughness or gravity. The platelet shape, the non-uniform surface charge distribution and slower sedimentation may account for the observed differences.

4.2 Introduction

Colloids are ubiquitous in surface and subsurface waters. Due to the high diversity in both organic and inorganic forms (e.g. clay colloids, humic substances and viruses/bacteria) and their transport and surface interaction behavior, colloids have become an important subject in environmental research for decades (Stumm, 1993). Contaminant transport in groundwater (Chrysikopoulos, 1999; Kretzschmar and Schäfer, 2005; McCarthy and Zachara, 1989; Weisbrod et al., 2002), colloid facilitated radionuclide transport (Geckeis et al., 2004; Kersting et al., 1999; Möri et al., 2003; Utsunomiya et al., 2009), pore clogging (Civan, 2011; Rosenbrand et al., 2014) and the local alteration of physical properties (e.g. permeability) due to the presence of clay material (Evans et al., 2005; Geiermann and Schill, 2010) are amongst other things, issues of current research. In the subsurface colloids are transported in porous and fractured media. Especially fractures serve as preferential conduits for colloids. This is due to (i) large apertures that enable high flow velocities compared to the surrounding rock matrix, (ii) mostly unfavorable conditions for attachment due to negatively charged surfaces of colloids and fracture walls under the circumneutural pH range expected in natural groundwater systems and (iii) negligible matrix diffusion of colloids in contrast to solutes (Alonso et al., 2007a; Chrysikopoulos, 1999; McKay et al., 2002; Schäfer et al., 2012). Colloid transport through both artificial and natural fractures has been studied extensively in the past (McCarthy and McKay, 2004; Mckay et al., 1993b; Vilks and Baik, 2001). Because of constant and well defined material properties (e.g. defined geometry, monodisperse size, surface charge and low density) surface functionalized polystyrene spheres are often used as an analogue for natural colloids (Litton and Olson, 1993; Roy and Dzombak, 1996). However, natural colloids show irregular shapes, higher densities and a heterogeneous surface charge distribution impacting the transport behavior.

Studies comparing colloids of different materials have been carried out amongst others by Zvikelsky et al. (2008) and Albarran et al. (2013). Zvikelsky et al. (2008) compared 1 µm latex microspheres with a polydisperse clay suspension (mean colloids size 1.34 µm) in transport experiments through a chalk rock fracture of 38.5 cm length. The results showed a lower clay colloid recovery compared to the latex spheres and a decrease in the mean colloid size of the mobile colloid fraction. Therefore, the authors accounted the higher density of the clay colloids for the observed colloid deposition and colloid size fractionation. Additional parameters possible triggering the colloid retention might be variable surface charge, irregular particle shape and polydispersity. The increase of colloid recovery while repeating the experiments was explained with full surface coverage because of the preceding experiments. This in turn results in fewer sites available for attachment. In the study of Albarran et al. (2013) the transport behavior of gold (40 nm and 100 nm), latex (30 nm, 115 nm, 220 nm and 500 nm) and smectite (< 500 nm) colloids in artificial granite fractures of 16–26 cm length under unfavorable attachment conditions was investigated (pH 7–10 and ionic strength of 5E–4 M $NaClO_4$). In contrast to Zvikelsky et al. (2008), higher colloid recovery of clay colloids compared to the latex and gold colloids of comparable sizes was observed. These results were attributed to the nature of the clay colloids: the charge distribution and the platelet shape. Apart from the different colloid sizes investigated in both studies, the observed deviations mentioned are most likely attributed to the substrates used. A chalk rock differs significantly in porosity, structure and Ca content from granite as substrate. James and Chrysikopoulos (2000) investigated numerically the transport behavior of monodisperse and polydisperse colloid suspensions in water saturated, two-dimensional fractures with different spatially variable, anisotropic aperture topographies. They found that the colloid plume of a polydisperse colloid suspensions shows a higher spreading in contrast to monodisperse ones. Additionally, under the assumption of spherical colloids they show that the retention of dense colloids is higher in contrast to buoyant ones.

Against this background, contrasting features between colloids of different materials need to be considered and the appropriateness of polystyrene spheres as analogues needs to be verified. In this respect, the present study is an extension to the work of Stoll et al. (2016), which examined the transport of fluorescent carboxylated polystyrene spheres (CPS) through an artificial parallel-plate fracture flow cell under laminar flow conditions (7 mL/h) using fluorescent spectroscopy. In those transport experiments at pH 5 and 1 mM NaCl background electrolyte, the influence of colloid size and surface roughness on colloid retention was investigated under varying parameters like residence time, colloid size, collector material and fracture orientation. Despite the low density of CPS of 1050 kg/m^3, it could be shown that large 1000 nm CPS undergo sedimentation and deposition on the surface with increasing residence time while collector interaction is not affected by surface roughness variation. In contrast, for the investigated 25 nm CPS diffusion-controlled transport dominated during stop-flow conditions and collector interaction appears to be controlled by surface inhomogeneities such as surface roughness. In this particular case, the surface roughness was measured by atomic force microscopy on an area of 64 µm^2 (root mean square roughness of granodiorite ≈ 350 nm and of acrylic glass ≈ 20 nm).

The aim of this study is to interrogate the use of low density CPS as appropriate analogues to simulate natural clay colloids. For this purpose, identical experimental conditions and setup as presented in Stoll et al. (2016) are used to perform experiments with polydisperse clay colloids (illite) spanning the size range 35–350 nm. Consequently, the experiments are carried out under laminar flow conditions (7 mL/h), a background electrolyte of 1 mM NaCl at pH 5. For crystalline systems the pH values vary over a large range (pH 5 to pH 9.6) (Bath, 2011). In this study and in the previous study we have chosen the lower end of the value range (pH 5) in order to investigate the effect of potential surface charge heterogeneities expected for crystalline rock. For detection and quantification of the clay colloids in the transport experiments Laser-Induced Breakdown Detection (LIBD) is applied. LIBD serves at this point as an alternative to light scattering techniques, which are frequently used to detect non-fluorescent particulate and colloid tracers in comparable experiments (e.g. Albarran et al., 2013). Due to Rayleigh scattering in the size range of < 100 nm, light scattering techniques require comparatively high solid concentrations, which in turn might result in significant to full collector surface coverage. Additionally, such high colloid concentrations do not reflect natural groundwater colloid load. LIBD is developed to detect and quantify colloid sized particles at ultra-trace concentrations down to ppt-levels. Therefore, a high colloid load is not required, and the afore mentioned side effects like surface coverage are not an issue. Thus, in contrast to light scattering techniques, experiments under more natural conditions can be conducted using LIBD.

4.3 Material and methods

4.3.1 Synthetic fracture flow cell and experimental setup

The synthetic fracture flow cell and experimental setup are schematically shown in Figure 25. A parallel-plate type fracture flow cell made of acrylic glass (Polymethyl methacrylate, PMMA, Plexiglas®) is used for the transport experiments. One fracture side always consists of acrylic glass and the opposite side material is exchangeable. Here either granodiorite or acrylic glass is used. The granodiorite from the Grimsel test site from the Aar Massif in Switzerland was cut using a diamond-studded saw blade. No further treatment on the disc was undertaken. The acrylic glass disc with identical dimensions has a cut and polished surface. Using streaming potential measurements (Anton Paar) both collector surfaces show negative overall zeta potentials under the experimental conditions (1 mM NaCl, pH 5.0 ± 0.1): Grimsel granodiorite –38 mV and acrylic glass –49 mV. The penny shaped fracture between both fracture sides is 38.3 mm in diameter with a constant aperture of 0.75 mm and a void volume of 0.86 mL. Including inlet and outlet channels within the acrylic glass it adds up to 0.99 mL. Further information on the granodiorite, the acrylic glass disc, and the fracture flow cell are detailed in Stoll et al. (2016).

In order to minimize potential colloid sorption in the experimental setup PEEK (Polyether ether ketone) tubing is used whenever possible (Kim and Walther, 2007). The inlet of the fracture flow cell is connected to the colloid/solute tracer and the background electrolyte. The outlet of the fracture flow cell is connected to a quartz glass flow-through cuvette of 220 µL internal volume (Hellma Analytics, Type 176.766-QS, Germany) within the LIBD system and subsequently linked to a peristaltic pump (REGLO Digital MS-4/8, Ismatec, Germany). In order to determine the exact flow rate and measure pH the eluate is collected at the outlet of the setup. To minimize artificial dispersion by the setup, the tubing volume and length are kept to a minimum and the pump is installed directly after the LIBD device. The utilized tubing is 750 µm in inner diameter. In experiments bypassing the fracture flow cell, the total dead volume of the setup has been quantified to be 330 µL. For switching between colloid and background electrolyte and for bypassing the fracture flow cell in stop-flow experiments three 3-way valves (3-Way Flow Switching Valve, Upchurch Scientific, Germany) are installed.

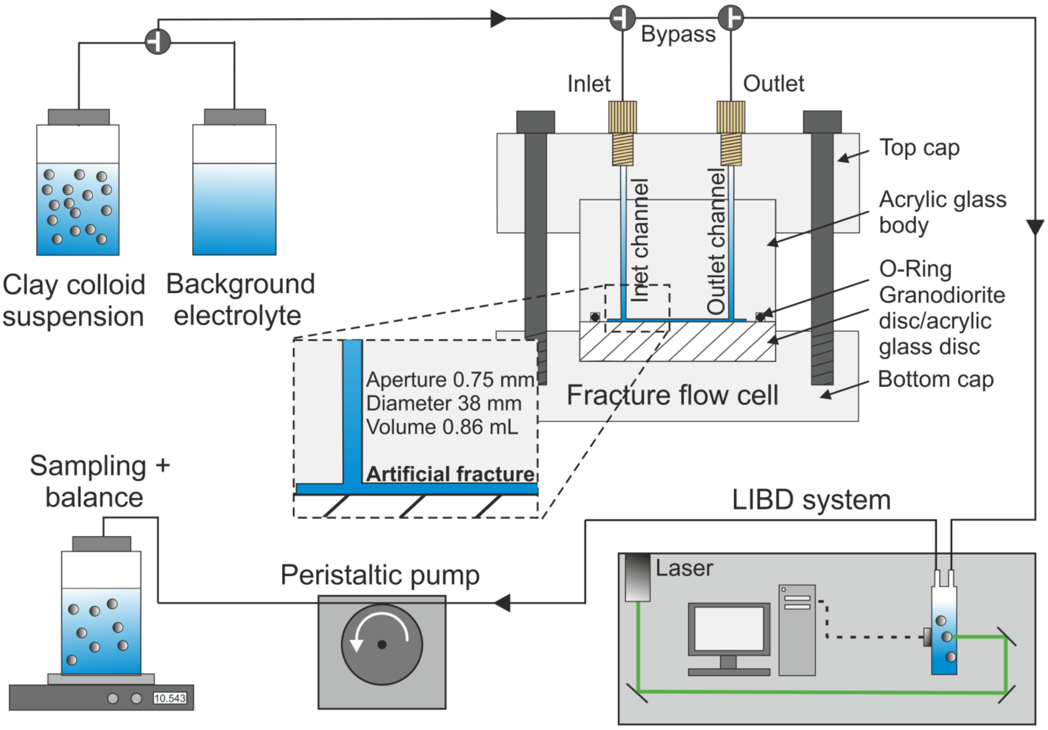

Figure 25: Scheme of the experimental setup (horizontal fracture orientation). The exchangeable disc in the synthetic fracture flow cell has a hatched marking.

4.3.2 Laser-Induced Breakdown Detection (LIBD)

LIBD is based on the detection of plasma formation induced by focusing a pulsed laser beam in an aqueous suspension (Kim and Walther, 2007). When a colloid passes the focal area of the laser beam a dielectric breakdown is formed. This breakdown event can be detected either optically i.e. by monitoring the optical plasma emission with a CCD camera (optical LIBD) (Bundschuh et al., 2001a; Jung et al., 2006) or acoustically by measuring the generated shock wave with a piezoelectric transducer (acoustic LIBD) (Bundschuh et al., 2001b; Kitamori et al., 1989; Scherbaum et al., 1996). The obtained breakdown probability (BDP; i.e. number of breakdown events per number of laser shots) for a fixed laser energy provides information about the colloid size and colloid concentration in a suspension. While optical LIBD is used to determine the mean colloid diameter, acoustic LIBD provides information about the colloid number and size distribution by using the so-called s-curve measurement. To conduct an s-curve measurement, the laser pulse energy is systematically increased in distinct energy intervals. In the course of this energy increase the BDP increases until reaching a maximum value. In this process, different colloid sizes are detected at different threshold energy values, starting with big particles at low energies up to small particles at high energies. Note that in polydisperse samples, the size distribution of the colloids is integrated by the system over the threshold of the biggest colloids in the suspension and over the slope of the s-curve. With this the mass concentration of the colloid suspension is calculated. For this purpose, the s-curve LIBD systems are calibrated using monodisperse polystyrene standards of different diameter (20 nm, 30 nm, 40 nm, 70 nm, 100 nm, 200 nm, 500 nm and 900 nm) and concentration. These colloid sizes represent the size classes of the output data (Table 7). Colloids with sizes between the different calibrated size classes are either counted to the smaller or bigger size class. The arithmetic mean of both classes is the separating value (see Table 7). Therefore, the output data gives the size classes and not the exact colloid size. Further information on the technique is provided by (e.g. Bitea, 2005; Hauser et al., 2002; Jung and Cho, 2012; Kim and Walther, 2007). In order to obtain breakthrough curves (BTC) in colloid transport experiments, the energy of the laser beam is fixed over the experimental duration.

Table 7: Size classes calibrated for s-curve LIBD using polystyrene standards and the size ranges covered.

LIBD size classes [nm]	Covered size range [nm]
20	20–25
30	25–35
40	35–55
70	55–85
100	85–150
200	150–350
500	350–700
900	> 700

4.3.3 Na-illite colloids

The Na-illite colloids used in this study were extensively characterized within the EU FP7 collaborative Project CP CatClay (Processes of cation migration in clayrocks) (Altmann et al., 2015). In order to obtain a homoionic Na-illite, natural Illite du Puy was acid treated, washed multiple times, dialyzed and freeze dried. For this study an illite colloid suspension of the Na-illite is prepared by centrifugation (20 min at 4000 rpm) of a 10 g/L suspension at pH 5 and 1 mM NaCl. Using Photon Correlation Spectroscopy (PCS; ZetaPlus system, Brookhaven Inc., USA) the colloid stability is measured. The colloid diameter remains constant for > 24 h, thus, we conclude that no coagulation occurs and the colloid suspension is considered stable throughout all performed transport experiments.

Physical properties of the illite colloids and the number of colloids in suspension are summarized in Table 8 and Figure 26. The LIBD measurements in ppb range are cross-checked with measurements of analytical methods, which require concentrations in the ppm range. This is PCS, Inductively Coupled Plasma Optical Emission Spectrometry (ICP-OES; Optima 8300DV, Perkin Elmer, USA) and Scanning Electron Microscopy (SEM; QUANTA 650 FEG, FEI, USA). The colloid number and size distribution are determined in s-curve LIBD measurements, the mean colloid diameter by optical LIBD and by PCS. The slightly larger mean colloid diameter measured by PCS compared to the LIBD measurement, is attributed to the higher sensitivity of PCS for larger colloid sizes (Plaschke et al., 2001). The zeta potential of the illite colloid suspension with –34 ± 2 mV measured by the Brookhaven zeta sizer is slightly less negative than the zeta potential of the CPS with –46 ± 1 mV (25 nm) and –42 ± 2 mV (1000 nm) (Stoll et al., 2016). The colloid mass concentration is back-calculated using the structural Aluminum concentration measured by ICP-OES based on the structural formula published by González Sánchez et al. (2008): $K_{0.69}$ $Ca_{0.05}$ $Na_{0.11}$ $Al_{1.18}$ $Fe_{0.36}$ $Mg_{0.39}$ ($Si_{3.48}$ $Al_{0.52}$) O_{10} $(OH)_2$. The ICP-OES measurement is performed using the prepared stock illite suspension. In order to measure the colloid size distribution (s-curve LIBD), the mean colloid size (optical LIBD), and for performing the colloid transport experiments the centrifuged stock suspension is diluted to 30 ppb. A preparation uncertainty due to the dilution procedure is not considered at this point. Therefore, the determined concentrations by ICP-OES and LIBD cannot be compared without further ado. The given errors refer to the analytical uncertainties of the method used. As depicted from Figure 26a, the nanoparticle suspension is dominated by 85–150 nm and 150–350 nm sized colloids (size classes 100 and 200 nm). The SEM image (Figure 26b) shows the different colloid sizes on a track etch membrane filter with 15 nm pores (Whatman plc, GE Healthcare Life Sciences, United Kingdom), which proves the dominance of larger over smaller colloids. In order to convert the colloid number concentration in a mass concentration an approximation is used because the colloids are considered spherical according to:

$$C = \frac{C_N \cdot \pi \cdot \rho_p \cdot d^3}{6 \cdot 10^{12}} \qquad \textbf{Equation 27}$$

where C [g/mL] is the mass concentration, C_N [1/mL] is the colloid number concentration, ρ_p [g/cm^3] is the colloid density and d [µm] is the colloid diameter.

Altmann et al. (2015) measured the thickness of single crystallites of this colloid type by using transmission electron microscopy to be 18 ± 6 nm. In literature there is no clear agreement concerning the density of clay colloids. Reported values range between 2000 and 2700 kg/m³ (Bergelin et al., 2007; Degueldre et al., 1998). In this study we assume the maximum possible density with 2700 kg/m³ and thus the maximum effect for sedimentation of the colloids.

Table 8: Physical properties of the illite colloids and the number of colloids in suspension. Improvement of Henry's mobility formula by Ohshima (2001) used to calculate zeta potential value.

Mean Colloid size [nm]	Zeta potential [mV]	Colloid concentration [ppb]	Colloid mass [%]	Colloid number per 5 mL pulse
259.2 ± 1.4 (PCS) 221.0 ± 7.6 (LIBD)	–34 ± 2	30.0 ± 0.2 (ICP-OES) 42.0 ± 8.0 (LIBD)	94.29 (150–350 nm) 5.67 (75–150 nm) 0.04 (35–55 nm)	2.65E+7 (Total) 1.73E+7 (150–350 nm) 8.33E+6 (75–150 nm) 8.95E+5 (35–55 nm)

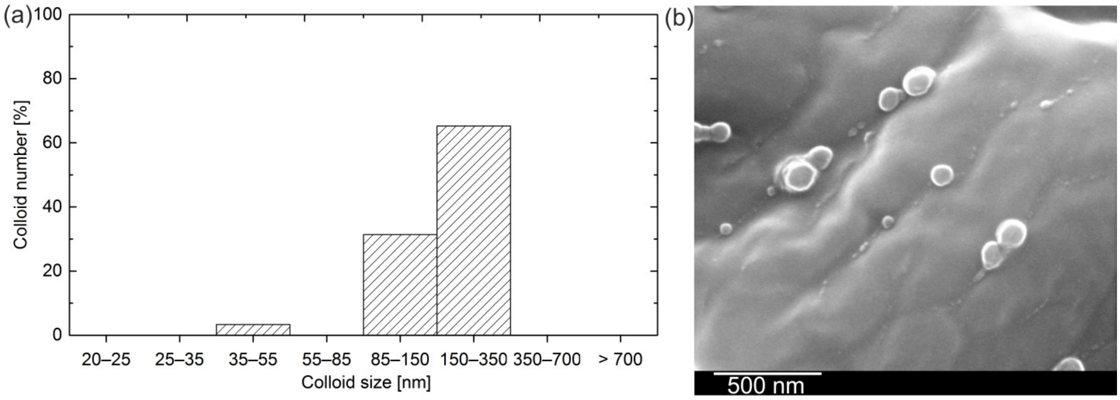

Figure 26: a) Colloid size distribution of Na-illite measured using s-curve LIBD (cut off 15 nm). b) SEM image of illite colloids on a track etch membrane filter.

4.3.4 Experimental procedure

Before starting each experiment, the whole setup is flushed with the background electrolyte for at least one hour including pH and flow rate control. C_0 is measured by injecting the colloid suspension directly into the flow-through cuvette using a syringe before and after every experiment. Thus, slight fluctuations in the output signal can be compensated by taking the mean BDP value as C_0. The laser pulse energy is set to 660 µJ for the whole experiment corresponding to a BDP of C_0 of 70 ± 2%. This value is not chosen arbitrarily. The higher the BDP value gets, the higher the probability of multiple plasma formations is, and thus, multiple breakdown events are induced by one laser shot. These multiple events cannot be distinguished by the acoustic LIBD and are, therefore, counted as single breakdown events. On the other hand, if the BDP is chosen too low, the signal to noise ratio is insufficient. Moreover, the threshold energy for all particle sizes may not be reached with such energy. Therefore, a combination of concentration and energy must be found: (i) to avoid multiple breakdown events; (ii) to get a sufficient statistic for the initial concentration and for the concentrations range in a BTC without losing the high time resolution and (iii) to overcome the threshold value for the smallest colloid class calibrated (here 20 nm). With the laser pulse energy selected the background BDP is < 2%. Due to the low colloid concentration in the experiments it can be assumed that there is no full colloid coverage on the fracture surfaces at any time. This is supported by the calculated maximum area occupied by the injected colloids of 0.75% of the flow-wet surface of one fracture side in a single experiment.

In order to conduct a continuous flow experiment, a volume of 5 mL of the colloid suspension is injected into the fracture flow cell with a constant flow rate of 7 mL/h, i.e. a residence time of 7.4 min, an average flow velocity of 5.5E–5 m/s and a Reynolds number of 4.1E–2. A volume of 5 mL is needed to ensure a constant colloid concentration in the whole fracture. After injecting the colloid pulse, the flow is switched to background electrolyte and the whole system is flushed keeping the 7 mL/h until the measured signal reaches the background level. Due to the limitation of the installed pump higher residence times are achieved by conducting stop-flow experiments. After injecting the colloid pulse, the fracture flow cell is bypassed and the whole tubing is flushed particle free using the background electrolyte. Thereby the colloid suspension is captured in the fracture flow cell. After residence times of 1 h, 6 h or 24 h the fracture flow cell is reconnected to the flow and the colloid containing fracture is flushed with the flow rate of 7 mL/h. The chosen residence times correspond to fictive average flow velocities of 1.9E–5 m/s, 4.4E–6 m/s and 1.8E–6 m/s, respectively. Consequently, the mobile colloids can be detected yielding a BTC. Besides varying the residence time in the fracture flow cell, the collector surface is changed between acrylic glass and granodiorite and the orientation of the fracture flow cell is varied to be either horizontal or vertical. In case of the vertical fracture orientation, the inlet and the outlet channels are oriented in the horizontal direction and the injection is always from the bottom, whereas for the horizontal fracture orientation the inlet and the outlet channels are positioned vertically.

With the purpose of characterizing the hydrodynamics in the fracture, conservative solute tracer experiments using 10 ppb UV-fluorescent 7-amino-1.3-naphthalene (Amino-G, Postnova Analytics GmbH, Germany) are conducted. The solute tracer is detected by fluorescence spectroscopy (Luminescence Spectrometer 55, Perkin Elmer, USA) using a smaller flow-through cuvette of 100 µL (Hellma Analytics, Germany).

4.3.5 Data evaluation

The output data of LIBD yields the laser energy and piezoelectric transducer signal for each laser pulse. A breakdown event is recorded as far as the piezoelectric transducer signal overcomes a set threshold value. To evaluate this data, the breakdown events are grouped in a histogram with classes of 20 sec each. A BTC is created by plotting the bins and the counts of this histogram. The normalized concentration C/C_0 (BDP of each bin divided by the BDP of C_0) is plotted as a function of replaced pore volume. Due to the polydispersity of the colloid suspension and the detection method, the plotted BTCs and the calculated colloid recoveries are colloid number concentrations. Due to the uncertainty of the colloid size distribution in different BTC fractions within the experiment, a calibration function to convert BDP into a colloid mass concentration is not reasonable.

4.4 Results and discussion

4.4.1 Comparison between LIBD and fluorescence

Prior to the main experiments, a comparability study between the single particle detection technique LIBD and fluorescence spectroscopy was carried out. A stop-flow experiment with 1000 nm CPS at horizontal fracture orientation, granodiorite as collector surface material and 24 h residence time was chosen as test case. The corresponding stop-flow experiments showed on both granodiorite and acrylic glass a significant double peak shape and the lowest recovery over the experimental data set (Stoll et al., 2016). The experiment on granodiorite was repeated using LIBD for detection. The injected colloid mass of 10 µg corresponds to 1.9E+7 colloids in the injected tracer pulse volume. In Figure 27, the LIBD BTC (C/C_0 over pore volume) is shown in comparison to the data acquired by fluorescence spectroscopy for (1) colloid injection period, (2) flushing of tubing and (3) flushing of fracture flow cell. The LIBD data shows higher scattering than the fluorescence spectroscopy data. This is due to the intrinsic nature of the LIBD technique being a single particle counting device and the statistical data evaluation method. However, both experimental BTCs are in good agreement with each other regarding the colloid recovery (both recording ≈ 11% after flushing the fracture flow cell after 24 h residence time) and the shape of the BTCs. Therefore, in order to monitor the colloid transport it is clearly verified that the data obtained by LIBD can directly be compared with experimental studies using fluorescence spectroscopy as colloid detection method, as presented in Stoll et al. (2016). The results and discussion section for the stop-flow experiments will focus on step (3), because step (1) and (2) will be the same, except the varying residence times during step (2).

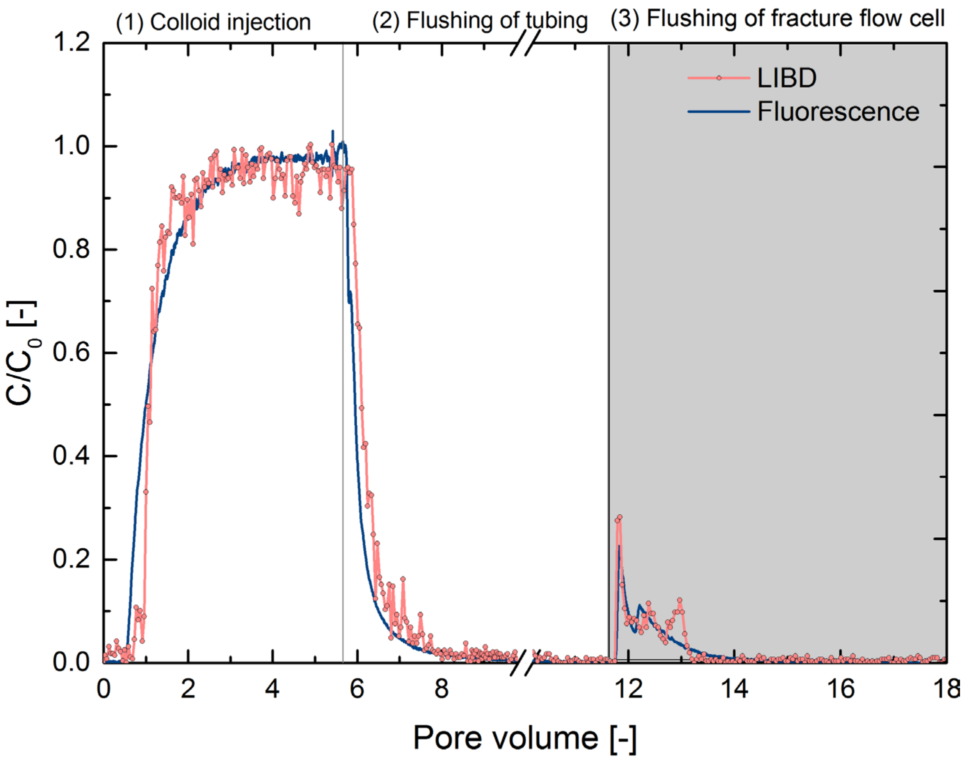

Figure 27: Comparison of LIBD and fluorescence spectroscopy for a transport experiment using 1000 nm CPS in a horizontal oriented granodiorite fracture. Grey shaded region will be shown in Figure 29 and Figure 30.

4.4.2 Continuous flow experiments

Continuous flow experiments are performed for both fracture orientations on granodiorite as collector material. Comparable to the CPS experiments in Stoll et al. (2016), the clay colloid recovery in continuous flow experiments is nearly 100% in both cases (horizontal 98% and vertical 96%). The error is estimated to be approximately 5%. Figure 28 compares the colloid transport BTCs to the BTC of the conservative tracer Amino-G and reveals earlier first arrival and a less pronounced tailing of the BTCs, but no dependence on fracture orientation. The earlier arrival of the colloids is likely due to size exclusion, charge exclusion and less Taylor dispersion (e.g. Becker et al., 1999; Zvikelsky and Weisbrod, 2006).

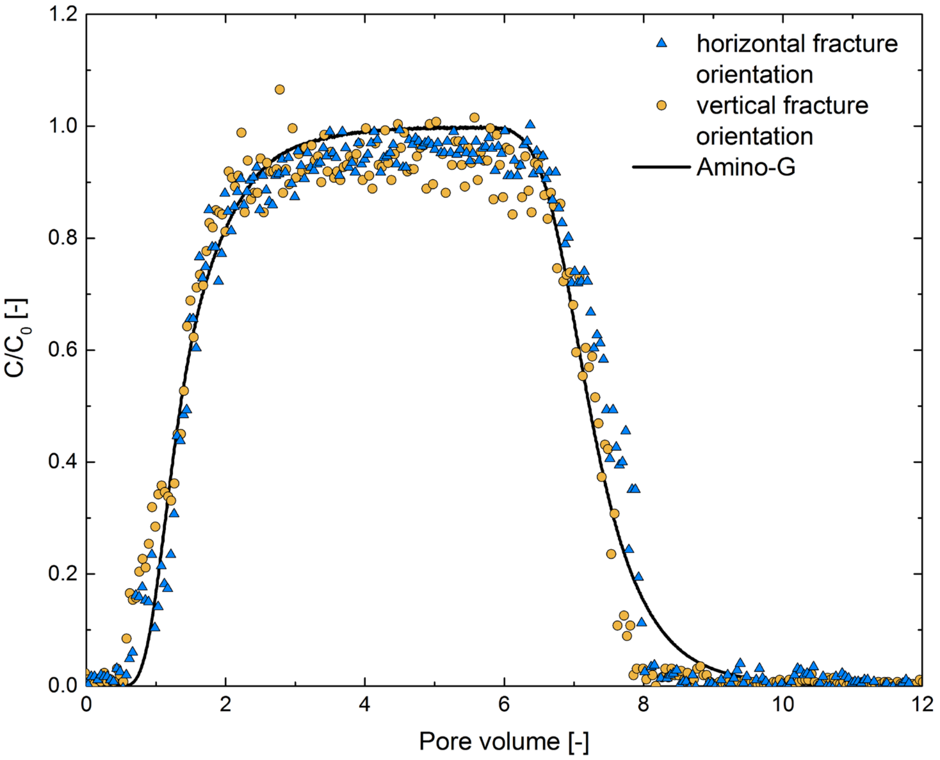

Figure 28: Continuous flow experiments using Na-illite and Amino-G on granodiorite (colloid/tracer pulse: 5 mL).

4.4.3 Stop-flow experiments

To investigate if an increase in colloid residence time within the fracture has an effect on the clay colloid retention, stop-flow experiments are performed with residence times of 1 h, 6 h and 24 h. Similar to the continuous flow experiments the orientation of the fracture flow cell has been varied between horizontal and vertical. To determine the impact of the collector material, the experiments are conducted with both the granodiorite and the acrylic glass disc. Figure 29 and Figure 30 depict step (3) (Figure 27) of the BTCs obtained by flushing the artificial fracture flow cell after 1 h and 24 h residence time for granodiorite and the acrylic glass, respectively. For comparison, the results of the experiments using 1000 nm and 25 nm CPS (Stoll et al., 2016) are depicted additionally. In all cases, the peak maxima of the BTCs decrease with increasing residence time. Moreover, with respect to the shape of the BTCs major differences in experiments with the same residence time cannot be detected clearly. By repeating experiments, it can be shown that main features of the BTCs are reproducible (recovery and the main shape of the peak). In the 1 h stop-flow experiments the peak amplitude of the illite experiments is similar to the 1000 nm CPS experiments with a maximum C/C_0 of ≥ 0.8 and thus higher than in the 25 nm CPS experiments (Figure 29). All 6 h stop-flow experiments are in an overall good agreement with a measured maximum C/C_0 of ≈ 0.75 (see A.II 1). In contrast to the CPS experiments the BTCs of the 24 h illite experiments (Figure 30) show broader and partly higher peaks of maximum C/C_0 of ≈ 0.4. The tailings of the granodiorite experiments are slightly more pronounced compared to acrylic glass and overall the illite experiments show a stronger tailing than the CPS experiments. While experiments with horizontal fracture orientation reveal a pronounced double peak when using CPS, with illite this variation is less pronounced but visible (see insets Figure 30). In contrast, a double peak shape is not visible in the vertical experiments.

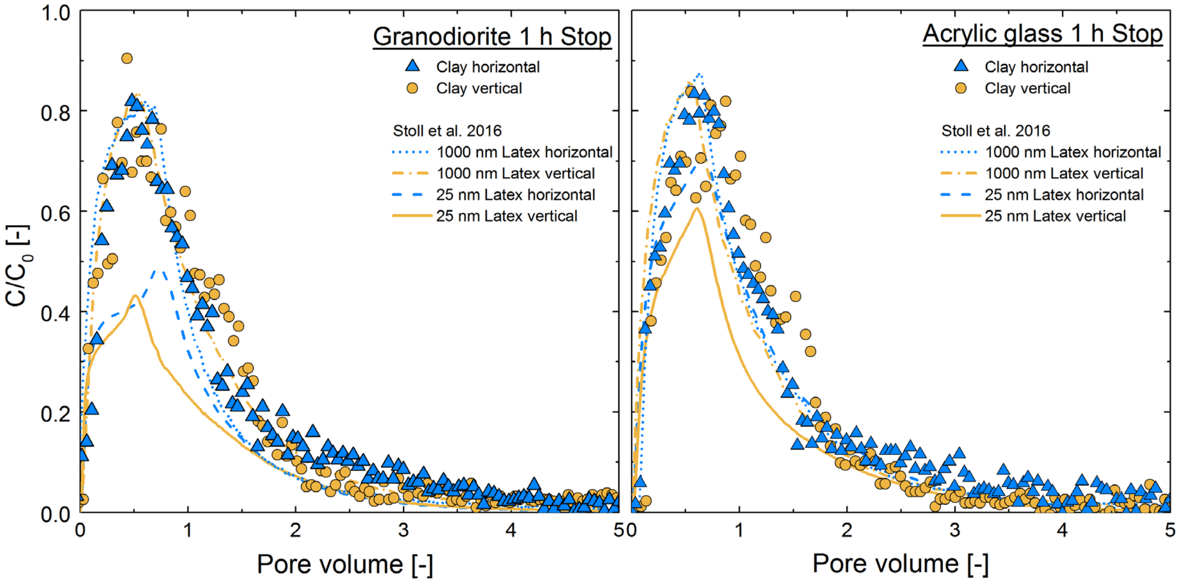

Figure 29: BTCs of 1 h stop-flow experiments on granodiorite (left) or acrylic glass (right) using Na-illite colloids for horizontal (triangles) and vertical (circles) fracture orientation. CPS experiments of Stoll et al. (2016) are plotted for comparison (lines).

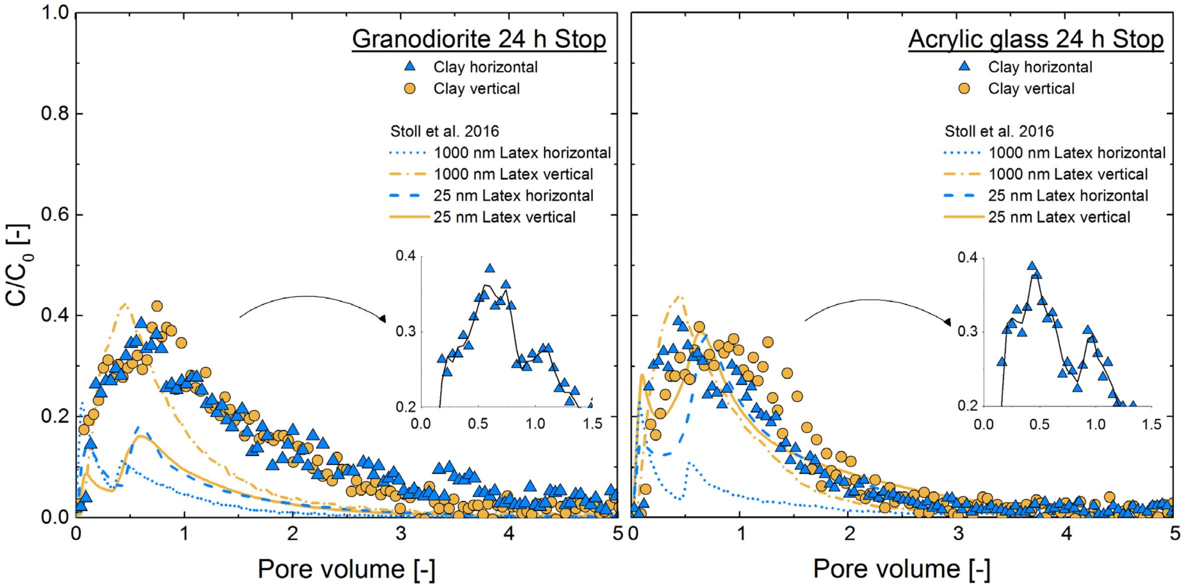

Figure 30: BTCs of 24 h stop-flow experiments on granodiorite (left) or acrylic glass (right) using Na-illite colloids for horizontal (triangles) and vertical (circles) fracture orientation. CPS experiments of Stoll et al. (2016) are plotted for comparison (lines). For better visibility a zoom-in of the peak area is given in the insets and a smoothing function (Savitzky-Goley, 5 data points, 2nd order polyn. Originlab software) is plotted to guide the eye visualizing the BTC double peak feature.

Figure 31 compiles the colloid recoveries of all experiments for different residence times. The calculated recoveries for each residence time are within the estimated experimental error of approximately 5% of the LIBD method and independent of the fracture orientation or collector surface material: 92–97% for the 1 h stop-flow, 83–86% for 6 h stop-flow and 43–49% for the 24 h stop-flow experiments. Additionally, Figure 31 shows the fit functions for the recoveries of the CPS experiments by Stoll et al. (2016). The CPS experiments showing comparable retention behavior are combined in one fit function. For example, the vertical 1000 nm CPS experiments show on both granodiorite and acrylic glass similar recoveries for each residence time.

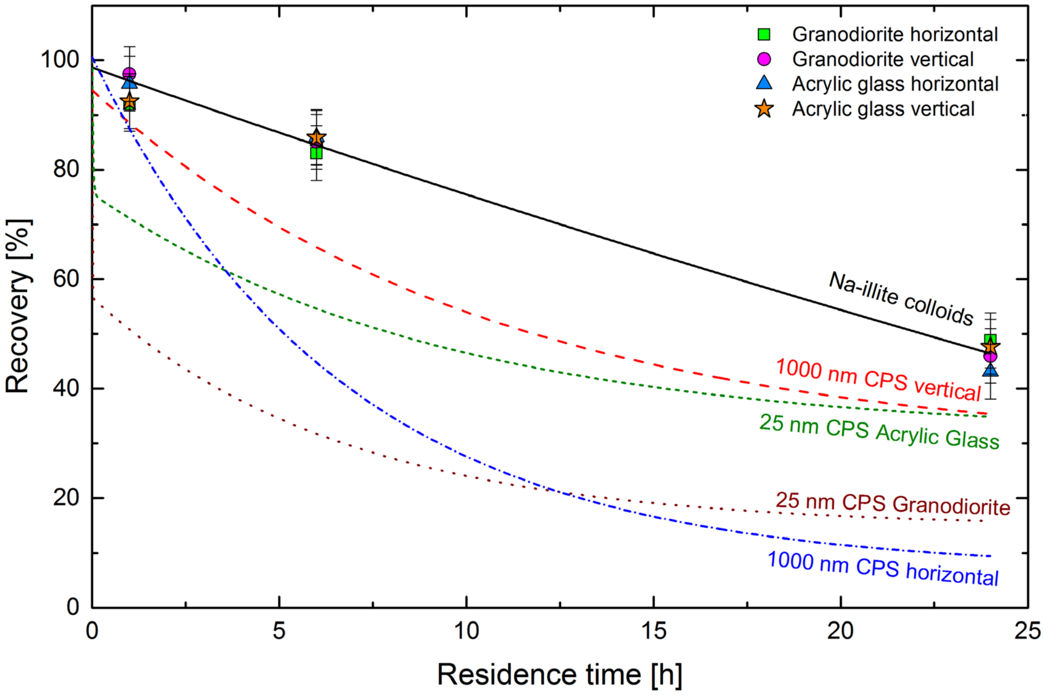

Figure 31: Calculated recoveries of the stop-flow experiments. The black solid line represents the fit function (first order experimental decay function) over the recoveries of the illite colloid transport experiments. Dashed and dotted lines represent the fit functions of the recoveries of the CPS stop-flow experiments by Stoll et al. (2016). For this, CPS experiments showing similar colloid retention behavior are combined (either the impact of fracture orientation (1000 nm) or the impact of the collector surface material (25 nm)). First order experimental decay function for the 1000 nm CPS, second order experimental decay function for the 25 nm CPS, respectively.

When comparing the recoveries of the illite experiments with ones of the 1000 nm and the 25 nm CPS, it is striking that the colloid recovery after 6 h and 24 h residence time is significantly higher than the recoveries of the CPS. Stoll et al. (2016) found that the colloid retention of 25 nm CPS is influenced by collector surface material and the retention of 1000 nm spheres by fracture orientation. In contrast, the investigated Na-illite colloids show no dependence of colloid retention on both fracture orientation and collector surface material for each residence time. The fact that the recoveries decrease with increasing residence time is an indication that a certain amount of the colloid suspension either diffuses into cracks and surface inhomogeneities, and/or deposits on the collector surface due to gravity.

In order to explain the observations, different factors and mechanisms will be discussed in the following. Mechanisms transporting colloids towards the collector surface, which in turn can result in an interaction and, possibly, retardation, are either sedimentation or Brownian motion. Colloid properties such as size, density and shape decide which mechanism is dominating. The residence time in the fracture has a major influence on the deposition forces. The L_S/L_D ratio is a tool to discriminate between these dominating forces acting on the colloids during the stop-flow phases (Becker et al., 1999). This ratio compares the characteristic sedimentation length L_S [m] and the diffusion length L_D [m] of colloids. For the non-spherical clay colloids, the calculation of the sedimentation length L_S is modified for the shape of the clay colloids. After Bernhardt (2012) the sedimentation length L_S for platelet shaped colloids (ellipsoid half-axes: a = b > c) is defined as:

$$L_S = \frac{2}{9} \cdot \frac{\Delta\rho \cdot g \cdot a \cdot c}{\eta} \cdot R_P \cdot t_R$$

$$R_{P,c} = \frac{3}{4}(A_1 \cdot \arccos p + B_1) \qquad R_{P,a} = \frac{3}{8}(A_2 \cdot \arccos p - B_1)$$

$$A_1 = \frac{1-2p^2}{(1-p^2)^{3/2}} \qquad \textbf{Equation 28}$$

$$A_2 = \frac{3-2p^2}{(1-p^2)^{3/2}}$$

$$B_1 = \frac{p}{1-p^2}$$

$$p = \frac{c}{a}$$

where $\Delta\rho$ [kg/m³] is the density difference between the colloid material and the liquid, g [m/s²] is the gravitational acceleration, a [m] and c [m] are the half-axes of the ellipsoid, η [kg/ms] is the dynamic viscosity in water, $R_{P,c}$ [-] and $R_{P,a}$ [-] are the correction factors for platelet shaped colloids for the two sedimentation directions and t_R [s] is the particular residence time in the fracture. In this calculation the half-axis c represents half of the height of a singular colloid with 9 nm. A shape factor correction to calculate L_D is not taken into account and, hence, L_D is calculated for spherical colloids. The diffusion length L_D is defined as:

$$L_D = \sqrt{2Dt_R} \qquad \textbf{Equation 29}$$

where D [m²/s] is the Stokes Einstein diffusion coefficient, which is defined by the Stokes-Einstein equation (Einstein, 1905):

$$D = \frac{k_B \cdot T}{6 \cdot \pi \cdot \eta \cdot a} \qquad \textbf{Equation 30}$$

where k_B [m²kg/(s²K)] is the Boltzmann constant and T [K] is the temperature. If the L_S/L_D ratio is ≈ 1, both mechanisms are expected to be in equilibrium. Otherwise, sedimentation (ratio > 1) or Brownian motion (ratio < 1) dominates.

Figure 32 shows the L_S/L_D ratios of the clay colloids of different sizes (40 nm, 150 nm and 350 nm in diameter) as a function of the residence time. A maximum possible colloid density of 2700 kg/m³ and a single colloid crystal thickness of 18 nm are assumed. These values are compared to the L_S/L_D ratios of the 1000 nm and 25 nm CPS. The deviation between both extreme cases for sedimentation along the a-axis and the c-axis is smaller than the symbol size in the diagram. Therefore the mean value of both values is shown. Figure 32 reveals that colloids of sizes ≥ 350 nm are clearly gravity dominated ($L_S/L_D > 1$) for residence times ≥ 14 h. In contrast, smaller colloids are clearly diffusion dominated over the maximum experimental time period. We may conclude that diffusion, which brings the colloids to the fracture surface, is the major process under the experimental conditions given. Note that in cases of a colloid density < 2700 kg/m³, the impact of gravity decreases for all colloid sizes.

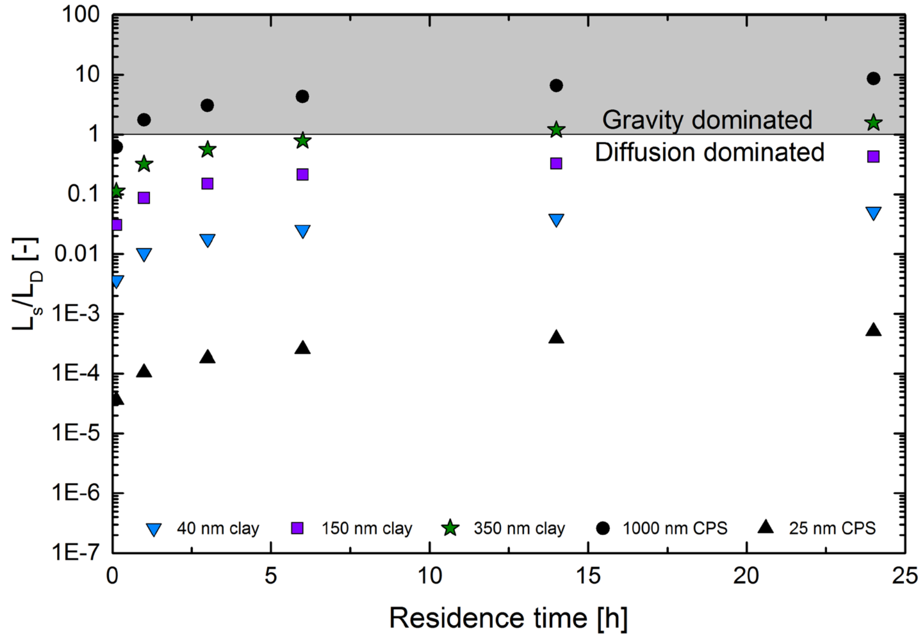

Figure 32: The L_S/L_D ratios of different sized clay colloids (40 nm, 150 nm and 350 nm) compared to 1000 nm and 25 nm CPS. Due to minor deviations between both extreme cases of sedimentation orientation the arithmetic mean of both L_S/L_D ratio values is shown.

The double peak shape observed in 25 and 1000 nm CPS experiment in Stoll et al. (2016) can be explained by a combination of (1) colloid sedimentation (in the horizontal fracture orientation) or diffusion to the fracture surfaces and (2) the fracture flow cell design. After the desired residence time, the flow is reconnected to the fracture and colloids near the fracture surface get retarded since they exhibit lower flow velocities due to the parabolic velocity profile in the fracture. Any kind of interaction of the colloids with the surface may lead to an additional retardation. Colloids in the inlet and outlet channels stay homogeneously distributed and form the two peaks after flushing the fracture flow cell. The first peak is the signal from the outlet channel and the second peak is the signal from both the inlet channel and remobilized colloids from the fracture. The higher the amount of colloids near the fracture surfaces due to sedimentation or diffusion, the more pronounced is the double peak shape.

The double peak observed in 1000 nm CPS experiments with a horizontal fracture orientation (Figure 30) was interpreted as the deposition of the colloids to the fracture bottom due to sedimentation. For the vertical fracture orientation no double peak shape was observed because the colloids settled in the horizontally orientated inlet and outlet channels but remain evenly distributed within the vertical fracture. This leads to a single peak. In experiments using 25 nm colloids this double peak shape was observed in horizontal and vertical experiments and more pronounced for granodiorite than for acrylic glass. This signal was attributed to colloid diffusion to the collector material (cracks and surface inhomogeneities) and a possible attachment to sites with a secondary energy minimum. In the herein represented illite experiments this double peak feature is less prominent and hardly to detect within the horizontal orientation (Figure 30). In experiments with vertical fracture orientation the double peak shape is completely missing. Based on the calculated L_S/L_D ratios, the here observed double peak features might be caused by gravity of the largest colloids due to the fact that this feature is only visible in the horizontal cases.

Nevertheless, the major decrease in colloid recovery is attributed to colloid diffusion. But in contrast to the study of Stoll et al. (2016) the polydispersity of the illite colloid suspension prevents the formation of prominent features like a double peak shape in the BTCs. The colloid recovery decreases with increasing residence time due to more rapid diffusion of the smaller illite colloids. Bigger colloids with smaller diffusion coefficients diffuse less quickly to the surface and are therefore less retained. Hence, these colloids may stay mobile within the fracture, which results in a BTC without a significant diffusion driven double peak shape in contrast to the 25 nm CPS. In the experiments on granodiorite with residence times of 24 h the illte BTCs show more tailing and the peak is slightly shifted compared to the experiments on acrylic glass. This might be an indication of a slightly higher diffusion to the granite surface of spherical colloids compared to the platy shaped illte colloids as the overall surface charge of both is quite similar. Due to the polydispersity of the colloid suspension with a size majority between 85 nm and 350 nm, colloid fractionation, e.g. due to sedimentation processes of bigger or diffusion processes of smaller colloids, is possible. It, however, could not be resolved in this study due to the selected standard suspensions > 100 nm used for LIBD calibration (see Table 7).

Our observations show that trace concentrations of illite clay colloids are considerably more mobile at least in short term experiments under residence times ≤ 24 h compared to CPS. Similar observations were made in column migration experiments with Grimsel granodiorite for shorter residence times (< 10 hours) using smectite colloids < 500 nm but significant higher suspension concentrations ≥ 100 ppm (Albarran et al., 2013). Here, we could undoubtedly show that this observation of higher clay colloid mobility can be expanded to ultra-trace colloid concentrations in the ppb range.

4.5 Summary and conclusion

In this study, the transport and the interaction of Na-illite colloids with a cut granodiorite surface (Grimsel granodiorite; Switzerland) and with an acrylic glass surface in a parallel-plate type fracture with a defined aperture were investigated. By means of transport experiments residence time and fracture orientation were varied for both collector surface materials. The experiments were conducted at pH 5 under low ionic strength (1 mM NaCl) and under laminar flow (7 mL/h) conditions (overall unfavorable attachment conditions). In order to detect the colloids and monitor the colloid transport within the experiments LIBD was applied. LIBD is developed as an analytical method for detecting and quantifying colloids at ultra-trace concentrations. LIBD allows measurements of colloids at such low concentrations that full surface coverage was impossible. S-curve LIBD measurements and SEM images showed a polydisperse illite colloid suspension ranging from 35–350 nm in colloid size. The BTCs obtained in continuous and stop-flow experiments were compared with the results of Stoll et al. (2016) using monodisperse CPS of 1000 nm and 25 nm in diameter. In continuous flow experiments the illite colloids showed an earlier first arrival than the solute tracer and full colloid recovery. Similar to the 1000 nm and 25 nm CPS, for the clay colloids a positive correlation was found between colloid retention and residence time.

However, in contrast to the CPS the recovery of the Na-illite colloids was significantly higher for long residence times (24 h). The geometry of the chosen fracture flow cell gives the opportunity to observe the impact of fracture orientation and collector surface material on colloid retention. Despite a minor, less prominent double peak in the horizontal illite experiments for 24 h residence time, prominent features as observed in the BTCs of the CPS were not detected in the BTCs of the illite colloids. Our results and results of similar studies (e.g. Albarran et al., 2013) show that the difference in shape, surface charge distribution, density and colloid size distribution of CPS compared to clay colloids may be responsible for the deviations in the experimental results. Therefore, in respect to the experimental setup and conditions used low density monodisperse CPS are no ideal analogue for natural illite colloids. Illite colloids show significant higher mobility and conservatism might not be given using functional synthetic CPS in order to estimate nanoparticles mobility.

4.6 Acknowledgments

MS and ES thank the HGF portfolio project “Geoenergy” under the Helmholtz topic “Geothermal Energy Systems” and FMH and TS the Helmholtz Program NUSAFE for support. The work has received partial funding by the Federal Ministry of Economics and Technology (BMWi) under the joint KIT-INE, GRS research projects “KOLLORADO-e” (02E11203B) and “KOLLORADO-e^2” (02E11456A), and the European 7th Framework Program (FP7/2007-2011) under grant agreement no. 295487 (BELBaR Project). We want to thank Dr. Ingo Blechschmidt (NAGRA) for providing the granodiorite drill core, Carmen Garcia and Franz Rinderknecht for introducing the LIBD method, Johannes Lützenkirchen for streaming potential measurements, Stephanie Kraft for the ICP-OES measurements and Eva Soballa for the SEM measurements.

5 Experimental and numerical investigations on the effect of fracture geometry and fracture aperture distribution on flow and solute transport in natural fractures

M. Stoll[1,2], F.M. Huber[1], M. Trumm[1], F. Enzmann[3], D. Meinel[4], A. Wenka[5], E. Schill[1,6], T. Schäfer[1,2]

[1]Karlsruhe Institute of Technology (KIT), Institute for Nuclear Waste Disposal (INE), P.O. Box 3640, 76021 Karlsruhe, Germany

[2]Friedrich-Schiller-University Jena (FSU), Institute of Geosciences, Applied Geology, Burgweg 11, 07749 Jena, Germany

[3]Johannes Gutenberg-University, Geosciences Institute, J.-J. Becherweg 21, 55099 Mainz, Germany

[4]Bundesanstalt für Materialforschung und -prüfung (BAM), Unter den Eichen 87, 12205 Berlin, Germany

[5]Karlsruhe Institute of Technology (KIT), Institute for Micro Process Engineering (IMVT), 76021 Karlsruhe, Germany

[6]Technical University of Darmstadt, Institute of Applied Geoscience, Schnittspahnstraße 9, 64287 Darmstadt, Germany

5.1 Abstract

The impact of flow channel geometry on non-reactive solute transport was investigated experimentally and numerically on two differently altered fractured granite drill cores. Using three injection and three extraction locations at top and bottom of the fractured cores, different dipole flow fields were examined. The conservative tracer (Amino-G) breakthrough curves were measured using fluorescence spectroscopy. Based on 3-D digital data obtained by micro computed tomography 2.5-D numerical models were generated for both fractures by mapping the measured aperture distributions to the 2-D fracture geometries. Fluid flow and tracer transport were simulated using COMSOL Multiphysics®. In order to study purely the physical transport process within the fractures neither chemical interactions with fracture surfaces (e.g. sorption) nor any matrix diffusion were incorporated in the models.

Corresponding to their geological history, both fractures are significantly different in terms of spatial heterogeneities, which are clearly reflected by the fluid flow and the solute transport behavior. Via numerical simulations and tomographic imaging experimentally observed breakthrough curves can be understood and qualitatively reproduced. The experiments and simulations suggest that fluid flow in the altered fracture is governed by the fracture geometry, while fluid flow in the unaltered fracture seems to be controlled by the aperture distribution. Moreover, we demonstrate that in our case parallel-plate models fail to describe the experimental findings and that pronounced tailings can be attributed to complex internal heterogeneities. The results presented implicate the necessity to incorporate complex domain geometries governing fluid flow and mass transport into both non-reactive and reactive transport modeling.

5.2 Introduction

Fractures or shear zones are the dominant structures for fluid flow and mass transport in crystalline rock of low or negligible matrix permeability. A full comprehension and prediction of fluid flow and coupled mass transport is of paramount importance for many applications of geo-engineering ranging from low flow rates, as expected in the nuclear waste disposal far-field (Geckeis et al., 2004; Vilks and Bachinski, 1996), to high flow rates, e.g., in geothermal systems (Schill et al., 2017). In this respect, the quantification of fluid flow in fractures is crucial and was extensively studied for decades (Bodin et al., 2003; Brown, 1987; Sahimi, 2011; Tsang, 1984; Witherspoon et al., 1980; Zimmerman et al., 2004).

In general, mass (solute and particulate) transport through fractured media is accompanied by hydrodynamic dispersion (Roux et al., 1998) including (i) Taylor dispersion, due to the parabolic velocity profile, induced by friction between two no-slip fracture walls; (ii) macrodispersion, due to spatial heterogeneities resulting in flow channeling (Bodin et al., 2003); and (iii) molecular diffusion due to a developing concentration gradient. Natural rock fractures possess complex geometries with rough and irregular fracture surfaces (asperities), highly variable aperture distributions and contact areas (asperity contacts) of different sizes between the opposite surfaces (Brown et al., 1998; Durham et al., 2001; Hakami and Larsson, 1996). Fracture and fracture network solute transport is directly affected by spatial heterogeneities inducing complex flow fields. Flow channeling is a typical fracture flow feature, which is provoked by strongly pronounced aperture distribution variabilities resulting in preferential flow paths of lower hydraulic resistance (Bodin et al., 2003; Huber et al., 2012; Keller et al., 1999; Moreno et al., 1988; Neretnieks et al., 1982; Tsang and Neretnieks, 1998). With respect to the entire fracture, elevated flow velocities prevail in those regions (Brown et al., 1998). In close proximity to these channels, depending on the geometry and given hydraulics, there are often hardly accessible areas for the main flow (low flow zones), where features like recirculation zones may form (Boutt et al., 2006). Solutes or particles may reach those areas by hydrodynamic dispersion and/or molecular diffusion. The increased residence time of solutes and colloids, and therefore increased time scales for chemical and physical interaction with the fracture surface, may then lead to higher retardation and retention (e.g. sorption kinetics, reduction kinetics or matrix diffusion). In consequence, the residence time distributions in systems described above show much more pronounced tailings.

Numerous analytical and numerical approaches are postulated to describe mass transport in single fractures and fracture networks. The elementary model of a single fracture is a smooth parallel-plate simplification with a constant aperture (Louis, 1969; Oda, 1986; Parsons, 1966; Snow, 1965). In this case, the hydraulic fracture conductivity (volumetric flow) is a cubic function of the aperture (Snow, 1965; Witherspoon et al., 1980). Neglecting rough fracture surfaces and tortuous flow paths, these geometrically simplified models cannot describe the flow dynamics (Brown, 1987; Sisavath et al., 2003) and overestimate fracture flow rates (Konzuk and Kueper, 2004; Nicholl et al., 1999). Consequently, this parallel-plate approach is applicable for smooth and wide fractures. Other simplified modelling approaches, like the local cubic law (Zimmerman et al., 1991), the Stokes equation or the lubrication equation (Pinkus and Sternlicht, 1961) are valid only under limited circumstances such as very low Reynolds numbers or mean apertures, which are much larger than the actual roughness. Additionally, those models explicitly cannot resolve spatial heterogeneities, such as intra-fracture stagnation zones (Cardenas et al., 2009). In contrast, the Navier-Stokes equation fully describes the motion of Newtonian fluids in a continuum media (Wilkes and Bike, 1999). Consequently, in complex geometries like natural fractures the Navier-Stokes equation (Batchelor, 1967) needs to be used to simulate precisely the fluid flow despite the much higher computational and numerical efforts necessary.

The isolated impact of fracture geometry and aperture distribution is less investigated and a distinction between the contribution of hydrodynamic dispersion and diffusion to low-velocity zones is challenging (Cardenas et al., 2007). Due to this lack of information, tailing effects in the residence time distribution are often attributed only to reactive interaction with the fracture surface or to matrix diffusion. However, effects of fracture geometry and hydrodynamic condition were found to be of influence and even more important with increasing Reynolds number, e.g., in 2-D numerical modelling of fluid flow and mass transport in a CT-scanned fracture (Cardenas et al., 2009). Here, velocity contrasts are generated by geometry-triggered features like eddies. Boutt et al. (2006) inferred the trapping of colloids in intra-fracture recirculation zones from 2-D numerical simulations for an aperture of 3.5 mm, with the upper fracture surface being rough while the lower side was considered flat. 3-D models indicate that flow heterogeneity and additional dispersion are affected by asperity contacts and surface roughness, even for small Reynolds numbers ($Re = 0.001$) (Zou et al., 2017).

Direct comparison of experimental data and numerical simulations of the same setting (e.g. Huber et al., 2012; Tenchine and Gouze, 2005) are rare, which creates a lack in benchmarking of these numerical simulations. A crucial step to tackle this is the high-resolution scanning of the complex fracture geometry. In particular, for laboratory experiments, tomographic methods such as computed tomography (µ-CT) represents a non-destructive way to image the internal, often complex structure of fractured media (Keller, 1998) and can be implemented in 2-D or 3-D numerical models (Huber et al., 2012; Petchsingto and Karpyn, 2009). Since the precision of 3-D simulations in fractured geometry highly depends on the resolution of the mesh and the CT-scans, in larger samples, intensive pre- and post-processing, increasing calculation time and hardware power is required.

In the present study, we investigate the impact of flow channel geometry on solute transport experimentally and numerically. For this purpose, a hydrothermally altered and an unaltered natural granitic fracture of about 9 cm length each are implemented in fracture flow cells with three inlets and three outlets at each side of the fracture. The injection and extraction locations of a conservative fluorescent solute tracer are systematically varied for two flow rates, 24 or 12 mL/h. µ-CT scans of both fractures provide the basis for 2.5-D numerical models on fluid flow and solute transport to which the experimental results are compared. In order to investigate the effect of the flow geometry, any chemical or physical retardation processes (e.g. matrix diffusion, sorption) are neglected in the numerical solutions.

5.3 Materials and methods

5.3.1 Fracture characterization

Both fractures were sampled from drill cores of the well EPS-1 at the Enhanced Geothermal System (EGS) reference site at Soultz-sous-Forêts, France, which is located about 70 km north of Strasbourg at the NNE-SSW trending western boundary of Upper Rhine Graben. At Soultz-sous-Forêts, three naturally fractured, granitic reservoirs with permeabilities of about 3E–17 to 3E–16 m^2 (Schill et al., 2017) and locally up to 3E–14m^2 (Kohl et al., 1997) occur underneath the Cenozoic and Mesozoic sedimentary cover below 1400 m depth. The Paleozoic granitic basement is characterized by a grey porphyritic monzogranite down to about 4000–4500 m, where it is penetrated by grey fine-grained two-mica-granite. Hydrothermal alteration, occurring mainly on fracture surfaces, via natural fluid circulation within the reservoir resulted in secondary phase formation such as clays (illite, smectite, tosudite), calcite, secondary quartz and sulfide (Genter et al., 2009; Genter et al., 2003).

From cores of diameters of 78.0 ± 0.4 mm with distinct hydrothermal alteration and macroscopically unaltered, respectively, sections with axial fractures were selected. The hydrothermal porphyroid red granite sample (length $L = 93.4 \pm 0.3$ mm) with moderate to high alteration is derived from 1462 m depth. The standard porphyroid granite sample ($L = 92.9 \pm 0.3$ mm) with a minor pervasive alteration is taken from 1957 m depth (Genter and Traineau, 1991). Further information is summarized in the supporting information (A.III 1).

To study the impact of fracture geometry and aperture distribution both fractures were characterized by digital microscopy of the open fracture surfaces and μ-CT of the final flow cell design. The former method provides high resolution information on the morphology and roughness of the fracture surfaces, while μ-CT gives detailed information on the fracture geometry and aperture distribution under μm resolution.

The fracture surfaces are scanned using a Keyence VR3200 Macroscope (magnification 12x). Based on the 3-D digital data sets, the surface roughness Rq [mm] is computed as the root mean squared surface deviation of the profile roughness (Jorgensen et al., 1993) (Equation 31):

$$Rq = \sqrt{\frac{1}{n}\sum_{i=1}^{n} z_i^2} \qquad \textbf{Equation 31}$$

where n is the number of points, z_i [mm] is the vertical distance from the mid plane to the i^{th} data point. To partially decouple the roughness from the overall curvature of the fracture surfaces we define a local surface roughness of node i, $R_{loc}(r)$ by restricting the sum in Equation 31 to points within a radius r of node i. Furthermore, only nodes with a distance larger than r to the surface boundaries are considered. For each radius between 1 mm and 27 mm (i.e. surface areas between 3 mm² and 2290 mm²) the local surface roughness $R_{loc}(r)$ is computed as the average over all discs of radius r.

μ-CT measurements were carried out at the Federal Institute for Materials Research and Testing (BAM, Berlin) after emplacing the fractures in acrylic glass setups (A.III 2). The granite cores are scanned with a GE xs|300 device (dxr-250 2k detector) (General Electric, USA) with following scan parameters: 280 kV, 90 uA, 0.5 mm Cu pre-filter, 3000 angel steps by 360° rotation. The reconstructed voxel dimension is 60.8 µm with the whole sample in the field of view. The raw data quality is high but contains medium beam hardening effects.

5.3.2 Experimental setup, conditions and procedure

The procedure of flow cell construction is described in detail in the supporting information (A.III 2). Conservative solute tracer experiments using 10 ppb UV-fluorescent 7-amino-1.3-naphthalene (Amino-G, Postnova Analytics GmbH, Germany) are conducted. The molecular diffusion coefficient of Amino-G in pure water is 4.47E-10 m^2/s (Bashar and Tellam, 2011). The solute tracer is measured continuously by fluorescence spectroscopy (Luminescence Spectrometer 55, Perkin Elmer, USA) using a flow-through cuvette of 100 µL (Hellma Analytics, Germany).

In order to determine a background electrolyte, remaining parts of the granite cores used in the transport experiments are crushed using a jaw crusher (BB50, Retsch, Germany). The composition of 30 mL Milli-Q water after equilibration with 10 g of the crushed material of a size of about 1 mm was measured after 7 and 30 days using inductively coupled plasma optical emission spectrometry (ICP-OES; Optima 8300DV, Perkin Elmer, USA) and ion chromatography (IC; Dionex ICS-1100, Thermo Scientific Inc., USA). Based on the resulting major cation and anion composition, two synthetic background electrolyte solutions were prepared (Table 9).

Table 9: Chemical composition of synthetic background electrolytes for the equilibration of the altered and the unaltered drill cores.

Rock type	NaCl [mol/L]	KCl [mol/L]	NaF [mol/L]	pH
Altered granite	3.94E–3	1.67E–3	1.34E–4	5.6
Unaltered granite	3.04E–4	5.43E–4	1.30E–4	5.6

Prior to the transport experiments both cores were flushed for two months with the respective background electrolyte at 5 mL/h using a peristaltic pump (REGLO Digital MS-4/8, Ismatec, Germany) for chemical equilibration. A scheme of the flow cell and the inlet/outlet locations along the fracture as well as the experimental setup is shown in Figure 33. Whenever possible PEEK (Polyether ether ketone) tubing of 0.75 mm inner diameter is used in order to minimize potential interaction (e.g. sorption) and dispersion. A peristaltic pump injects the background electrolyte out of its reservoir into the fracture via a three-way flow switching valve (Upchurch Scientific, Germany). The outlets are connected to a quartz glass flow-through cuvette of 100 µL internal volume (Hellma Analytics, Type 176.751-QS, Germany) within the fluorescence spectrometer (Luminescence Spectrometer 55, Perkin Elmer, USA). The tracer fluorescence signal is measured continuously yielding tracer residence time distributions (i.e. breakthrough curves, BTC). Time-dependent measurements at a constant wavelength (excitation wavelength $\lambda_{ex} = 350$ nm and emission wavelength $\lambda_{em} = 445$ nm of Amino-G) were acquired using BL studio software (time drive). The data interval is set to $\Delta t = 3$ s. The eluate is collected and weighed at the outlet of the setup after passing the fluorescence detection spectroscopy to determine the flow rate and pH. In experiments bypassing the fracture flow cell, the dead volume of the setup has been quantified to be 610 ± 40 µL. The resulting BTC for determination of the setup dead volume under the two different flow rates chosen is later directly applied as injection function in the numerical modeling to implicitly include any artificial dispersion caused by the experimental setup.

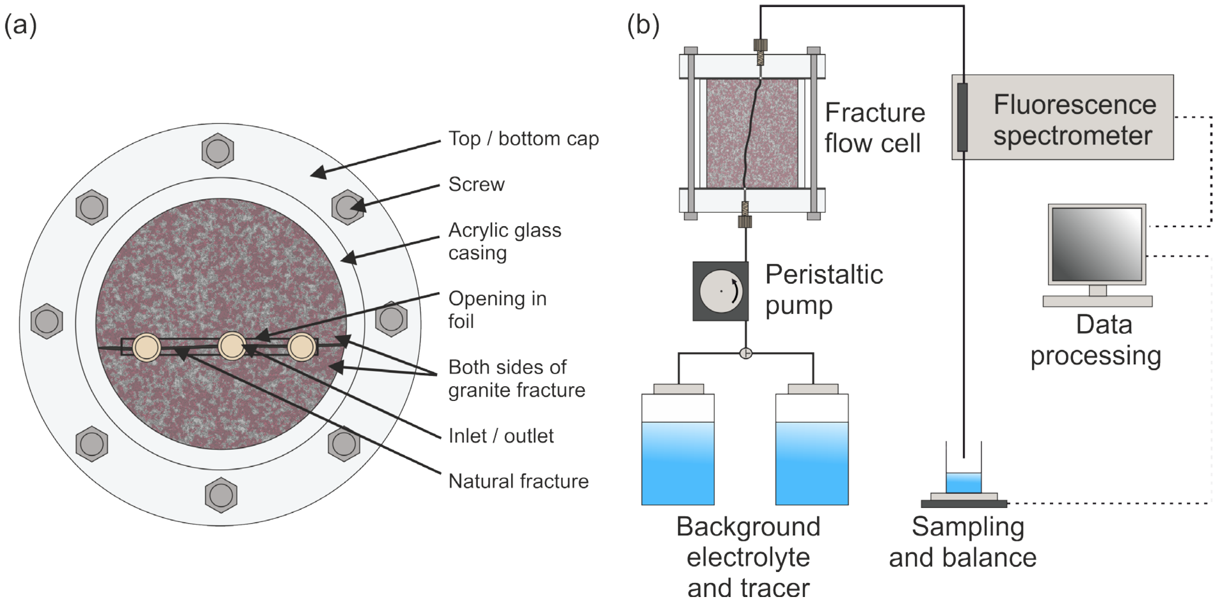

Figure 33: a) Top/Bottom view on the fracture flow cell. Three inlets/outlets are arranged along the fracture in different distances. b) Scheme of the experimental setup.

The initial mean concentration, C_0, is determined by injecting the tracer solution directly into the flow-through cuvette using a syringe before and after every experiment. In the transport experiments, a tracer volume of 4 mL is injected at constant flow rates of 24 or 12 mL/h. After injecting the tracer pulse, the flow is switched to tracer-free background electrolyte keeping the set flow rate until the initial background level is reached. A calibration curve is applied to convert the fluorescence intensity into concentration.

5.3.3 Model generation

5.3.3.1 Model preprocessing

Based on the µ-CT datasets of both drill cores 3-D digital models for both fractures are generated using segmentation routines. To get segmentable binary structural spatial data of the fracture overall within the sample, it is necessary to remove beam hardening effects and noise. This was done by an own method (Jovanović et al., 2013; Khan et al., 2015). Low noise removal was done with a 3-D non-local means filter (Buades et al., 2005) extremely fast, implemented in the GeoDict software package (**Geo**metric Models and Pre**Dict**ions of Properties (GeoDict, 2015)). After correction of the reconstructed raw data (2k 16bit datasets), the fracture was segmented by watershed/thresholding segmentation procedure implemented in the 3-D software Avizo (FEI Visualization Sciences Group, France).

The segmented 3-D fracture geometry from Avizo is exported in STL format without any mesh error correction (errors like e.g. overlapping triangles, low-quality triangles etc.) for further preprocessing. Due to the resulting voxel size of 60 µm, parts smaller than the resolution are not interpreted as part of the open fracture space and are therefore not exported as geometry. That is, those areas are hydraulically not available in the simulation. The low µ-CT scan resolution in relation to the spatial fracture aperture dimensions results in erroneous segments in the uncorrected STL-mesh (e.g. flat elements without extension in z-direction and torn patches). Using the finite element pre-processor Hypermesh© (HyperWorks, Altair Engineering, USA) an envelope around the fracture geometry was generated using the built-in shrinkwrap meshing option to obtain a watertight triangular surface mesh. The shrinkwrap option artificially inflates the original geometry and aperture distribution depending on the maximum element size chosen in the meshing algorithm. This compromise had to be taken to obtain the necessary watertight surface mesh without altering the natural geometry substantially. Moreover, the resulting fracture geometry and surface roughness of the watertight mesh is smoothed slightly. This watertight STL mesh is further remeshed to improve element quality and remove any leftover mesh errors with the help of the software 3-matic Research 11.0© (Materialise Mimics Innovation Suite 19.0, Belgium). With the aforementioned steps, complete error-free triangulated 3-D models with inlet and outlet of both cores are obtained. The experimental tubing locations are implicitly included in the 3-D model by placing cylinders of 0.75 mm in diameter and 5 mm in length at their respective positions at the fracture model inlets/outlets. This was done to establish a fully developed flow profile before entering the fracture while keeping an isolated injection point into the fracture. These 3-D models served as the base for the creation of the 2-D models used in the numerical simulations. To obtain the aperture distribution and the 2-D model geometry a fracture midplane was created, which is located precisely in the middle of both main fracture planes. By automatically calculating the distance between the main planes (on each node of the triangular mesh) the aperture distribution is obtained within 3-matic. The midplane was geometrically transformed from 3-D to 2-D by projection onto the x-y plane. The 2-D midplane is imported afterwards into COMSOL Multiphysics® (COMSOL AB, Stockholm, Sweden) (COMSOL, 2017) for the numerical model generation and simulation setup. In order to compensate the artificial increase of the aperture distribution by the shrink-wrapping step explained above, the mean aperture of the original uncorrected STL mesh from Avizo is compared to the mean aperture of the STL mesh after the shrink-wrapping yielding the factor to scale down the aperture values. Consequently, the aperture distribution used in COMSOL has the same mean aperture value as determined by µ-CT. The aperture values of the tubing remain unaffected.

5.3.3.2 Governing equations and boundary conditions

Flow and transport modelling was performed using version 5.2a of the finite element code COMSOL Multiphysics® Modeling Software. The Navier-Stokes equations are solved using the Laminar Flow module, in which steady-state laminar flow of an incompressible, single phase Newtonian fluid of constant viscosity is expressed by two equations in vector form:

(i) the momentum balance equation:

$$\rho(u \cdot \nabla)u = \nabla \cdot [-pI + \eta(\nabla u + (\nabla u)^T)] + F$$ **Equation 32**

(ii) the continuity equation:

$$\rho\nabla(u) = 0$$ **Equation 33**

Here, ρ [kg/m³] denotes the fluid density, u [m/s] the fluid velocity vector, p [Pa] the static pressure, I the identity matrix, η [kg/(ms)] the fluid dynamic viscosity and F [kg/(m²s²)] the body force applied to the fluid.

Given the large number of experiments and considering necessary computational times simulating the highly complex geometrical structures in 3-D, in this study, an advanced 2-D simulation approach was applied. Despite the reduction in dimensionality from 3-D to 2-D, and thus a loss in geometric information, the model approach used in this work tried to incorporate as much as possible geometric information from the µ-CT datasets. Fractures possess extreme gradients in spatial scales with apertures much smaller (µm to mm scale) than the fracture length and width (cm to m scale). A Navier-Stokes flow model in the x-y plane perpendicular to the fracture z-direction (aperture distribution) fails to describe the flow correctly if it assumes a unit height in z-direction (e.g. 1 m as used by many flow solvers, which is orders of magnitude bigger than the actual fracture height) because the impact of the boundaries (top and bottom wall perpendicular to the flow direction) are not considered appropriately. In order to model in 2-D, the impact of the fracture aperture on the fluid flow using the Navier-Stokes equation the so-called shallow channel approximation available in COMSOL is applied (Bruus, 2007). This approximation adds an additional resistance term (Equation 34) to the Navier-Stokes equation representing the influence of the aperture *a* [m]. This term introduces the resistance of the top and bottom wall to the fluid flow.

$$F = -12\frac{\eta u}{a_z^2} \qquad \textbf{Equation 34}$$

The measured (and re-calculated as mentioned above) aperture distribution is imported into COMSOL to be used as a variable in an interpolation function (x, y, a), which is applied as channel thickness in the shallow channel approximation. The interpolation function maps the aperture distribution onto the fracture geometry. Although the resulting model incorporates the aperture distribution, the geometrical information in z-direction is still lacking, which is e.g. the tortuosity in z-direction perpendicular to the flow direction is not reflected by the model. Nevertheless, the use of the aperture distribution measured by µ-CT in the 2-D model is clearly more realistic compared to models using a simple mean aperture.

A normal inflow velocity boundary condition is applied at the inlet and a pressure boundary condition (prescribed gauge pressure = 0 Pa; suppress backflow) at the outlet. The applied velocity was calculated based on the tubing radius and applied mass flow (24 mL/h or 12 mL/h) in the experiments, which results in a flow velocity of 0.015 or 0.0075 m/s. The fracture walls are treated as “no-slip” boundary conditions, which specify the velocity at the walls as zero (*u*=0). Using the dimensionless Reynolds number *Re* [-] the fluid dynamics of the flow in the fracture (Equation 35) and in the inlet and outlet pipes (Equation 36) are characterized as:

$$Re = \frac{u \cdot L}{v}$$ **Equation 35**

or

$$Re = \frac{Q \cdot d}{v \cdot A}$$ **Equation 36**

where *L* [m] is the characteristic length (here the arithmetic mean of the aperture), *v* [m^2/s] the kinematic viscosity, *Q* [m^3/s] the volumetric flow rate, *d* [m] the inner diameter of the pipe and *A* [m] the pipe's cross-sectional area. Fluid flow through a narrow rough fracture can be classified as laminar when $Re < 100$. For $Re > 100$ a turbulent hydraulic flow regime prevails (Kohl et al., 1997).

The stationary flow field is used in the transient solute transport simulation by a one-way coupling approach. For solving the solute transport, the time dependent convection-diffusion equation is used:

$$\frac{\partial c_i}{\partial t} + \nabla \cdot (-D_i \nabla c_i) + u \cdot \nabla c_i = R_i$$ **Equation 37**

where *c* [kg/m^3] is the total concentration of the species *i*, *t* [s] is the time, *D* [m^2/s] is the diffusion coefficient, *u* [m/s^2] is the mass species velocity and *R* is the sinks and sources of the species *i*.

The dimensionless Péclet Number *Pe* [-] describes the ratio between molecular diffusion and convection on the solute transport. *Pe* is defined as:

$$Pe = \frac{u \cdot L}{D}$$ **Equation 38**

where *u* [m/s] is the mean flow velocity, *L* [m] indicates the characteristic length, which is in transport in fractures generally equal to the mean aperture. In case of $Pe > 1$ convection dominates, however, for $Pe < 1$ the solute transport is mainly controlled by diffusion.

The tracer was introduced at the inlet of the model using the experimental injection function (as described above). By using the experimental injection function as model input, mixing and dilution effects in the experimental setup are implicitly incorporated. Before tracer injection, the initial tracer concentration in the fracture is $c = 0$.

The numerical mesh used consists of purely triangular elements. A part of the mesh is depicted in the supporting information (A.III 3). The mesh is created in an adapted way with a finer mesh resolution near the model boundaries. The mesh was refined until a mesh independent solution of the flow field was achieved (less than 1% deviation between two refined model simulations was deemed sufficient). In parallel, it was assured that the mesh has at least twice the number of elements than the number of aperture values imported to avoid numerical instabilities of the interpolation function in areas of high aperture value gradients.

The direct solver PARDISO (Parallel Sparse Direct Solver) was chosen for flow and solute transport calculations with a relative tolerance of 1E–8 for the flow and 1E–6 for the transport, respectively. In order to obtain the BTCs a boundary probe is applied at the respective outlet. The time steps are taken automatically by the solver to reach convergence in dependence on the set tolerance. The simulation time is chosen long enough for each model BTC to reach at least C/C_0 of 1E–4 in the BTC tailing.

5.4 Results and discussion

This section is subdivided in the results of the fracture characterization and the surface roughness measurements (Section 5.4.1), the fluid flow simulation (Section 5.4.2), the comparison of experimental and modeled solute transport BTCs (Section 5.4.3), the investigation of the impact of aperture distribution and geometry (Section 5.4.4) and a discussion about the µ-CT data uncertainties and the model limitations (Section 5.4.5).

5.4.1 Fracture analysis by µ-CT and digital microscopy

5.4.1.1 Altered fracture

This fracture model is featured by a highly complex geometry with irregular boundaries and heterogeneously distributed asperity contacts. The width of the altered fracture model varies between 66.0 ± 0.1 and 76.7 ± 0.1 mm and the length is 87.3 ± 0.1 mm (without the cylinders/inlet and outlet tubes) (see Figure 34). The model shows to be ≈ 6 mm shorter compared to the total fracture length. This is most likely attributed to the µ-CT measurement procedure. Within the given resolution of 60 µm both fracture sides are touching each other at some areas. In the model those areas are hydraulically unavailable because all apertures smaller than 60 µm are interpreted as nonexistent (Figure 35). However, a possible presence of apertures smaller than the resolution cannot be excluded. The irregular shape of the fracture margins is maybe an artifact of the utilized glue in order to seal the fracture along its sides. As expected the aperture field shows a heterogeneous distribution with apertures from 0 (theoretically calculated) to 1.013 mm with a mean aperture of 0.162 mm (Figure 36). The major amount of the aperture values (66%) is between 0.075 and 0.175 mm (24% bigger and 10% smaller). The total volume of the fracture is 0.9 mL. Area and volume were evaluated by a surface integration of the geometry and the aperture file, respectively. All data is summarized in Table 10.

5.4.1.2 Unaltered fracture

The geometry of the unaltered fracture model is less complex compared to the altered one (see Figure 34 and Figure 35). In addition, the number of contact areas is less abundant and the sizes are significantly smaller. The spatial dimensions are 91.8 ± 0.1 mm in length and between 64.0 ± 0.1 mm and 74.0 ± 0.1 mm in width. This is a deviation to the original fracture of ≈ 1.1 mm in length. The 3-D model (Figure 34) shows a step in the lower part of fracture at the right side, above the right inlet (see red ellipse in Figure 34). This geometrical feature cannot be resolved in the 2-D model due to the missing z-dimension. In contrast to the altered fracture, the mean aperture is more than two times bigger with a value of 0.357 mm. 79% of all apertures are between 0.255 and 0.435 mm (11% bigger and 10% smaller) (Figure 36). Consequently, the total volume of the fracture is with 2.2 mL more than twice as high. Fracture properties are summarized in Table 10.

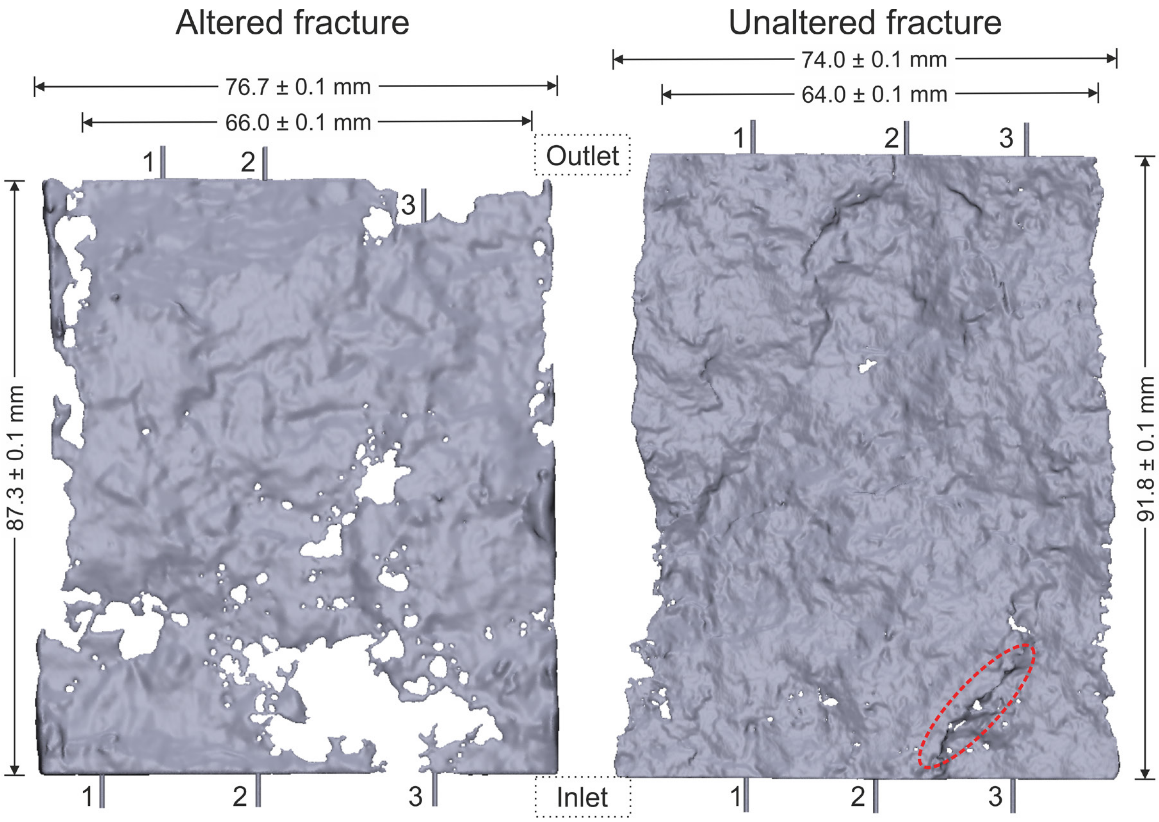

Figure 34: 3-D models of the altered fracture (left) and the unaltered fracture (right). Red ellipse shows the vertical step in the unaltered fracture morphology.

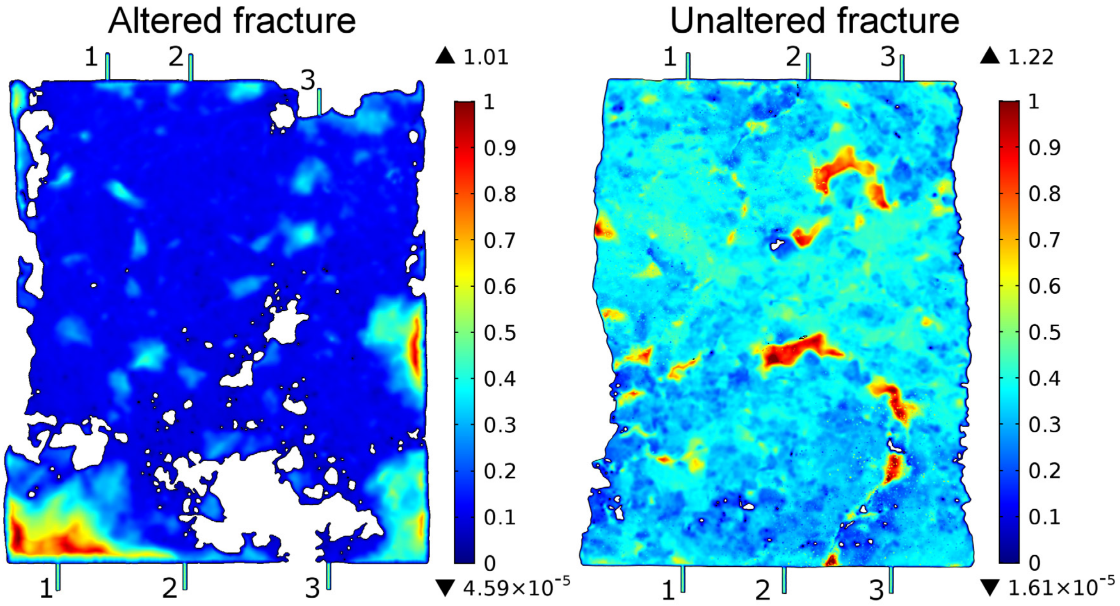

Figure 35: Aperture distributions [mm] mapped on 2-D models of the altered fracture (left) and the unaltered fracture (right) (Maximum values given above the color chart).

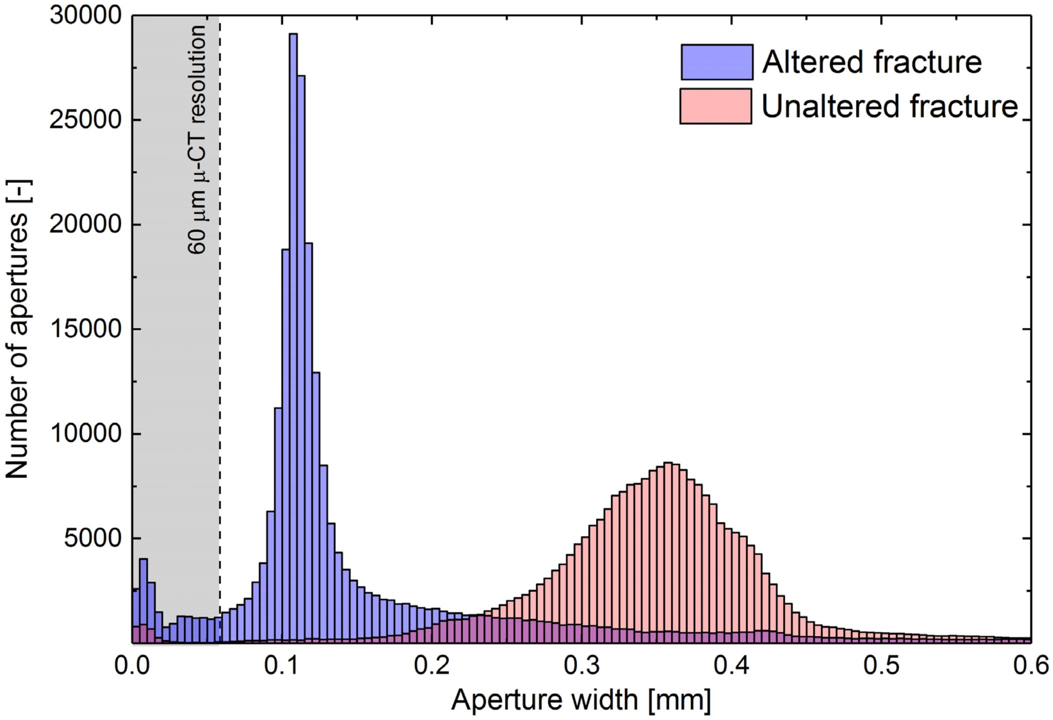

Figure 36: Aperture distributions of the altered and the unaltered fracture with a class size of 0.005 mm. The graph is cut at 0.6 mm aperture width because of the insufficient visibility due to the decreasing number of apertures above 0.6 mm. A graph with log scale is displayed in supporting information (A.III 4).

Table 10: Model derived values (The minimum apertures are theoretical calculated values, because they are smaller than 60 µm µ-CT resolution).

	Altered fracture	**Unaltered fracture**
Min. aperture [mm]	4.592E–5	1.612E–5
Max. aperture [mm]	1.013	1.215
Mean aperture [mm]	0.162	0.357
Std. deviation [mm]	0.132	0.112
Variance [mm]	0.017	0.012
Total volume [mm^3]	921.5	2,250.7
# Elements in 2.5-D Model [-]	561,935	581,877
# Aperture values [-]	257,380	252,806
Surface area of 2.5-D model [m^2]	5.615E–3	6.245E–3

Figure 37 displays the local surface roughness $R_{loc}(r)$ [mm] of both fracture sides of the altered and the unaltered core. The error bars represent the standard deviation of $R_{loc}(r)$. For all cases $R_{loc}(r)$ increases with surface area with the unaltered core showing a larger slope. However, the standard deviations do not converge to zero for the unaltered core hinting at a non-uniform distribution of the roughness along the fracture. Those observations correspond well with the findings made in statistical studies of surface profiles of Soultz-sous-Forêts granite fractures (Sausse, 2002), suggesting a correlation between surface roughness and fracture alteration. The surface roughness and tortuosity decrease with increasing alteration. Additionally, Sausse (2002) observed with higher alteration a decrease in mean aperture and a more homogeneous local aperture distribution. Note that the presented local surface roughness information will not be implemented in the numerical simulation of fluid flow and solute transport, but serves as additional information to interpret the results.

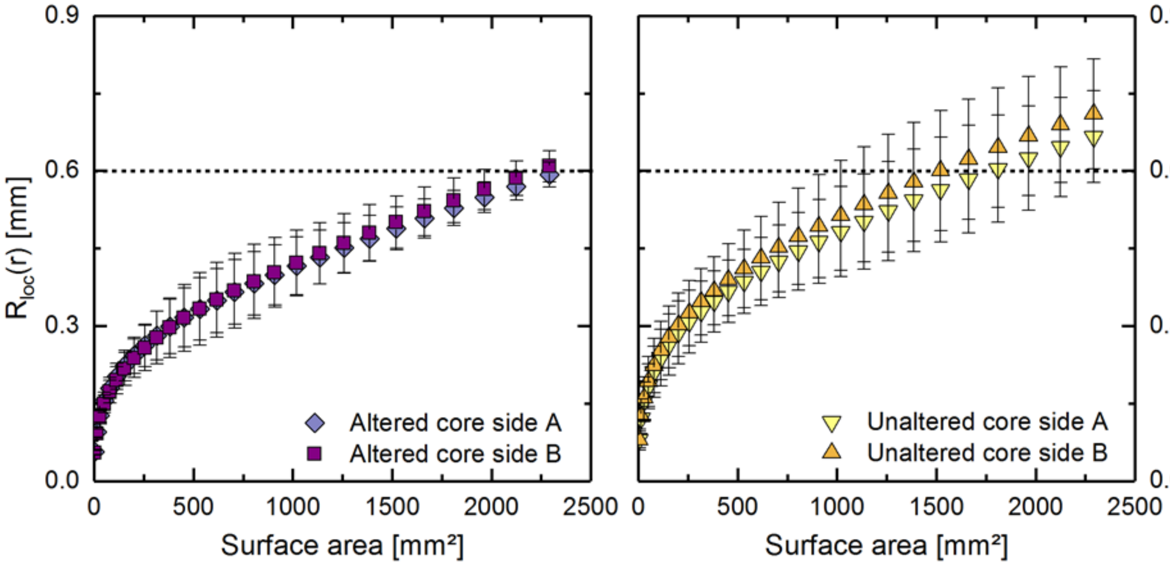

Figure 37: Local fracture surface roughness *$R_{loc}(r)$* of both fracture sides of the altered core (left) and the unaltered core (right) as a function of fracture surface area. Error bars depict the standard deviation of the roughness around the average value. For comparison reasons, the dotted lines depict the maximum local surface roughness of the altered fracture.

5.4.2 Fluid flow modelling

The modelled flow regimes in both fractures with the flow rate of 24 mL/h are depicted in Figure 38 and Figure 39. The displayed color range indicates high flow velocities in red and low flow velocities in blue. The highest flow velocities predominate in the inlet and outlet tubes, which is due to the small cross-section area of the tubing compared to the bigger cross-section area of the fracture. For better visibility of the flow field, the color range is limited to flow velocities between 0 and 1E–3 m/s. The maximum flow rates are depicted on the right side of the upright arrows. Numbers at top and bottom of the images depict the numbering of the inlets and outlets for each fracture. In order to describe the respective inlet and outlet combinations, the numbers of inlet and outlet are separated by a hyphen. Within the text, in order to distinguish the fractures an A for altered or a U for unaltered are placed in front.

When using, for example, the combination inlet 1 and outlet 1 of the altered fracture, this results in the text in A1-1 and in figures mentioning the fracture in 1-1.

The morphologic complexity of both fractures clearly affects the flow fields. The flow field in the altered core is strongly influenced by the fracture geometry (Figure 38), in particular, by the numerous asperity contacts. In case of the middle inlet position, the flow is forced to move to the left side and pass a bottleneck between two asperity contacts, which results in high flow velocities in this area. The same applies to the left inlet. Fluid flow induced through the right inlet, however, is limited at the left side by a large contact area and thus the flow is forced to the right fracture boundary. There are regions in the upper half of the fracture where the flow velocity increases again. This is an indication of flow channeling due to aperture variability. The impact of the applied dipole flow field becomes especially obvious in the inlet-outlet combinations at the long boundaries of the fracture (A1-1 and A3-3). One half of the fracture is dominated by high flow velocities while the flow velocities in the other half of the fracture remain very low. The difference is most striking in case of A3-3. In the cases A3-1, A3-2 and A3-3 the region beneath/in front of the bottleneck is most likely only accessible for the solutes by diffusion. The same applies to the corner areas of the fracture.

In contrast to the altered fracture, the flow in the unaltered fracture spreads more evenly and shows to have less flow velocity variations (Figure 39). Because of the fully open fracture, the dipole flow field can evolve in its more characteristic shape. However, when injecting through inlet 1 (top series) or inlet 3 (bottom series), resulting elevated flow velocities remain within the first third of the fracture from the respective inlet, in the vicinity of the fracture boundaries. In contrast, while injecting through inlet 2, the flow velocities decline more rapidly. A comparable elevated flow velocity area can be observed extracting through outlet 1 or outlet 3. Those observations show that the flow velocity distribution in the evenly appearing fracture is obviously affected by the aperture distribution provoking fluid flow channeling, which is slightly less pronounced compared to the altered fracture (compare colors in color bars).

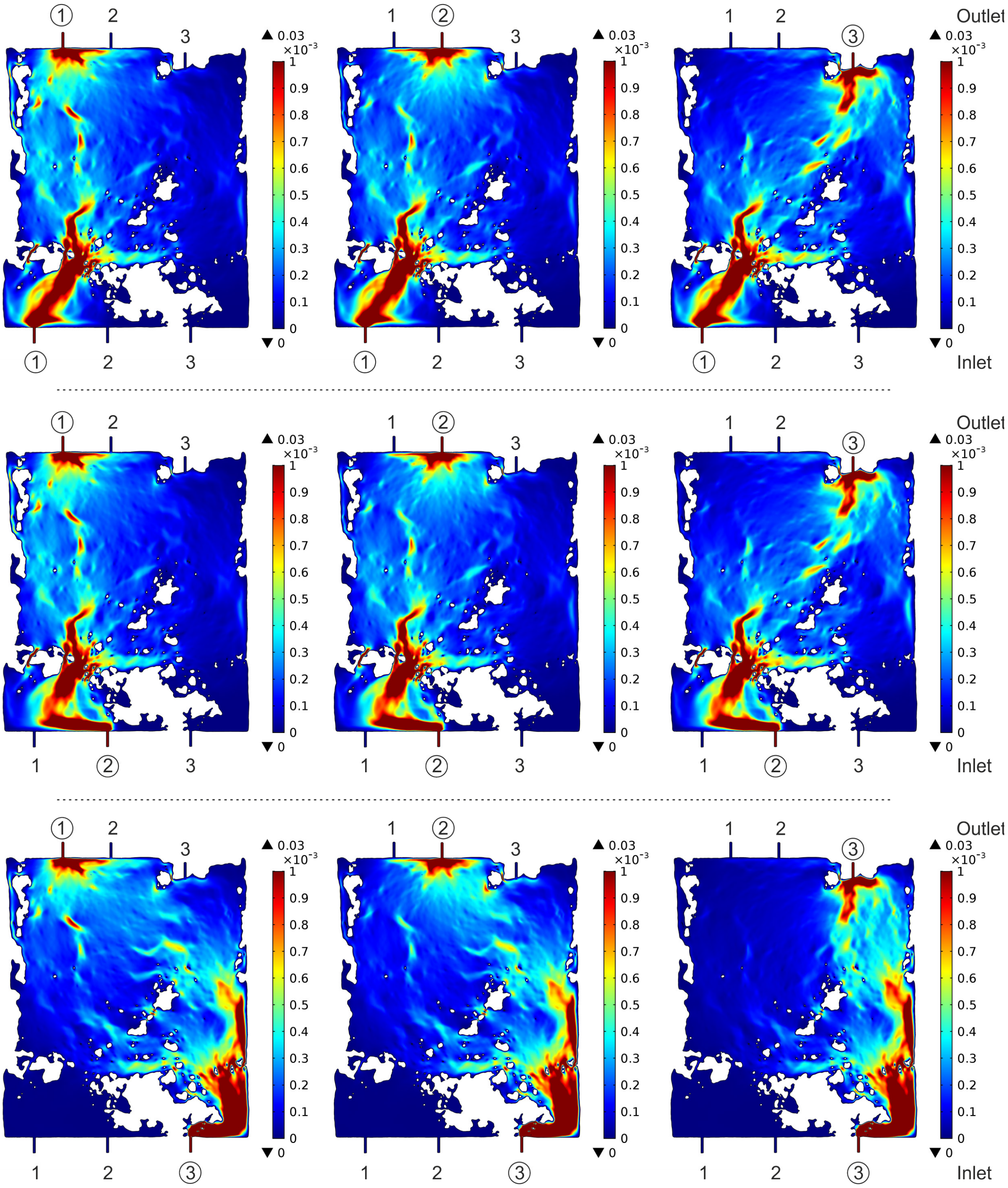

Figure 38: Velocity fields [m/s] of the altered fracture. The numbers at the fracture top and bottom depict the different inlets and outlets. For better visibility of the flow field, the color range is limited to flow velocities between 0 and 1E–3 m/s. The maximum flow rates are depicted on the right side of the upright arrows.

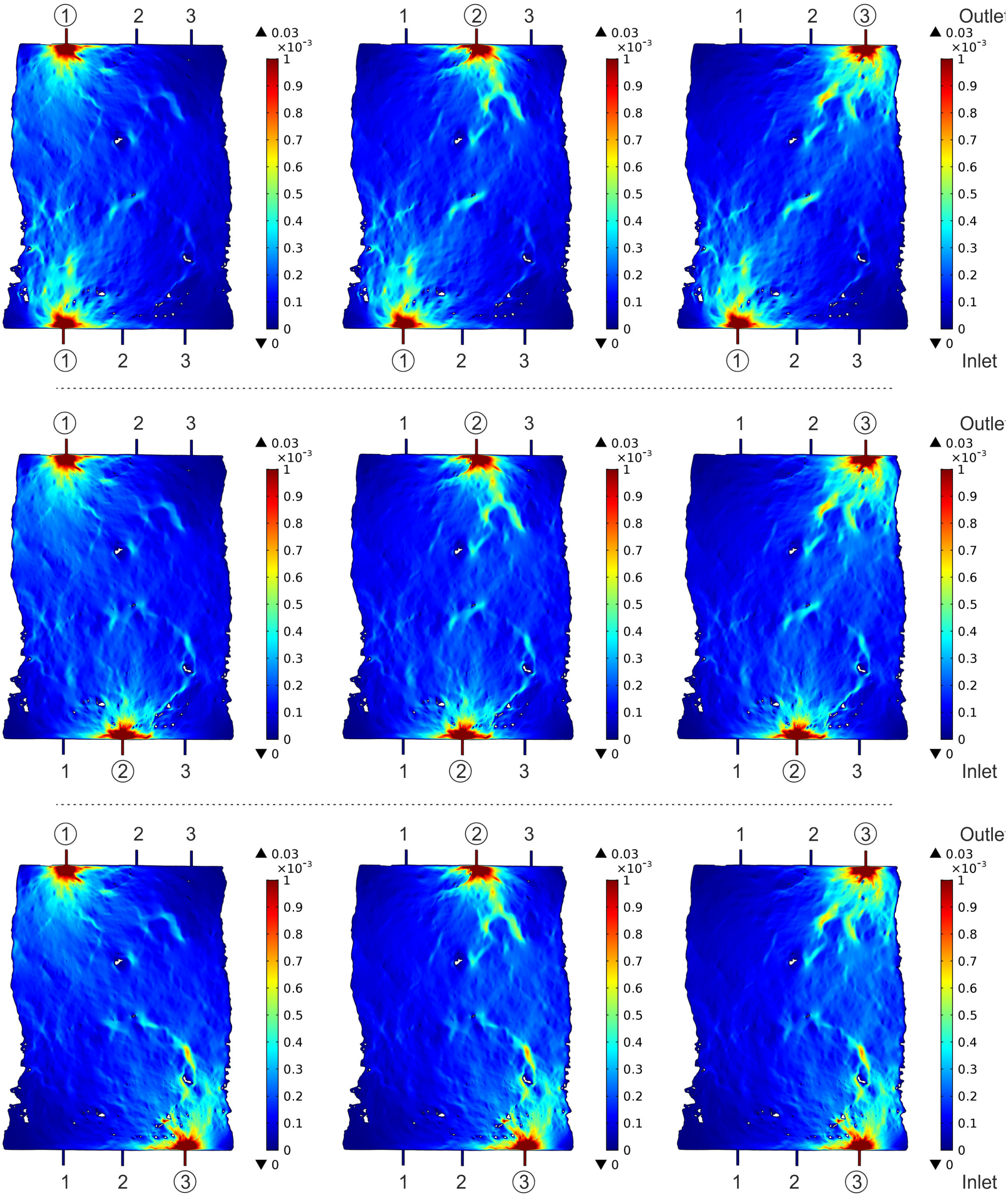

Figure 39: Velocity fields [m/s] of the unaltered fracture. The numbers at the fracture top and bottom depict the different inlets and outlets. For better visibility of the flow field, the color range is limited to flow velocities between 0 and 1E–3 m/s. The maximum flow rates are depicted on the right side of the upright arrows.

Model-derived values over all dipole options are averaged in Table 11. The mean flow velocity values are directly extracted from the model. The mean flow velocity of the altered core is higher compared to the unaltered one, which can be explained by the different mean apertures and the total volumes of both fractures as mentioned above. The Reynolds numbers for those flow rates are in the range of laminar flow and the mean Péclet number shows clearly advection controlled systems. A table of the flow velocities and Reynolds numbers for each case can be found in the supporting information (A.III 5 and A.III 6).

Table 11: Model-derived values.

	Altered fracture		Unaltered fracture	
Flow rate [mL/h]	24 ml/h	12 mL/h	24 ml/h	12 mL/h
Mean flow velocity [m/s]	2.54E–4	1.27E–4	2.30E–4	1.15E–4
Mean Reynolds number [-]	6.20E–3	3.10E–3	5.15E–3	2.58E–3
Mean Péclet number [-]	92.10	46.04	184.01	92.00

5.4.3 Solute transport experiments and modelling

The variation of injection and extraction location with three inlets and outlets for each fracture results in nine separate experimental cases. In this section the transport experiments and the corresponding modelling is shown.

Before investigating the experimental and model results in detail, all experimental results are solely shown in Figure 40 for both flow rates per fracture. In all cases, the tracer is recovered quantitatively (98 ± 2%) within the uncertainties given. The BTCs of the altered fracture are more irregular and broader compared to the BTCs of the unaltered fracture. However, except A1-1, A2-3 and A3-3 the variations between the different BTCs are quite narrow. In contrast, a bigger spreading is visible within the BTCs of the unaltered fracture and the overall maximum C/C_0 is slightly higher (max. $C/C_0 \approx 0.94$).

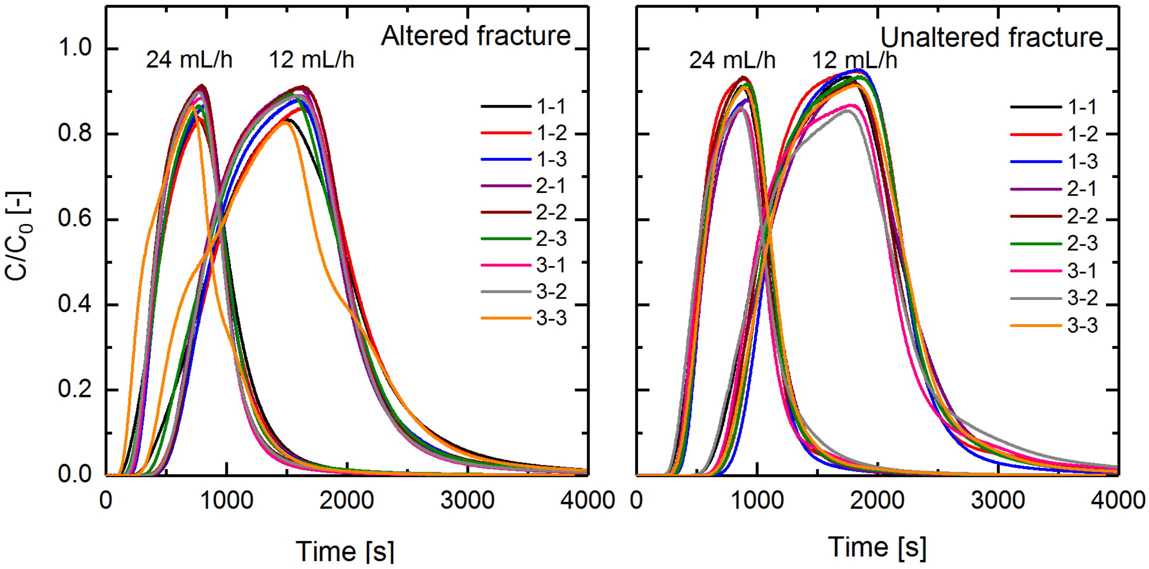

Figure 40: Comparison of experimental results for both flow rates of the altered fracture (left) and the unaltered fracture (right).

In the following sections a comparison of the model and the experimental BTCs is made both (i) visually and (ii) quantitatively:

(i) Figure 41 and Figure 44 display the experimental BTCs in conjunction with the respective simulation for both fractures. The injection and extraction location is depicted in the right upper corner of each diagram. In order to investigate the long-term behavior, a linear scale for the x-axis and a logarithmic scale for the y-axis are chosen. Both the 24 mL/h and the 12 ml/h experiments are displayed per diagram. All BTCs are dead volume corrected.

(ii) Figure 43 and Figure 46 show the quantitative comparison of experimental and model results in respect of three specific moments in time. This is (1) the time of the first arrival of the tracer ($C/C_0 >$ 5E–4), (2) the time of the peak maximum and (3) the time of 50% tracer recovery. The x-axis shows the experimental time and the y-axis the modeled time.

5.4.3.1 Altered fracture

Generally speaking, a good agreement can be seen by comparing the corresponding experimental and model BTCs (Figure 41). In cases of A1-2, A1-3, A2-2 and A2-3 the tailing is well described by the model. However, the modeled BTCs show to be more pronounced for the extraction out of outlet 1 (A1-1; A2-1). The injection through inlet 3 results in the simulations in more irregular shaped tailings and the formation of secondary peaks or shoulders (A3-1 and A3-2: shoulder after 4000 s (24 mL/h) and 8000 s (12 mL/h); A3-3: secondary peak after 2000 s (24 mL/h) and 4000 s (12 mL/h)). Those features are very likely model artifacts from additional flow paths. Inlet 3 is located on the right side of a big contact area in the middle of the fracture (see Figure 35 and Figure 38) and therefore isolated from inlet 1 and 2. There are no obvious differences observed between the obtained BTCs with 12 mL/h and 24 mL/h for one inlet–outlet combination, experimentally and numerically. Therefore, the tracer transport behavior is insensitive to the flow rate within the experimental conditions chosen.

Figure 42 compares the tracer transport through the fracture exemplarily for A1-3 (top series) and A3-3 (bottom series) at 200 s, 900 s and 1200 s after injection. Model A1-3 is well matching with the experimental results while experiment and model of A3-3 show the deviations mentioned above. In general, while injecting a tracer through one inlet and extracting it through one outlet the tracer cloud spreads into the fracture and enlarges by hydrodynamic dispersion. When flushing with background electrolyte the tracer cloud is split into two isolated parts, which are retarded compared to the tracer mass located along the direct flow path between inlet and outlet. This is due to the typical velocity distribution in a dipole flow field. In case of A1-3 after 200 s the tracer flow is concentrated through the bottleneck while small quantities spread into the area in front. After 900 s, part of the tracer mass remains in this small area while the two retarded parts of the separating tracer cloud are located in the main part of the fracture. Those solute masses are flushed out along the right and the left side of the fracture evenly, resulting in a BTC without the formation of shoulders or secondary peaks. The modeled BTCs from inlet 1 and inlet 2 are nearly congruent when extracting through the same outlet. This indicates that the information from the bottleneck superimposes the signal from the different inlets. Such a clear congruency as seen in the modelling cannot be observed by comparing the respective experimental results (see Figure 40).

In case of A3-3 (Figure 42 bottom series) the inlet–outlet combination and the geometry of the fracture cause the highest flow velocities near the right fracture boundary concentrating the tracer cloud in this region. However, a significant amount of tracer is percolated to the middle of the fracture and a minor amount is transported to the area below the bottleneck. These parts of the tracer mass are flushed out considerably slower compared to the major amount of the tracer near the right fracture boundary. Thus, the tracer mass on the right side leaves the fracture domain much faster than the part on the left side. This misbalance results in the formation of the secondary peak. This secondary peak is not visible in the experimental results. A possible explanation is an overestimation of the spreading into the left side of the fracture. In case of A3-1 and A3-2 the formation of the shoulder in the BTC is solely because of tracer quantities reaching the bottleneck area via slow flow paths. The velocities in this region are around one order of magnitude smaller compared to the mean flow velocity. Because of those low flow velocities the impact of molecular diffusion and hydrodynamic dispersion on the tracer transport increases. This leads to a tracer accumulation below the bottleneck of the fracture, which retards the last quantities of the tracer and which results in longer tailings in the BTCs.

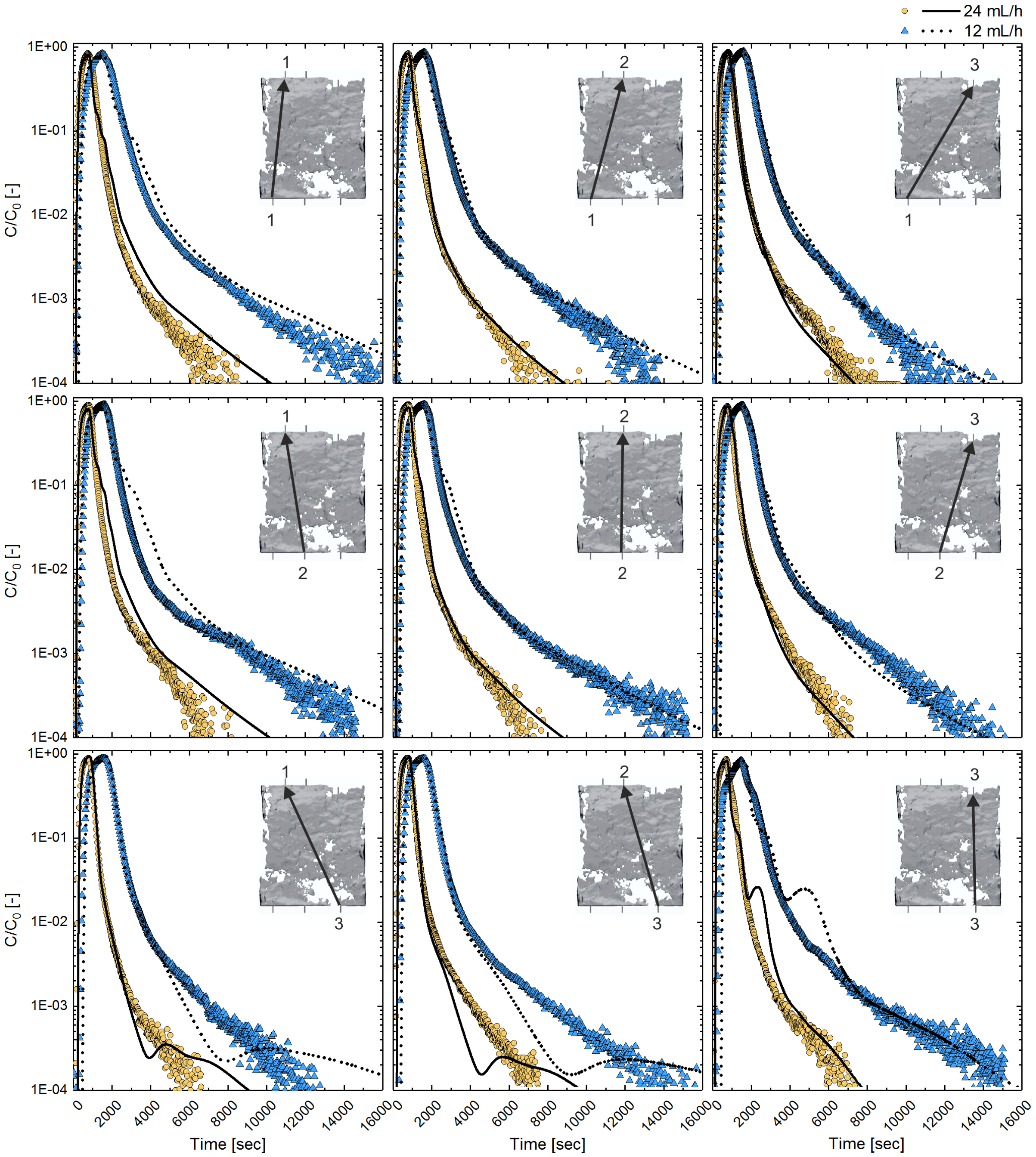

Figure 41: Experimental BTCs (yellow circles and blue triangles) in comparison to the simulated BTCs (solid and dotted lines) in case of the altered fracture. The circles and the solid lines and the triangles and the dotted lines depict cases with an applied flow rate of 24 mL/h and of 12 mL/h, respectively. The image in the right corner of each graph is a visualization of the respective injection–extraction combination.

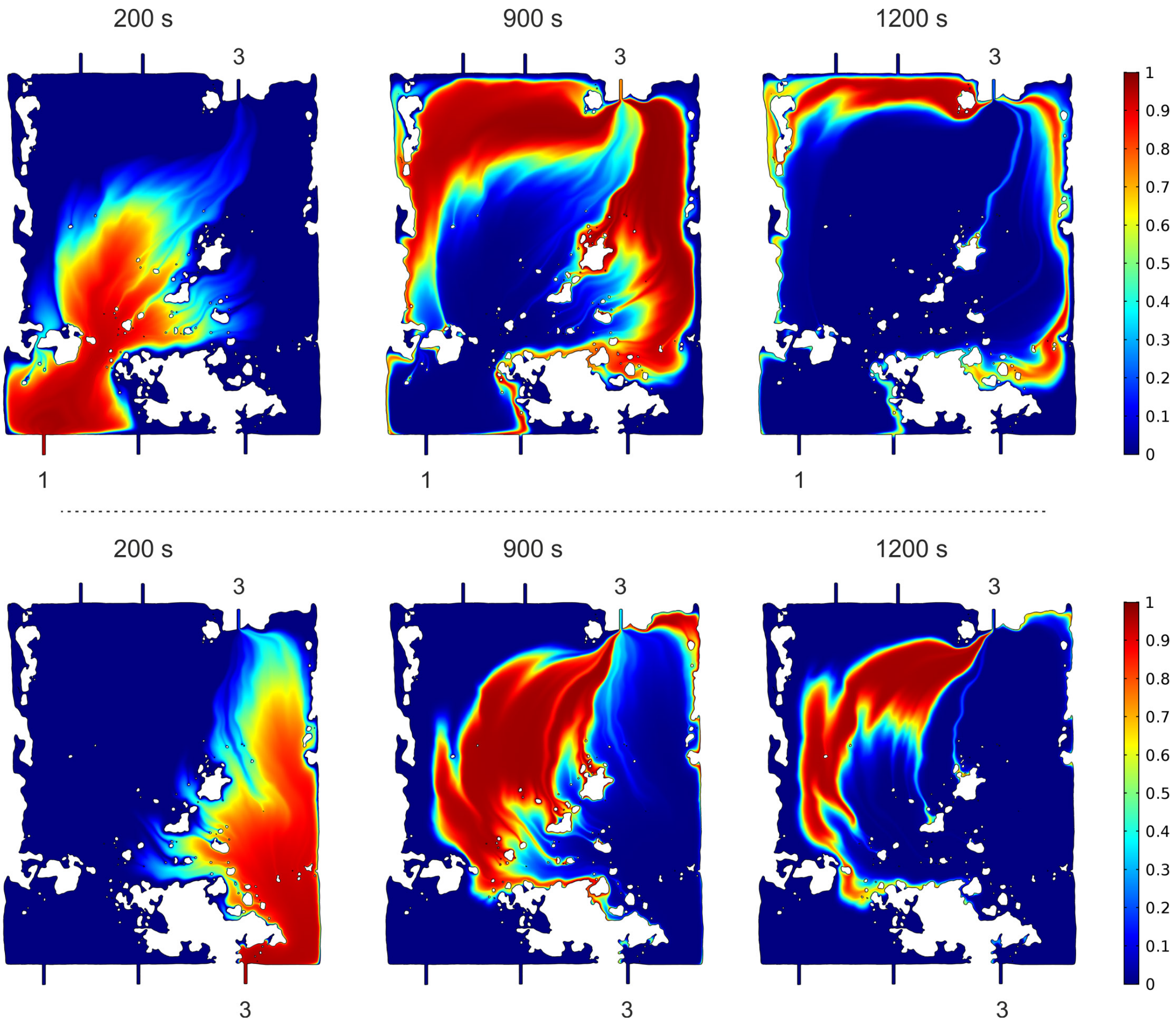

Figure 42: Snapshots of the solute transport through the altered granite fracture with 24 mL/h at 200 s, 900 s and 1200 s. Top series shows combination A1-3 and bottom series shows combination A3-3.

The quality of correlation of the experimental and the modeled BTCs is shown in Figure 43 by means of a comparison of the time of the first arrival, the time of the peak maximum and the time of 50% recovery. The experiments scatter around the line of origin. Markings of experiments lying directly on this line represent the perfect correspondence for the respective moment between experiment and model. Symbols above the line represent an earlier event in the experiment compared to the model and vice versa when the symbol is located below the line. The scattering for the time of the first arrival for both flow rates is comparably high with 20.4 ± 14.4%. Significantly fewer deviations show the comparisons in the peak position with 3.1 ± 2.5% and in the time of 50% tracer recovery with 3.1 ± 2.1%. Analogous to the matching in the tailing the experiment and simulations of inlet 1 and inlet 2 correlate quite well. As expected the experiments and models along the long sides of the fracture (A1-1 and A3-3) show both the earliest first arrival and in case of the experiment A3-3 the earliest peak and 50% recovery. The time of the first arrival for the majority of simulations is later than in the experiments.

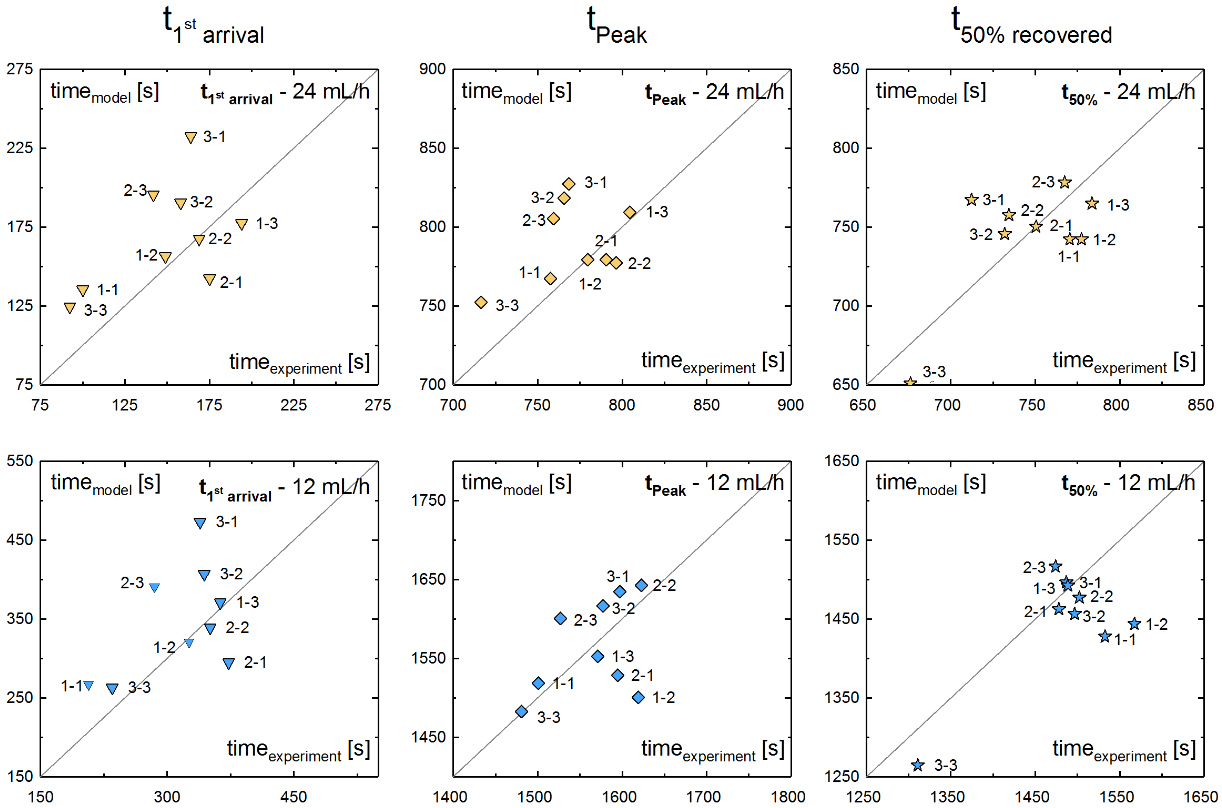

Figure 43: Comparison of experiment and simulation for three specific times (the time of the first arrival ($C/C_0 > 5E{-}4$), the time of the peak maximum and the time of 50% tracer recovery) in the case of the altered fracture. The modeled time (y-axis) is shown against the respective experimental time (x-axis). A line of origin is plotted to guide the eye.

The elution times follow the geometry of the fracture, which means that the shortest way through the fracture leads to faster elution times. This explains the fast elution times for A3-3. Moreover, this dependence on the geometry results in the irregular shape of the experimental BTCs (Figure 40). Their narrow distribution can be explained by fluid flow channeling. This can be seen especially in case of inlet 1 and 2. The presented BTCs (Figure 41), the snapshots of solute transport (Figure 42) and the evaluation of the three defined moments ($t_{1st\ arrival}$, t_{Peak}, $t_{50\%\ \mathrm{recovered}}$) (Figure 43) lead to the conclusion that the flow through the altered fracture is well reproduced by the model and is clearly controlled by the complex fracture geometry.

5.4.3.2 Unaltered fracture

In contrast to the altered fracture, there is minor congruency between the experimental and the modeled BTCs of the unaltered fracture (Figure 44). The model overestimates the tailing and the first arrival is shifted to longer residence times for the majority of the modeled combinations. Furthermore, the shape of the tailing is less well described. In addition, both cases (U1-1 and U3-3) along the boundaries of the fracture show either a secondary peak or a highly irregular evolution in the tailing region. Those features in the modeled BTCs are indications that the fracture is less well described as it was the case for the altered fracture. In contrast to the modelling results, a major amount of the experimental BTCs shows a less pronounced tailing between $C/C_0 =$ 1E-1 to 1E–3. Comparable to the altered fracture experiments, there are no obvious differences between the obtained BTCs with 12 mL/h and 24 mL/h.

Figure 45 shows in the top series U3-1, an example, which shows a good agreement between experiment and model, and in the bottom series U1-1, which shows significant deviations. For both cases and in contrast to the altered fracture experiments, the spreading of the tracer after injection is significantly less forced by the fracture geometry. Like in A1-3, after 900 s the two separated tracer parts in the fracture are flushed out evenly without the formation of a secondary peak or shoulder. However, example U1-1, which is located at the boundary of the fracture shows the same behavior as A3-3. Due to the fast direct flow path, one of the isolated tracer clouds is eluted faster compared to the tracer mass, which is located in the opposite part of the fracture. This mass is influenced only by smaller flow velocities, which results in a higher retardation and the formation of a secondary peak in the BTC. Therefore, we can conclude that the simulation of the experiments along the fracture boundaries (A3-3; U1-1 and U3-3) underlay the same effect during flushing of the fracture leading to the observed deviations. However, A1-1 is not affected by this boundary effect because of the direct fluid flow forcing through the bottleneck.

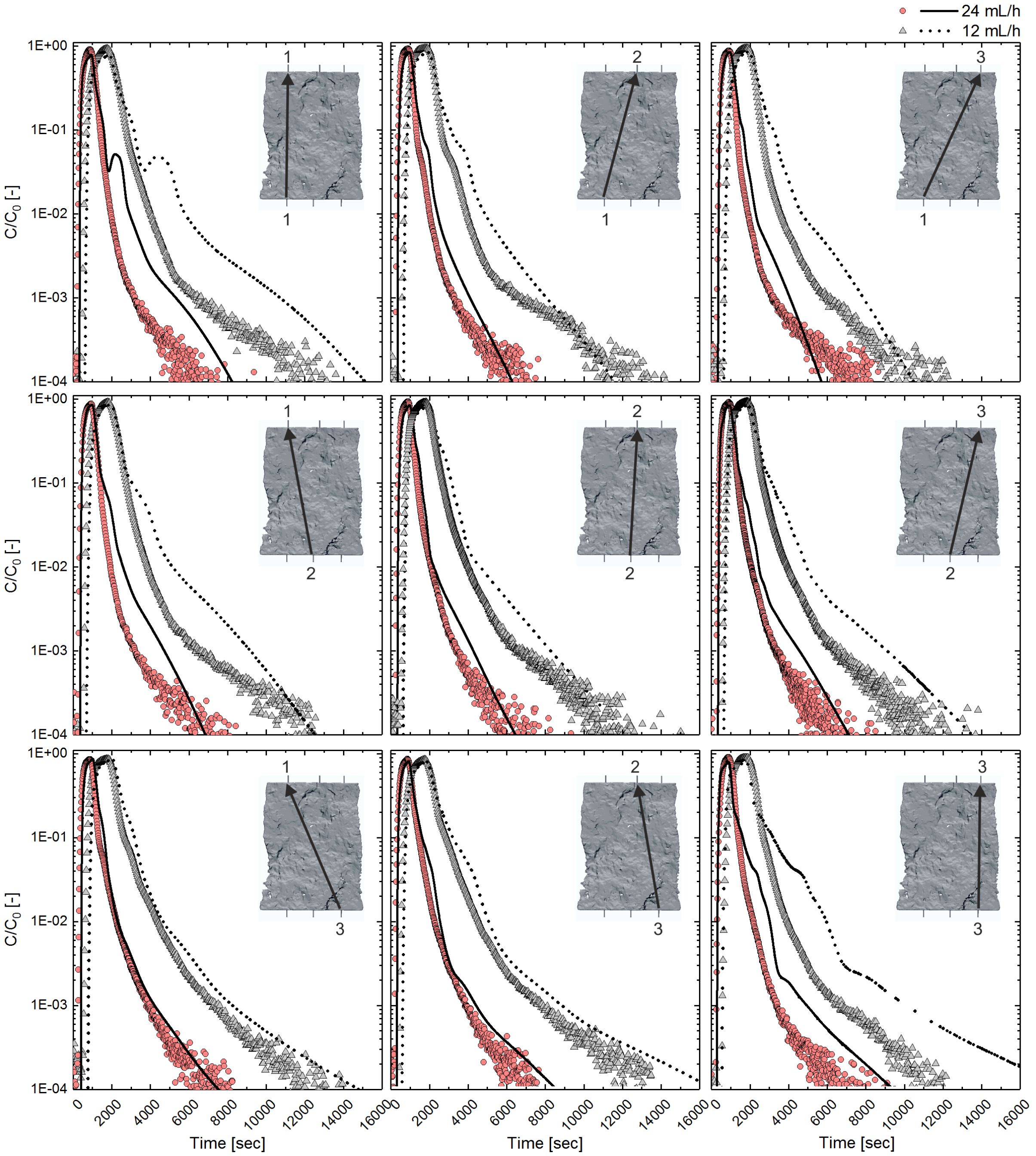

Figure 44: Experimental BTCs (red circles and grey triangles) in comparison to the simulated BTCs (solid and dotted lines) in case of the unaltered fracture. The circles and the solid lines and the triangles and the dotted lines depict cases with an applied flow rate of 24 mL/h and of 12 mL/h, respectively. The image in the right corner of each graph indicates the respective injection–extraction combination.

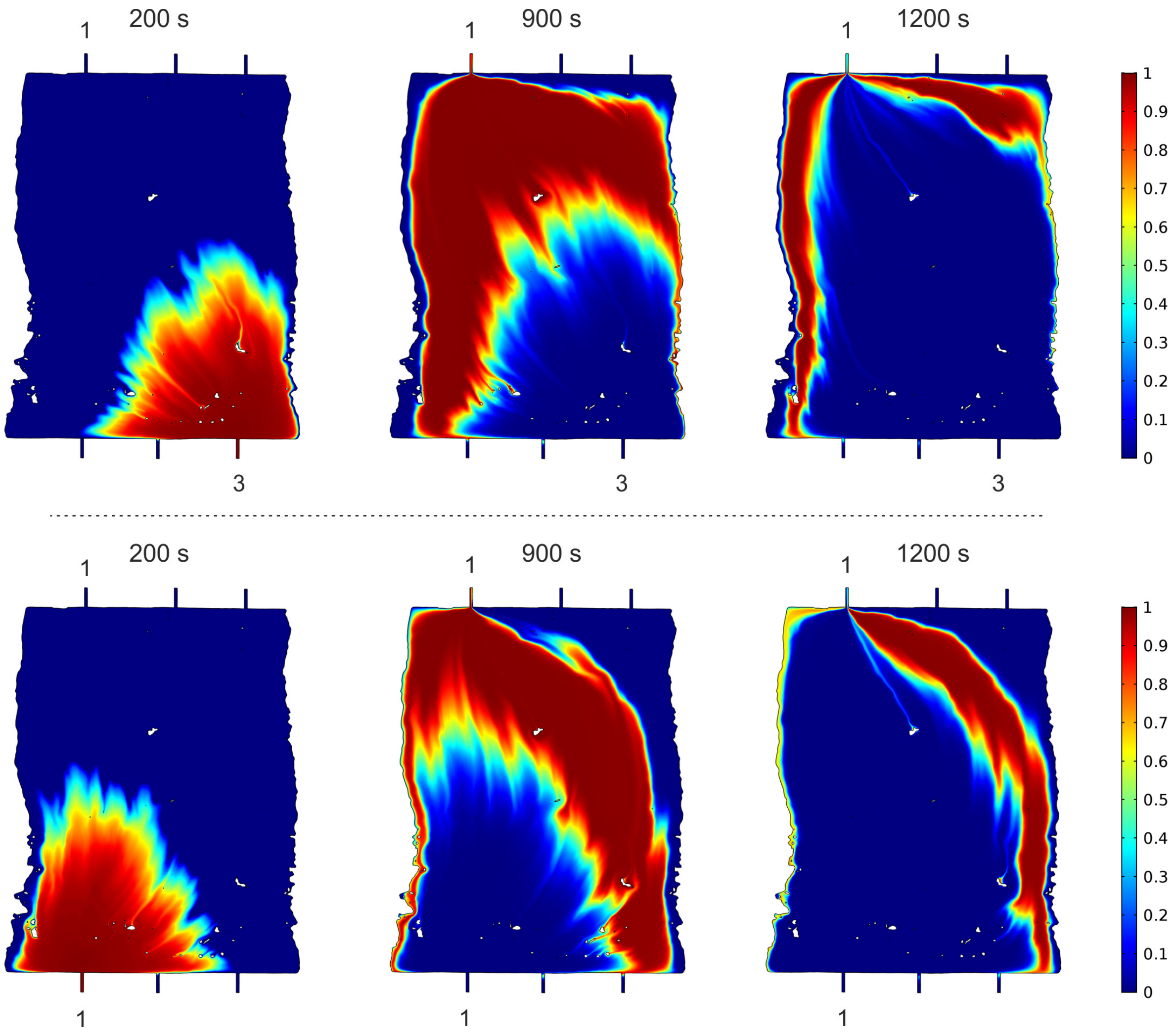

Figure 45: Time captures of solute transport through unaltered granite fracture with 24 mL/h at 200 s, 900 s and 1200 s. Top series shows combination U3-1 and bottom series shows combination U1-1.

The contrasting juxtaposition of simulation and experiment (Figure 46) confirms the observations made in Figure 44. In contrast to the altered fracture the major amount of the data points are located above the line of origin, which means that the experiments reach the specific moments earlier compared to the simulation. This relativizes the more pronounced tailing due to the positive time offset (shift to longer elution times) over the total BTC in all cases. This results in a deviation of 25.0 ± 14.6% for the time of the first arrival, 5.7 ± 3.7% for the time of the peak position and 5.8 ± 3.1% for the time when 50% of the tracer is recovered.

Despite the well-described tailing region (Figure 44) the largest deviation compared to the experimental result shows case U3-1. The simulation represents a significant positive time shift. However, in contempt of the position of the inlet and outlet, the experimental result shows comparable small specific moments. It might be that the model overestimates the impact of the flow distance through the fracture. The fact that all simulations tend to longer residence times in the fracture leads to the conclusion that either the fracture geometry or the fracture aperture distribution or both are not entirely captured by the model.

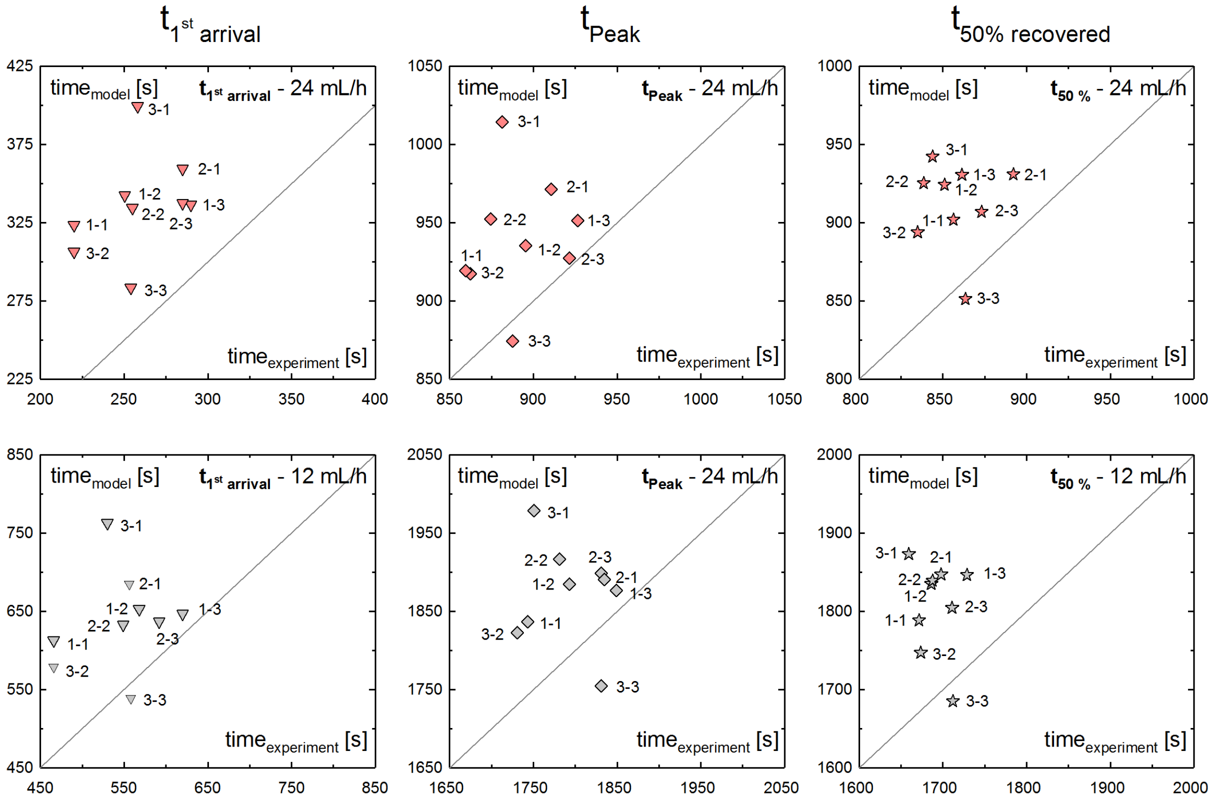

Figure 46: Comparison of experiment and simulation for three specific times (the time of the first arrival ($C/C_0 > 5E{-}4$), the time of the peak maximum and the time of 50% tracer recovery) in the case of the unaltered fracture. The modeled time (y-axis) is shown against the respective experimental time (x-axis). A line of origin is plotted to guide the eye.

By comparing the experimental results with each other (see Figure 40) and in contrast to the altered fracture experiments, there is less variation in the shape and the tailing of the BTCs. But the variation between the BTCs shows a bigger spreading. Both observations might be attributed to the more homogenous fracture, the small amount of contact zones and the bigger aperture. However, the experiments do not follow the excepted percolation time based on the position of the inlets and outlets, which is not captured in the modelling (see for example case U3-1 in Figure 44). This deviation might be caused by the missing tortuosity in the 2.5-D model approach and the distinct rough and irregular fracture surfaces (see Figure 37). Depending on inlet–outlet combination the slightly higher roughness might have an influence on the solute transport, which cannot be simulated by applying this model. In case of the altered fracture, the impact of roughness might be less visible or overlaid by the contribution of the complex fracture geometry.

5.4.4 Impact of aperture distribution and geometry

Additionally to the presented 2.5-D model results, the modelling is extended by performing simulations with decreasing model complexity based on the mean fracture aperture. The purpose of those simulations is (i) to obtain a reference breakthrough curve without the impact of geometry and aperture distribution based on a simple parallel-plate model and (ii) to investigate the impact of the fracture aperture distribution, the fracture geometry and the asperity contacts. Therefore, three approaches have been made: (1) real 2-D fracture geometry with asperity contacts, (2) real 2-D fracture geometry without asperity contacts and (3) a simple parallel-plate model with no asperity contacts and rectangular fracture geometry. Those simulations are done for two cases per fracture. For each fracture a simulation, which shows good agreement with the respective experimental tailing and a simulation that shows distinct deviations (e.g. a secondary peak or pronounced shoulder) are chosen. In case of the altered fracture A1-3 and A3-3 are selected, and in case of the unaltered core U1-1 and U3-1 are chosen. The 2.5-D simulations with 24 mL/h are used for this comparison. Each change and each decrease in complexity from the initial model alters the fracture volume or the geometry. In order to consider this impact, the applied flow velocity is adjusted in order to obtain the same mean fluid flow velocity in the models (maximum deviation of the resulting mean flow velocity is 5E-7 m/s). The biggest adjustment in the applied velocity at the inlet needs to be done for the rectangular parallel-plate model for the altered fracture (from 1.5E-2 m/s to 2.2E-2 m/s). Figure 47 shows the direct comparison of the four model approaches with the experimental curves. In all examined cases the decrease in complexity of the models results in less pronounced tailings. Furthermore, the first arrival of the tracer is affected by means of a shift to longer elution times eventuating in an increasing offset.

Based on the deviation between each model approach the isolated effect of the simplification can be investigated. In case of the well matching simulations (A1-3 and U3-1), by reducing the aperture distribution to the mean aperture a significant deviation in the tailing at $C/C_0 = 1\text{E-}2$ can be observed. The tailing is less pronounced and smoother compared to the initial model (black line). For the less matching two cases (A3-3 and U3-1) this deviation appears already at $C/C_0 = 1\text{E-}1$ accompanied by a distinct reduction of the secondary peak. Thus, the secondary peaks for both fractures are derived by the implemented aperture distribution and are not attributed to the model geometry. However, for A3-3 a new shoulder forms after 4000 s, which resembles the shoulder after 4000 s in A3-1 and A3-2 (Figure 41).

In case of the altered core, this shoulder is clearly an artifact derived by the model geometry, more exactly by the bottleneck feature already described.

In case of the unaltered core, the high impact of aperture distribution on the modelling can be seen when comparing the BTC of the initial model approach with the BTC when the mean aperture is applied (solid black marking and alternating dotted and dashed blue marking). Thus, a better matching result is not achieved by reduction to the mean aperture. Due to the low number of asperity contacts in the unaltered core a minor deviation can be seen with a further reduction of the model since both curves are nearly congruent (blue and dashed green marking). This deviation is higher in case of the altered core, due to the high number of asperity contacts. Furthermore, the deviation towards the next simplification, the reduction to a rectangular parallel-plate, is again more pronounced in the altered fracture simulations. Those observations lead to the conclusion that the flow through the altered core is governed by the fracture geometry and to a minor extent by the aperture distribution. However, the flow through the unaltered core clearly shows to be more influenced by its aperture distribution since the mean aperture is more than two times bigger and the fracture geometry is quite homogeneous lacking any major asperity contacts.

Therefore, this comparison proves that a simplification would not result in an improvement. Moreover, with each reduction, there are (i) adjustments in the applied flow velocity, (ii) less pronounced tailings and (iii) time shifts in the first arrival to longer elution times. Despite some observed deviations, especially in case of the unaltered fracture, the utilization of the aperture distribution, resulting in the 2.5-D model approach presented shows the best matching results. The parallel-plate approach cannot reproduce the observed tailings as well as the 2.5-D approach. However, alongside with the 2.5-D approach, the next best result is archived by reducing the aperture distribution to the mean aperture while keeping the asperity contacts and the fracture geometry in the x-y plane.

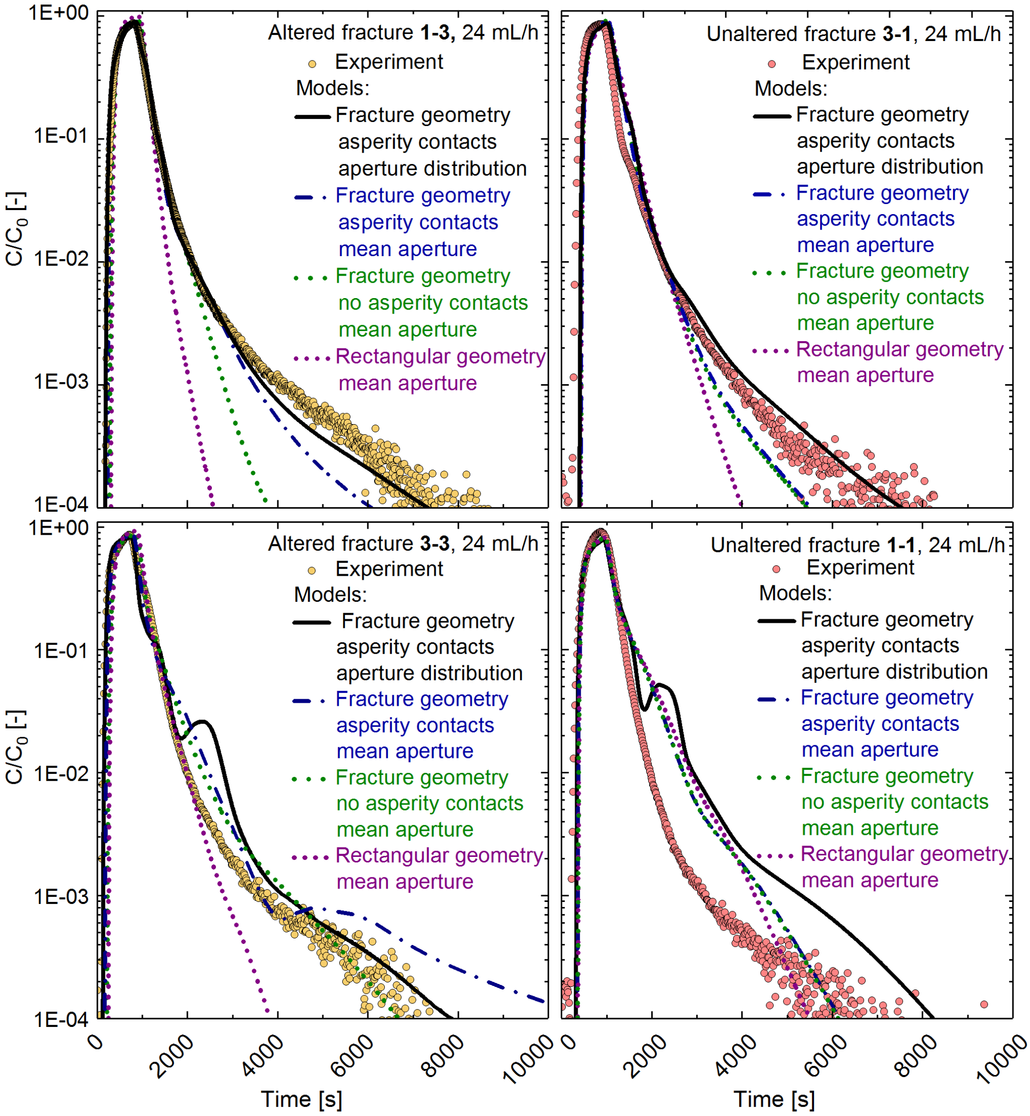

Figure 47: Comparison of the different model approaches with the respective experimental BTCs. The simulations containing both fracture geometry and the aperture distribution is shown in black (solid line), the simulations with the fracture geometry and the mean aperture in blue (alternating dotted and dashed line), the simulations with the mean aperture and fracture geometry without asperity contacts in green (dashed line) and the simulations simplified to an rectangular shape with the mean aperture in purple (dotted line), respectively.

5.4.5 Uncertainties in the µ-CT analysis and limitations of the model

In order to make estimations about the goodness of the modelling, the uncertainties of the µ-CT measurements need to be taken into account. Since the resolution of the µ-CT measurements is limited to 60 µm, regions with smaller apertures are directly interpreted as closed, resulting in asperity contacts in the model. Especially, for the altered core with the small mean aperture, a correct interpretation is crucial because its flow paths are directly linked to the fracture geometry. Furthermore, the segmentation of the fractures is error-prone, especially when the fractures are sealed with glue. Due to the material contrasts, this glue might be interpreted as void space in contrast to the solid fracture sides, which can result in an overall wider fracture in the x-y plane.

Besides the uncertainties in the μ-CT data evaluation, there are also limitations of the 2.5-D model approach. The aperture distribution is projected onto the 2-D geometry, which gives the flow different vicious drag forces/frictional resistances while passing the fracture, but it cannot represent the real fracture morphology and tortuosity. Thus, this model cannot fully substitute a 3-D model, especially in case of the unaltered fracture.

5.5 Summary and conclusions

In this work, the impact of flow channel geometry on solute transport was investigated on two differently altered, fractured, granitic drill cores. By scanning the drill cores using μ-CT the internal structures of the fractures are accessible, showing the altered fracture to be more complex in geometry with a smaller mean aperture compared to the unaltered one. In contrast, the unaltered fracture shows to have a geometry with a minor number of asperity contacts and a larger mean aperture. The obtained μ-CT data served as input for 2.5-D models of both fractures. The surface roughness quantification was done using a 3-D surface scanning technique. In contrast to the altered fracture, the local surface roughness of the unaltered fracture is slightly higher and the roughness distribution along the fracture shows to be non-uniform. This for sure was expected due to the geological history of both cores. The altered fracture might be percolated considerably longer compared to the unaltered one. The formation of secondary minerals and the fluid flow smooth the fracture surfaces, which result in the smaller roughness variation. Those observations are in good agreement with the findings of Sausse (2002).

With the help of three injection and three extraction spots for each core, different dipole flow fields were induced. The solute transport through both fractures can be qualitatively and partly quantitatively predicted based on the 2.5-D modelling approach. Compared to full 3-D models, the utilized model approach needs considerably less computational time, which offered the opportunity to simulate all the different experimental cases. However, the representation of the z-direction is still lacking, e.g. the tortuosity in z-direction cannot be represented in this model approach.

Already by comparing the experimental data from the altered and the unaltered fracture, the BTCs of the transport experiments through the altered fracture are less homogenous compared to the ones through the unaltered fracture, which confirms the tomographic imaging. In case of the altered fracture, there is good agreement between modeled and experimental BTCs. We conclude that fluid flow through this fracture is overall dominated by the complex fracture geometry and the high number of contact points. This has been proven by differently complex model approaches.

The BTCs for the different experimental cases through the unaltered fracture show less deviation but a wider spreading between each other. The large aperture might decrease the impact of fracture wall interaction and the fully open fracture might be the reason for the higher conformity in the BTCs. However, there is a minor congruency between the experimental and modeled BTCs. The modeled BTCs show to be more irregular compared to the experimental ones with an overestimation in the tailing region. The reason for this deviation is unclear based on the given information and results (e.g. higher fracture roughness and no tortuosity in the model approach). We conclude that the fluid flow in this fracture is majorly influenced by the aperture distribution rather than the fracture geometry.

It has to be stated that there are uncertainties and limitations due to the simplification of the models. The large dimensions of the drill cores decrease the resolution of the μ-CT measurement, which might result in a less accurate dataset. The use of such an inaccurate dataset in the model pre-processing and development eventually influence the numerical results. Therefore, a dataset with a sufficiently high resolution to fully capture the fracture geometry and aperture distribution needs to be achieved as far as possible. Besides the reasons mentioned above, the deviations in the modelling of the unaltered fracture solute transport experiments may be caused by an alteration along with the pre-processing. In contrast, the geometry of the altered fracture dominates the fluid flow and a possible alteration by the pre-processing may have a minor impact.

By simplifying the models we can qualitatively show that the congruency of the modeled solute transport with the experimental data decreases. The decrease in complexity results in a less pronounced and more even formed tailing of the derived BTCs without the occurrence of double peaks. An improvement in case of already well described BTCs was not observed. But it is obvious that the formation of the double peaks in the model BTCs is affiliated to the implemented aperture distribution.

We conclude that the fluid flow and the mass transport in both fractures are significantly deviating. The fracture geometry and the aperture distribution are needed to describe precisely fluid flow and mass transport to understand mechanisms prevailing in natural rough fractures. Which feature (asperity contacts or aperture distribution) dominates surely depends on the investigated fracture. The results presented provide important implications with respect to e.g. reactive transport modeling (RTM). Due to the complexity of RTM simulations, they are often conducted in 1-D or very simple 2-D geometries, thus, focusing on the description of the (geo-)chemical aspects and processes. In consequence, the domain geometry and thus, in turn, the fluid flow is dramatically reduced and its effect on solute transport drastically underestimated. As shown in this work, solute transport in real fractures can lead to complex transport behavior reflected in e.g. pronounced long-term residence behavior. A 1-D simulation of such experiments would fail in even reproducing the conservative transport BTC. Moreover, when applying reactive solutes possible processes, like sorption or reduction, which are often kinetically controlled, even enhance the transport behavior complexity, increasing e.g. the BTC tailing furthermore. The application of a 1-D RTM simulation in such systems would therefore describe the BTC tailing, caused by hydrodynamic dispersion, by the application of erroneous chemical (equilibrium or kinetically controlled) parameters, like e.g. K_d values, sorption or reduction rates. Thus, the correct description of the flow field in RTM simulations is of paramount importance to correctly calibrate the geochemical conceptual model and to derive reliable and valid chemical input parameters, suitable for general use.

Moreover, we showed the major advantage in knowing the internal structure and the spatial heterogeneities of single fractures in order to interpret and understand solute transport in natural rock fractures. We also show the importance of tomographic images for the generation of 3-D and 2-D numeric models. Despite the simplification from a fully 3-D to a 2.5-D model, the presented results provide a step forward in understanding and interpreting solute transport through natural single fractures.

5.6 Acknowledgment

MS and ES thank the HGF portfolio project “Geoenergy” under the Helmholtz topic “Geothermal Energy Systems” and FMH and TS the Helmholtz Program NUSAFE for support. The work has received partial funding by the Federal Ministry of Economics and Technology (BMWi) under the joint KIT-INE, GRS research projects “KOLLORADO-e” (02E11203B) and “KOLLORADO-e^2” (02E11456A), and the European 7th Framework

Program (FP7/2007-2011) under grant agreement no. 295487 (BELBaR Project).We want to thank GEIE Groupement européen d'intérêt économique), especially Julia Scheiber and Albert Genter for providing the granite fracture material. The data used are listed in the references, tables, and supplements.

6 Colloid transport experiments of nanoparticulate illite through natural granite fractures investigated by Laser-Induced Breakdown Detection (LIBD)

M. STOLL[1*], F. M. HUBER[1], J. LÜTZENKIRCHEN[1], E. SCHILL[1], T. SCHÄFER[1]

6.1 Introduction

Completing the experimental investigations on flow and transport in natural fractures, the transport of nanoparticulate Na-illite in the ultra-trace concentration range in the same two granite fractures at different alteration stage is presented. Section 4 served as the primary stage for this work, introducing Laser-Induced Breakdown Detection (LIBD) as monitoring technique for obtaining colloid breakthrough curves (BTC). The results of the conservative solute transport experiments (Section 5) serve as comparison for understanding colloid transport through both rock fractures. The retardation factor R_f [-] is a way to compare the colloid transport velocity with the water flow velocity (conservative solute tracer). In order to quantify retardation in the system the retardation factor is defined here as:

$$R_f = \frac{R_{0.5\,[colloid]}}{R_{0.5\,[solute]}}$$ **Equation 39**

where $R_{0.5\,[colloid]}$ [s] and $R_{0.5\,[solute]}$ [s] are the elution times when the normalized concentration of the BTC reaches the first time $C/C_0 = 0.5$ of the colloid and the solute, respectively (Knapp et al., 2000). $C/C_0 = 0.5$ was chosen because of the different thresholds of detection of the first arrival of the colloid and the tracer (fluorescence spectroscopy $C/C_0 = 1E{-}4$; LIBD $C/C_0 = 5E{-}3$). Moreover, comparing the elution times at this normalized concentration, instead at e.g. the first arrival time, sensitivity issues between the different detection methods are minimized and representative retardation factors are obtained.

In case of colloid transport the term retardation is often misleading. Both in porous (e.g. Bales et al., 1989) and fractured media (e.g. McKay et al., 2000; Reimus, 1995), it was demonstrated that colloids show in average faster percolation times compared to water molecules and molecular-scaled conservative tracers (see Section 1.2.4.1). Therefore, Sirivithayapakorn and Keller (2003), who investigate colloid transport through porous media, supposed to use the term "acceleration factor" instead, since colloid exclusion effects would dominate.

After Reimus (1995) the velocity of the streamline in the center of a pure parallel-plate channel is around 1.5 times faster compared to the average flow velocity. Therefore, colloids, which are majorly transported in the center of a fracture, will be earlier eluted at the fracture outlet compared to a molecular-scaled solute tracer. Moreover, rapid colloid transport through fractured media is often reported in literature and well established with retardation factors < 1 (Bales et al., 1989; Champ and Schroeter, 1988; Knapp et al., 2000; McKay et al., 1993a; Toran and Palumbo, 1992). As already mentioned, this effect is referred to charge exclusion, size exclusion and Taylor dispersion (Becker et al., 1999; Zvikelsky and Weisbrod, 2006).

Note that the low colloid concentrations used in the LIBD experiments minimize the probability of flocculation (Elimelech, 1995), since flocculation would affect the deposition rate. Moreover, due to the low colloid concentration required for LIBD, it can be assumed that there is no full colloid coverage on the fracture surfaces at any time. This assumption is supported by the approximated maximum area occupied by the injected colloids in one experiment: ≈ 0.02% of the total area of the fracture surface would be occupied, if the colloids in one experiment would be retained by 100%.

6.2 Material and methods

6.2.1 Granite fracture flow cells

The fracture flow cell setup and the preparation needed before starting the experiments are elucidated in Section 5. The unaltered fracture shows to have less buffer capacity compared to the altered fracture. The equilibration with the background electrolyte (pH 5.6 ± 0.1) results in a pH at the outlet of the unaltered fracture of 5.9 ± 0.1, while the resulting pH at the outlet of the altered fracture was 6.5 ± 0.1. This observation is attributed to the higher amount of secondary phases (e.g. clay minerals) on the fracture surface of the altered drill core. The higher number of substitution sites might strip the protons from the background electrolyte and, thus, the pH increases. Therefore, a complete equilibration was not reached for the altered fracture. Streaming potential measurements have been carried out to determine the surface charge of the fracture walls under the geochemical conditions prevailing in the experiments for both granites. A SurPass Apparatus (Anton Paar, dimensions streaming channel: 10.0 × 20.0 × 0.5 mm) (Lützenkirchen and Richter, 2013) is utilized for this purpose. For both the background electrolytes and equivalent ionic strength NaCl solutions the determined zeta potential remains negative for the observed pH range between pH 4 to pH 10. In the pH range 5.0–6.4 the zeta potential of the altered granite with the respective background electrolyte ranges between –49.7 mV and –50.1 mV. In the pH range 4.9–6.9 the zeta potential of the unaltered granite with the respective background electrolyte ranges between –55.2 mV and –57.9 mV. The full dataset of the streaming potential measurements is shown in the appendix (see A.IV 5). Despite the overall negative charge, charge heterogeneities on the fracture surfaces, impacting colloid interaction, cannot be excluded.

6.2.2 Na-illite

The Na-illite colloids used in this study are described in Section 4. For this study two stable illite colloid suspensions are prepared each by centrifugation of a 10 g/L suspension of Na-illite and the fracture respective background electrolyte (see Table 9, Section 5). In order to generate the colloid suspensions, three centrifugation cycles are needed: cycle 1 and 2 at 4000 rpm for 1 h and cycle 3 at 4000 rpm for 30 min. The supernatant accrued after cycle 1 and 2 is taken off carefully and is replaced by fresh background electrolyte. Finally, the supernatant formed after cycle 3 is used in the transport experiments. The colloid stability is measured by photon correlation spectroscopy (PCS) by using a colloid concentration of 6 ppm. The colloid diameter remains constant for > 24 h. Thus, it can be concluded that no coagulation occurs and the colloid suspension is considered stable throughout the transport experiments, especially, after the dilution step from the PSC to the LIBD colloid concentration (dilution factor 187.5).

The relevant colloid properties are determined according to Section 4.3.3 and are summarized in Table 12. Whereas the PCS determined mean colloid size in the unaltered granite suspension is smaller compared to the colloid size in the altered one, the mean colloid size is nearly similar when determined by optical LIBD.

Table 12: Physical properties of the Na-illite colloids used in the colloid transport experiments for the altered and the unaltered fracture.

Suspension	Mean Colloid size [nm]	Zeta potential [mV]	Colloid concentration LIBD [ppb]	Colloid concentration PCS [ppm]
Altered granite	238.3 ± 6.6 (PCS) 184.6 ± 5.5 (LIBD)	–34 ± 3	32 ± 1	6 ± 0.2
Unaltered granite	161.3 ± 5.3 (PCS) 182.5 ± 3.2 (LIBD)	–44 ± 6	32 ± 1	6 ± 0.2

6.2.3 Experimental procedure

The modified experimental setup with exchange of the fluorescence spectrometer by LIBD is shown in Figure 48a. The fracture flow cells were continuously flushed. In the inter-experimental periods a flow rate of 2 mL/h was applied. Before starting each experiment, the flow rate was increased to the flow rate used in the experiment (either 24 mL/h or 12 mL/h) and the fracture was flushed for at least 2 h. The laser pulse energy is set to 660 µJ throughout the whole experiment corresponding to a breakdown probability (BDP) of C_0 of 80 ± 2%. C_0 is measured before and after every experiment. In order to compensate slight fluctuations in the output signal, the mean BDP value of those measurements was taken as C_0. At the selected laser pulse energy, the background BDP is < 10%. In order to compare the colloid transport experiments directly with the solute transport experiments in Section 5, the same volume of colloid suspension of 4 mL has been injected. Further details on experimental procedure are according to Section 4. The dead volume in all experiments, as mentioned in Section 5, is 610 ± 40 µl. For each fracture there are nine inlet–outlet combinations (see Section 5). The colloid transport experiments are limited to five cases each, representing the geometrically shortest ways (1-1, 2-2 and 3-3), and the geometrically longest ways through the fracture (1-3 and 3-1) (Figure 48b). The injection is always from the bottom.

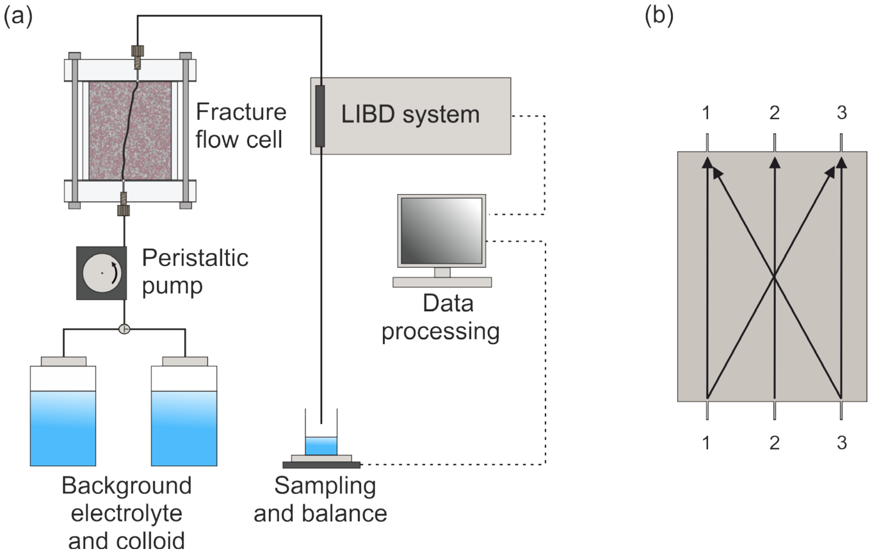

Figure 48: (a) Experimental setup with the laser-induced breakdown detection (LIBD) as monitoring method. (b) Experimental cases chosen in colloid transport experiments.

6.3 Results and discussion

Figure 49 and Figure 50 depict the comparison of the colloid with the solute tracer transport experiments for the chosen inlet–outlet combinations for both fracture flow cells. For each experimental case the retardation factor and the colloid recovery is determined. For the retardation factor an error of 10 s is assumed, which is based on the measuring interval of 20 s. This results in an error for the retardation of $R_f = \pm 0.02$. As in Section 4, the experimental error of the LIBD method is estimated to be approximately 5%.

In all experimental cases the colloids are almost fully recovered with recoveries $\geq 90 \pm 5\%$ (see Figure 49d and Figure 50d). This high recovery is attributed to the applied relatively high flow rates and the unfavorable attachment conditions (electrostatic repulsion between negative charged colloids and negative charged fracture surface). Within the uncertainty, the overall recovery appears to be slightly higher in the unaltered fracture experiments. Again within the uncertainty, a trend of higher colloid recovery with higher flow rate appears in most of the experiments. This trend seems to be more pronounced in the unaltered fracture. Note that a significant link between residence time and colloid retention was already demonstrated in Section 2 and 4. For both fractures, the colloids are always eluted earlier, compared to the solute tracer.

In case of the altered fracture (Figure 49) the determined retardation factors range within $\Delta R_f = \pm 0.02$ between 0.54 and 0.64 for 24 mL/h and between 0.58 and 0.68 for 14 mL/h. Consequently, within the uncertainty, the acceleration is slightly higher at higher flow rate. When comparing the retardation factors at experimental case level, it appears that within the error bars the cross-experiments A1-3 and A3-1 reveal a comparably higher retardation factor, and thus, smaller acceleration. Comparably small retardation factors are observed for both flow rates in the experiment A3-3. As shown in Section 5, for this combination the solute tracer showed high flow velocities at the fracture boundary and the fastest elution times of the solute tracer. Therefore, the early elution of the colloids may be attributed to this direct connection along the fracture boundary. Most probably, the high flow velocities along this connection and the colloidal transport on the fastest streamlines in the center of the fracture cause those retardation factors. According to the migration time, the earliest arrival of the colloids at the outlet show the cases A1-1 and A3-3, which correlates well with the experiments using the solute tracer in Section 5. Analyzing the BTCs, it appears that the tailing of the solute transport is either comparable in shape (with a time delay in the order of 300–400 s) or more pronounced.

The experiments though the unaltered fracture (Figure 50) show retardation factors ranging within $\Delta R_f = \pm 0.02$ between 0.62 and 0.68 for 24 mL/h and between 0.69 and 0.79 for 12 mL/h. Therefore, in contrast to the altered fracture, the colloid plume seems to be less accelerated while migrating through the fracture. Furthermore, significantly higher retardation factors are observed for all five experiments at lower flow rate. The difference is largest in the experimental case U1-1. The recovery is comparable among the different experiments within the uncertainty, but a trend of higher recovery for higher flow rates appears. The tailings of the BTCs are more pronounced for a major amount of experiments, however, the colloid signal reaches the background level at least with the solute tracer. Therefore, we do not consider this to be a tailing in the sense of sorption. Experimental case U1-1 shows for both flow rates the earliest arrival among the transport experiments, which is in a good agreement with the respective solute transport experiments (see Figure 46).

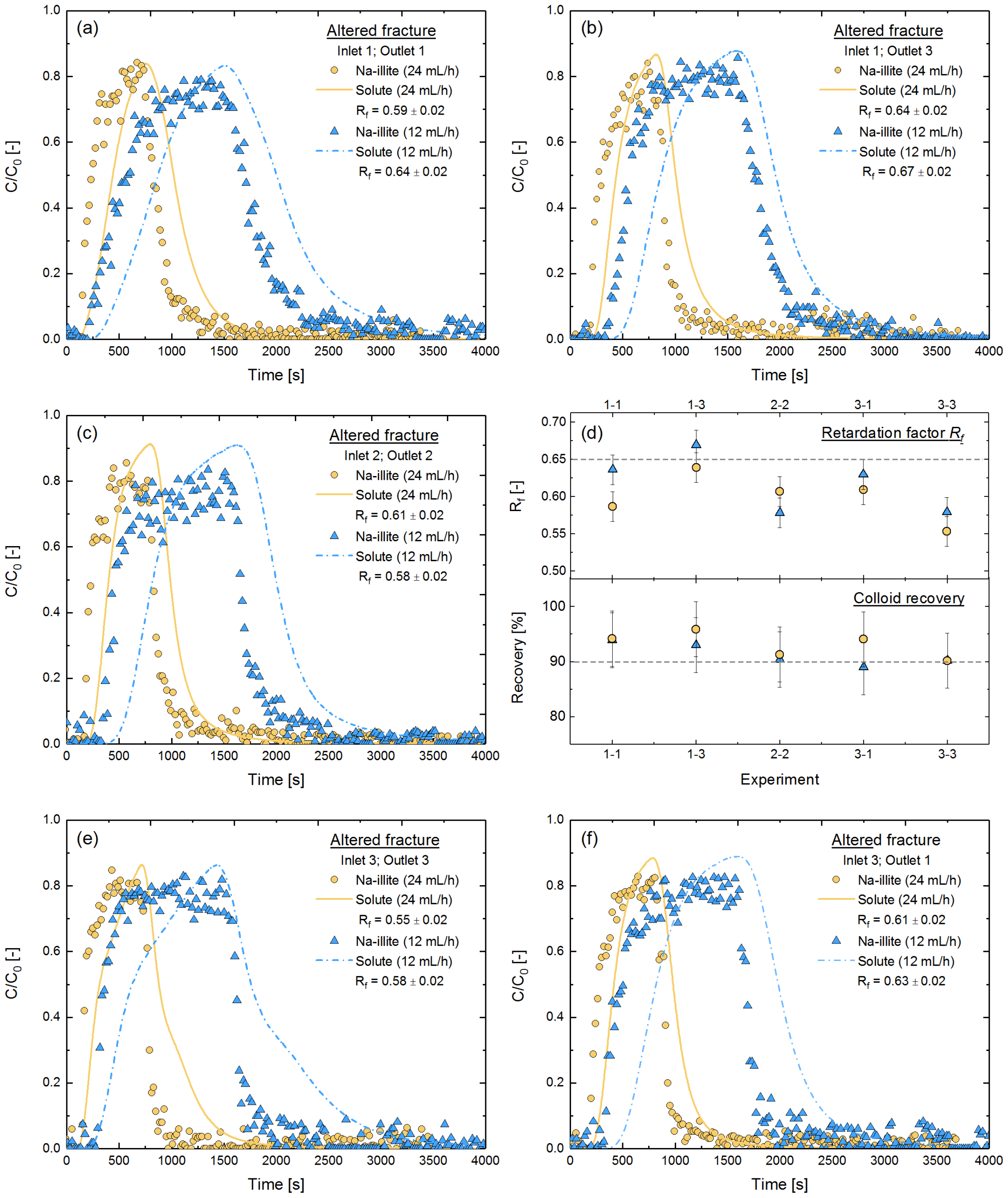

Figure 49: BTCs of Na-illite and Amino-G of transport experiments through the altered fracture (colloid/tracer pulse: 4 mL). Top series: inlet 1; middle left: inlet 2; bottom series: inlet 3. The solute transport experiments are depicted as solid (24 mL/h) and dashed lines (12 mL/h). The graphs in the middle on the right show the retardation factors (top) and the colloid recovery (bottom) for both flow rates and for each experiment (yellow circles: 24 mL/h; blue triangles: 12 mL/h).

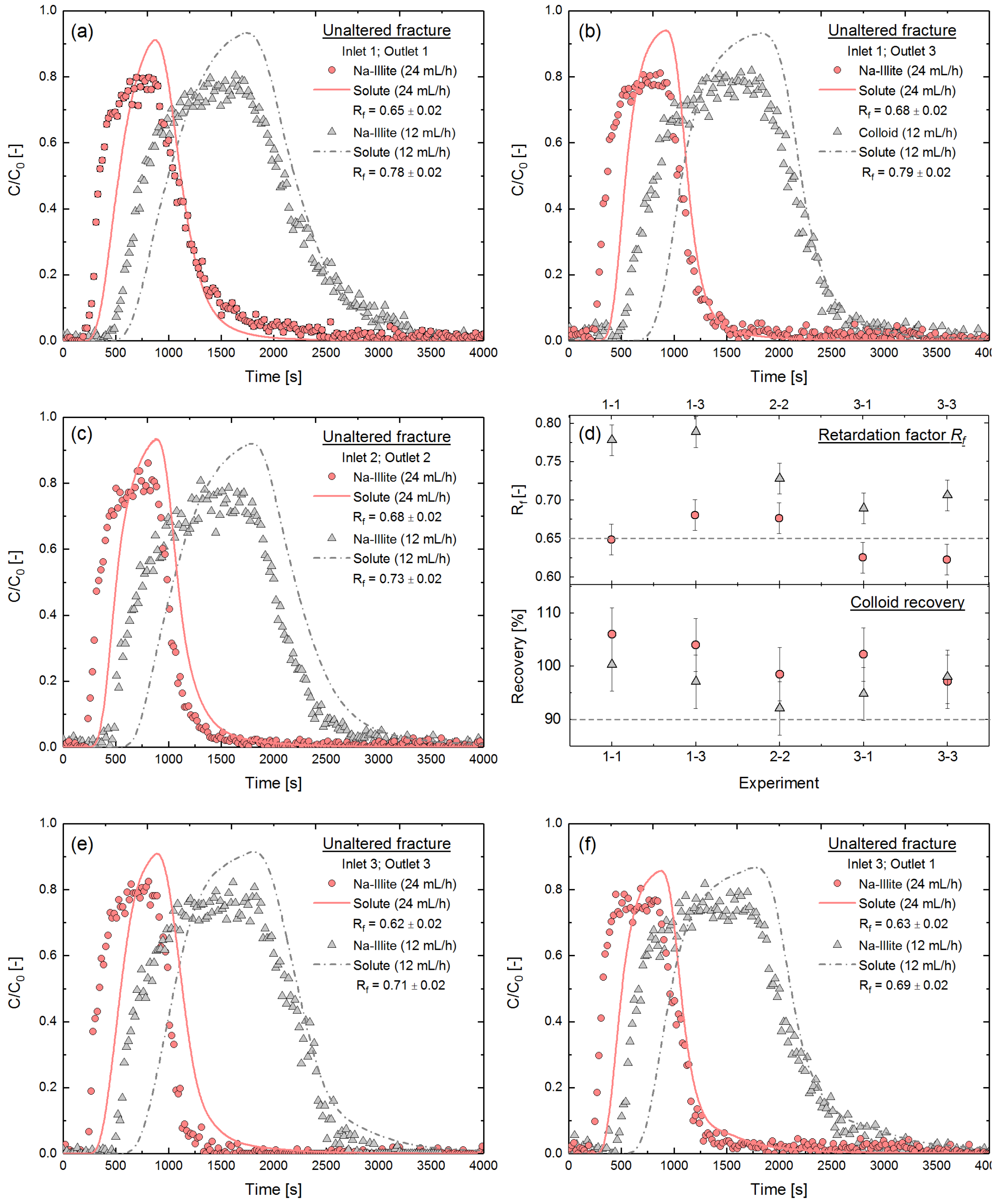

Figure 50: BTCs of Na-illite and Amino-G of transport experiments through unaltered fracture (colloid/tracer pulse: 4 mL). Top series: inlet 1; middle left: inlet 2; bottom series: inlet 3. The solute transport experiments are depicted as solid (24 mL/h) and dashed lines (12 mL/h). The graphs in the middle on the right show the retardation factors (top) and the colloid recovery (bottom) for both flow rates and for each experiment (red circles: 24 mL/h; grey triangles: 12 mL/h).

Although the tendency of flow rate dependent recovery is not satisfactorily significant in this study, other studies under laminar flow conditions show that colloid recovery increases with increasing fluid flow velocity (e.g. Vilks and Bachinski, 1996; Vilks et al., 2008). A higher flow rate leads to smaller residence times within the fracture, which decreases the probability of colloid collision with the fracture surfaces and therefore decreases the possibility of interaction by means of colloid attachment. Moreover, increasing the flow rate, increases the hydrodynamic shear force, which increases the probability of colloid detachment (Ryan and Elimelech, 1996).

For a parallel-plate channel with a solute to colloid flow velocity ratio of 1:1.5 (Reimus, 1995) $R_f = 0.66$. Except from experiment A1-3 at 12 mL/h, the R_f values obtained for the altered fracture are significantly below this value. For the unaltered fracture all experiments at 12 mL/h reveal significantly higher values, whereas, in tending experiments at 24 mL/h R_f values revealed are significantly below or around R_f of *0.66.* This is an indication that fracture geometry and aperture variability are additional properties to consider. Based on the retardation factors and recoveries obtained, a certain amount of each fracture is not accessible for the colloids during the transport process. The observation that the effect of applied flow rate on both retardation and recovery is larger in experiments through the unaltered fracture, might be attributed to the less complex internal geometry and/or wider aperture. The complex geometry and/or narrow aperture of the altered fracture may reduce this effect.

The rapid colloid transport is detectable for experiments in both fractures and is generally explained by exclusion and dispersion effects mentioned above. Those mechanisms reduce the effective volume in which the colloids are transported. Based on the determined retardation factors, the colloids, migrating through the altered fracture, seem to be more accelerated, than the colloids in the unaltered fracture. Possible explanations for the smaller retardation factors in the altered fracture are (i) the higher mean flow velocity (see Section 5) and the narrower aperture, resulting in a more pronounced velocity profile and thus higher flow velocities in the middle of the fracture, where usually colloids are transported; (ii) fluid flow channeling, due to a more complex fracture geometry and numerous aperture contacts (see Section 5) and (iii) the narrow mean aperture may cause a higher size and/or charge exclusion.

The slightly higher recoveries in the experiments in the unaltered fracture, are in agreement with the numerical simulations by James and Chrysikopoulos (1999), which show that colloid deposition is inversely proportional to the fracture aperture. Possible explanation for this observation is an increase in fracture wall collisions with decreasing fracture aperture, resulting in higher probability of attachment.

Comparable to the here presented results, Bales et al. (1989) showed in experiments through soil columns an inverse correlation between applied flow rate and retardation factor. Albarran et al. (2013) extensively studied the transport of different colloid types, sizes and flow rates through five granite fractures, however, they observed a slight positive correlation between applied flow rate and retardation factor. Moreover, independent of colloid type and size, the observed correlation between retardation factor and aperture, is inferred also from our experiments. They conclude that the small retardation factor is an indication for higher colloid exclusion. Zvikelsky and Weisbrod (2006) observed this dependence between retardation factor and (equivalent hydraulic) aperture as well and explained this observation on basis of the Taylor dispersion. In our experiments the mean colloid size is similar in both colloid suspensions used, thus, an effect of colloid size can be excluded, and the Taylor dispersion coefficients can be compared. The Taylor dispersion coefficient D_{Taylor} [m²/s] is defined as (Zvikelsky and Weisbrod, 2006):

$$D_{Taylor} = D + \frac{2}{945}\frac{u_{max}^2 a^2}{D} \quad \textbf{Equation 40}$$

where D [m²/s] is the colloid diffusion coefficient (according to Equation 13), u_{max} [m/s] is the maximum flow velocity obtained by the ratio of the fracture length [m] and the time of the first arrival [s] of the colloids and a [m] is the mean fracture aperture (see Section 5). The time of the first arrival of the colloids is defined here as the elution time when the concentration of the BTC reaches the first time $C/C_0 > 0.02$.

Figure 51 shows the comparison of the Taylor dispersion coefficient for the different experimental cases of both fractures. For both fractures the dispersion coefficient increases significantly with increasing flow rate. Due to the larger aperture, the calculated Taylor dispersion in the unaltered fracture is higher for both applied flow rates. Zvikelsky and Weisbrod (2006) attribute the smaller retardation factors in comparably narrow fractures to larger Taylor dispersion coefficients. Thus, in our experiments, the dispersion coefficients do not justify the early colloid arrival and the higher acceleration in the altered fracture compared to the unaltered one. But, the high Taylor coefficients in the unaltered fracture may explain the observed pronounced tailings in the BTCs of the colloid transport experiments. Abdel-

Salam and Chrysikopoulos (1995b) and Chrysikopoulos and Abdel-Salam (1997) describe a positive correlation between fracture aperture fluctuations and dispersion, in terms of spreading from numerical simulations. Therefore, the higher spreading in the experiments in the unaltered fracture may be related with the slightly higher roughness, the wider aperture and the higher Taylor dispersion coefficient.

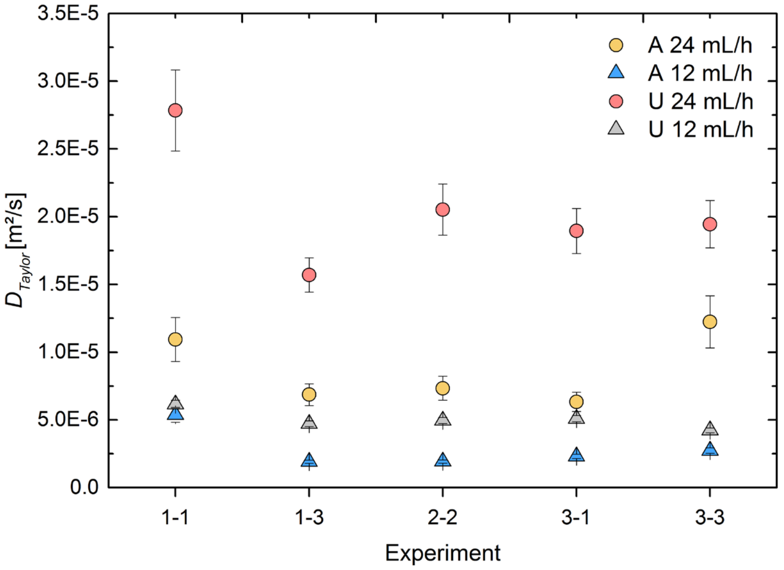

Figure 51: Taylor dispersion coefficients for the different experimental cases on both fractures (A = altered fracture; U = unaltered fracture).

On numerical basis, Abdel-Salam and Chrysikopoulos (1995b) showed an impact of size exclusion on solute and colloid transport in fractures with variable apertures. They found pronounced fingering and enhanced colloid transport in simulation when colloids are a subject of size exclusion, which results in an earlier breakthrough. Therefore, in case of the altered fracture the sum of the exclusion mechanisms (size and charge) and Taylor dispersion might cause the early colloid arrival. But, they also described an increased spreading due to size exclusion, which was not observed in terms of pronounced tailing in the experiments in the altered fracture. In the calculation of Taylor dispersion coefficient, the fracture geometry is not implemented, but the mean aperture. Since it was shown in the experiments presented in Section 5 on solute transport that the fracture geometry has a paramount importance on the transport processes, exclusion mechanisms as size or charge exclusion on basis of the fracture geometry and spatial heterogeneities need to be investigated beyond Taylor dispersion.

6.4 Summary and conclusion

Colloid transport experiments using a polydisperse Na-illite suspension were carried out for both fractured granite cores. Under overall electrostatic conditions unfavorable for attachment, the colloids were almost fully recovered and in all experiments the colloids eluted earlier than the solute tracer. It was found that the colloid transport through the narrower, more altered fracture is more accelerated compared to the unaltered fracture. These findings might be attributed to the narrow aperture and/or complex geometry. The slightly higher flow rate, fluid flow channeling and/or the sum of the exclusion effects plus Taylor dispersion may explain this finding. Taylor dispersion alone, which does not consider fracture geometry and spatial heterogeneities, fails to explain this effect. The effect of flow rate on recovery and retardation factor was found to be more pronounced in experiments through the less complex and wider fracture. The more complex geometry and/or the narrow aperture of the altered fracture may reduce such effect. In order to quantify the influence of different aspects on colloid transport (e.g. geometry and aperture heterogeneity) numerical simulations or further investigation are necessary.

7 Synthesis of the results and perspective

The thesis was build up as a bottom-up approach in order to understand isolately the transport behavior and physico-chemical retention mechanisms of monodisperse polystyrene and natural illite colloids through artificial and natural fractures, respectively. The complexity in the chosen fractured media and in the utilized colloids increased stepwise within the program of the thesis. All experiments were performed under laminar flow conditions ($Re < 1$) and chemical conditions unfavorable for colloid attachment. This part presents the major conclusions of the different steps introduced in Section 1.3 and the future perspectives.

7.1 Major conclusions / Key findings

- Step 1: The first step of the working approach reveals that (i) the size of the colloids, (ii) the material properties of the surface, (iii) the fracture orientation and (iv) the residence time in the fracture affect the transport behavior under stop-flow conditions. Beyond a certain diameter and for long residence times, the influence of gravity exceeds the influence of molecular diffusion even for low density colloids (here 1.05 g/cm³), which results in colloid sedimentation. It was shown that the impact of sedimentation on colloid retention is dependent on the potential sedimentation length and thus the impact is maximum in horizontally orientated fractures. Moreover, fracture roughness (here cut unpolished granodiorite $Rq \approx 350$ nm and polished acrylic glass $Rq \approx 20$ nm) does not affect the transport and deposition behavior of 1000 nm colloids. Under continuous flow and transport conditions a small fraction (maximum 5%) of colloids is retained on the collector surface material. Because of overall unfavorable attachment condition those colloids are homogeneously distributed on the granodiorite surface and are therefore independent of mineralogy. In contrast, even for long residence times, small 25 nm colloids are completely diffusion dominated. The depletion of those mobile colloids in suspensions was attributed to their small size and large diffusion coefficients. Small colloids reach fracture/collector surfaces earlier and can interact with the surface more frequently due to their higher diffusion coefficient. Even minor surface roughness (cut granodiorite) or surface heterogeneities on polished surfaces, such as cracks (acrylic glass) show to retain those colloids significantly. Those observations were made independent of fracture orientation.

- Step 2: Based on the findings of the first step, the second step shows that the residence time behavior of polydisperse clay suspensions possess similarities to the behavior of carboxylated polystyrene microspheres (e.g. positive correlation between residence time and colloid retention). However, especially for long residence times and despite the higher density (2.0–2.7 g/cm³), polydisperse clay suspensions underlie significantly less retention and stay mobile in suspension for longer times. Despite comparable average zeta potentials, differences in shape, surface charge distribution, density and colloid size distribution of spherical carboxylated polystyrene spheres compared to platelet-shaped clay colloids might be responsible for less retardation. Therefore, with respect to the experimental conditions and setup, low density monodisperse carboxylated polystyrene spheres are non-ideal analogues for natural clay colloids. Clay colloids can have significant higher mobility, which is not given using functional synthetic carboxylated polystyrene spheres, in order to estimate nanoparticles mobility.

- Step 3: The geometry and aperture distribution in natural fractures can be highly complex and heterogeneous, in respect of the geological history of the fractured media. Fracture flow and solute transport through a hydrothermally altered and fractured granite core with a narrow mean aperture (here 0.162 mm) and complex geometry including numerous asperity contacts, was shown to be dominated by the fracture geometry. In contrast, flow and mass transport in a fully open unaltered fractured core (mean aperture here 0.357) seems to be controlled only by the aperture distribution. Numerical models with stepwise decreasing spatial complexity, prove that the breakthrough curves, especially the tailing, can only be satisfactory reproduced by implementing a high resolution aperture distribution and real geometry of the investigated fracture. Examined simplifications, e.g. mean aperture instead of measured distribution or even a rectangular parallel-plate model approach significantly underestimate the extent of the tailing and delay the first arrival of the tracer to longer percolation times. Therefore, detailed information about the fracture geometry and the aperture distribution are needed to describe precisely fluid flow and mass transport in natural rough fractures.

- Step 4: The final step represents the most complex part of this thesis. Illite colloid transport in the fractured granite cores was investigated experimentally. The results reveal that colloids are transported faster compared to molecular-scaled tracers. It was demonstrated that an increase in flow rate, increases the colloid acceleration. The extent of this acceleration was shown to be dependent on the fracture aperture and/or the complexity of the internal geometry. In contrast to wide and open fractures, for a specific discharge, colloids travel faster while migrating through narrower and partly closed fractures. The effect of an increase in flow rate on accelerated transport was observed to be more intense in wide and open fractures. More pronounced tailings in the BTCs of experiments through the unaltered granite core were attributed to increased Taylor dispersion.

The presented results deliver detailed insights in colloid migration under laminar flow conditions in both parallel-plate type and natural rough fractures. The results and the conclusions show that solute and colloid transport under controlled and stabilized conditions are highly dependent on fracture domain geometry and hydrodynamic conditions. Therefore, precise knowledge about those boundary conditions can significantly improve the quality of predictions and estimations on flow and mass transport.

Notably, with respect to reactive transport modelling those findings provide important implications, since reactive transport simulations are often conducted in 1-D or simple 2-D geometries, mainly due to the complexity of the chemical processes to be modeled. The focus of those models is most often only on geochemical aspects and processes and less on the impact of domain geometry and the resulting flow field heterogeneity. Thus, such models are prone to misinterpretation of complex transport behavior, which is shown to be also attributed to the spatial properties of natural fractures. Especially the formation of tailings in the BTCs can only be described in 1-D models by chemical interactions or matrix diffusion and not by hydrodynamic features induced by the fracture spatial structure.

7.2 Future perspectives

The experiments in this thesis were all conducted under controlled laminar flow conditions with a geochemical background electrolyte establishing overall unfavorable attachment conditions and a colloid load preventing colloid agglomeration. Based on the presented results the next steps on the solute and colloid transport experiments through the natural fractures might be the variation in flow velocity over several orders of magnitude, in order to investigate more deeply a flow velocity dependence. Furthermore, direct numerical simulations of colloid transport by means of e.g. particle tracking models would deepen the understanding of transport and retention processes.

However, the chemical, thermal and hydrodynamic circumstances in natural systems (e.g. geothermal reservoirs) are often highly variable affecting fluid flow, mass transport, colloid–

colloid and colloid–surface interactions, respectively. Consequently, to understand solute and colloid transport under such highly complex conditions the results of this study need to be distinctly expanded. Possible scenarios approaching more complex conditions are the performance of transport experiments:

- using a high colloid load and investigating the evolution of permeability (clogging effects) over time.
- under turbulent conditions investigating the impact on fluid flow, colloid recovery and colloid–colloid / colloid–surface interactions.
- under high ionic strength conditions and/or under the presence of divalent cations provoking colloid agglomeration, in order to investigate the impact of aggregates on fracture permeability (clogging effects) and mass transport (colloid aggregation kinetics during dynamic experiments compared to static aggregation).

8 References

Abdel-Salam, A. and Chrysikopoulos, C.V., 1994. Analytical solutions for one-dimensional colloid transport in saturated fractures. Advances in Water Resources, 17(5): 283-296.

Abdel-Salam, A. and Chrysikopoulos, C.V., 1995a. Analysis of a model for contaminant transport in fractured media in the presence of colloids. Journal of Hydrology, 165(1-4): 261-281.

Abdel-Salam, A. and Chrysikopoulos, C.V., 1995b. Modeling of colloid and colloid-facilitated contaminant transport in a two-dimensional fracture with spatially variable aperture. Transport in Porous Media, 20(3): 197-221.

Abelin, H., Birgersson, L., Widén, H., Ågren, T., Moreno, L. and Neretnieks, I., 1994. Channeling experiments in crystalline fractured rocks. Journal of Contaminant Hydrology, 15(3): 129-158.

Adamczyk, Z., 2006. Particles at Interfaces: Interactions, Deposition, Structure. Elsevier Science, 700 pp.

Adler, P.M. and Thovert, J.F., 1999. Fractures and Fracture Networks. Springer Netherlands, 431 pp.

Adler, P.M., Thovert, J.F. and Mourzenko, V.V., 2012. Fractured Porous Media. OUP Oxford, 175 pp.

Albarran, N., Missana, T., Alonso, U., García-Gutiérrez, M. and López, T., 2013. Analysis of latex, gold and smectite colloid transport and retention in artificial fractures in crystalline rock. Colloids and Surfaces A: Physicochemical and Engineering Aspects, 435: 115-126.

Alonso, U., Missana, T., Patelli, A., Ceccato, D., Albarran, N., García-Gutiérrez, M., Lopez-Torrubia, T. and Rigato, V., 2009. Quantification of Au nanoparticles retention on a heterogeneous rock surface. Colloids and Surfaces A: Physicochemical and Engineering Aspects, 347(1-3): 230-238.

Alonso, U., Missana, T., Patelli, A. and Rigato, V., 2007a. Bentonite colloid diffusion through the host rock of a deep geological repository. Physics and Chemistry of the Earth, Parts A/B/C, 32(1-7): 469-476.

Alonso, U., Missana, T., Patelli, A., Rigato, V. and Ravagnan, J., 2007b. Colloid diffusion in crystalline rock: An experimental methodology to measure diffusion coefficients and evaluate colloid size dependence. Earth and Planetary Science Letters, 259(3-4): 372-383.

Altmann, S., Aertsens, M., Appelo, T., Bruggeman, C., Gaboreau, S., Glaus, M., Jacquier, P., Kupcik, T., Maes, N., Montoya, V., Rabung, T., Robinet, J.-C., savoye, S., Schaefer, T., Tournassat, C., Van Laer, L. and Van Loon, L., 2015. Processes of cation migration in clayrocks: Final Scientific Report of the CatClay European Project, 128 pp.

Aris, R., 1956. On the dispersion of a solute in a fluid flowing through a tube. Proceedings of the Royal Society of London. Series A. Mathematical and Physical Sciences, 235(1200): 67-77.

Assemi, S., Nalaskowski, J. and Johnson, W.P., 2006. Direct force measurements between carboxylate-modified latex microspheres and glass using atomic force microscopy. Colloids and Surfaces A: Physicochemical and Engineering Aspects, 286(1–3): 70-77.

Bales, R., Gerba, C., Grondin, G.H. and Jensen, S.L., 1989. Bacteriophage Transport in Sandy Soil and Fractured Tuff. Applied Environmental Microbiology, 55(8): 2061-2067.

Bashar, K. and Tellam, J.H., 2011. Sandstones of unexpectedly high diffusibility. Journal of Contaminant Hydrology, 122(1): 40-52.

Batchelor, G.K., 1967. An Introduction to Fluid Dynamics. Cambridge University Press, 615 pp.

Bath, A., 2011. Infiltration of dilute groundwaters and resulting groundwater compositions at repository depth. Strålsäkerhetsmyndigheten, 92 pp.

Becker, M.W., Metge, D.W., Collins, S.A., Shapiro, A.M. and Harvey, R.W., 2003. Bacterial Transport Experiments in Fractured Crystalline Bedrock. Ground Water, 41(5): 682-689.

Becker, M.W., Reimus, P.W. and Vilks, P., 1999. Transport and Attenuation of Carboxylate-Modified Latex Microspheres in Fractured Rock Laboratory and Field Tracer Tests. Ground Water, 37(3): 387-395.

Becker, M.W. and Shapiro, A.M., 2000. Tracer transport in fractured crystalline rock: Evidence of nondiffusive breakthrough tailing. Water Resources Research, 36(7): 1677-1686.

Bedrikovetsky, P., Siqueira, F.D., Furtado, C.A. and Souza, A.L.S., 2011. Modified particle detachment model for colloidal transport in porous media. Transport in Porous Media, 86(2): 353-383.

Bedrikovetsky, P., Zeinijahromi, A., Siqueira, F.D., Furtado, C.A. and de Souza, A.L.S., 2012. Particle detachment under velocity alternation during suspension transport in porous media. Transport in Porous Media, 91(1): 173-197.

Bergelin, A., Lindquist, A., Nilsson, K., Wacker, P. and Nilsson, A.-C., 2007. Forsmark site investigation - Hydrochemical characterisation in borehole KFM08D - Results from two investigated borehole sections at 669.7–676.8 m and 828.4–835.5 m. SKB P-07-190. Stockholm. 95 pp.

Berkowitz, B., 2002. Characterizing flow and transport in fractured geological media: A review. Advances in Water Resources, 25(8-12): 861-884.

Bernhardt, I.C., 2012. Particle Size Analysis: Classification and sedimentation methods. Springer Netherlands, 428 pp.

Bird, R.B., 2002. Transport phenomena. Applied Mechanics Reviews, 55(1): R1-R4.

Bitea, C., 2005. Laser-induzierte Breakdown Detektion (LIBD): Quantifizierung der Kolloidbildung vierwertiger Actiniden und Homologen. Forschungszentrum Karlsruhe, 187 pp.

Blume, H.P., Brümmer, G.W., Scheffer, F., Horn, R., Kandeler, E., Schachtschabel, P., Kögel-Knabner, I., Welp, G., Kretzschmar, R. and Thiele-Bruhn, S., 2009. Scheffer/Schachtschabel: Lehrbuch der Bodenkunde. Spektrum Akademischer Verlag, 578 pp.

Bodin, J., Delay, F. and De Marsily, G., 2003. Solute transport in a single fracture with negligible matrix permeability: 1. fundamental mechanisms. Hydrogeology Journal, 11(4): 418-433.

Boutt, D.F., Grasselli, G., Fredrich, J.T., Cook, B.K. and Williams, J.R., 2006. Trapping zones: The effect of fracture roughness on the directional anisotropy of fluid flow and colloid transport in a single fracture. Geophysical Research Letters, 33(21): 6 pp.

Bradford, S.A. and Torkzaban, S., 2008. Colloid transport and retention in unsaturated porous media: A review of interface-, collector-, and pore-scale processes and models. Vadose Zone Journal, 7(2): 667-681.

Bradford, S.A. and Torkzaban, S., 2013. Colloid Interaction Energies for Physically and Chemically Heterogeneous Porous Media. Langmuir, 29(11): 3668-3676.

Brown, S., Caprihan, A. and Hardy, R., 1998. Experimental observation of fluid flow channels in a single fracture. Journal of Geophysical Research: Solid Earth, 103(B3): 5125-5132.

Brown, S.R., 1987. Fluid flow through rock joints: The effect of surface roughness. Journal of Geophysical Research: Solid Earth, 92(B2): 1337-1347.

Brush, D.J. and Thomson, N.R., 2003. Fluid flow in synthetic rough-walled fractures: Navier-Stokes, Stokes, and local cubic law simulations. Water Resources Research, 39(4): 15 pp.

Bruus, H., 2007. Theoretical microfluidics. Oxford university press Oxford, 368 pp.

Buades, A., Coll, B. and Morel, J., 2005. A nonlocal algorithm for image enhancement. IEEE Comput. Vis. Pattern Recognit, 2: 60-65.

Bundschuh, T., Hauser, W., Kim, J.I., Knopp, R. and Scherbaum, F.J., 2001a. Determination of colloid size by 2-D optical detection of laser induced plasma. Colloids and Surfaces A: Physicochemical and Engineering Aspects, 180(3): 285-293.

Bundschuh, T., Knopp, R. and Kim, J.I., 2001b. Laser-induced breakdown detection (LIBD) of aquatic colloids with different laser systems. Colloids and Surfaces A: Physicochemical and Engineering Aspects, 177(1): 47-55.

Butt, H.-J., Graf, K. and Kappl, M., 2006. Physics and Chemistry of Interfaces. Wiley, 373 pp.

Cardenas, M.B., Slottke, D.T., Ketcham, R.A. and Sharp, J.M., 2007. Navier-Stokes flow and transport simulations using real fractures shows heavy tailing due to eddies. Geophysical Research Letters, 34(14): 6 pp.

Cardenas, M.B., Slottke, D.T., Ketcham, R.A. and Sharp, J.M., 2009. Effects of inertia and directionality on flow and transport in a rough asymmetric fracture. Journal of Geophysical Research-Solid Earth, 114(B6): 11 pp.

Chae, B., Ichikawa, Y., Jeong, G., Seo, Y. and Kim, B., 2004. Roughness measurement of rock discontinuities using a confocal laser scanning microscope and the Fourier spectral analysis. Engineering Geology, 72(3): 181-199.

Champ, D.R. and Schroeter, J., 1988. Bacterial Transport in Fractured Rock — A Field-Scale Tracer Test at the Chalk River Nuclear Laboratories. Water Science & Technology, 20(11): 81-87.

Chapman, D.L., 1913. LI.A contribution to the theory of electrocapillarity. Philosophical Magazine Series 6, 25(148): 475-481.

Chen, Z., Qian, J., Zhan, H., Zhou, Z., Wang, J. and Tan, Y., 2017. Effect of roughness on water flow through a synthetic single rough fracture. Environmental Earth Sciences, 76(4): 186.

Chinju, H., Kuno, Y., Nagasaki, S. and Tanaka, S., 2001. Deposition Behavior of Polystyrene Latex Particles on Solid Surfaces during Migration through an Artificial Fracture in a Granite Rock Sample. Journal of Nuclear Science and Technology, 38(6): 439-443.

Chrysikopoulos, C.V., 1999. Transport of Colloids in Saturated Fractures. In: M.H. Aliabadi (Editor), Advances in Fracture Mechanics: Fracture of Rock. Computational Mechanics Publications WIT Press, Southampton, UK, pp. 297-331.

Chrysikopoulos, C.V. and Abdel-Salam, A., 1997. Modeling colloid transport and deposition in saturated fractures. Colloids and Surfaces A: Physicochemical and Engineering Aspects, 121(2-3): 189-202.

Chrysikopoulos, C.V. and James, S.C., 2003. Transport of Neutrally Buoyant and Dense Variably Sized Colloids in a Two-Dimensional Fracture with Anisotropic Aperture. Transport in Porous Media, 51(2): 191-210.

Civan, F., 2011. Reservoir formation damage. Gulf Professional Publishing, 1042 pp.

COMSOL, 2015. COMSOL Multiphysics®. Version 5.0. COMSOL AB, Stockholm, Sweden. http://www.comsol.com/.

COMSOL, 2017. COMSOL Multiphysics®. Version 5.2a. COMSOL AB, Stockholm, Sweden. http://www.comsol.com/.

Cosgrove, T., 2010. Colloid Science: Principles, Methods and Applications. John Wiley & Sons, 394 pp.

Council, N.R., 1996. Rock Fractures and Fluid Flow: Contemporary Understanding and Applications. The National Academies Press, Washington, DC, 568 pp.

Cumbie, D.H. and McKay, L.D., 1999. Influence of diameter on particle transport in a fractured shale saprolite. Journal of Contaminant Hydrology, 37(1-2): 139-157.

Darbha, G.K., Fischer, C., Lützenkirchen, J. and Schäfer, T., 2012a. Site-specific retention of colloids at rough rock surfaces. Environ Sci Technol, 46(17): 9378-87.

Darbha, G.K., Fischer, C., Michler, A., Lützenkirchen, J., Schäfer, T., Heberling, F. and Schild, D., 2012b. Deposition of latex colloids at rough mineral surfaces: an analogue study using nanopatterned surfaces. Langmuir, 28(16): 6606-17.

Darbha, G.K., Schäfer, T., Heberling, F., Lüttge, A. and Fischer, C., 2010. Retention of latex colloids on calcite as a function of surface roughness and topography. Langmuir, 26(7): 4743-52.

Degueldre, C., Baeyens, B., Goerlich, W., Riga, J., Verbist, J. and Stadelmann, P., 1989. Colloids in water from a subsurface fracture in granitic rock, Grimsel Test Site, Switzerland. Geochimica et Cosmochimica Acta, 53(3): 603-610.

Degueldre, C., Scholtis, A. and Thomas, B., 1998. Opalinus Clay Groundwaters and Colloids. A Sampling and Analysis Exercise at Mt. Terri (June/July 1997), Analytical Results. Technical Note TN 97-20A, Berne, Switzerland.

Derjaguin, B.V. and Landau, L., 1941. Theory of the Stability of Strongly Charged Lyophobic Sols and of the Adhesion of Strongly Charged Particles in Solutions of Electrolytes. Acta Phys. Chim. URSS, 14: 633-662.

Detwiler, R.L., Rajaram, H. and Glass, R.J., 2000. Solute transport in variable-aperture fractures: An investigation of the relative importance of Taylor dispersion and macrodispersion. Water Resources Research, 36(7): 1611-1625.

Dokou, E., Barteau, M.A., Wagner, N.J. and Lenhoff, A.M., 2001. Effect of Gravity on Colloidal Deposition Studied by Atomic Force Microscopy. J Colloid Interface Sci, 240(1): 9-16.

Durham, W.B., Bourcier, W.L. and Burton, E.A., 2001. Direct observation of reactive flow in a single fracture. Water Resources Research, 37(1): 1-12.

Einstein, A., 1905. Über die von der molekularkinetischen Theorie der Wärme geforderte Bewegung von in ruhenden Flüssigkeiten suspendierten Teilchen. Annalen der Physik, 322(8): 549-560.

Elimelech, M., 1995. Particle deposition and aggregation: measurement, modelling, and simulation. Butterworth-Heinemann, 441 pp.

Elimelech, M., Gregory, J. and Jia, X., 2013. Particle deposition and aggregation: measurement, modelling and simulation. Butterworth-Heinemann, 441 pp.

Elimelech, M. and O'Melia, C.R., 1990. Effect of particle size on collision efficiency in the deposition of Brownian particles with electrostatic energy barriers. Langmuir, 6(6): 1153-1163.

Evans, A.A. and Donahue, R.E., 2008. Laser scanning confocal microscopy: a potential technique for the study of lithic microwear. Journal of Archaeological Science, 35(8): 2223-2230.

Evans, K.F., Genter, A. and Sausse, J., 2005. Permeability creation and damage due to massive fluid injections into granite at 3.5 km at Soultz: 1. Borehole observations. Journal of Geophysical Research-Solid Earth, 110(B4): 19 pp.

Fischer, C., Michler, A., Darbha, G.K., Kanbach, M. and Schäfer, T., 2012. Deposition of mineral colloids on rough rock surfaces. American Journal of Science, 312(8): 885-906.

Frimmel, F.H. and Delay, M., 2010. Introducing the “Nano-world”. Nanoparticles in the Water Cycle, Springer Berlin Heidelberg, 245 pp.

Geckeis, H., Schafer, T., Hauser, W., Rabung, T., Missana, T., Degueldre, C., Mori, A., Eikenberg, J., Fierz, T. and Alexander, W.R., 2004. Results of the colloid and radionuclide retention experiment (CRR) at the Grimsel Test Site (GTS), Switzerland - impact of reaction kinetics and speciation on radionuclide migration. Radiochimica Acta, 92(9-11): 765-774.

Geiermann, J. and Schill, E., 2010. 2-D Magnetotellurics at the geothermal site at Soultz-sous-Forêts: Resistivity distribution to about 3000 m depth. Comptes Rendus Geoscience, 342(7–8): 587-599.

Genter, A., Fritsch, D., Cuenot, N., Baumgärtner, J. and Graff, J.-J., 2009. Overview of the Current Activities of the European EGS Soultz Project: from Exploration to Electricity Production Thirty-Fourth Workshop on Geothermal Reservoir Engineering, Stanford University, Stanford, California, pp. 7 pp.

Genter, A., Guillou-Frottier, L., Feybesse, J.-L., Nicol, N., Dezayes, C. and Schwartz, S., 2003. Typology of potential Hot Fractured Rock resources in Europe. Geothermics, 32(4-6): 701-710.

Genter, A. and Traineau, H., 1991. Geological survey of the HDR borehole EPS1, Soultz-sous-Forêts, Bas-Rhin. Open file report BRGM/RR-32433-FR, SGN, IRG.

GeoDict, 2015. Geometric Models and PreDictions of Properties. Math2Market, Kaiserslauter, Germany. http://www.geodict.com.

Goldman, A.J., Cox, R.G. and Brenner, H., 1967. Slow viscous motion of a sphere parallel to a plane wall—I Motion through a quiescent fluid. Chemical Engineering Science, 22(4): 637-651.

González Sánchez, F., Van Loon, L.R., Gimmi, T., Jakob, A., Glaus, M.A. and Diamond, L.W., 2008. Self-diffusion of water and its dependence on temperature and ionic strength in highly compacted montmorillonite, illite and kaolinite. Applied Geochemistry, 23(12): 3840-3851.

Gouy, L.G., 1909. Sur la constitution de la charge électrique à la surface d'un electrolyte. In: Bachelier and Gauthier-Villars (Editors), Comptes Rendus de l'Académie des science, Paris, Fance, pp. 654–657.

Gouze, P., Melean, Y., Le Borgne, T., Dentz, M. and Carrera, J., 2008. Non-Fickian dispersion in porous media explained by heterogeneous microscale matrix diffusion. Water Resources Research, 44(11): 19 pp.

Graham, T., 1861. Liquid Diffusion Applied to Analysis. Philosophical Transactions of the Royal Society of London, 151(0): 183-224.

Grahame, D.C., 1947. The electrical double layer and the theory of electrocapillarity. Chemical reviews, 41(3): 441-501.

Gregory, J. and O'Melia, C.R., 1989. Fundamentals of flocculation. Critical Reviews in Environmental Science and Technology, 19(3): 185-230.

Grindrod, P., 1993. The Impact of Colloids on the Migration and Dispersal of Radionuclides within Fractured Rock. Journal of Contaminant Hydrology, 13(1-4): 167-181.

Grindrod, P. and Lee, A.J., 1997. Colloid migration in symmetrical non-uniform fractures: particle tracking in three dimensions. Journal of Contaminant Hydrology, 27(3-4): 157-175.

Grisak, G.E. and Pickens, J.F., 1980. Solute transport through fractured media: 1. The effect of matrix diffusion. Water Resources Research, 16(4): 719-730.

Hakami, E. and Larsson, E., 1996. Aperture measurements and flow experiments on a single natural fracture. International Journal of Rock Mechanics and Mining Sciences & Geomechanics Abstracts, 33(4): 395-404.

Hauser, W., Geckeis, H., Kim, J.I. and Fierz, T., 2002. A mobile laser-induced breakdown detection system and its application for the in situ-monitoring of colloid migration. Colloids and Surfaces A: Physicochemical and Engineering Aspects, 203(1–3): 37-45.

Henry, C., Minier, J.P. and Lefevre, G., 2012. Towards a description of particulate fouling: from single particle deposition to clogging. Adv Colloid Interface Sci, 185-186: 34-76.

Hinsby, K., McKay, L.D., Jorgensen, P., Lenczewski, M. and Gerba, C.P., 1996. Fracture Aperture Measurements and Migration of Solutes, Viruses, and Immiscible Creosote in a Column of Clay-Rich Till. Ground Water, 34(6): 1065-1075.

Hofmann, T., 2004. Kolloide: Die welt der vernachlässigten dimensionen. Chemie in unserer Zeit, 38(1): 24-35.

Huber, F., Enzmann, F., Wenka, A., Bouby, M., Dentz, M. and Schäfer, T., 2012. Natural micro-scale heterogeneity induced solute and nanoparticle retardation in fractured crystalline rock. J Contam Hydrol, 133: 40-52.

Ippolito, I., Daccord, G., Hinch, E.J. and Hulin, J.P., 1994. Echo tracer dispersion in model fractures with a rectangular geometry. Journal of Contaminant Hydrology, 16(1): 87-108.

Ippolito, I., Hinch, E.J., Daccord, G. and Hulin, J.P., 1993. Tracer dispersion in 2-D fractures with flat and rough walls in a radial flow geometry. Physics of Fluids A: Fluid Dynamics, 5(8): 1952-1962.

James, S.C. and Chrysikopoulos, C.V., 1999. Transport of polydisperse colloid suspensions in a single fracture. Water Resources Research, 35(3): 707-718.

James, S.C. and Chrysikopoulos, C.V., 2000. Transport of polydisperse colloids in a saturated fracture with spatially variable aperture. Water Resources Research, 36(6): 1457-1465.

James, S.C. and Chrysikopoulos, C.V., 2003. Effective velocity and effective dispersion coefficient for finite-sized particles flowing in a uniform fracture. Journal of Colloid and Interface Science, 263(1): 288-295.

James, S.C. and Chrysikopoulos, C.V., 2004. Dense colloid transport in a bifurcating fracture. Journal of colloid and interface science, 270(1): 250-254.

James, S.C. and Chrysikopoulos, C.V., 2011. Monodisperse and polydisperse colloid transport in water-saturated fractures with various orientations: Gravity effects. Advances in Water Resources, 34(10): 1249-1255.

Jasmund, K. and Lagaly, G., 1993. Tonminerale und Tone: Struktur, Eigenschaften, Anwendungen und Einsatz in Industrie und Umwelt. Steinkopff, 490 pp.

Jing, L. and Stephansson, O., 2007. Fundamentals of Discrete Element Methods for Rock Engineering: Theory and Applications. Elsevier Science, 562 pp.

Jokelainen, L., Meski, T., Lindberg, A., Soler, J., Siitari-Kauppi, M., Martin, A. and Eikenberg, J., 2013. The determination of 134Cs and 22Na diffusion profiles in granodiorite using gamma spectroscopy. Journal of Radioanalytical and Nuclear Chemistry, 295(3): 2153-2161.

Jorgensen, J.F., Carneiro, K. and Madsen, L.L., 1993. The scanning tunneling microscope and surface characterization. Nanotechnology, 4(3): 152-158.

Jovanović, Z., Khan, F., Enzmann, F. and Kersten, M., 2013. Simultaneous segmentation and beam-hardening correction in computed microtomography of rock cores. Computers & geosciences, 56: 142-150.

Jung, E. and Cho, H., 2012. Characteristics of the Laser-Induced Breakdown Detection of Colloidal Nanoparticles for Determining Particle Size. Nanotechnology and Nanomaterials » "The Delivery of Nanoparticles". INTECH Open Access Publisher.

Jung, E.C., Yun, J.-I., Kim, J.I., Park, Y.J., Park, K.K., Fanghänel, T. and Kim, W.H., 2006. Size measurement of nanoparticles using the emission intensity distribution of laser-induced plasma. Applied Physics B, 85(4): 625-629.

Kaszuba, M., Corbett, J., Watson, F.M. and Jones, A., 2010. High-concentration zeta potential measurements using light-scattering techniques. Philosophical Transactions of the Royal Society of London A: Mathematical, Physical and Engineering Sciences, 368(1927): 4439-4451.

Keller, A.A., 1998. High resolution, non-destructive measurement and characterization of fracture apertures. International Journal of Rock Mechanics and Mining Sciences, 35(8): 1037-1050.

Keller, A.A., Roberts, P.V. and Blunt, M.J., 1999. Effect of fracture aperture variations on the dispersion of contaminants. Water Resources Research, 35(1): 55-63.

Kersting, A.B., Efurd, D.W., Finnegan, D.L., Rokop, D.J., Smith, D.K. and Thompson, J.L., 1999. Migration of plutonium in ground water at the Nevada Test Site. Nature, 397(6714): 56-59.

Khan, F., Enzmann, F. and Kersten, M., 2015. Beam-hardening correction by a surface fitting and phase classification by a least square support vector machine approach for tomography images of geological samples. Solid Earth Discussions, 7(4): 3383-3408.

Kim, J.-I. and Walther, C., 2007. Laser-Induced Breakdown Detection, Environmental Colloids and Particles. John Wiley & Sons, Ltd, pp. 555-612.

Kim, J.I., Buckau, G., Baumgärtner, F., Moon, H.C. and Lux, D., 1983. Colloid Generation and the Actinide Migration in Gorleben Groundwaters. MRS Online Proceedings Library Archive, 26: 31-40.

Kinzelbach, W. and Rausch, R., 1995. Grundwassermodellierung: eine Einführung mit Übungen. Borntraeger.

Kitamori, T., Yokose, K., Sakagami, M. and Sawada, T., 1989. Detection and Counting of Ultrafine Particles in Ultrapure Water Using Laser Breakdown Acoustic Method. Japanese Journal of Applied Physics Part 1-Regular Papers Short Notes & Review Papers, 28(7): 1195-1198.

Knapp, R.B., Chiarappa, M.L. and Durham, W.B., 2000. An experimental exploration of the transport and capture of abiotic colloids in a single fracture. Water Resources Research, 36(11): 3139-3149.

Kohl, T., Evans, K., Hopkirk, R., Jung, R. and Rybach, L., 1997. Observation and simulation of non-Darcian flow transients in fractured rock. Water Resources Research, 33(3): 407-418.

Konzuk, J.S. and Kueper, B.H., 2004. Evaluation of cubic law based models describing single-phase flow through a rough-walled fracture. Water Resources Research, 40(2): 17 pp.

Kosakowski, G., 2004. Anomalous transport of colloids and solutes in a shear zone. J Contam Hydrol, 72(1-4): 23-46.

Kretzschmar, R. and Schäfer, T., 2005. Metal Retention and Transport on Colloidal Particles in the Environment. Elements, 1(4): 205-210.

Landkamer, L.L., Harvey, R.W., Scheibe, T.D. and Ryan, J.N., 2013. Colloid transport in saturated porous media: Elimination of attachment efficiency in a new colloid transport model. Water Resources Research, 49(5): 2952-2965.

Langguth, H.R. and Voigt, R., 2013. Hydrogeologische Methoden. Springer-Verlag.

Lead, J.R. and Wilkinson, K.W., 2007. Current Knowledge and Future Developments. Environmental Particles. IUPAC Series on Analyical and Pysical Chemistry of Environmental Systems, Vol. 10, Lewis, Boca Raton, FL, 159-171 pp.

Lee, J., Kang, J.M. and Choe, J., 2003. Experimental analysis on the effects of variable apertures on tracer transport. Water Resources Research, 39(1): 11 pp.

Li, X., Zhang, P., Lin, C.L. and Johnson, W.P., 2005. Role of Hydrodynamic Drag on Microsphere Deposition and Re-entrainment in Porous Media under Unfavorable Conditions. Environmental Science & Technology, 39(11): 4012-4020.

Lindstrom, F., Boersma, L. and Stockard, D., 1971. A theory on the mass transport of previously distributed chemicals in a water saturated sorbing porous medium: isothermal cases. Soil Science, 112(5): 291-300.

Litton, G.M. and Olson, T.M., 1993. Colloid deposition rates on silica bed media and artifacts related to collector surface preparation methods. Environmental science & technology, 27(1): 185-193.

Logan, B.E., 2012. Environmental Transport Processes. Wiley, 479 pp.

Louis, C., 1969. A study of groundwater flow in jointed rock and its influence on the stability of rock mass. Imperial ollege Rept., London, 10, 90 pp.

Lützenkirchen, J. and Richter, C., 2013. Zeta-potential measurements of OTS-covered silica samples. Adsorption, 19(2-4): 217-224.

Markl, G., 2014. Minerale und Gesteine: Mineralogie – Petrologie – Geochemie. Springer Berlin Heidelberg, 608 pp.

Matschullat, J., Tobschall, H.J. and Voigt, H.J., 2013. Geochemie und Umwelt: Relevante Prozesse in Atmo-, Pedo- und Hydrosphäre. Springer Berlin Heidelberg, 442 pp.

McCarthy, J.F. and McKay, L.D., 2004. Colloid transport in the subsurface: Past, present, and future challenges. Vadose Zone Journal, 3(2): 326-337.

McCarthy, J.F., McKay, L.D. and Bruner, D.D., 2002. Influence of Ionic Strength and Cation Charge on Transport of Colloidal Particles in Fractured Shale Saprolite. Environmental Science & Technology, 36(17): 3735-3743.

McCarthy, J.F. and Zachara, J.M., 1989. Subsurface Transport of Contaminants - Mobile Colloids in the Subsurface Environment May Alter the Transport of Contaminants. Environmental Science & Technology, 23(5): 496-502.

McKay, L.D., Cherry, J.A., Bales, R.C., Yahya, M.T. and Gerba, C.P., 1993a. A field example of bacteriophage as tracers of fracture flow. Environmental Science & Technology, 27(6): 1075-1079.

Mckay, L.D., Gillham, R.W. and Cherry, J.A., 1993b. Field Experiments in a Fractured Clay Till .2. Solute and Colloid Transport. Water Resources Research, 29(12): 3879-3890.

McKay, L.D., Harton, A.D. and Wilson, G.V., 2002. Influence of flow rate on transport of bacteriophage in shale saprolite. J Environ Qual, 31(4): 1095-105.

McKay, L.D., Sanford, W.E. and Strong, J.M., 2000. Field-Scale Migration of Colloidal Tracers in a Fractured Shale Saprolite. Ground Water, 38(1): 139-147.

Meunier, A. and Velde, B.D., 2013. Illite: Origins, Evolution and Metamorphism. Springer Berlin Heidelberg, 288 pp.

Missana, T., Alonso, U., García-Gutiérrez, M. and Mingarro, M., 2008. Role of bentonite colloids on europium and plutonium migration in a granite fracture. Applied Geochemistry, 23(6): 1484-1497.

Molina, F.V., 2016. Soil Colloids: Properties and Ion Binding. CRC Press, 545 pp.

Mondal, P.K. and Sleep, B.E., 2012. Colloid transport in dolomite rock fractures: effects of fracture characteristics, specific discharge, and ionic strength. Environ Sci Technol, 46(18): 9987-94.

Mondal, P.K. and Sleep, B.E., 2013. Virus and virus-sized microsphere transport in a dolomite rock fracture. Water Resources Research, 49(2): 808-824.

Montoya, V., Baeyens, B., Glaus, M.A., Kupcik, T., Marques Fernandes, M., Van Laer, L., Bruggeman, C., Maes, N. and Schäfer, T., 2017. Sorption of Sr, Co and Zn on illite: Batch experiments and modelling including Co in-diffusion measurements on compacted samples. Geochimica et Cosmochimica Acta, 223: 1-20.

Moreno, L., Tsang, Y.W., Tsang, C.F., Hale, F.V. and Neretnieks, I., 1988. Flow and tracer transport in a single fracture: A stochastic model and its relation to some field observations. Water Resources Research, 24(12): 2033-2048.

Möri, A., Alexander, W.R., Geckeis, H., Hauser, W., Schäfer, T., Eikenberg, J., Fierz, T., Degueldre, C. and Missana, T., 2003. The colloid and radionuclide retardation experiment at the Grimsel Test Site: influence of bentonite colloids on radionuclide migration in a fractured rock. Colloids and Surfaces A: Physicochemical and Engineering Aspects, 217(1–3): 33-47.

Morrow, C.A., Moore, D.E. and Lockner, D.A., 2001. Permeability reduction in granite under hydrothermal conditions. Journal of Geophysical Research-Solid Earth, 106(B12): 30551-30560.

Neretnieks, I., 1980. Diffusion in the rock matrix: An important factor in radionuclide retardation? Journal of Geophysical Research: Solid Earth, 85(B8): 4379-4397.

Neretnieks, I., 1990. Solute transport in fractured rock-applications to radionuclide waste repositories, Swedish Nuclear Fuel and Waste Management Co.

Neretnieks, I., 2014. Stress-mediated closing of fractures: Impact of matrix diffusion. Journal of Geophysical Research: Solid Earth, 119(5): 4149-4163.

Neretnieks, I., Eriksen, T. and Tähtinen, P., 1982. Tracer movement in a single fissure in granitic rock: Some experimental results and their interpretation. Water Resources Research, 18(4): 849-858.

Neuman, S.P., 2005. Trends, prospects and challenges in quantifying flow and transport through fractured rocks. Hydrogeology Journal, 13(1): 124-147.

Nicholl, M.J., Rajaram, H., Glass, R.J. and Detwiler, R., 1999. Saturated flow in a single fracture: Evaluation of the Reynolds equation in measured aperture fields. Water Resources Research, 35(11): 3361-3373.

Oda, M., 1986. An equivalent continuum model for coupled stress and fluid flow analysis in jointed rock masses. Water Resources Research, 22(13): 1845-1856.

Ohshima, H., 1998. Sedimentation Potential in a Concentrated Suspension of Spherical Colloidal Particles. Journal of Colloid and Interface Science, 208(1): 295-301.

Ohshima, H., 2001. Approximate Analytic Expression for the Electrophoretic Mobility of a Spherical Colloidal Particle. Journal of Colloid and Interface Science, 239(2): 587-590.

Ohshima, H., 2012. Electrical Phenomena at Interfaces and Biointerfaces: Fundamentals and Applications in Nano-, Bio-, and Environmental Sciences. Wiley, 775 pp.

Okrusch, M. and Matthes, S., 2006. Mineralogie: Eine Einführung in die spezielle Mineralogie, Petrologie und Lagerstättenkunde. Springer Berlin Heidelberg, 522 pp.

Park, C.-K., Vandergraaf, T.T., Drew, D.J. and Hahn, P.-S., 1997. Analysis of the migration of nonsorbing tracers in a natural fracture in granite using a variable aperture channel model. Journal of Contaminant Hydrology, 26(1): 97-108.

Parsons, R., 1966. Permeability of idealized fractured rock. Society of Petroleum Engineers Journal, 6(02): 126-136.

Pekdeger, A. and Matthess, G., 1983. Factors of bacteria and virus transport in groundwater. Environmental Geology, 5(2): 49-52.

Petchsingto, T. and Karpyn, Z.T., 2009. Deterministic Modeling of Fluid Flow through a CT-scanned Fracture Using Computational Fluid Dynamics. Energy Sources Part a-Recovery Utilization and Environmental Effects, 31(11): 897-905.

Pinkus, O. and Sternlicht, B., 1961. Theory of hydrodynamic lubrication, 465 pp.

Pirajno, F. and Cawood, P., 2008. Hydrothermal Processes and Mineral Systems. Springer Netherlands, 1250 pp.

Plaschke, M., Schäfer, T., Bundschuh, T., Ngo Manh, T., Knopp, R., Geckeis, H. and Kim, J.I., 2001. Size Characterization of Bentonite Colloids by Different Methods. Analytical Chemistry, 73(17): 4338-4347.

Poinssot, C. and Geckeis, H., 2012. Radionuclide Behaviour in the Natural Environment: Science, Implications and Lessons for the Nuclear industry. Elsevier Science, 744 pp.

Reiche, T., Noseck, U. and Schäfer, T., 2016. Migration of Contaminants in Fractured-Porous Media in the Presence of Colloids: Effects of Kinetic Interactions. Transport in Porous Media, 111(1): 143-170.

Reid, C., Lunn, R., El Mountassir, G. and Tarantino, A., 2015. A mechanism for bentonite buffer erosion in a fracture with a naturally varying aperture. Mineralogical Magazine, 79(6): 1485-1494.

Reimus, P.W., 1995. The Use of Synthetic Colloids in Tracer Transport Experiments in Saturated Rock Fractures, University of New Mexico, Albuquerque, 264 pp.

Reno, M.D., James, S.C. and Altman, S.J., 2006. Colloid dispersion in a uniform-aperture fracture. J Colloid Interface Sci, 300(1): 383-90.

Rosenbrand, E., Haugwitz, C., Jacobsen, P.S.M., Kjøller, C. and Fabricius, I.L., 2014. The effect of hot water injection on sandstone permeability. Geothermics, 50: 155-166.

Roux, S., Plouraboue, F. and Hulin, J.P., 1998. Tracer dispersion in rough open cracks. Transport in Porous Media, 32(1): 97-116.

Roy, S.B. and Dzombak, D.A., 1996. Colloid release and transport processes in natural and model porous media. Colloids and Surfaces A: Physicochemical and Engineering Aspects, 107: 245-262.

Russel, W.B., Saville, D.A. and Schowalter, W.R., 1989. Colloidal Dispersions. Cambridge University Press, 525 pp.

Ryan, J.N. and Elimelech, M., 1996. Colloid mobilization and transport in groundwater. Colloids and Surfaces A: Physicochemical and Engineering Aspects, 107: 1-56.

Sahimi, M., 2011. Flow and transport in porous media and fractured rock: from classical methods to modern approaches. John Wiley & Sons.

Sausse, J., 2002. Hydromechanical properties and alteration of natural fracture surfaces in the Soultz granite (Bas-Rhin, France). Tectonophysics, 348(1-3): 169-185.

Schäfer, T., Geckeis, H., Bouby, M. and Fanghänel, T., 2004. U, Th, Eu and colloid mobility in a granite fracture under near-natural flow conditions. Radiochimica Acta, 92(9-11): 731-737.

Schäfer, T., Huber, F., Seher, H., Missana, T., Alonso, U., Kumke, M., Eidner, S., Claret, F. and Enzmann, F., 2012. Nanoparticles and their influence on radionuclide mobility in deep geological formations. Applied Geochemistry, 27(2): 390-403.

Scherbaum, F., Knopp, R. and Kim, J., 1996. Counting of particles in aqueous solutions by laser-induced photoacoustic breakdown detection. Applied Physics B, 63(3): 299-306.

Schill, E., Genter, A., Cuenot, N. and Kohl, T., 2017. Hydraulic performance history at the Soultz EGS reservoirs from stimulation and long-term circulation tests. Geothermics, 70(Supplement C): 110-124.

Schneider, C.A., Rasband, W.S. and Eliceiri, K.W., 2012. NIH Image to ImageJ: 25 years of image analysis. Nat Meth, 9(7): 671-675.

Shen, C., Huang, Y., Li, B. and Jin, Y., 2010. Predicting attachment efficiency of colloid deposition under unfavorable attachment conditions. Water Resources Research, 46(11): 12 pp.

Shen, C., Wang, F., Li, B., Jin, Y., Wang, L.P. and Huang, Y., 2012. Application of DLVO energy map to evaluate interactions between spherical colloids and rough surfaces. Langmuir, 28(41): 14681-92.

Shojaei, A. and Shao, J., 2017. Porous Rock Fracture Mechanics: with Application to Hydraulic Fracturing, Drilling and Structural Engineering. Elsevier Science, 336 pp.

Singhal, B.B.S. and Gupta, R.P., 2010. Applied Hydrogeology of Fractured Rocks: Second Edition. Springer Netherlands, 408 pp.

Sirivithayapakorn, S. and Keller, A., 2003. Transport of colloids in saturated porous media: A pore-scale observation of the size exclusion effect and colloid acceleration. Water Resources Research, 39(4): 12 pp.

Sisavath, S., Al-Yaaruby, A., Pain, C.C. and Zimmerman, R.W., 2003. A Simple Model for Deviations from the Cubic Law for a Fracture Undergoing Dilation or Closure. pure and applied geophysics, 160(5): 1009-1022.

Smith, P.A. and Degueldre, C., 1993. Colloid-Facilitated Transport of Radionuclides through Fractured Media. Journal of Contaminant Hydrology, 13(1-4): 143-166.

Snow, D.T., 1965. A parallel plate model of fractured permeable media, University Microfilms, Ann Arbor, Mich., 359 pp.

Stern, O.Z., 1924. Theory of the electrical double layer (In German). Electrochemistry, 30: 508.

Stoll, M., Huber, F.M., Darbha, G.K., Schill, E. and Schäfer, T., 2016. Impact of gravity, collector surface roughness and fracture orientation on colloid retention kinetics in an artificial fracture. Journal of Colloid and Interface Science, 475: 171-183.

Stumm, W., 1993. Aquatic colloids as chemical reactants: surface structure and reactivity. Colloids and Surfaces A: Physicochemical and Engineering Aspects, 73: 1-18.

Stumm, W. and Morgan, J.J., 1996. Aquatic chemistry: chemical equilibria and rates in natural waters. Wiley, 1022 pp.

Suresh, L. and Walz, J.Y., 1996. Effect of surface roughness on the interaction energy between a colloidal sphere and a flat plate. Journal of Colloid and Interface Science, 183(1): 199-213.

Suresh, L. and Walz, J.Y., 1997. Direct measurement of the effect of surface roughness on the colloidal forces between a particle and flat plate. Journal of Colloid and Interface Science, 196(2): 177-190.

Tadros Tharwat, F., 2015. Interfacial Phenomena and Colloid Stability: Basic Principles, 358 pp.

Tang, X.Y. and Weisbrod, N., 2009. Colloid-facilitated transport of lead in natural discrete fractures. Environ Pollut, 157(8-9): 2266-74.

Taylor, S.G., 1953. Dispersion of soluble matter in solvent flowing slowly through a tube. Proceedings of the Royal Society of London. Series A. Mathematical and Physical Sciences, 219(1137): 186-203.

Tchistiakov, A.A., 2000. Physico-Chemical Aspects of Clay Migration and Injectivity Decrease of Geothermal Clastic Reservoirs, World Geothermal Congress 2000, Kyushu - Tohoku, Japan, pp. 3087-3095.

Tenchine, S. and Gouze, P., 2005. Density contrast effects on tracer dispersion in variable aperture fractures. Advances in Water Resources, 28(3): 273-289.

Teuten, E.L., Saquing, J.M., Knappe, D.R.U., Barlaz, M.A., Jonsson, S., Björn, A., Rowland, S.J., Thompson, R.C., Galloway, T.S., Yamashita, R., Ochi, D., Watanuki, Y., Moore, C., Viet, P.H., Tana, T.S., Prudente, M., Boonyatumanond, R., Zakaria, M.P., Akkhavong, K., Ogata, Y., Hirai, H., Iwasa, S., Mizukawa, K., Hagino, Y., Imamura, A., Saha, M. and Takada, H., 2009. Transport and release of chemicals from plastics to the environment and to wildlife. Philosophical Transactions of the Royal Society of London B: Biological Sciences, 364(1526): 2027-2045.

Toran, L. and Palumbo, A.V., 1992. Colloid transport through fractured and unfractured laboratory sand columns. Journal of Contaminant Hydrology, 9(3): 289-303.

Tsang, C.-F. and Neretnieks, I., 1998. Flow channeling in heterogeneous fractured rocks. Reviews of Geophysics, 36(2): 275-298.

Tsang, Y., 1984. The effect of tortuosity on fluid flow through a single fracture. Water Resources Research, 20(9): 1209-1215.

Tsang, Y.W. and Tsang, C.F., 1989. Flow channeling in a single fracture as a two-dimensional strongly heterogeneous permeable medium. Water Resources Research, 25(9): 2076-2080.

Tufenkji, N. and Elimelech, M., 2004. Correlation equation for predicting single-collector efficiency in physicochemical filtration in saturated porous media. Environ Sci Technol, 38(2): 529-36.

Utada, M., 1980. Hydrothermal alteration related to igneous activity in Cretaceous and Neogene formations of Japan. Mining geology japanese special issue, 8: 67-83.

Utsunomiya, S., Kersting, A.B. and Ewing, R.C., 2009. Groundwater nanoparticles in the far-field at the Nevada Test Site: mechanism for radionuclide transport. Environ Sci Technol, 43(5): 1293-8.

Van de Ven, T., 1989. Effects of electrolytes, polymers and polyelectrolytes on particle deposition and detachment. Colloids and surfaces, 39(1): 107-126.

Van Olphen, H., 1977. An Introduction to Clay Colloid Chemistry: For Clay Technologists, Geologists, and Soil Scientists. Interscience Publishers, 301 pp.

van Oss, C.J., Giese, R.F. and Costanzo, P.M., 1990. DLVO and non-DLVO interactions in hectorite. Clays and Clay Minerals, 38(2): 151-159.

Vandamme, D., Foubert, I. and Muylaert, K., 2013. Flocculation as a low-cost method for harvesting microalgae for bulk biomass production. Trends in Biotechnology, 31(4): 233-239.

Velde, B., 1995. Origin and Mineralogy of Clays: Clays and the Environment. Springer Berlin Heidelberg, 335 pp.

Velde, B.D. and Meunier, A., 2008. The Origin of Clay Minerals in Soils and Weathered Rocks. Springer-Verlag, Berlin Heidelberg, 426 pp.

Verwey, E.J.W. and Overbeek, J.T.G., 1955. Theory of the stability of lyophobic colloids. Journal of Colloid Science, 10(2): 224-225.

Vilks, P. and Bachinski, D.B., 1996. Colloid and suspended particle migration experiments in a granite fracture. Journal of Contaminant Hydrology, 21(1-4): 269-279.

Vilks, P. and Baik, M.H., 2001. Laboratory migration experiments with radionuclides and natural colloids in a granite fracture. J Contam Hydrol, 47(2-4): 197-210.

Vilks, P., Miller, N.H. and Vorauer, A., 2008. Laboratory bentonite colloid migration experiments to support the Äspö Colloid Project. Physics and Chemistry of the Earth, Parts A/B/C, 33(14-16): 1035-1041.

Wan, J. and Wilson, J.L., 1994. Colloid transport in unsaturated porous media. Water Resources Research, 30(4): 857-864.

Weisbrod, N., Dahan, O. and Adar, E.M., 2002. Particle transport in unsaturated fractured chalk under arid conditions. Journal of Contaminant Hydrology, 56(1-2): 117-136.

Weisbrod, N., Nativ, R., Adar, E.M. and Ronen, D., 1999. Impact of intermittent rainwater and wastewater flow on coated and uncoated fractures in chalk. Water Resources Research, 35(11): 3211-3222.

Wilkes, J.O. and Bike, S.G., 1999. Fluid Mechanics for Chemical Engineers. Prentice Hall PTR, 752 pp.

Witherspoon, P.A., Wang, J.S., Iwai, K. and Gale, J.E., 1980. Validity of cubic law for fluid flow in a deformable rock fracture. Water resources research, 16(6): 1016-1024.

Wypych, G., 2016. Handbook of Fillers. Elsevier Science, 327 pp.

Yao, K.-M., Habibian, M.T. and O'Melia, C.R., 1971. Water and waste water filtration. Concepts and applications. Environmental Science & Technology, 5(11): 1105-1112.

Zhang, W., Tang, X., Weisbrod, N. and Guan, Z., 2012. A review of colloid transport in fractured rocks. Journal of Mountain Science, 9(6): 770-787.

Zhou, Q., Liu, H.-H., Molz, F.J., Zhang, Y. and Bodvarsson, G.S., 2007. Field-scale effective matrix diffusion coefficient for fractured rock: Results from literature survey. Journal of Contaminant Hydrology, 93(1): 161-187.

Zimmerman, R.W., Al-Yaarubi, A., Pain, C.C. and Grattoni, C.A., 2004. Non-linear regimes of fluid flow in rock fractures. International Journal of Rock Mechanics and Mining Sciences, 41: 163-169.

Zimmerman, R.W. and Bodvarsson, G.S., 1996. Hydraulic conductivity of rock fractures. Transport in Porous Media, 23(1): 1-30.

Zimmerman, R.W., Kumar, S. and Bodvarsson, G.S., 1991. Lubrication theory analysis of the permeability of rough-walled fractures. International Journal of Rock Mechanics and Mining Sciences & Geomechanics Abstracts, 28(4): 325-331.

Zou, L., Jing, L. and Cvetkovic, V., 2017. Modeling of Solute Transport in a 3D Rough-Walled Fracture–Matrix System. Transport in Porous Media, 116(3): 1005-1029.

Zvikelsky, O. and Weisbrod, N., 2006. Impact of particle size on colloid transport in discrete fractures. Water Resources Research, 42(12): 12 pp.

Zvikelsky, O., Weisbrod, N. and Dody, A., 2008. A comparison of clay colloid and artificial microsphere transport in natural discrete fractures. J Colloid Interface Sci, 323(2): 286-92.

Appendix I

Supporting Information to the article “Impact of gravity, collector surface roughness and fracture orientation on colloid retention kinetics in an artificial fracture”

M. STOLL[1*], F. M. HUBER[1], G. K. DARBHA[1,2], E. SCHILL[1], T. SCHÄFER[1,3]

A.I 1 Modeling

Data treatment

Breakthrough curves are obtained within COMSOL MULTIPHYSICS® by counting the number of colloids reaching the outlet for every solution time stored in the simulation (each second in case of injection simulation). This yields a cumulative curve of colloids at the outlet versus time. This dataset is post-processed with the software Origin 9.1. By temporal derivation of the breakthrough curve one obtains the residence time distribution of the colloids.

Governing equations

Flow

The governing equations describing fluid flow through arbitrary geometries are the Navier-Stokes equations. For a steady state laminar flow of a single phase, incompressible Newtonian fluid with constant viscosity can expressed in vector form (Equation 41 & Equation 42) as (Batchelor, 1967):

$$\nabla \cdot \mathbf{u} = 0 \quad \textbf{Equation 41}$$

$$\nabla \cdot (\rho\, \mathbf{u}\, \mathbf{u}) = -\nabla p + \nabla \cdot (\tau) \quad \textbf{Equation 42}$$

where ρ is the fluid density [kg/m³], p the static pressure [Pa], $\mathbf{u}$ [ux, uy, uz] the velocity vector [m/s] and τ the stress tensor [Pa].

Colloid transport

The colloid transport in the model is described by Lagrangian Tracing, drag force and gravity. *Lagrangian Particle Tracing:* The momentum of a colloid in a fluid can be described by Newton´s second law stating that the part total forces acting on a colloid equals the time rate of change of the linear momentum in an inertial reference frame (COMSOL, 2015) (Equation 43):

$$\frac{d}{dt}(m_p u_C) = F_D + F_g + F_{ext} \quad \textbf{Equation 43}$$

where, m_p is the mass of the colloid [kg], u_C is the colloid velocity [m/s], F_D is the drag force [N], F_G is the gravity force [N] and F_{ext} [N] are any other additional forces acting on the colloid (e.g. electrostatic or thermophoretic).

Drag Force: F_D (Equation 41) is defined as Equation 44:

$$F_D = (\frac{1}{\tau_p})m_p(u - u_C) \qquad \textbf{Equation 44}$$

where u is the fluid velocity [m/s] and τ_p the colloid velocity response [s]. The latter is defined assuming spherical colloids in a laminar flow field as Equation 45:

$$\tau_p = \frac{\rho_p d_p^2}{18\eta} \qquad \textbf{Equation 45}$$

where η is the fluid viscosity [kg/m·s], ρ_p is the colloid density [kg/m^3] and d_p is the colloid diameter [m]. Equation 43 is also known as Stokes drag law. With respect to the spherical colloid shape and the colloid Re numbers (<< 1) used in the study, no correction of the drag law (as e.g. Schiller-Naumann) is required.

Gravity: F_g (Equation 43) is defined as Equation 46:

$$F_g = m_p g \frac{(\rho_p - \rho)}{\rho_p} \qquad \textbf{Equation 46}$$

where ρ is the fluid density [kg/m^3] and g is the gravity vector.

Brownian motion: One of the additional forces (F_{ext}) in Equation 43 is, among others, the Brownian motion (F_B), which can be added to Equation 43 with the following term Equation 47:

$$F_B = \alpha \sqrt{\frac{12\pi k_B \eta T R}{\Delta t}} \qquad \textbf{Equation 47}$$

where Δt is the solver time step [s], R is the colloid radius [m], T is the absolute fluid temperature [K], k_B is the Boltzmann constant and α is a normally distributed random number with a mean of zero and a unit standard variation. Every time step, a different value of α is chosen for each single colloid by the software. Generally, as it is the case for diffusion of solutes, the Brownian motion leads to spreading of colloids from areas of higher colloid density to lower colloid density.

A.I 2 Colloid transport experiments

Preparation of the acrylic glass disc

After cutting the acrylic glass disc, the surfaces are sanded down using a granulation size up to 1000. In the next step the surfaces of the disc are polished using polishing paste (Fakopol®, Fako, Germany) and all remains are removed by ultrasound. Before inserting the disc into the setup, the disc is cleaned using first ethanol and afterwards Milli-Q water.

Equilibration of the granodiorite disc

A saturation and equilibration of the granodiorite disc overnight was sufficient. The electrolytic solution for equilibration drifted slightly to neutral pH (ΔpH < 0.3) most likely because of the partial pressure of CO_2 on top of the solution. Flushing the whole setup after installation of at least 1 h was sufficient as well since the pH measured at the outlet was constantly pH 5 ± 0.1. Due to experimental conditions, almost every time the flushing takes longer (> 6 h).

We also checked the calcium content to be sure that we are below the critical coagulation concentration (CCC). Therefore, using ICP-MS we measure the calcium content of the fluid in the fracture, which was in contact with the granodiorite for 3 days. In ≈ 1 mL fluid the concentration of calcium was 159.8 ± 0.5 µg/L ($I = 0.008$).

Overview of the stop-flow experiments

A.I 1: Table of stop-flow experiments

#	Colloid Size [nm]	Collector Surface material	Orientation	Residence Time [h]	Recovery [%]	Repeated
1	1000	Granodiorite	Horizontal	1	84.7	
2	1000	Granodiorite	Horizontal	3	66.6	
3	1000	Granodiorite	Horizontal	14	16.6	x
4	1000	Granodiorite	Horizontal	24	11.3	
5	1000	Granodiorite	Vertical	1	81.2	x
6	1000	Granodiorite	Vertical	3	75.5	
7	1000	Granodiorite	Vertical	14	49.0	
8	1000	Granodiorite	Vertical	24	33.0	x
9	1000	Acrylic Glass	Horizontal	1	90.2	
10	1000	Acrylic Glass	Horizontal	3	69.0	x
11	1000	Acrylic Glass	Horizontal	14	15.9	x
12	1000	Acrylic Glass	Horizontal	24	10.1	

13	1000	Acrylic Glass	Vertical	1	85.1	x
14	1000	Acrylic Glass	Vertical	3	77.1	
15	1000	Acrylic Glass	Vertical	14	50.7	x
16	1000	Acrylic Glass	Vertical	24	33.6	x
17	25	Granodiorite	Horizontal	1	50.0	x
18	25	Granodiorite	Horizontal	3	46.2	
19	25	Granodiorite	Horizontal	14	19.2	
20	25	Granodiorite	Horizontal	24	13.6	
21	25	Granodiorite	Vertical	1	42.0	
22	25	Granodiorite	Vertical	3	42.4	x
23	25	Granodiorite	Vertical	14	17.2	x
24	25	Granodiorite	Vertical	24	14.8	
25	25	Acrylic Glass	Horizontal	1	75.4	x
26	25	Acrylic Glass	Horizontal	3	70.4	x
27	25	Acrylic Glass	Horizontal	14	36.9	
28	25	Acrylic Glass	Horizontal	24	31.8	
29	25	Acrylic Glass	Vertical	1	63.7	x
30	25	Acrylic Glass	Vertical	3	64.4	
31	25	Acrylic Glass	Vertical	14	42.2	
32	25	Acrylic Glass	Vertical	24	35.7	x

A.I 3 Modeled BTCs

1000 nm colloids

A.I 2 shows the modeled colloid breakthrough curves after flushing the cell with 7 mL/h for 2 h after 1 h, 3 h, 6 h, 14 h and 24 h stop-flow both for unfavorable (no sorption) and favorable (full sorption) attachment conditions, respectively (horizontal case (a and b) and vertical case (c and d)). Similar to the experimental BTCs we see that with increasing residence time the height and the width of the BTCs decrease in all cases. As expected in cases of favorable attachment conditions there is a noticeable higher decrease and a shorter tailing, which reaches $C/C_0 = 0$ after four pore volumes compared to unfavorable attachment conditions. Comparable to the experimental findings in case of horizontal fracture orientation a double peak evolves after 6 h residence time both in case of full sorption and no sorption. Contrary to that and similar to the experiments with vertical fracture orientation in both cases a single peak develops between 6 and 14 hours. Comparing these results the development of either a double or a single peak results due to fracture orientation, more precisely to gravity and the geometry of the artificial fracture.

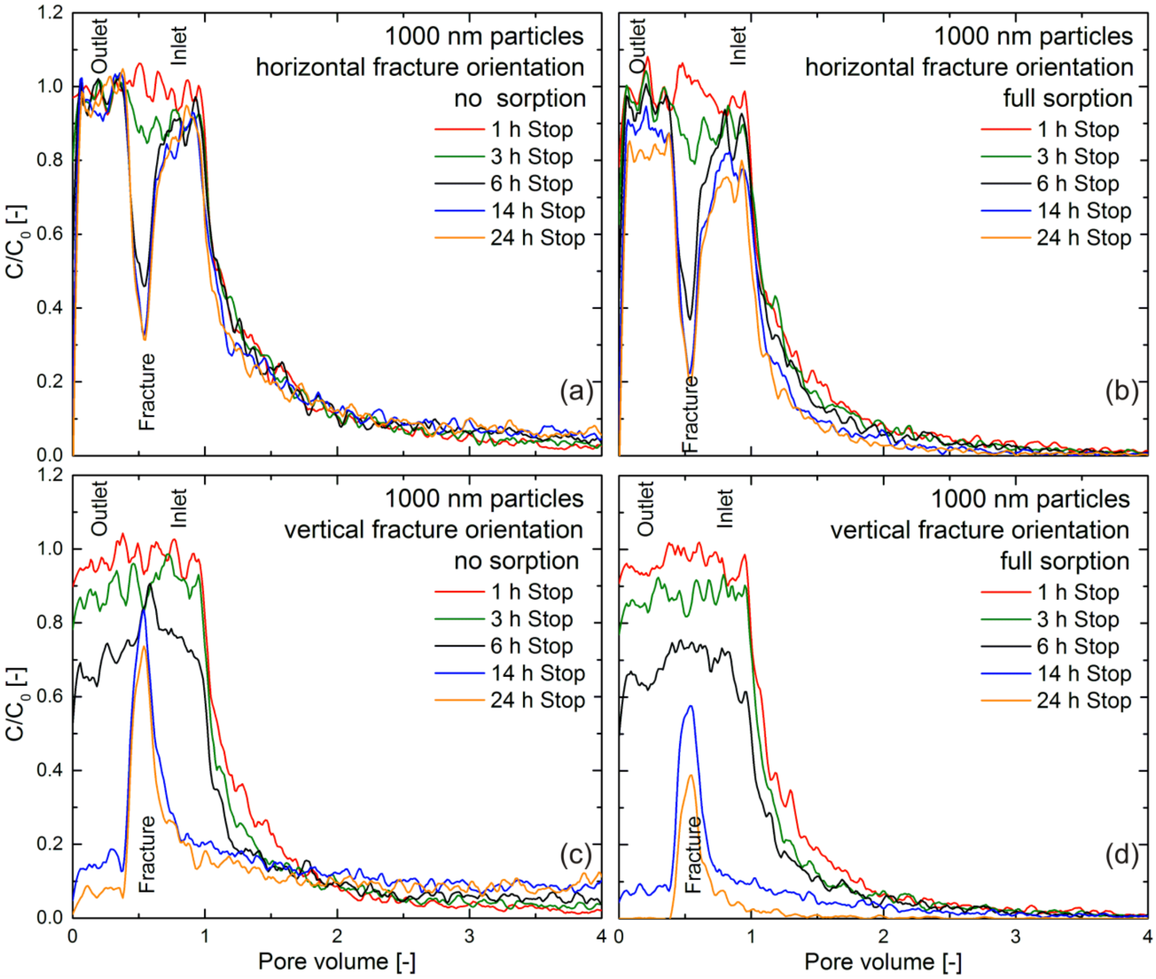

A.I 2: Modeled BTCs after of the 1000 nm colloid experiments flushing the cell with 7 mL/h for 2 h after 1 h, 3 h, 6 h, 14 h and 24 h stop-flow both for unfavorable (no sorption) and favorable (full sorption) attachment conditions for the vertical fracture orientation. The expected signal of the inlet, the outlet and the fracture are marked in the diagrams.

25 nm colloids

A.I 3 shows the modeled colloid breakthrough curves after flushing the cell with 7 mL/h for 2 h after 1 h, 3 h, 6 h, 14 h and 24 h stop-flow both for unfavorable (no sorption) and favorable (full sorption) attachment conditions, respectively (horizontal case (a and b) and vertical case (c and d)). Similar to the experimental BTCs we see that with increasing residence time the height and the width of the BTCs decrease in all cases as well. As expected in case of favorable attachment conditions the decreases of the BTCs is higher and the tailings shorter ($C/C_0 = 0$ after 2.5 pore volume) compared to unfavorable attachment conditions. Comparable to the experimental findings, there is no difference between the horizontal and vertical fracture orientation. In case of “no sorption” no double peak evolves with increasing residence time. In case of full sorption a double peak shape of the BTCs is already visible after 1 h contact time in both cases. Comparing these results with the experimental findings the retention within the fracture cell and the development of the double peak shape is due to attachment of the colloids to the fracture/setup material and not due to gravity of the colloids.

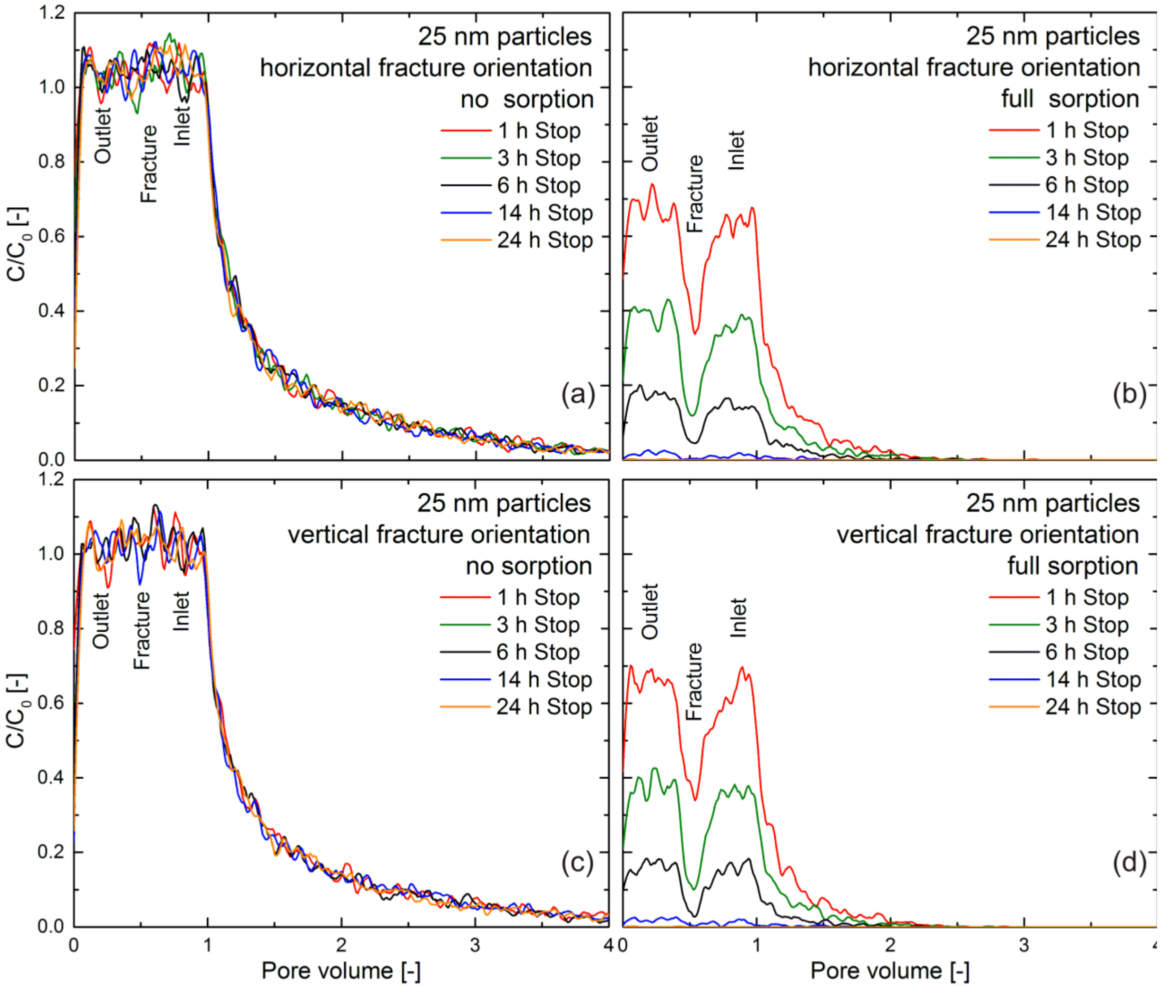

A.I 3: Modeled BTCs of 25 nm colloids experiments after flushing the cell with 7 mL/h for 2 h after 1 h, 3 h, 6 h, 14 h and 24 h stop-flow both for unfavorable (no sorption) and favorable (full sorption) attachment conditions for the vertical fracture orientation. The expected signal of the inlet, the outlet and the fracture are marked in the diagrams.

A.I 4 AFM

Diffuse layer potential of the collector surface materials

A.I 4 shows the approach force curves obtained by AFM measurements using the colloid probe technique (1000 nm carboxylated polystyrene colloid). These approach force curves are fitted using the DLVO theory to obtain the diffuse layer potential. In the shape of the curves it is visible that repulsive forces dominate while approaching the colloid to the surface. In respect on the overall negative diffuse layer potentials it is safe to assume that the observed colloid retention is not due to electrostatic interaction.

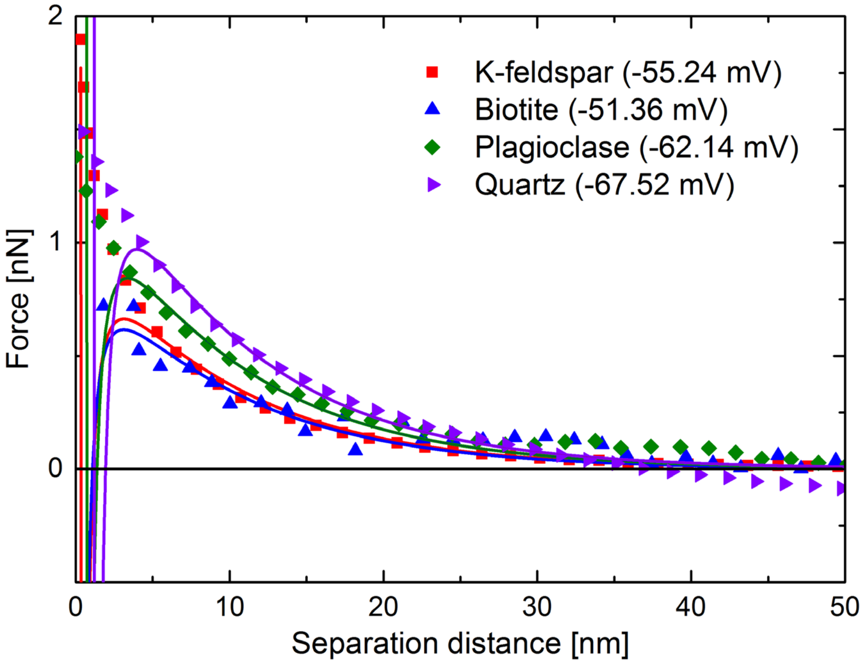

A.I 4: Approach force curves obtained with AFM and the colloid probe technique using one 1000 nm polystyrene colloid. Approach force curves are fitted using DLVO theory to predict diffuse layer potential.

Procedure for the calculation of zeta potentials of the minerals on granodiorite surface using AFM colloid probe technique and DLVO theory

The zeta potential of the acrylic glass (–48.7 mV) was determined by using streaming potential analysis at pH 5 and 1 mM NaCl. The AFM colloid probe technique is applied to obtain force curves under the similar conditions between acrylic glass and polystyrene colloid (carboxylate functionality) modified cantilever (purchased from Nova scan technologies, USA) of 1000 nm. The force curves are processed in SPIP software (Image metrology, Denmark) to correct the baseline and hysteresis. The unknown diffuse layer potential of the colloid is predicted to be –58.9 mV by fitting the approach curve using DLVO theory according to Assemi et al. (2006). A code was developed using python software to import the force curves and to fit the DLVO equation. For fitting, the Hamaker constant of the polystyrene-water-acrylic glass system is taken to be 4.7E–21 J calculated from their individual values according to Bradford and Torkzaban (2008). Similarly, the force curves are obtained on granodiorite surface at various pre-identified spots according to their mineralogy (SEM/EDX). Further, the similar procedure is followed to predict the unknown surface potential of these minerals. Here in case of granodiorite, as calculated by Chinju et al. (2001) the Hamaker constant of granodiorite-water-polystyrene is considered to be 1.96E–20 J.

A.I 6 References

Assemi, S., Nalaskowski, J. and Johnson, W.P., 2006. Direct force measurements between carboxylate-modified latex microspheres and glass using atomic force microscopy. Colloids and Surfaces A: Physicochemical and Engineering Aspects, 286(1–3): 70-77.

Batchelor, G.K., 1967. An Introduction to Fluid Dynamics. Cambridge University Press, 615 pp.

Bradford, S.A. and Torkzaban, S., 2008. Colloid Transport and Retention in Unsaturated Porous Media: A Review of Interface-, Collector-, and Pore-Scale Processes and Models All rights reserved. No part of this periodical may be reproduced or transmitted in any form or by any means, electronic or mechanical, including photocopying, recording, or any information storage and retrieval system, without permission in writing from the publisher. Vadose Zone Journal, 7(2): 667-681.

Chinju, H., Kuno, Y., Nagasaki, S. and Tanaka, S., 2001. Deposition Behavior of Polystyrene Latex Particles on Solid Surfaces during Migration through an Artificial Fracture in a Granite Rock Sample. Journal of Nuclear Science and Technology, 38(6): 439-443.

COMSOL, 2015. COMSOL Multiphysics®. Version 5.0. COMSOL AB, Stockholm, Sweden. http://www.comsol.de/

Appendix II

Supporting Information to the article “Nanoparticulate illite transport experiments in the ultra-trace concentration range investigated by Laser-Induced Breakdown Detection (LIBD)”

M. STOLL[1*], F. M. HUBER[1], E. SCHILL[1], T. SCHÄFER[1]

A.II 1 Breakthrough curves of the 6 h stop-flow experiments

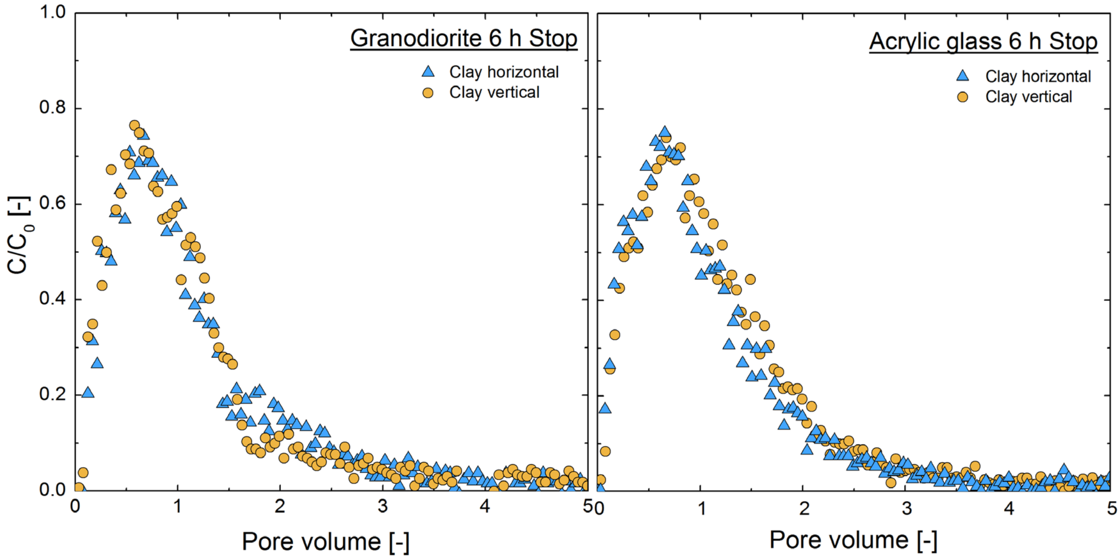

A.II 1: BTCs of 6 h stop-flow experiments on granodiorite (left) or acrylic glass (right) using Na-illite colloids for horizontal (triangles) and vertical (circles) fracture orientation.

Appendix III

Supplementary information to the article “Experimental and numerical investigations on the effect of fracture geometry and fracture aperture distribution on flow and solute transport in natural fractures”

M. STOLL, F.M. HUBER, M. TRUMM, F. ENZMANN, D. MEINEL, A. WENKA, E. SCHILL, T. SCHÄFER

A.III 1

The modal Variscan Soultz porphyritic granite consists of orthoclase (18.8%), oligoclase (39.9%), quartz (28.4%), biotite (8.4%) and amphibole (4.5%) (Ledésert (1999) after Genter (1989)). In some zones, the composition of the granite is strongly altered: primary quartz shows to be totally dissolved, oligoclase is replaced by illite or tosudite (clay minerals), biotite and amphibole by chlorite and epidote (Ledésert & Hébert, 2012).

The altered fractured granite core was described as a cataclased, hydrothermal porphyroid red granite:

- pervasive degree = 0; no pervasive alteration or no information about pervasive alteration (the range of pervasive alteration ranges from 0 to 7)
- vein alteration = 4 (moderate to high) (the range of vein alteration ranges from 0 to 7)
- cataclase intensity = 3 (high) (the range of cataclase intensity ranges from 0 to 3)
- megacryst K-feldspar fracturation = 3 (high) (the range of megacryst K-feldspar fracturation ranges from 0 to 3)
- reddish biotites
- soft-clayed yellow and pink hematized plagioclases
- orange and red-brick K-feldspar

The unaltered fractured granite core was described as a standard porphyroid granite (grey-white):

- pervasive degree = 1 (low) (the range of pervasive alteration ranges from 0 to 7)
- The standard granite is described in Genter et al. (1997): “The standard granite is fairly, homogeneous and composed of a porphyritic granite with abundant K-feldspar megacrysts (1–7 cm in size) in a coarse-grained matrix including: quartz, plagioclase, K-feldspar, biotite, hornblende and accessory minerals (titanite, Fe-Ti oxides, apatite, zircon, allanite, sulfides). This mineralogical assemblage gives a whole grey-pink

color to sound granite facies. Average chemical composition of the porphyritic standard granite suggests a granodiorite to monzogranite. Range of content of the main elements is: SiO_2 (68%), TiO_2 (0.50%), Al_2O_3 (14.8%), Fe_2O_3 (3%), CaO (2.2%), Na_2O (4%), K_2O (4.5%), U (10 ppm) and Th (30–35 ppm)".

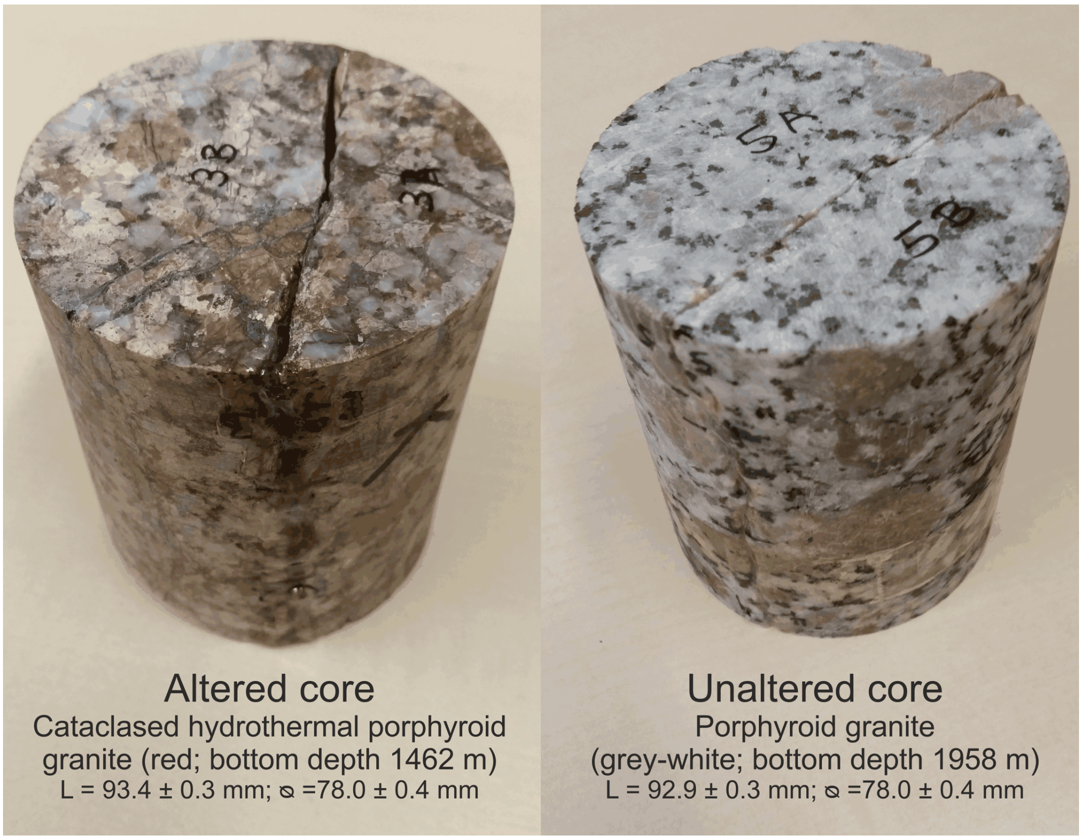

A.III 1: Selected and cut granite fracture samples of exploration well EPS-1. Drill core dimensions after cutting are ≈ 93 mm in length and ≈ 78 mm in diameter.

A.III 2

- Prior to emplacing the granite fractures in acrylic glass tubes (Polymethyl methacrylate, PMMA, trademark Plexiglas®), the two fracture sides were cleaned to remove loose particles, debris and dust using compressed air. In the next step, the sutures at the long sides of the cores are sealed using two-component glue (UHU Epoxy Adhesives 2-Component). Care is taken to prevent as much as possible the intrusion of the resin into the fracture by always placing the core side upside down during the application of several thin layers of glue. The sealing of the opposite open core side is done after the glue has been hardened completely on the first side. This sealing procedure minimizes any unwanted intrusion of the bedding material (acrylic glass glue) into the fracture while preparing the flow cell. The sealed core is emplaced inside an acrylic glass cylinder, and the remaining space is filled up with acrylic glass glue. Two endcaps with three inlets/outlets each are assembled at the open sides (both top and bottom) of the fracture. Between the fracture inlet/outlet and the cap a 1 mm thick elastic plastic foil (Mipolan) is placed to keep the fracture flow cell leak-proof. To minimize any artificial dispersion the tubing was placed directly above fracture inlets and outlets.

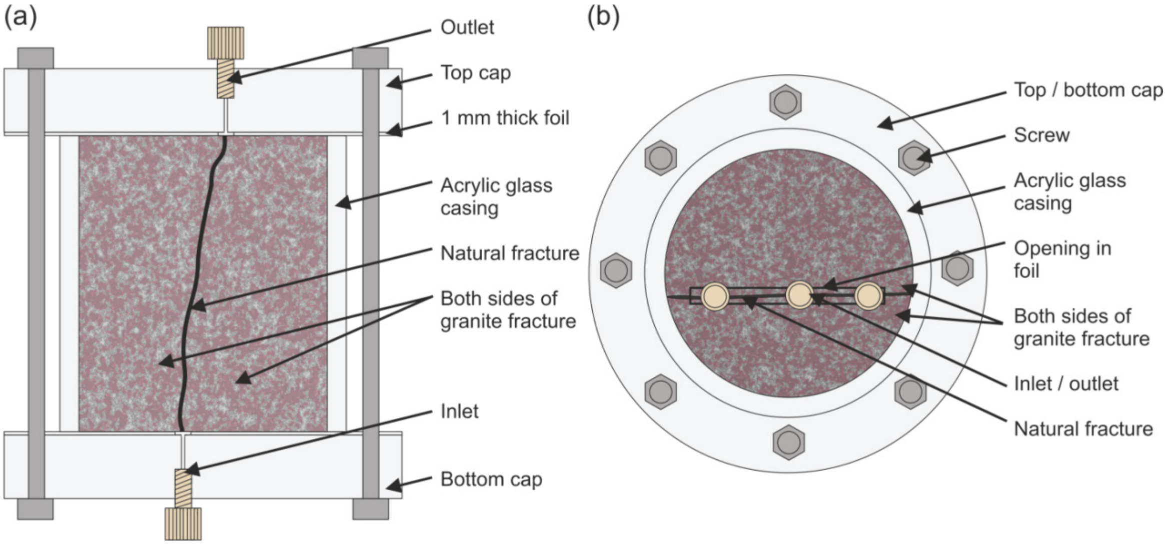

A.III 2: (a) Scheme of the fracture flow cell containing the natural fractured drill core. (b) Top/Bottom view on the fracture flow cell. Three inlets/outlets are arranged along the fracture in different distances.

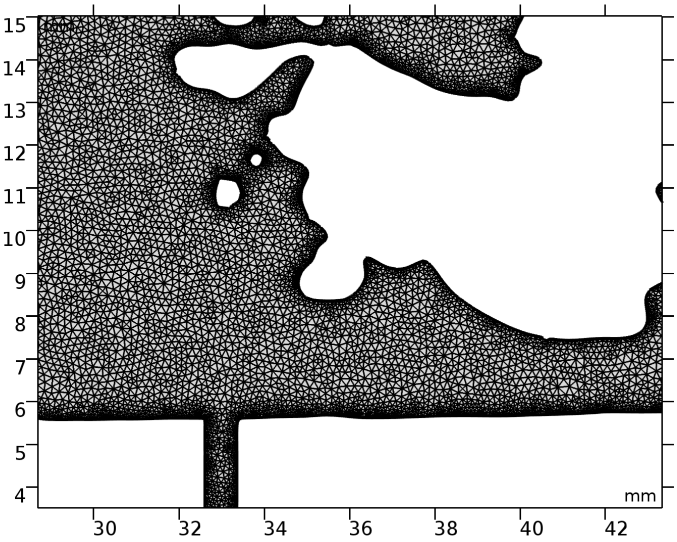

A.III 3: Zoom around the second inlet of the altered fracture of the model mesh. The element size of the mesh in the vicinity of the fracture boundaries decreases.

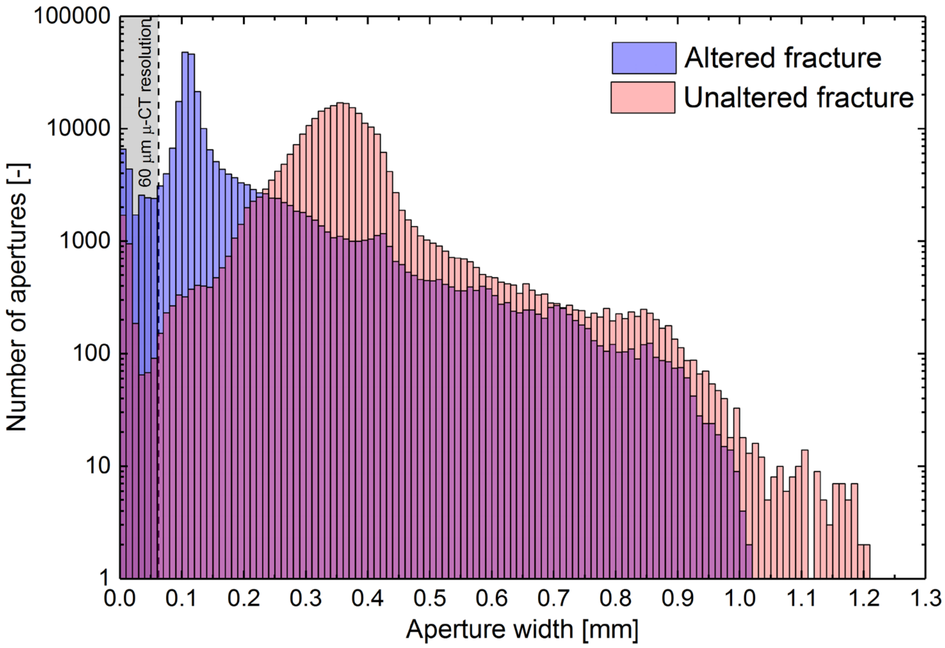

A.III 4: Aperture distributions of altered and unaltered fracture with a class size of 0.01 mm. Resolution of the µ-CT measurement is 60 µm.

A.III 5: Statistic of the model derived flow velocities and Reynolds numbers of the experimental cases through the altered fracture.

Altered fracture experiments	*Flow velocity [m/s]*					*Reynolds number [-]*				
Experiment	Mean	Standard deviation	Variance	Minimum	Maximum	Mean	Standard deviation	Variance	Minimum	Maximum
A1-1_12 mL/h	1.22E–04	5.01E–04	2.51E–07	0	0.01488	0.00297	0.00905	8.19E–05	0	0.32786
A1-1_24 mL/h	2.44E–04	0.001	1.00E–06	0	0.02998	0.00594	0.01811	3.28E–04	0	0.65486
A1-2_12 mL/h	1.22E–04	5.05E–04	2.55E–07	0	0.01477	0.00298	0.00909	8.26E–05	0	0.33093
A1-2_24 mL/h	2.45E–04	0.00101	1.02E–06	0	0.02937	0.00595	0.01815	3.29E–04	0	0.65929
A1-3_12 mL/h	1.26E–04	5.01E–04	2.51E–07	0	0.01496	0.00309	0.00921	8.49E–05	0	0.34106
A1-3_24 mL/h	2.52E–04	0.001	1.00E–06	0	0.02967	0.00618	0.01843	3.40E–04	0	0.68097
A2-1_12 mL/h	1.25E–04	5.01E–04	2.51E–07	0	0.01443	0.00306	0.00933	8.71E–05	0	0.31812
A2-1_24 mL/h	2.51E-04	0.001	1.01E-06	0	0.02906	0.00613	0.01867	3.49E-04	0	0.63502
A2-2_12 mL/h	1.26E-04	5.05E-04	2.55E-07	0	0.01432	0.00307	0.00937	8.78E-05	0	0.32024
A2-2_24 mL/h	2.51E-04	0.00101	1.02E-06	0	0.02849	0.00613	0.01871	3.50E-04	0	0.63862
A2-3_12 mL/h	1.29E-04	5.01E-04	2.51E-07	0	0.01451	0.00318	0.00948	8.99E-05	0	0.33071
A2-3_24 mL/h	2.59E-04	0.001	1.00E-06	0	0.02878	0.00635	0.01896	3.60E-04	0	0.66034
A3-1_12 mL/h	1.39E-04	5.06E-04	2.56E-07	0	0.01438	0.00339	0.00932	8.68E-05	0	0.28758
A3-1_24 mL/h	2.77E-04	0.00101	1.02E-06	0	0.02895	0.00677	0.01864	3.47E-04	0	0.57374
A3-2_12 mL/h	1.34E-04	5.11E-04	2.61E-07	0	0.0145	0.00326	0.00938	8.80E-05	0	0.29466
A3-2_24 mL/h	2.68E–04	0.00103	1.05E–06	0	0.03099	0.00652	0.01882	3.54E–04	0	0.59303
A3-3_12 mL/h	1.20E–04	5.09E–04	2.59E–07	0	0.01446	0.0029	0.00955	9.12E–05	0	0.29700
A3-3_24 mL/h	2.40E–04	0.00102	1.05E–06	0	0.03099	0.0058	0.01919	3.68E–04	0	0.60162

A.III 6: Statistic of the model derived flow velocities and Reynolds numbers of the experimental cases through the unaltered fracture.

Unaltered fracture experiments	*Flow velocity [m/s]*					*Reynolds number [-]*				
Experiment	Mean	Standard deviation	Variance	Minimum	Maximum	Mean	Standard deviation	Variance	Minimum	Maximum
U1-3 12 mL/h	1.16E–04	5.04E–04	2.54E–07	0	0.01272	0.00263	0.00736	5.41E–05	0	0.27012
U1-3 24 mL/h	2.32E–04	0.00101	1.02E–06	0	0.02544	0.00526	0.01472	2.17E–04	0	0.53877
U1-2 12 mL/h	1.13E–04	5.04E–04	2.54E–07	0	0.01272	0.00255	0.00738	5.45E–05	0	0.27522
U1-2 24 mL/h	2.26E–04	0.00101	1.02E–06	0	0.02544	0.00509	0.01477	2.18E–04	0	0.55
U1-1 12 mL/h	1.16E–04	5.23E–04	2.73E–07	0	0.01272	0.00256	0.00728	5.31E–05	0	0.27012
U1-1 24 mL/h	2.32E–04	0.00105	1.09E–06	0	0.02544	0.00511	0.01457	2.12E–04	0	0.53877
U2-3 12 mL/h	1.15E–04	5.16E–04	2.66E–07	0	0.01275	0.00258	0.00741	5.50E–05	0	0.25789
U2-3 24 mL/h	2.31E–04	0.00103	1.06E–06	0	0.02547	0.00517	0.01483	2.20E–04	0	0.51629
U2-2 12 mL/h	1.13E–04	5.16E–04	2.66E–07	0	0.01279	0.00253	0.00743	5.53E–05	0	0.27772
U2-2 24 mL/h	2.26E–04	0.00103	1.06E–06	0	0.02554	0.00505	0.01486	2.21E–04	0	0.555
U2-1 12 mL/h	1.18E–04	5.34E–04	2.85E–07	0	0.01272	0.00259	0.00733	5.37E–05	0	0.2548
U2-1 24 mL/h	2.35E–04	0.00107	1.14E–06	0	0.02544	0.00517	0.01465	2.15E–04	0	0.5074
U3-3 12 mL/h	1.14E–04	5.03E–04	2.53E–07	0	0.01278	0.00257	0.00742	5.51E–05	0	0.26372
U3-3 24 mL/h	2.28E–04	0.00101	1.01E–06	0	0.0255	0.00514	0.01485	2.20E–04	0	0.52721
U3-2 12 mL/h	1.13E–04	5.03E–04	2.53E–07	0	0.01278	0.00254	0.00744	5.53E–05	0	0.2767
U3-2 24 mL/h	2.25E–04	0.00101	1.01E–06	0	0.0255	0.00508	0.01488	2.21E–04	0	0.55297
U3-1 12 mL/h	1.19E–04	5.21E–04	2.71E–07	0	0.01278	0.00265	0.00732	5.36E–05	0	0.26372
U3-1 24 mL/h	2.38E–04	0.00104	1.08E–06	0	0.0255	0.0053	0.01464	2.14E–04	0	0.52721

A.III.5 References

Genter, A., 1989. Géothermie Roches Chaudes Sèches : le granite de Soultz-sous-Forêts (Bas Rhin, France). Fracturation naturelle, altérations hydrothermales et interaction eau–roche., Univ. Orléans, 201 pp.

Genter, A., Traineau, H. and Artignan, D., 1997. Synthesis of geological and geophysical data at Soultz-sous-Forêts (France). Rapport BRGM R 39440, p.36, 10 figures, 11 tableaux, 4 annex.

Ledesert B., B.G., Meunier A., Genter A., Bouchet A., 1999. Diagenetic-type reactions related to hydrothermal alteration in the Soultz-sous-Forêts granite, France. European Journal of Mineralogy, 1(11): 731-741.

Ledésert, B.A. and Hébert, R.L., 2012. The Soultz-sous-Forêts' enhanced geothermal system: a granitic basement used as a heat exchanger to produce electricity, Heat Exchangers-Basics Design Applications. InTech.

Appendix IV

Supporting Information to Section 5 “Colloid transport experiments of nanoparticulate illite in the ultra-trace concentration range through natural granite fractures investigated by Laser-Induced Breakdown Detection (LIBD)”

M. STOLL, F. M. HUBER, J. LÜTZENKIRCHEN, E. SCHILL, T. SCHÄFER

A.IV 5 Streaming potential measurements

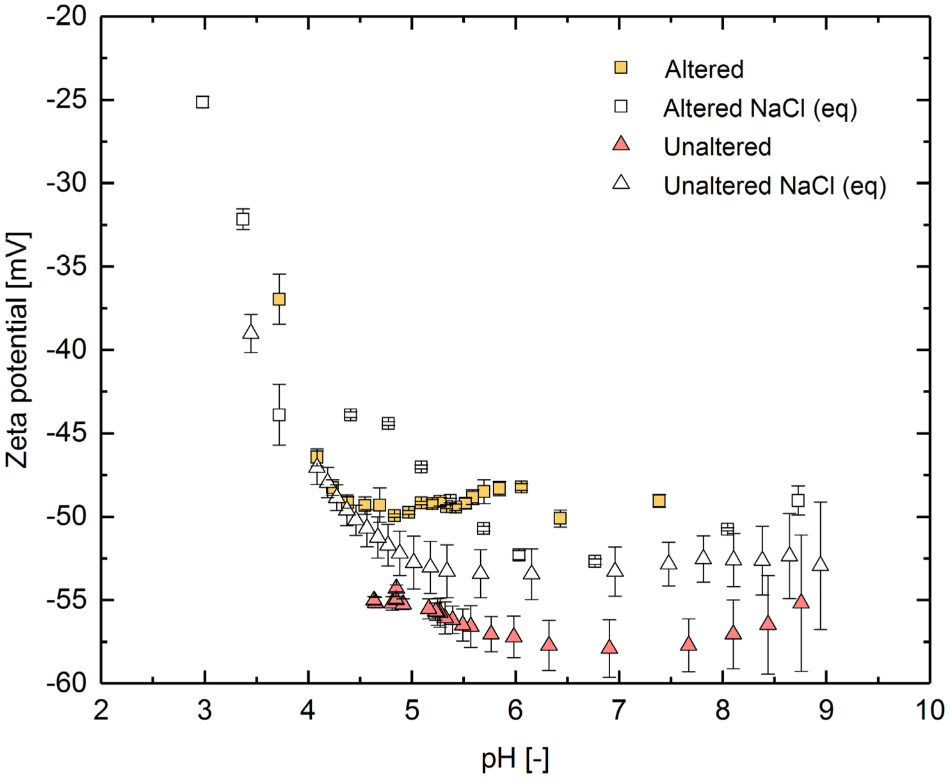

A.IV 1: Streaming potential measurements of background electrolytes for the altered and the unaltered granite fracture and equivalent NaCl suspensions.